الجمهورية الجزائرية الديمقراطية الشعبية

PEOPLE'S DEMOCRATIC REPUBLIC OF ALGERIA MINISTRY OF HIGHER EDUATION AND SCIENTIFIC RESEARCH FARHAT ABBAS UNIVERSITY SETIF-1- ALGERIA



PhD Thesis

Presented at Institute of Optics and Mechanics of Precision

To obtain the title of

Doctor in Materials & Engineering

Option: Mechanics of Precision

By:

HAMDANI SOUMIA

THEME

"Contribution to Study the Effect of Semi-coherent Interfaces on the Mechanical Behavior of Metallic Multilayers by MD Simulations"

Defended on 12/07/2025 in front of a Jury Composed of:

OUAKDI El hadj	U. F.A. SETIF -1-	Professor	President
ABDESLAM Saad	U. F.A. SETIF-1-	Professor	Reporter
HARTMAIER Alexander	U. Bochum Germany	Professor	Co- Reporter
REDJAIMIA Abdelkrim	U. Lorraine, France	Professor	Examiner
DAOUD Saleh	U.B.B.A	Professor	Examiner
SELMANI Houssem	U. F.A. SETIF-1-	MCA	Examiner

International and National Communications during this PhD Journey:

- Hamdani S, Abdeslam S, Hartmaier A, Janisch R. "Atomistic Simulations of Model Size Effects on the Mechanical Behavior of Fe and V Single Crystals under Nano-Indentation" *Poster communication* at National Conference. (November 2024) Constantine, Algeria.
- Hamdani S, Abdeslam S, Hartmaier A, Janisch R. "Atomistic Insights into the Inverse Effects of Semi-Coherent Interfaces on Plastic Deformation of V-Fe Bilayer during Nano-indentation". Oral communication at International Conference. (October 2024) Setif, Algeria.
- Hamdani S, Abdeslam S, Hartmaier A, Janisch R. "The Influence of V Layer Thickness on the Mechanical Behavior of V/Fe Bilayers under Nano-indentation" *Poster communication at National Conference (May 2024)*. *Algers, Algeria*.
- Hamdani S, "Nano-indentation of bcc Vanadium: Atomistic Simulation of Plastic Deformation".
 Poster communication at International Conference. (November 2023) Sétif, Algeria.
- Hamdani S, Abdeslam S, "Interatomic Potential Effect on the Mechanical Behavior of Fe and V Single Crystals, At Molecular Dynamic Simulation". *Oral communication at international conference*.
 (October 2022) Ourgela, Algeria.
- Hamdani S, Abdeslam S, "The effect of Semi-coherent interface existence on the mechanical behavior of V/Fe bilayer". Oral communication at International Conference. (November 2021) Khenchela, Algeria.
- Hamdani S, Abdeslam S, "Temperature Effect on the Plasticity of Vanadium Single Crystal" Oral communication at International Conference. (September 2021) Oran, Algeria.
- Hamdani S, Abdeslam S, "Probing the Mechanical Properties of Single Crystal Iron (Fe) at Nano-scale With Nano-Indentation by Molecular Dynamic Simulation". Poster communication at International Conference. (September 2019) Sétif, Algeria.

Publications:

Hamdani S, Abdeslam S, Hartmaier A, Janisch R. "Atomistic simulation of the influence of semi-coherent interfaces in the V/Fe bilayer system on plastic deformation during nanoindentation. Modelling and Simulation in Materials Science and Engineering". Published online April 18, 2024. DOI: https://doi.org/10.1088/1361-651x/ad3b28. From a Mother to Her Mother and Son...
(A Story of Sacrifice in Pursuit of Knowledge).



Acknowledgement

First and foremost, I am profoundly grateful to Allah for granting me strength, patience, and guidance throughout this PhD journey. Without His countless blessings and mercy, none of this would have been possible. Alhamdulillah.

I would like to express my deepest gratitude to my supervisors, Prof. SAAD ABDESLAM and Prof. ALEXANDER HARTMIER, for their dedicated support, insightful guidance, and invaluable advice throughout this journey. Your mentorship and encouragement have been indispensable not only in shaping this research but also in my development as a researcher.

I am especially grateful to Dr. REBCCA JANISCH for her exceptional support and collaboration throughout this work. Her keen insights, meticulous attention to details, and dedication have been invaluable at every step of this research. Her expertise in simulations has significantly enhanced the quality of our publication, and her collaboration has made this journey both enriching and rewarding. Thank you, REBECCA, for being an outstanding co-author and research guide.

I am also immensely grateful to the members of my dissertation committee, for their time, constructive feedback, and expertise, which helped me refine my research and push it to a higher level.

I extend my sincere gratitude to Prof. CHAOUI ZINE EL ABIDINE, Prof. KHALED BOUAMAMA, Prof. BELKHIR NABIL, Dr. ASHISH CHAUNIYAL, Dr. ABDELAZIZ OUATIZERGA, Dr. MEHDI BRAHIM, and Dr. RIADH BOURZAMI for their invaluable support and the enriching discussions we have shared. Your support and encouragement have been a constant inspiration throughout this journey.

I would also like to acknowledge the financial support provided by Sétif-1 University and Bochum University, which played a crucial role in facilitating this research.

Finally, my most serious and heartfelt gratitude goes to my dearest family for their persistent love and support. To my husband, my sisters, my brother and my parents, thank you for your endless patience, love, and strength, especially during the most challenging moments of this journey. Alhamdulillah, this achievement is a piece of evidence of your prayers, sacrifices, and resolute belief on me.



Abstract

This thesis investigates the role of BCC/BCC semi-coherent interfaces on the mechanical response of V/Fe bilayers under nano-indentation, tension, and compression. Using atomistic simulations, we analyze the effects of layer thickness, indenter position, and crystallographic orientation. Our findings reveal that the V/Fe interface acts as a dislocation barrier during nano-indentation, enhancing hardness through blocking dislocation propagation. This effect is more pronounced in thinner vanadium layers, aligning with the Hall-Petch model. On the other hand, in Fe/V bilayers, the interface promotes dislocation propagation, allowing the decomposition of lattice dislocations in the substrate and leading to a softening effect consistent with the inverse Hall-Petch effect. These results are also observable in the V-Fe-V and Fe-V-Fe multilayers.

Under uniaxial loading, analytical investigations of plastic deformation mechanisms during tension and compression reveal a complex interplay between anti-twinning/ twinning and slip deformations in both V and Fe layers. Tension strengthens the V/Fe bilayer due to the decomposition of misfit dislocation inside V layer and anti-twinning in Fe. Whereas, Softening is observed during compression as deformation initiates in the softer V layer via phase transition. While misfit dislocations decompose inside Fe, activating slip deformation. This tension/compression asymmetry of the V/Fe bilayer is driven by shear strain evolution at the interface.

This study provides fundamental insights into dislocation-interface interactions, strengthening mechanisms, and deformation anisotropy in nano-scale metallic multilayers.

Keywords: Semi-coherent interface, Multilayer, Nano-indentation, Dislocation-interface interaction, Misfit Dislocation (MFD), Tension/Compression asymmetry, Atomistic simulation.

TABLE OF CONTENTS

General introduction	1
Chapter I: literature review	4
I.1 Interfaces types	5
I.2 Effect of different interface types on the mechanical response	of multilayers under
indentation	6
I.3 Layer thickness effect	8
I.4 Tension and compression of multilayers with semi-coherent interfa	ces9
I.5 Deformation mechanisms of BCC metals	11
I.6 Conclusion	12
Chapter II : Simulations methodology and computational details	13
II.1 Overview of MD simulations	14
II.2 Calculation Principal	
II.3 LAMMPS code	15
II.4 Simulation methodology of nano-indentation	16
II.4.1 Interatomic potential	16
II.4.2 Sampling description	17
II.4.3 Computational details	18
II.4.4 Hardness calculation	18
II.4.5 Stress calculation	19
II.5 Simulation methodology of uniaxial tension and compression	19
II.5.1 Model description and Computational details	19
II.5.2 Stress calculation	20
II.5.3 Defects characterization	20
Chapter III: Atomistic study of the effect of semi-coherent interface	on nano-indentation
of V/Fe bi-layer	21
III.1 Structural description of V/Fe(010) interface	22
III.2 Indentation response of V/Fe(010) bi-layer vs. single-crystals	23
III.2.1 Deformation mechanisms of V ₍₀₁₀₎ single-crystal	24
III.2.2 Deformation mechanisms of Fe ₍₀₁₀₎ single-crystal	26

III.2.3 Deformation mechanisms of V/Fe ₍₀₁₀₎ bi-layer	28
III.2.4 Evolution of dislocations under (111) indentation	30
III.3 The effect of V layer thickness on the Aresponse of V/Fe	31
III.3.1 Indentation curves of V/Fe bi-layer with different V layer thicknesses	31
III.3.2 Deformation mechanisms of $\ \ \ \ \ \ \ \ \ \ \ \ \ \ \ \ \ \ \$	32
III.4 Indenter position effect	35
III.4.1 Indentation response of V/Fe for different indenter positions	35
III.4.2 deformation mechanisms in V/Fe ₍₀₁₀₎ for different indenter positions	36
III.5 Discussion	39
III.5.1 Blocking effect induced by V/Fe ₍₀₁₀₎ semi-coherent interface	39
III.5.2 Barrier Mechanics	40
III.6 Conclusion	41
Chapter IV: Atomistic investigation of the crystallographic orientation effect on V/F	e bi-layer
response during nano-indentation	42
IV.1 Indentation response of V/Fe(110) bi-layer vs. single-crystals	43
IV.1.1 Deformation mechanisms of V ₍₁₁₀₎ single-crystal	44
IV.1.2 Deformation mechanisms of Fe ₍₁₁₀₎ single-crystal	45
IV.1.3 Structural description of V/Fe ₍₁₁₀₎ interface	46
IV.1.4 Deformation mechanisms of V/Fe(110) bi-layer	47
IV.1.5 Evolution of dislocations under (110) indentation	48
IV.2 Indentation response of V/Fe(111) bi-layer vs. single-crystals	49
IV.2.1 Deformation mechanisms of V ₍₁₁₁₎ single-crystal	50
IV.2.2 Deformation mechanisms of Fe ₍₁₁₁₎ single-crystal	51
IV.2.3 Structural description of V/Fe(111) interface	52
IV.2.4 Deformation mechanisms of V/Fe(111) bi-layer	53
IV.2.5 Evolution of dislocations under (111) indentation	54
IV.3 Discussion	55
IV.3.1 Anisotropic plasticity of BCC V and Fe	55
IV.3.2 Influence of semi-coherent interfaces for different crystallographic orientations .	58
IV.4 Conclusion	60

Chapter V: Atomistic insights into the inverse effect of semi-coherent interfaces during n	1ano-
indentation of Fe/V bi-layer, Fe-V-Fe, and V-Fe-V multi-layers	61
V.1 Indentation response of $Fe/V_{(010)}$ and $Fe-V-Fe, V-Fe-V$ multi-layers	62
V.1.1 Deformation mechanisms of Fe/V(010) bi-layer	62
V.1.2 Deformation mechanisms of Fe-V-Fe multilayer	64
V.1.3 Deformation mechanisms of V-Fe-V multilayer	65
V.2 The effect of Fe layer thickness on the response of Fe/V	66
V.2.1 Indentation curves of Fe/ V bi-layer with different Fe layer thicknesses	66
V.2.2 Deformation mechanisms of Fe/V bi-layer with different Fe layer thicknesses	67
V.3 Discussion	70
V.3.1 MFDs From barrier to transmitter	70
V.3.2 Koehler Theory	71
V.3.3 Effect of Fe layer thickness	73
V.4 Conclusion	73
Chapter VI: Atomistic investigation of the mechanical response of V/Fe bi-layer du	uring
uniaxial tension and compression	74
VI.1 Stress-strain (σ-ε) curves of V/Fe bi-layer vs. single-crystals	75
VI.2 Deformation mechanisms of single-crystals under uniaxial tension	and
compression	77
VI.2.1 Deformation mechanisms of Fe single-crystal during tension	77
VI.2.2 Deformation mechanisms of V single-crystal during tension	79
VI.2.3 Deformation mechanisms of Fe single-crystal during compression	81
VI.2.4 Deformation mechanisms of V single-crystal during compression	82
VI.3 The mechanical response of V/Fe during Tension and Compression	84
VI.3.1 Deformation mechanisms of V/Fe bi-layer during uniaxial tension	84
VI.3.2 Deformation mechanisms of V/Fe bi-layer during uniaxial compression	87
VI.3.3 Deformation mechanisms of interface during in-plane tension and compression	90
VI.4 Discussion	92
VI.4.1 Anisotropic plasticity of V and Fe single-crystals	92
VI.4.2 Tension/compression asymmetry of V/Fe Bi-layer	94
VI.5 Conclusion	98

Limitations of MD simulations	99
General Conclusion	100
Future work	101
References	102
Appendix A: Evaluation and selection of interatomic potential	117
Appendix B: Atomistic insights into the invers effects of semi-coherent interfaces d	uring nano-
indentation of Ta/W and W/Ta bi-layers	123

List of Abbreviations:

NMMs: Nano-scale Metallic Multilayers / Metallic Multilayer Nano-composites

BCC: Body-Centered Cubic

FCC: Face-Centered Cubic

HCP: Hexagonal Close-Packed

HPC: High-Performance Computing

MD: Molecular Dynamics

LAMMPS: Large-scale Atomic/Molecular Massively Parallel Simulator

Ovito: Open Visualization Tool

DXA: Dislocation Extraction Algorithm

CAN: Common Neighbor Analysis

CSP: Centro-Symmetry Parameter

EAM: Embedded-Atom Method

MEAM: Modified Embedded-Atom Method

a_f: Lattice constant

δ: Lattice mismatch

h_f: Film thickness

MFD: Misfit Dislocation

MFS: Misfit Dislocation Spacing

 \mathcal{E}_{xx} : Lattice strain

F(r): Repulsive force

K:i: Force constant unit

R: Indenter radius

NVT: Canonical, isothermal ensemble

NVE: Microcanonical ensemble

CG: Conjugate_Gradient_algorithm

A_c: Projected_contact_area

P_{max}: Maximum_indentation_force

H: Hardness

d: Indentation depth

 $\sigma_{zz}\!\!:$ Normal stress along z-axis

 σ_v : Von-Mises stress

 τ_{zx} : Shear stresse

L_{disl}: Total dislocations_length

 N_{disl} : Dislocation_segment_number

ρ: Dislocations density

σ-ε: Stress-strain

E: Young's modulus

 σ_y : Yield strength

 ε_y : Strain to yielding

 σ_f : Flow stress

List of figures:

- Fig I.1 Conceptual depiction of deformation mechanisms in metallic multilayers concerning layer thickness variations from the micrometer to nanometer scale.
- Fig II.1 Schematic illustration of the simulated V/Fe bimetal, displaying indentation settings.
- Fig II.2 Schematic description of V/Fe bilayer system under the uniaxial tension along the x-axis.
- Fig III.1 Structural configuration of the MFD pattern at V/Fe₍₀₁₀₎ interface. (Perfect BCC atoms are omitted, while defect-associated atoms are shown in gray).
- Fig III.2 (a) Top and bottom views of interfacial stress. (b) y-directional plot of the average normal stresses $\sigma_{average}$ (GPa).
- Fig III.3 Indentation load-depth & hardness-depth curves of $V_{(010)}$, $Fe_{(010)}$ single-crystals and $V/Fe_{(010)}$ bi-layer.
- Fig III.4 CSP and DXA analysis of the atomic defects evolution across indentation of pure $V_{(010)}$.
- Fig III.5 Close-up of the atomic defects along plastic regime of indented $V_{(010)}$ single crystal.
- Fig III.6 CSP and DXA analysis of the atomic defects evolution across indentation of pure $Fe_{(010)}$.
- Fig III.7 Close-up of the atomic defects along plastic regime of indented Fe₍₀₁₀₎ single crystal.
- Fig III.8 Deformation mechanisms in $V_{(010)}$ and $Fe_{(010)}$ single-crystals at d = 15Å, DXA.
- Fig III.9 A) CSP analysis of the atomic defects evolution across indentation of V/Fe₍₀₁₀₎.
- B) DXA snapshots of dislocations dynamics across plastic regime of the indented V/Fe₍₀₁₀₎ bi-layer.
- Fig III.10 (a) Development of dislocations length L_{disl} along indentation of $V_{(010)}$, $Fe_{(010)}$ single-crystals and $V/Fe_{(010)}$ bi-layer (Excluding MFD length). (b) Evolution of the dislocation segment number N_{disl} across indentation (including MFD).
- Fig III.11 Indentation load-depth & hardness-depth curves for pure $V_{(010)}$ and $V/Fe_{(010)}$ bi-layer with various V layer thicknesses ($h_V = A13, 15, 22, 30, 50, 120 \text{ Å}$).

Fig III.12 DXA snapshots of dislocation evolution in V/Fe bi-layer with various V layer thicknesses (h_V =13, 30, 50, 80, 120 Å) along plastic regime.

Fig III.13 Comparison of hardness between V/Fe bilayer and single crystals as a function of V layer thickness.

Fig III.14 Schematic illustration of the different indenter positions cases (A, B, C) above the indented surface.

Fig III.15 Load-depth & Hardness-depth curves of V/Fe₍₀₁₀₎ for different indenter position.

Fig III.16. DXA snapshots of dislocations dynamics across plastic regime of the indented $V/Fe_{(010)}$ bi-layer for various indenter positions.

Fig III.17 Dislocation-interface interaction in V/Fe for different indenter positions, at d=15Å.

Fig III.18 Potential energy distribution of defected atoms surrounding MFD in the Relaxed V/Fe interface.

Fig IV.1 Indentation load-depth & hardness-depth curves of $V_{(110)}$, $Fe_{(110)}$ single-crystals and $V/Fe_{(110)}$ bi-layer.

Fig IV.2 CSP and DXA analysis of the atomic defects evolution across indentation of pure $V_{(110)}$.

Fig IV.3 Close-up of the atomic defects along plastic regime of indented $V_{(110)}$ single-crystal, for d=6.01 and 8.01Å showing the diamond_ shaped structure.

Fig IV.4 CSP and DXA analysis of the atomic defects evolution across indentation of pure $Fe_{(110)}$.

Fig IV.5 (a) Structural configuration of the MFD pattern of V/Fe₍₁₁₀₎ interface. (b) Top and bottom views of interfacial stress.

Fig IV.6 DXA snapshots of dislocations dynamics across plastic regime of the indented $V/Fe_{(110)}$ bi-layer.

Fig IV.7 (a) Development of dislocations length L_{disl} along indentation of $V_{(110)}$, $Fe_{(110)}$ single-crystals and $V/Fe_{(110)}$ bi-layer (Excluding MFD length). (b) Evolution of the dislocation segment number N_{disl} across indentation (including MFD).

Fig IV.8 Indentation load-depth & hardness-depth curves of $V_{(111)}$, $Fe_{(111)}$ single-crystals and $V/Fe_{(111)}$ bi-layer.

Fig IV.9 CSP and DXA analysis of the atomic defects evolution across indentation of pure $V_{(111)}$.

Fig IV.10 Close-up of the atomic defects along plastic regime of indented $V_{(111)}$ single crystal.at d=5.35 and 8.44Å showing three-point star structure.

Fig IV.11 CSP, DXA analysis of atomic defects evolution across indentation of pure Fe₍₁₁₁₎.

Fig IV.12 (a) Structural configuration of the MFD pattern of V/Fe₍₁₁₁₎ interface. (b) Top and bottom views of interfacial stress.

Fig IV.13 DXA snapshots of dislocations dynamics across plastic regime of the indented $V/Fe_{(110)}$ bi-layer.

Fig IV.14 (a) Development of dislocations length L_{disl} along indentation of $V_{(111)}$, $Fe_{(111)}$ single-crystals and $V/Fe_{(111)}$ bi-layer (Excluding MFD length). (b) Evolution of the dislocation segment number N_{disl} across indentation (including MFD).

Fig IV.15 A) MD images of indented $V_{(010)}$, $V_{(110)}$, and $V_{(111)}$ showing the twinning anisotropy of Vanadium.

Fig IV.16 Indentation load-depth & hardness-depth curves of V/Fe bi-layer for different crystallographic orientations.

Fig IV.17. Atomic shear strain and Von_Mises stress dispersions in V/Fe bilayer for different orientations, at d=13Å.

Fig IV.18 a) DXA snapshots of dislocation dynamics of V/Fe. b) Total dislocations length-depth along plastic stage of $V/Fe_{(010)}$, $V/Fe_{(110)}$, and $V/Fe_{(111)}$ bi-layers.

FigV.1 Indentation load-depth & hardness-depth of V/Fe, Fe/V bi-layers and, Fe-V-Fe, and V-Fe-V multi-layers.

FigV.2 DXA snapshots of dislocation dynamics along plastic deformation of Fe/V bi-layer for specific depths.

FigV.3 DXA snapshots of dislocation dynamics along plastic deformation of Fe-V-Fe multilayer for specific depths.

FigV.4 Close-up picture showing the blocking effect of V/Fe_(MFDs) interface at the end of indentation.

FigV.5 DXA snapshots of dislocation dynamics along plastic deformation of V-Fe-V multilayer for specific depths.

FigV.6 Indentation load-depth & hardness-depth curves for pure $Fe_{(010)}$ and $Fe/V_{(010)}$ bilayer with various Fe layer thicknesses ($h_{Fe} = 22, 30, 50, 80, 100 \text{ Å}$).

FigV.8 DXA snapshots of dislocation dynamics along plastic deformation of Fe/V bi-layer designed for various Fe film thickness for different indentation depths.

Fig V.9 Illustration of the asymmetry of Hardness variation in Fe/V and V/Fe bi- layers based on film thickness, compared to pure Fe and V.

FigV.10 Schematic illustration of the difference in stress and energy of MFDs for V/Fe and V/Fe bi-layers.

FigV.11 Shear stress τ_{xz} (GPa) distribution in V and Fe atoms for both Fe/V and V/Fe bilayer systems at different indentation depths.

FigVI.2 Common neighbor analysis of Fe single-crystal during uniaxial tension at different strain rates (ε =8.4, 9, 9.5, 10.5, 15, 20, 25, and 30%).

FigVI.3 A) DXA snapshots of dislocation in Fe single-crystal under tension. B) Evolution of dislocation segments number along plastic regime.

Fig VI.4 Common neighbor analysis of V single-crystal during uniaxial tension at different strain rates (ε =6.2, 8, 9, 10.5, 15, 20, 25, and 30%). Histogram of structure type rate gray color represents amorphous structure.

Fig VI.5 A) DXA snapshots of dislocation in V single-crystal under tension. B) Evolution of dislocation segments number along plastic regime.

Fig VI.6 Common neighbor analysis of Fe single-crystal during uniaxial compression at different strain rates (ε =18, 19, 20, 25, and 30%). Histogram of structure type rate gray color represents amorphous structure.

Fig VI.7 A) DXA snapshots of dislocation in Fe single-crystal under compression. B) Evolution of dislocation segments number along plastic regime.

Fig VI.8 Common neighbor analysis of V single-crystal during uniaxial Compression at different strain rates (ε =18, 19, 20, 25, 30%). Histogram of structure type rate gray color represents amorphous structure.

Fig VI.9 A) DXA snapshots of dislocation in V single-crystal under compression. B) Evolution of dislocation segments number along plastic regime.

FigVI.10 Common neighbor analysis of V/Fe bi-layer system during in-plane uniaxial tension at different strain rates (ε =6.2, 7, 8, 10, 15, 25, and 30%).

FigVI.11 A) DXA snapshots of dislocation in V/Fe bi-layer under tension. B) Evolution of dislocation segments number along plastic regime.

FigVI.12 Common neighbor analysis (CN) of V/Fe bi-layer during in-plane uniaxial compression at different strain rates (ε =4, 4.3, 5.9,7, 10, 15, 20, 30%).

FigVI.13 Histogram of structure type rate during the tensile and compressive loadings showing the ratio of phase transition during deformation of V/Fe bi-layer.

Fig VI.14 A) DXA snapshots of dislocation in V/Fe bi-layer under compression. B) Evolution of dislocation segments number along plastic regime.

FigVI.15 Schematic illustration of the creation of shear strain induced by MFD's decomposition during the plastic response of V/Fe bi-layer.

FigVI.16 Atomistic shear strain in V/Fe during uniaxial in-plane Tension and compression before and along the initiation of plastic deformation (Strain rates ε =2.5, 4, and 6%).

List of tables:

Table IV.1 Total dislocations length L_{dsil} for V and Fe single-crystals at $d=15\text{\AA}$ for different crystallographic orientations.

Table VI.1 Values of Young's modulus E, yield strength σ_y , strain to yielding ϵ_y and Flow stress σ_f , during uniaxial tension and compression of V and Fe single crystals and V/Fe bilayer.

Introduction

General Introduction

Background

Surface treatment using hard coatings for cutting tools industry and other domains, remains a crucial area of research in materials science, owing to its role in enhancing durability and achieving higher performance. Especially, after the integration of nanotechnology, which has expanded the scope of these coatings further, providing innovative solutions that allow substantial improvements in performance and adaptability across various applications. Transition metals have involved as leading candidates for hard coating applications, due to their outstanding mechanical properties. What is more, nano-scale metallic multilayers NMMs are engineered structures composed of alternating thin layers of different metals. These layers are only a few nanometers thick and deposited one on other, creating a frame sequence with unique physical and mechanical properties that differ significantly from those of individual metals. Numerous studies have proven that, the interfaces created between those layers can govern the overall mechanical behavior of multilayers. Moreover, the nano-scale layer thickness enable NMMs to exhibit outstanding characteristics, such as enhanced mechanical behaviors (hardening/ strengthening), which make them valuable in various advanced coatings. In light of these advancements, understanding the mechanical behavior of nano-scale metallic multilayers has become indispensable for an accurate selection of materials suited to specific requirements. The quick advance of nanotechnology, which has introduced new challenges and opportunities in optimizing material performance, has also magnified this requirement. Nevertheless, we strongly believe that to understand the overall mechanical behavior of multilayers, it is crucial to understand the mechanical behavior of bilayers first and determine the influence of each type of interface. For that, simulations studies can be a vital tool in offering detailed insights into the mechanical behavior under different mechanical stress. Especially that, simulations can provide a mode of testing the key properties of materials in some challenging situations where experimental resources might seem limited.

Problem statements

A number of researches have demonstrated that the overall mechanical behavior of metallic bilayers or multilayers under mechanical loading is strongly influenced by the existed interfaces type (coherent, semi-coherent or incoherent). These interfaces can induce either a hardening or softening effects on the overall mechanical behavior of these materials.

In particular, semi-coherent interfaces have shown a significant impact in many face-centered cubic (FCC/FCC) systems, besides various systems with incoherent interfaces (FCC/BCC, BCC/HCP, and HCP/FCC). In which their presence can substantially alter the mechanical properties.

Through understanding interface-dislocations interactions during the mechanical loading, it has been proven that semi-coherent interfaces can govern the mechanical behavior of multilayers. However, there is a noticeable lack of research on body-centered cubic (BCC/BCC) bilayers with semi-coherent interfaces. This gap in literature raises vital questions about the behavior of BCC/BCC systems under different conditions. That highlights the need of further investigations into how semi-coherent interfaces can affect the mechanical behavior of multilayers. In the present thesis, we have selected vanadium and iron BCC metals among transition metals to investigate the mechanical response of bilayer under nano-indentation and uniaxial tension and compression, aiming to address the role that semi-coherent interfaces may play in BCC/BCC bilayers, and provide valuable insights into the fundamental deformation mechanisms in this system during mechanical loading. Accordingly, help to link the knowledge gap between BCC/BCC metallic multilayers, with the exited studies for different semi-coherent interfaces and incoherent interfaces.

Objectives

The primary aim of this thesis is to examine the effect of BCC/BCC semi-coherent interfaces on the plastic deformation of V-Fe bilayer during nano-indentation, tension, and compression. Therefore, systematic investigations for the best description of the mechanical behavior of V/Fe, Fe/V bilayer systems, and V-Fe-V, Fe-V-Fe multilayers, in contrast to single crystals are presented. Furthermore, we aim to examine the effects of key factors such as film thickness, indenter position, and crystallographic orientation during nano-indentation of V/Fe. Additionally, we shed the light on the loading direction dependency in the study of tension and compression tests for both V, Fe single crystals, and V/Fe bilayer.

Methodology

In view of the fact that, atomistic simulations particularly molecular dynamics (MD) are beneficial for detailed investigations of the mechanical behavior of metallic multilayers at nano-scale, we employed classical molecular dynamics simulations using LAMMPS (Large-scale Atomic/Molecular Massively Parallel Simulator) code in our study. So that, LAMMPS was chosen for its versatility and efficiency in conducting large-scale atomic simulations, making it ultimate for examining plastic deformation mechanisms of metals. our simulations were carried out consuming the computational resources provided by Setif-1-university, at "Research Unit for Emerging Materials". Within, simulations were executed using a CPU with 8-core in parallel (MPI). Some simulations were also conducted on specialized hardware, "The High-Performance Computing (HPC)", of physics department (Sétif -1-univesity) and the cluster of Bochum university (ICAMS), to accelerate the calculation time for considerably large systems and ensuring the efficient control of large datasets and complex calculations.

The outputs data generated from the simulations were treated using Microsoft Excel to create complete plots that illustrate key mechanical properties and deformation trends. Additionally, Ovito software was used to visualize the atomistic configuration of the simulated systems, and get information of the stress and potential energy for each atom, enabling deeper analysis of the plastic deformation mechanisms. Namely, dislocation extraction algorithm (DXA), common neighbor analysis (CNA), centro-symmetry parameter (CSP), and atomic strain calculations were employed to track dislocations evolution, phase transitions, twinning for each time step, besides atomic shear strain, offering best insights into the atomic-level defects that govern plastic deformation.

Thesis structure

This thesis is organised into six chapters to facilitate the clear presentation of our research findings.

Chapter I provides an introductory overview of the theoretical aspects and the literature review that define our research. Chapter II outlines the basics of our simulations methodology and all computational details.

Chapters III, IV, V and VI address the contribution of our study to materials and engineering field and present our published results. Each one of these chapters contains detailed discussions of its relevant results.

In Chapter III, we investigate the impact of semi-coherent interfaces on the mechanical response of V-Fe bilayer compared to V and Fe single crystals during nano-indentation process. Moreover, we examine the effect of V film thickness, and indenter position along the indentation of V/Fe bilayer.

In Chapter IV, we examine the crystallographic orientation dependency with the impact of semi-coherent interfaces on the mechanical response of V/Fe bilayer compared to V and Fe single crystals during (110) and (111) Nano-indentation.

In Chapter V, the invers effect of semi-coherent interfaces on the mechanical performance of Fe/V bilayer system, and V-Fe-V, Fe-V-Fe multilayer systems is considered. Besides, we examine the effect of Fe film thickness on Fe/V bilayer.

In Chapter VI, we explore the mechanical performance of Fe, V single crystals, and V/Fe bilayer system with semi-coherent interface under uniaxial tension and compression tests.

Finally, significant conclusions are drawn in the concluding section of this thesis once we highlight the limitations of our simulations.

Chapter I: Literature review

Summary

This chapter offers a concise overview of the key theoretical concepts and researches that are directly related to the core of our study. A detailed clarification is given to illustrate how metallic interfaces influence the mechanical behavior of multilayers according to previous studies in the literature.

By laying out these foundational theories, we establish the necessary background for the more detailed investigations and discussions that follow in the subsequent chapters.

Since the 1800s, Enhancing mechanical properties such as strength, elasticity, fracture toughness...etc. is still an ongoing contest in material science. Specifically as metallic multilayer nano-composites (MMNs) have attracted successive appeal due to their outstanding mechanical properties [1]. Gradually over time, the range of industrial applications of MMNs extends due to their exceptional mechanical, optical, electrical, and magnetic properties.

A key advantage of MMNs is their ability to surpass the mechanical limitations of individual metals. In particular, hard coatings derived from multilayer structures often demonstrate superior mechanical performance. However, it is well established that the mechanical behavior of these materials is strongly influenced by two critical factors: the thickness of each individual layer and the characteristics of the interface between different phases. The interaction between these factors dictates the material's overall response to external stresses, influencing its hardness, toughness, and resistance to deformation.

Therefore, understanding and optimizing these parameters have become focal points in recent research. While significant progress has been made, many fundamental questions remain unanswered, highlighting the need for further experimental and theoretical investigations to fully unravel the complex mechanical behavior of MMNs.

I.1 Interface type:

Overall, an interface is the constructed boundary when two different phases face each other. The umbrella term "interface type" encompasses a broad category of interfaces, which can be classified based on material composition, crystallographic structure, or atomic continuity (i.e., coherency).

Based on material composition, there is two type of interfaces, homogenous and heterogeneous. Homogenous interface constructs when two materials have identical structure and chemical composition, but have different crystallographic orientation or defect structure. E.g., grain boundary, twin boundary, or phase boundary [4].

Heterogeneous interface would be created when two materials have different chemical or electrical properties, but have the same structure (crystallographic orientation). That could be metal/ceramic, metal/semi-conductor...etc. Heterogeneous interface could be coherent, semi-coherent or incoherent depending on the lattice mismatch. Such as {111} in FCC and {0001} in HCP structures (e.g. Ge/Si, Cu/Si) [2]. That brings another classification of interfaces.

Grounded in lattice mismatch or coherency stress, an interface can be: coherent, semi-coherent, or incoherent [2-4]. Such lattice mismatch; between two phases leads to the creation of interfacial stress, which act quite differently in the three types.

Coherent interface would be formed, when two crystals or parts of a crystal exhibit a strong lattice alignment, meaning that the lattices, of phase α and β , remain continuous across the interface [2-4]. That means, regardless the chemical composition when the interfacial plane shares the same atomic arrangement in both phases, an example could be the above-mentioned example of Ge/Si system. Alternatively, the case of metals with identical crystal structures and minimal lattice mismatch (<5%) can be introduce a coherent interface. However, the lower lattice mismatch can be accommodated by straining one or both lattices (e.g. Cu/Ni). This lattice straining (Elastic strain) creates a residual stress without major defects generation at the interface.

A perfectly coherent interface has very low energy, typically a few mJ.m⁻². Nevertheless, if there is a slight strain near the interface, the interfacial energy increases to around 200 mJ.m⁻²⁵ [2].

For the case of semi-coherent interface, the mismatch between lattices (phase α and β) on either side of an interface is a bit higher (about 5-15%). In addition, the resulting strain can exceed the elastic limit of the crystals. In such case, the coherency strain is relieved through the formation of periodic dislocations in the interfacial plane with localized stress surrounding defects, known as misfit dislocations MFDs. These dislocations periodically accommodate the mismatch, ensuring a good fit across the interface in the coherent regions. When the misfit is small, the energy associated with dislocations is approximately proportional to their density and inversely proportional to the distance D between them. The energy of semi-coherent interfaces typically ranges between 200 and 500 mJ.m⁻²[2].

In-coherent interface includes a large lattice mismatch (>15%) which make the strain accommodation intolerable, resulting in higher density of dislocations at the interface and higher localized stress. In this case, the discrete nature of the dislocations is lost. An incoherent interface can also arises when two crystals are oriented arbitrarily relative to each other. The energy of incoherent interfaces generally ranges from 500 to 1000 mJ.m⁻² and is largely unaffected by changes in the orientation of the interface plane [2].

Romanov et al. [4], have summarized the definition of an incoherent interface according to the rigid contact of two crystal lattices. They considered that there is no periodicity in the arrangement of atoms along the interface. While, both coherent and semi-coherent interfaces have periodic arrangements of atoms along the interface.

I.2 Effect of different interface types on the mechanical response of multilayers under indentation:

As outlined earlier, the mechanical response of nano-scale metallic multilayers (NMMs) under nano-indentation process is deduced to have a crucial relation with the interface types in many previous researches. In the research corpus, the FCC/FCC are the most studied cases

as coherent and semi-coherent interfaces [5-30]. While there are a variety of studied cases for incoherent interfaces [31-38].

According to these studies, semi-coherent interfaces in particular, can aid in the hardening or a softening of multilayers, by acting as a barrier to dislocations propagation or inducing dislocation nucleation in the softer layer along the plastic deformation. These opposite effects showed a great reliance with the indented layer.

For instance, the plastic deformation during indentation of Ni/Cu (FCC/FCC) multilayers using MD simulations by Saraev et al. [5]. Have demonstrated dislocation pile-up at the interface, dislocation cross-slip and movement of misfit dislocations. Whereby, the misfit dislocations began to glide from the down side of interface into the lower crystal of copper, as they started indenting the nickel coating. When misfit dislocations moved into copper film, the top layer of nickel had not yielded yet. Moreover, they observed that if misfit dislocations intersect in coherent regions of the interface. The free dislocations nucleated in nickel could easily transmit into copper.

In contrast, Guiqiang et al. [15], have demonstrated that the existence of semi-coherent interface in the Cu/Ni bilayer film was advantageous for dislocations to transmit the semi-coherent region into the nickel film, which turned into strengthening effect. Within, the semi-coherent interface blocked dislocation propagation.

In the same way, when simulations of indentation have carried out on Ni/Al (FCC/FCC) by Cao et al. [6], the semi-coherent interface acted as a barrier to dislocation slip, causing an apparent strengthening of the multilayer. However, dislocation nucleation and emission from interface, and dislocation propagation in Ag layer have driven the plastic deformation of Cu/Ag (FCC/FCC) multilayers along nano-indentation, in the study of Tian et al. [7].

Correspondingly, Li et al. [14] have observed both strengthening and softening effects induced by interface during nano-indentation of Cu–Ag bilayer. They have deduced inconsistent interactions in Cu/Ag and Ag/Cu interfaces. For Cu/Ag interface, the plastic deformation was subjected mainly in the softer substrate (Ag). Whereas, both layers have experienced plastic deformation along nano-indentation of Ag/Cu bilayer film. Furthermore, Zhao et al. [22], have also reported that indentation of Ni₍₀₀₁₎/Ag₍₀₀₁₎ and Ni₍₁₁₁₎/Ag₍₁₁₁₎ demonstrated an easy transmission of dislocations from the semi-coherent interface for both orientations, within defects have emitted from misfit dislocations. That was related to layer thickness. Within, the small modulation period could transform this softening effect into obvious hardening.

The above-mentioned studies and others [27-29] have found similar results in terms of strengthening or softening effects induced by semi-coherent interfaces, which may not be observed for systems with coherent interfaces. Hoagland et al. [28], have found that in bimetals with coherent interface, the coherency strain could obscure the role of slip resistance by

interface. They depicted coherent interfaces as transparent, due to the continuation of slip planes and vectors. Li et al. [27] have also confirmed that transparent interfaces have lower resistance to dislocation transmission during nano-indentation, in comparison with incoherent and semi-coherent interfaces.

In addition, many experimental studies and simulations have devoted to incoherent interfaces [31-38]. Demonstrating the importance of defect-interface interactions, for the understanding of the mechanical response of multilayers under indentation. They have shown the role of incoherent interfaces to resist dislocation transmission.

For case in point, the nano-indentation study of Feng et al. [32], performed using MD simulations on Ti-V (HCP/BCC) multilayers, the formation of a prismatic loop in the pure vanadium was observed. However, that was not seen in V-Ti-V-Ti multi-layers, due to the insufficient thickness, resulting in the hardening of this system. While, dislocations were absorbed through the interface in Ti-V-Ti-V example, causing a softening of indentation force and hardness. Moreover, Dislocations were not able to transmit the interface during indentation of Cu/Nb. On the contrary, dislocations have easily transferred to Cu during indentation of Nb/Cu [37]. Meaning that, the Cu-Nb (FCC/BCC) incoherent interface can also absorb dislocation and behave as a key obstacle to dislocation propagation throughout nano-indentation.

I.3 Layer thickness effect:

In light of prior investigations [39-42], the strengthening of MMNs is not ascribed only to the existence of lattice mismatch or interfacial defects. Moreover, the film thickness can strongly affect the role of an interface during the mechanical response of multilayers. According to Misra et al. [42], the effect of film thickness h_f on the hardness of multilayers can differ in three scaled domains: For sub-micrometer to micron length scales, hardness corresponds with Hall–Petch model. Where, the yield strength σ_y is inversely proportional to the square root of film thickness h_f , and dislocation pile-ups at grain boundaries assists well deformation [42].

In the case of h_f less than 50 nm, the hardness increases with decreasing layer thickness, and deformation implicate in slip of single dislocation confined to individual layer (CLS) [41, 42]. When h_f is ranged from two to five nm, the hardness of multilayer may attain a maximum. In this incident, the alteration of the fundamental processing step from CLS to interface crossing of single dislocation can be perceived. Within, the interface resistance to single dislocation transmission sets strength. This is well known as the inverse Hall–Petch effect. In this regime, the interface induced plasticity. Whereby, further decrease of film thickness can lead to softening of the system [41].

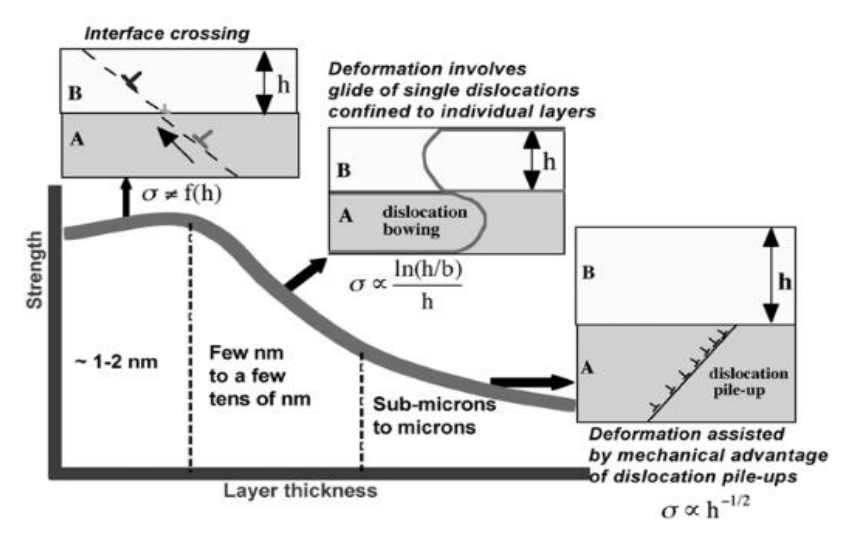


Fig I.1 Conceptual depiction of deformation mechanisms in metallic multilayers concerning layer thickness variations from the micrometer to nanometer scale [42].

I.4 Tension and compression of multilayers with semi-coherent interfaces:

The mechanical response of MMNs can also be influenced by interfaces between the constituent layers under tension or compression loadings. Therefore, understanding how interfaces effect is crucial for optimizing the performance of multilayers in practical applications. Many studies [43-49], have examined the mechanical behavior of metallic multilayers with various interface types under tension and compression. For instance Gao et al. [44], have simulated uniaxial tension of Cu/Fe nano-multilayered films with different modulation periods (λ). They found that by the end of elastic regime, dislocations nucleated from the interface, and glided into Cu layers. The defects were mainly {111} stacking faults surrounded by <112> partial dislocations. Then dislocations glided in both Cu and Fe layers, contributing to plastic flow in the multilayered film showing different mechanisms with the variety of modulation period.

Chauniyal and Janisch [45, 46] have demonstrated that γ/γ interfaces have driven the plastic deformation in lamellar TiAl alloys during the simulations of uniaxial tensile tests along different directions. In addition, Lu et al. [47] have performed uniaxial tension to study the effect of interface and modulation periods (k) on deformation mechanisms of Cu/Ta nano-scale metallic multilayers (NMMs). They have found that the Cu₍₁₁₁₎/Ta₍₁₁₀₎ interface could function as a source of dislocation nucleation and the barrier impeding the motion of dislocation. Within, dislocations have firstly nucleated and propagated in Cu layer causing the first yielding. Then, dislocations nucleated and propagated in Ta layer.

Further simulations studies [50-58], of bilayers system with semi-coherent interfaces have shown that the semi-coherent interface was a source of dislocation nucleation during both tensile and compression loadings. Whereby, nodes could act as initiative sites for dislocation nucleation inside the softer layer:

Shao et al. [50] have observed dislocations nucleation from dislocation nodes at semi-coherent {111} Cu—Ni interfaces during biaxial tension/compression applied parallel to the interface, it was shown that the nucleation of lattice dislocation was preferred at the nodes. Nevertheless, an asymmetry of the transformation of the volume-smeared nodes into different patterns was noticed under tension, and compression.

Moreover, Hoagland et al. [51] have demonstrated that the interface dislocation segments near nodes serve as a source of dislocation nucleation. However, they have considered Cu-Ag interfaces weaker than Cu-Ni interfaces, and this difference was primarily attributable to the higher misfit parameter of Cu-Ag in comparison to Cu/Ni. Within, the mobility of misfit dislocations reduced coherency stress. Therefore, Cu-Ag interface was very weak in shear. Which had implications for Koehler force. The shear stress components of glide dislocations residing in either Ag or Cu layers must be limited to the critical stress to move the misfits and so, since this was rather small, the Cu-Ag interface was more like a free surface. Consequently, the greatly reduced to non-existent coherency stresses and reduced Koehler forces, perfect dislocations, in either layer were not prevented from the interface (as in Cu/Ni). Moreover, despite the various nucleation mechanisms of lattice dislocations, a fundamental condition must be satisfied if a nucleation event was to happen is the interfacial dislocation that serves as nucleation sources/sites must align with the slip trace.

Schwarz et al. [56], have approved that the vast majority of dislocations are formed in the Ni layer, during the compression of Al/Ni bimetal.

In the main, semi-coherent interfaces have shown an observable impact on the mechanical response of several bimetals. Experimental and simulations studies; which have dedicated to dislocation—interface interaction during nano-indentation; have proven that the semi-coherent interfaces can behave as a strong barrier to dislocation propagation. While, semi-coherent interfaces were considered as a source of dislocation nucleation along tension and compression tests. Therefore, this type of interfaces can control the strength multilayers.

Nevertheless, as per the author's review, there is a lack of research about the influence of BCC/BCC semi-coherent interfaces on the mechanical behavior of multilayers [54, 55, 59, 60].

Mi et al. [54] have studied the atomic structure, tensile property, and dislocation behavior of $Fe_{(110)}/W_{(110)}$ interface by MD simulations, they observed the nucleation of dislocation loops from interface, demonstrating that semi-coherent interface was a source of dislocations nucleation. Ding et al. [55] have investigated the evaluation of structural and mechanical strength of symmetric W/Fe interface. However, their study did not describe the overall plastic deformation of this bilayer

Other atomistic simulations have considered BCC/BCC bimetals with semi-coherent interfaces, disregarding dislocations—interface interaction. Namely, the study of Chen et al.[59], where different misfit dislocation patterns for U–Zr bimetal have been examined and described. Above and beyond, the investigation of nucleation and growth of helium bubbles at W/Ta semi-coherent interface The interfacial defects of the (001) and (110) orientations have also examined [60].

Still, a detailed insight, specifically in the perspective of the effect of BCC/BCC bilayer systems in the fundamental mechanisms leading to hardening or softening during mechanical loading is missing.

Considering the significant role of crystallographic structure in determining the mechanical properties and behavior of metals, particularly in response to stress, temperature changes, even to radiation damage. It is crucial to reveal the mechanical behavior of BCC/BCC bimetals at different mechanical stress.

I.5 Deformation mechanisms of BCC metals:

Body-centered cubic (BCC) metals are a class of metals characterized by their unique crystal structure, where atoms are arranged at the corners of a cube with an additional atom at the center of this cube. This structure is known for its high strength and resistance to deformation at low temperatures. When BCC metals deform irreversibly by any mechanical force (For example tensile, compression, shear or indentation tests), exceeding the elastic limit or the yield strength. The plastic deformation arises through two main mechanisms, slip, or twining deformations, or both.

The slip deformation involves the nucleation and motion of a large number of dislocations. Which take place along the close packed slip systems [61]. For BCC crystals, there is about 48-slip systems, in three closed packed planes {110}, {112}, {123}, and an only closed packed direction <111>. Slip along each plane does not occur simultaneously across the entire body, but instead progresses gradually, moving gradually through the material by the motion of dislocations [61-67]. It is common for BCC metals that dislocations with Burgers vectors a/2<111> glide in {110} and {112}<111> slip systems, and a dislocation with Burgers vector a<100> can be created during the interaction of two 1/2<111> dislocations [64, 65, 67]. According to Schmid's law [63], the motion of dislocations occurs when the applied stress reaches a certain critical value, known as critical resolved shear stress (CRSS). This critical stress is referred as the resolved shear stress (RSS), which is the component of the applied external stress that is projected onto the slip system.

In addition to slip deformation, BCC metals can also deform plastically by twinning. However, this mechanism differs to that of slip. The slipped regions have the same orientation as the original grain. Whereas, twinning occurs when a portion of the crystal is divided by a

homogeneous simple shear of parent lattice, creating a "twin" region where the crystal lattice mirrors the original structure. That results in a reorientation of the crystal lattice without breaking atomic bonds. [72]

The classical definition of twinning states that the twin and parent (or original) lattices are related either by reflection across a specific plane or by rotation around a particular axis [69]. The formation of deformation twins occurs in two stages: nucleation and growth. Twin nuclei can develop due to an applied stress. According to many surveys the most common twin systems in BCC crystals are {112} <111> and {110} <111> [68-72].

In despite of the difference between slip and twining deformations, BCC metals can deform plastically by both mechanisms. Nevertheless, twinning deformation becomes the most important deformation in BCC crystals at low temperature and higher strain rate or both [69]. Which make it until nowadays a subject of debate due to the anisotropic nature of BCC metals.

I.6 Conclusion:

The limited researches on the mechanical behavior of multilayers with BCC/BCC semi-coherent interfaces, make some questions on different perspectives of this area arise. From a different standpoints, Vanadium and Iron can be potential candidates to exemplify hard BCC bimetals intended for advanced requests. In our contribution, we select the V-Fe bimetal to represent a bilayer system model, aiming to study the effect of BCC/BCC semi-coherent interface on the mechanical behavior of multilayers during nano-indentation, tension, and compression using molecular dynamics simulations.

Chapter II: Simulations Methodology and Computational details

Summary

This chapter illuminates the foundational principles of molecular dynamics simulations, which are essential for a comprehensive understanding of the subject of the present research. It provides an explanation of our simulations methodology, for both nano-indentation and tension/compression tests, including all the computational details.

II.1 Overview of MD simulations

As its name indicates, molecular dynamics (MD) simulations is a calculation tool to study the properties of a classical many-body system. Whereby, the constituent particles obey the laws of classical mechanics, which based on (Newton's low of motion and energy function). It reveals how atoms/molecules move in an atomistic scale. MD simulations is an excellent approximation for the translational and rotational motion of a wide range of molecules [75]. It can be used when an experiment is almost impossible.

Molecular dynamics simulations were initiated by Alder and Wainwright in the 1957s after the simulations of condensed matter systems which had activated in the 1950s, through two fundamental techniques: the Monte Carlo (MC) sampling method and molecular dynamics (MD).

In 1964, Rahman published the first simulation results for a realistic model system of liquid argon showing that MD simulations could be conducted using smooth potentials [76, 77]. Over time, a growing body of scientific literature highlighted the effectiveness of molecular simulations in interpreting experimental results and predicting them.

A significant milestone occurred in 1971 when Rahman and Stillinger published the first MD study on a model of liquid water, marking a shift to simulation of systems composed of molecules rather than just individual atoms [77]. Nowadays, MD simulations continue to advance rapidly, driven by improvements in computational power, algorithms, and the development of more sophisticated force fields, allowing researchers to explore increasingly complex systems with unprecedented detail.

II.2 Calculation Principal

Similarly to experimentation, MD calculations go through stages from sample preparation; where we create a typical system consisting of N particles and we solve Newton's equations of motion for this system properties (i.e., we equilibrate the system). Then we carry out the definite measurement or deformation under the desired conditions. Hence, any MD simulation follows three essential and standard steps:

- 1. Initialization: creation and initialization of system state.
- 2. Force calculation: introduce interaction potential between atoms.
- 3. Integrating the equation of motion: predict how particles will move.

1. Initialization

It starts by the creation of a sample with a given number of atoms N, and then we define the initial state of the system by setting the initial position (r), type, and velocity (v) for each atom. We also need to specify every parameters that set the conditions of the run in case of liquid simulation (e.g., initial temperature, number of particles, density, and time step, etc...) [75].

2. Force calculation

This step contains the core of MD simulation. It Computes the forces acting bewteen particles and integrate Newton's equations of motion. Then the process repeat itself for the desired length of time. The force between particles is determined by the potential energy function (or force field). Common force fields include Lennard-Jones potentials for van der Waals interactions, and embedded atom models for metals. Using the positions of all particles, forces are calculated by taking the negative gradient of the potential energy function ($F=-\nabla U$). The force on each particle is the sum of contribution from all other particles, depending on the type of interactions (e.g. pairwise, multi-body for metalsetc.).

3. Integrating the equations of motion

Using Newton's second law (F=ma), the forces are used to update the particles' velocities and positions over a minor step Δt . Algorithms like the Verlet or Leapfrog integration methods are typically used to propagate the system forward in time by updating the positions and velocities based on the calculated forces [77].

After completing a set number of time steps or reaching a predefined simulation time, the output data (e.g., trajectories, forces, energies) can be analyzed to derive properties such as diffusion coefficients, mechanical strength, or atomic structure.

II.3 LAMMPS code:

LAMMPS (Large-scale Atomic/Molecular Massively Parallel Simulator) is a classical molecular dynamics simulation code focusing on materials modeling, which was designed to run efficiently on parallel computers and to be easy to extend and modify. Originally developed at the mid-1990s by Sandia national laboratories, a US department of energy facility, where Steve Plimpton led the most of coding efforts. LAMMPS is an open source code since 2004, that is a rewrite in C++, which includes various features [73, 78].

LAMMPS adapt and extend functionalities easily. It efficiently supports large-scale simulations with parallel computing across thousands of processors and accommodates a wide range of interatomic potentials and force fields for diverse materials. It offers flexible input scripts, multiple time-stepping algorithms, and the ability to simulate non-equilibrium processes. Its integration with visualization tools enhances its usage.

II.4 Simulation methodology of nano-indentation:

II.4.1 Interatomic potential:

Since the interatomic potential is a fundamental component in MD simulations, selecting the appropriate potential for a specific study is an essential step to ensure reliable simulations' results. A review by Plimpton et al. [79], demonstrates the interatomic potentials evolution in the last three decades. Many researchers [80-84] have proven that, the selection of interatomic potential is crucial. It must accurately capture the bonding, repulsion, and interaction forces between atoms. This accuracy ensures that simulated mechanical properties to match experimental observations. Müser et al. [80], have reported that the embedded-atom potentials are the best inspired from density-functional theory for metals. In addition, it is recommended that any potential should be verified for its aptitude to generate the elastic tensor of crystalline structures, defect energies, bond breaking, bond formation...etc.

To that end, we have collected the suitable interatomic potentials for V-Fe binary system that are available in the literature. Then, preliminary simulations of nano-indentation for V and Fe single-crystals have performed using three different interatomic potentials. The reader is referred to (Appendix. A), within a detailed study is shown.

After a careful evaluation of those interatomic potentials, aiming for the best account of the mechanical properties of Fe and V metals. The EAM potential developed by Mendelev is nominated to be used for the whole studies in this thesis.

The EAM potential established by Mendelev et al. [86], is identified as the proper for our research, due to its correspondence with "Hertzian solution". In addition, it provides reasonable formation of dislocation, twining boundaries and phase transition, during the plastic deformation of both vanadium and iron single-crystals. While, the EAM potential by Olsson [85]; over-generates dislocations without providing any information about phase transition or twining deformation, although, they are indispensable deformation mechanisms for BCC metals. It is important to note that, the embedded-atom method (EAM) interatomic potential developed by Mendelev et al. [86], have created to describe the metallic bonding between Fe and V atoms. This potential was developed with a focus on defect properties. It mainly reproduces the interaction between Fe impurities, as well as vacancy and interstitial diffusion in V. This potential is convenient for dynamics of defects in large simulation cells.

Whereas, negligible dislocation activity can be detected using the 2NN_MEAM (Lee) potential [87]. Moreover, it gave a flat indentation curves without any observable yield point due to its underestimation of dislocation motion during deformation. One can deduce that MEAM potential is more compatible with the phase transition description.

II.4.2 Sampling description

For simulations of nano-indentation, a cube-on-cube V film was deposited on Fe substrate along the [010] direction as depicted in Fig II.1.

With identical crystallographic orientation x// [100], y// [010], z// [001], and a bit of difference in lattice constants av = 3.0299 Å, and $a_{Fe} = 2.8553 \text{Å}$. It is expected that a semi-coherent interface would be created in the V/Fe bilayer system, due to the lattice mismatch δ , between V and Fe layers (about 6.11 %). Which can be defined as follows[89]:

$$\delta = (a_V - a_{Fe})/a_{Fe} \tag{2}$$

To accommodate this lattice mismatch, the lateral size of both layers should approve the following equation:

$$m.a_{Fe} = n.a_{V} \tag{3}$$

Such \mathbf{m} and \mathbf{n} are positive integers, and \mathbf{a}_{V} and \mathbf{a}_{Fe} are lattice constants of V and Fe, respectively.

For that, the length of 300 Å, is consistent with n=99 for V and m=105 for Fe metals. Accordingly, the whole simulation box measurements are set as $(300\text{Å}\times(104+h_V)\text{ Å}\times300\text{Å})$ along x, y and z directions, respectively. Within, h_V is V layer's thickness (about 951840 atoms for the case of h_V=22 Å), See Fig II.1.

Thus, by using these dimensions, the lattice mismatch is almost adjusted, causing a negligible compressive strain in V of $\mathcal{E}_{xx} = \mathcal{E}_{zz} = -0.00288$, and a minor tensile strain in Fe atoms of $\mathcal{E}_{xx} = \mathcal{E}_{zz} = 0.03057$.

The size of the simulated V and Fe single crystals are $300\text{Å}\times103\text{Å}\times300\text{Å}$, in x, y, and z axes. The non-periodic boundary conditions were applied along y-axis, where indentation proceeds. While, periodic conditions were used on the lateral x and z directions.

Moreover, we have fixed a bottom layer of Fe substrate (about 10 Å of thickness, avoiding any rigid motion of atoms during deformation along y-axis.

The spherical indenter applies a repulsive force on each atom; denoted F and given by:

$$F(r) = \begin{cases} -K(r-R)^2 & r < R \\ 0 & r \ge R \end{cases} \tag{4}$$

Whereby, \mathbf{K} is the force constant units, about 100 eV/Å³, and \mathbf{r} is the distance from an atom to indenter center, and \mathbf{R} symbolizes the indenter radius [73].

Chapter II: Simulations Methodology and Computational details

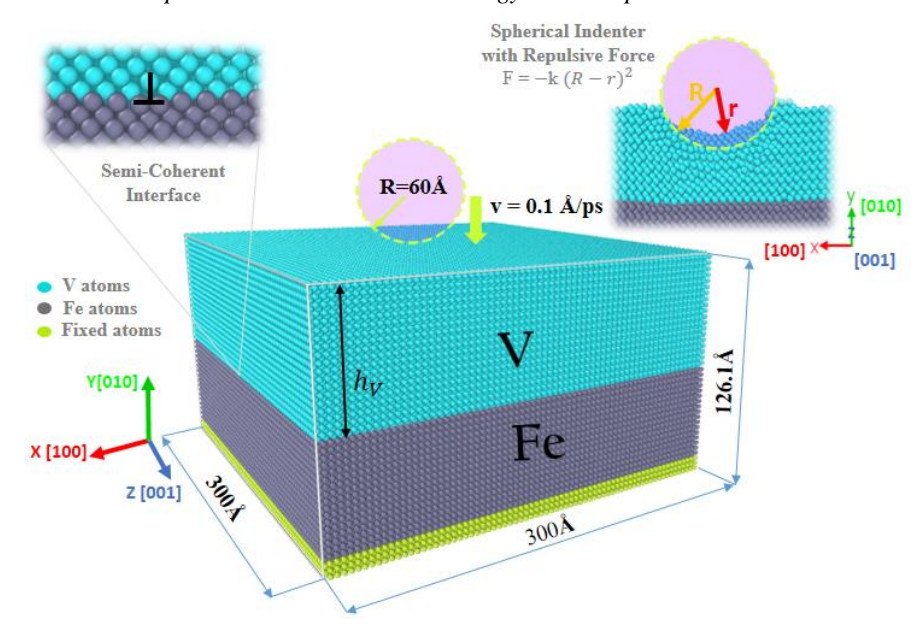


Fig II.1 Schematic illustration of the simulated V/Fe bimetal, displaying indentation settings.

II.4.3 Computational details

An Earlier relaxation step of the simulated models have performed, before indentation proceeds, following two stages: First, the convergence criteria of energy (eV) and force (eV/Å) were set to be 10^{-15} , in the minimization stage, using the conjugate gradient algorithm. Then, an equilibration stage lasts for 50 ps using NVT ensemble (with a Nosé-Hoover thermostat) [73], to thermostat the system under T=10K. This low temperature is selected to avert the kinetic effects, that may influence defects evolution responsible of deformation mechanisms.

With a well-relaxed sample, indentation can proceeds under an NVE ensemble. The repulsive indenter of a radius R = 60Å; placed in the center and 3Å directly above the free surface; forced down for a depth about 15Å with a velocity v = 0.1Å/ps (10m/s).

II.4.4 Hardness calculation

It is acknowledged that nano-indentation deformation results in a non-uniform pressure distribution, and the indentation load plot allows for the calculation of hardness. This key mechanical property is defined by:

$$H = P_{\text{max}} / A_c \tag{5}$$

Where: P_{max} represents the maximum indentation—force and A_c is the projected—contact—area. A typical selection might be the Brinell contact—area A_c (e.g. [90-93]), determined via:

$$A_c = \pi (2R - d)d \tag{6}$$

Where R is the spherical indenter radius and d is indentation depth.

Otherwise, the shape of the projected contact area can be identified based on the positions of atoms interacting with indenter.

In our methodology, we consider the contact area $A_{elliptic}$, resulting from the coordinates of atoms along the x and z axes, as proposed by Ziegenhain et al. [94]. In this approach, an ellipse is utilized to approximate the curved boundary, using this ellipse's major and minor diameters, $(x_{max} - x_{min})$ and $(z_{max} - z_{min})$ of the atoms in interaction with indenter.

$$A_{elliptic} = \frac{\pi}{4} \left(x_{\text{max}} - x_{\text{min}} \right) \left(z_{\text{max}} - z_{\text{min}} \right) \tag{7}$$

When the indenter interacts with only a few atoms, this approach may introduce observable fluctuations in the contact area, which might occur within the elastic regime. Nevertheless, it demonstrates greater accuracy in the plastic regime or at increased indentation depths. As a result, the hardness ratio can be determined with enhanced precision.

II.4.5 Stress calculation:

In LAMMPS, several techniques are used to calculate the overall and local stresses during deformation. "Compute stress/atom" computes the per-atom stress tensor, which involves both a kinetic and a virial contribution. Whereas, "compute /cartesian" and "compute /mop styles" are based on evaluating the atomic flux via a plane [73]. Due to its suitability for dislocation analysis, we voted for the virial stress and used Ovito to visualize stresse for each atom [74]. As the per-atom stress is expressed in pressure*volume units. It needed to be divided by the atomic volume to obtain stress in GPa units, using Voronoi analysis (built into Ovito program).

II.5 Simulation methodology of uniaxial tension and compression:

II.5.1 Model description and computational details:

For tension and compression studies, a specimen with (300*200.46*151 Å) size in x, y, and z directions respectively, and 100 Å of thickness for each one of V and Fe layers have created, containing about 741780 atoms. It represents the V/Fe bilayer model with (010) BCC/BCC semi-coherent interface (See Fig II.2). Periodic boundary conditions were applied on the deformation direction (x-axis), while non-periodic conditions were set for y and z directions, to mimic a free surface. The equilibrium configuration has been obtained after an energy minimization using the conjugate gradient algorithm (CG) where the convergence criteria of energy (eV) and force (eV/Å) were set to be equal to 10^{-15} . Before the onset of tension or compression deformation, the specimen was firstly relaxed under an NVT ensemble (with a Nosé-Hoover thermostat), at a fixed temperature T=10K for 50ps. Then, an in-plane uniaxial deformation proceeds along the x direction with a fixed strain rate about 10^9 s⁻¹ (0.001), under the same thermostatic conditions NVT (T=10K).

Chapter II: Simulations Methodology and Computational details

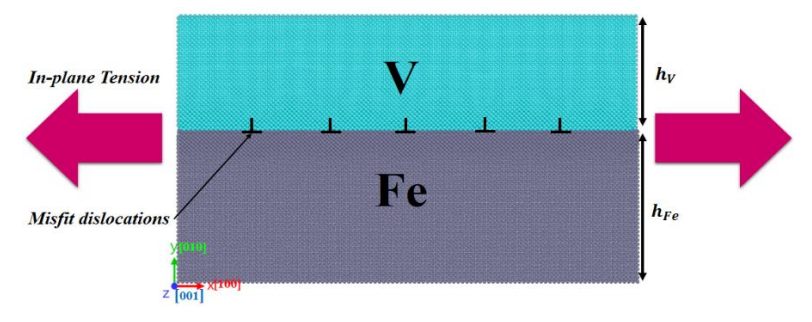


Fig II.2 Schematic description of V/Fe bilayer system under the uniaxial tension along x-axis.

II.5.2 Stress Calculation

The obtained stress tensor associated to all atoms during tension and compression tests, was calculated using the virial theorem [95] implemented in LAMMPS code. This stress was used to plot the stress-strain curves. It accounts for both kinetic contributions (due to atomic velocities) and potential contributions. The Von-Mises stress for each atom was calculated using "compute stress/atom" command [73]. Which calculates the von-Mises stress based on this definition:

$$\sigma_{V} = \sqrt{1/2 \left[\left(\sigma_{xx} - \sigma_{yy} \right)^{2} + \left(\sigma_{yy} - \sigma_{zz} \right)^{2} + \left(\sigma_{zz} - \sigma_{xx} \right)^{2} + 6 \left(\tau_{xy}^{2} + \tau_{yz}^{2} + \tau_{zx}^{2} \right) \right]}$$
(8)

Where σ_{xx} , σ_{yy} and σ_{zz} are the normal stresses in the x, y, and z directions, respectively, and τ_{xy} , τ_{yz} , and τ_{zx} are the shear stresses on the respective planes.

II.6 Defects characterization:

In the present study, OVITO software [96] was used to visualize and analyze the atomic configurations of V/Fe bilayer system for the whole simulations. dislocation evolution and atomic defects during plastic deformation of V/Fe bilayer, and V, Fe single crystals were analyzed and characterized using three devoted approaches employed by Ovito . **The CNA** (**Common neighbor analysis**) was used as a powerful tool to classify the crystallographic structure types for each atom, for the aim of a precise understanding of which atoms are associated to which phases, and which are associated with defects or amorphous structure [98]. It suits the identification of phase transition and twinning boundaries detection. **The Centro-Symmetry Parameter** (**CSP**) **analysis** [98] was used to determine the local atomic configuration of defected atoms during simulation. This parameter is defined as follows:

$$CSP = \sum_{i=1}^{N/2} \left| R_i - R_{i+N/2} \right| \tag{9}$$

Where the center atom is connected to a specific pair of closest neighbours by the vectors $\mathbf{R_i}$ and $\mathbf{R_{i+N/2}}$. There are eight nearest neighbor atoms in the BCC lattice. We also utilized **The DXA** (**Dislocation Extraction Algorithm**) analysis, to characterize the topological structure of dislocations. This convenient method calculates the Burgers vectors of dislocations that are found and converts them into continuous lines [98, 99].

Chapter III: Atomistic Study of the Effect of Semi-Coherent Interface on nano-indentation of V/Fe Bi-layer

Summary

In this chapter, we aim to comprehend the effect of BCC/BCC semi-coherent interfaces on the mechanical response of V/Fe bimetal system along nano-indentation.

For that, systematic investigations of the deformation mechanisms in V/Fe were conducted and compared with V and Fe single crystals. Giving insights on dislocation-interface interaction.

Moreover, V layer thickness and indenter position effects are examined.

III.1 Structural description of $V/Fe_{(010)}$ interface:

Given that, the role of semi-coherent (010) interface can be crucial for the deformation of V/Fe bilayer, this subsection considers the structural characteristics of this interface type. As was the case stated in [59, 60], the (010) BCC/BCC semi-coherent interface produces a misfit dislocation network with a square grid shape after the relaxation process to accommodate the lattice mismatch between Fe and V (Fig. III.1).

The resultant network is composed of two perpendicular periodic dislocation lines with Burgers vectors: $\overrightarrow{b_1} = [1\ 0\ 0], \overrightarrow{b_2} = [0\ 0\ -1]$ with nodes located at their intersections. The average spacing of the misfit dislocations MFDS depends on the misfit and is on the order of α_{Fe}/δ . [89]

The misfit dislocation (MFD) lines and nodes exhibit structurally unstable regions characterized by elevated stress.

The average of the three principal stresses (σ_{xx} , σ_{zz} , and σ_{yy}) in atoms near misfit dislocations can reach higher magnitudes 8.69 GPa (positive) in the V lattice, indicating compressive stress, and -7.87 GPa (negative) in the Fe lattice, signifying tensile stress, as illustrated in Fig. III.2

In contrast, the coherent regions within the interfacial zone exhibit stable structures with significantly lower stress levels. In these regions, Fe experiences compressive stress, while V undergoes tensile stress. Furthermore, the average stress in the central part of each layer tends to approach zero.

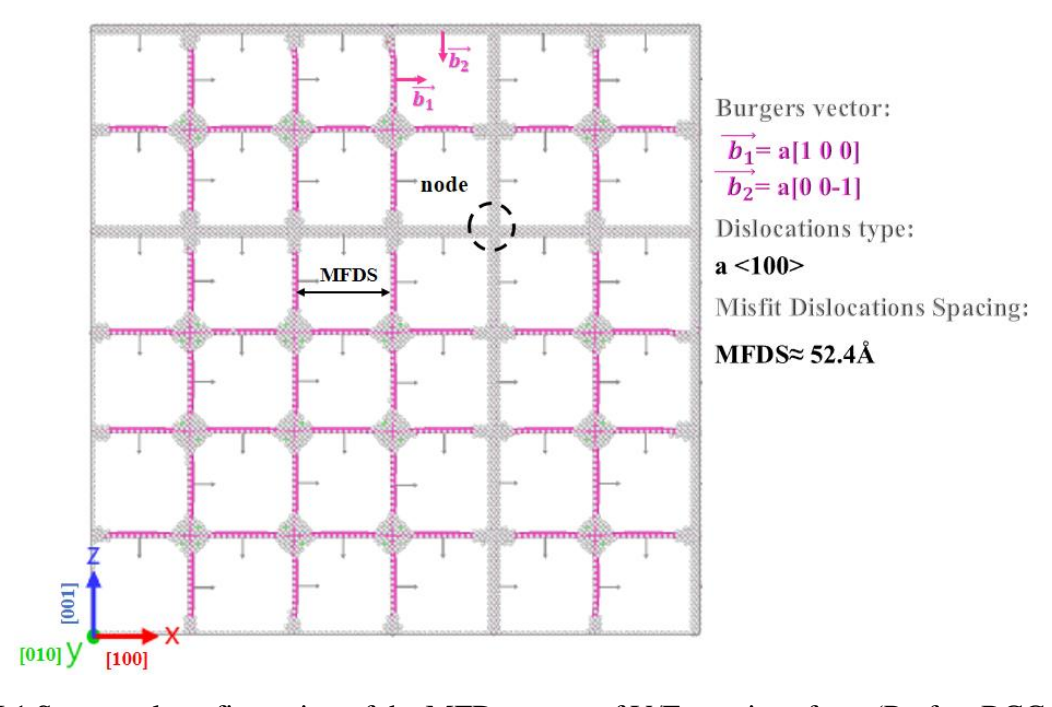


Fig III.1 Structural configuration of the MFD pattern of V/Fe₍₀₁₀₎ interface. (Perfect BCC atoms are omitted, while defect-associated atoms are shown in gray).

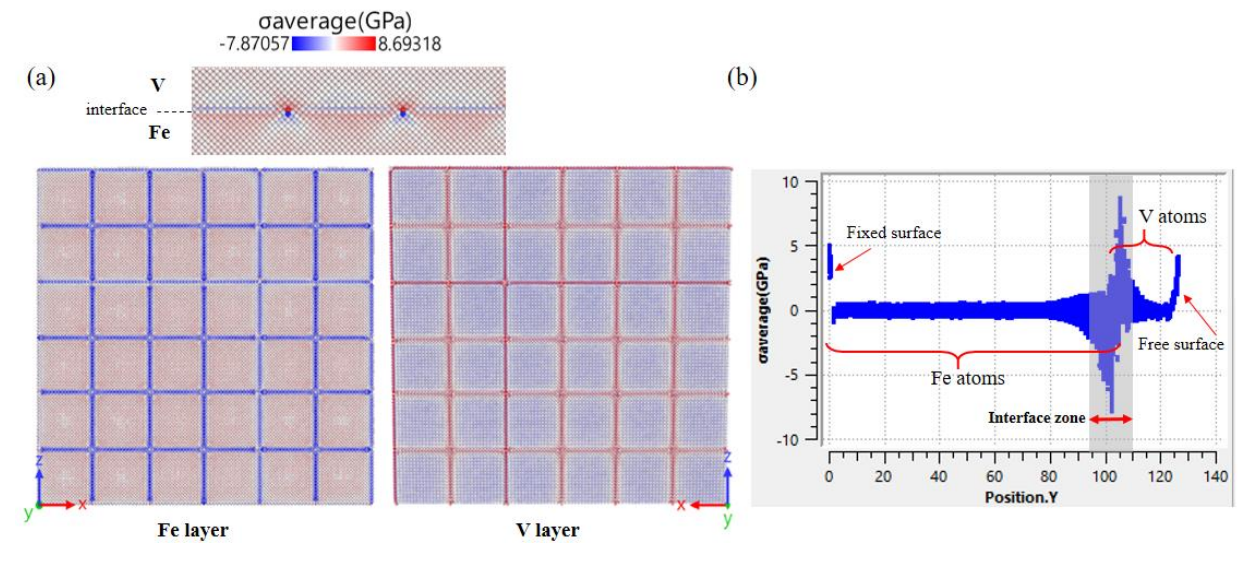


Fig III.2 (a) Top and bottom views of the interfacial stress. (b) y-directional plot of the average normal stresses $\sigma_{average}$ (GPa).

III.2 Indentation response of $V/Fe_{(010)}$ bi-layer vs. single-crystals:

Figure III.3 shows the load curves (a) and hardness curves (b) vs. indentation depth of V, Fe and V/Fe systems. It is grasped that all load curves follow the Hertzian analytical law in their elastic deformation stage.

Before analyzing the deformation mechanisms of the V/Fe bimetal and single-crystals under indentation, we first examine indentation curves. Figure III.3 presents load & hardness curves as functions of indentation depth for V/Fe bilayer and V, Fe single-crystals. It is evident that all load curves follow to the Hertzian analytical law during the elastic deformation stage.

The Hertzian theory, developed by Heinrich Hertz in the late 19th century [100, 101], defines the indentation force as:

$$F = \frac{4}{3} \times \mathbf{E}^* \times \mathbf{R}^{1/2} \times \mathbf{h}^{3/2} \times 10^{-2} \text{ (nN)}$$

Where: E* is the effective modulus of the system, R is the indenter radius and h is the indenter displacement (depth), the effective modulus is defined as:

$$\frac{1}{F_{i}^{*}} = \frac{1 - v_{Fe}^{2}}{E_{Fe}} + \frac{1 - v_{i}^{2}}{E_{i}} \tag{11}$$

For a repulsive indenter, the modulus E_i is considered infinite, so the second term in the calculation of the effective modulus tends to be zero. While the modulus of Fe and V metals are E_{Fe} =200GPa, and E_{V} =128GPa.

Furthermore, the indentation load for the all studied systems increases gradually with increasing indentation depth until plastic yielding occurs, as indicated by the pop-in event. However, compared to both V and V/Fe, the sharper Fe curve shows a higher peak value during plastic yielding, which is evident in both the load and hardness curves. Additionally, the hardening effect in the V/Fe system becomes more pronounced at greater indentation depths,

Chapter III: Atomistic Study of the Effect of Semi-Coherent Interface on nano-indentation of V/Fe Bilayer resulting in an increase in both indentation force and hardness values for V/Fe compared to single crystals. Importantly, Fig. III.3.b demonstrates that V/Fe exhibits higher hardness values compared to Fe and V at the final indentation stage, with respective averages of 23.25 GPa, 21.2 GPa and 15.15 GPa. To gain a deeper understanding of their deformation behavior, we first examine each material separately, starting by V and Fe single crystals.

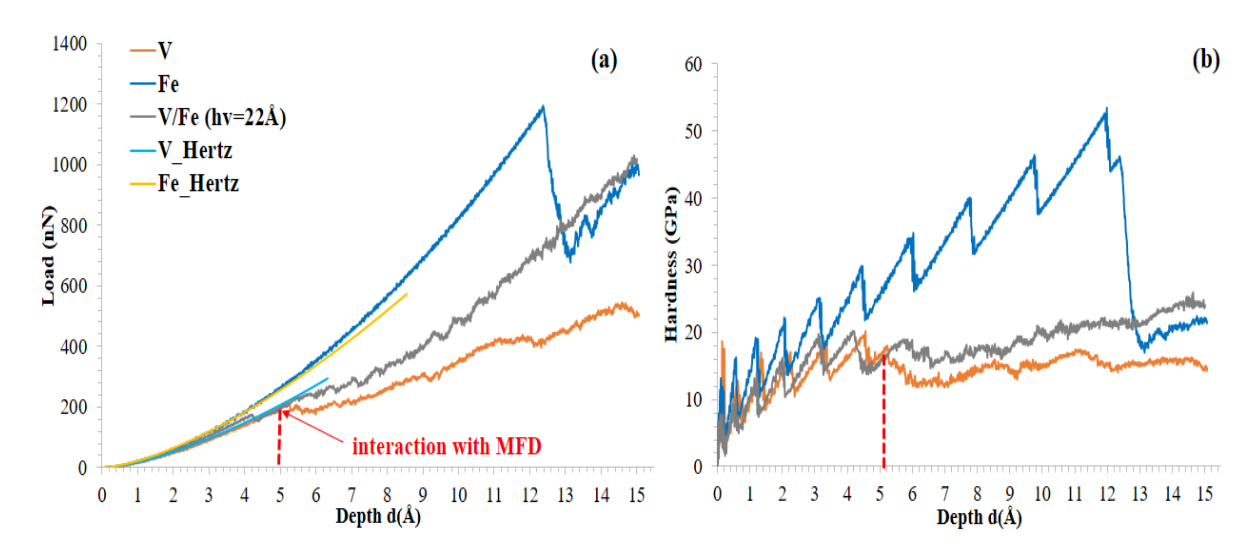


Fig III.3 Indentation load-depth & hardness-depth curves of $V_{(010)}$, $Fe_{(010)}$ single-crystals and $V/Fe_{(010)}$ bi-layer.

III.2.1 Deformation mechanisms of $V_{(010)}$ single-crystal:

It is clear from the indentation curve of V single crystal that, at the beginning of the indentation process, the material undergoes elastic deformation, following Hertzian curve. During this stage, no defects are observed in the material. As indentation continues, one can observe the plastic yielding in load curve, demonstrating the onset of permanent deformations. Figure III.4 visualizes the evolution of defected atoms in pure V and dislocations at various indentation depths. (Ranging from 5.07 to 15.1 Å). At plastic yielding d = 5.07 Å, planar defects begin to nucleate beneath the indenter without the emission of dislocations. As the indenter reaches d = 5.37 Å, two perfect dislocations with Burgers vectors a/2<111>, each with a magnitude of 2.15 Å, are nucleated. With further indentation at d = 5.87 Å, additional dislocations and planar defects result in the formation of a flowershaped twin structure with four symmetric contours, due to defects multiplication gliding in four different directions. At d = 10.7 Å, the 1/2 < 111 > dislocations evolve into shear loops and multiply. Some of these loops then connect to form a <100> dislocation at d = 12.5 Å. As indentation depth increases, the shear loops with Burgers vector a/2<111> continue to develop and multiply.

Towards the end of indentation loading d=15.1 Å, there is a noticeable extension and multiplication of shear loops with Burgers vector a/2<111>, which are observed to move toward the bottom of the cell.

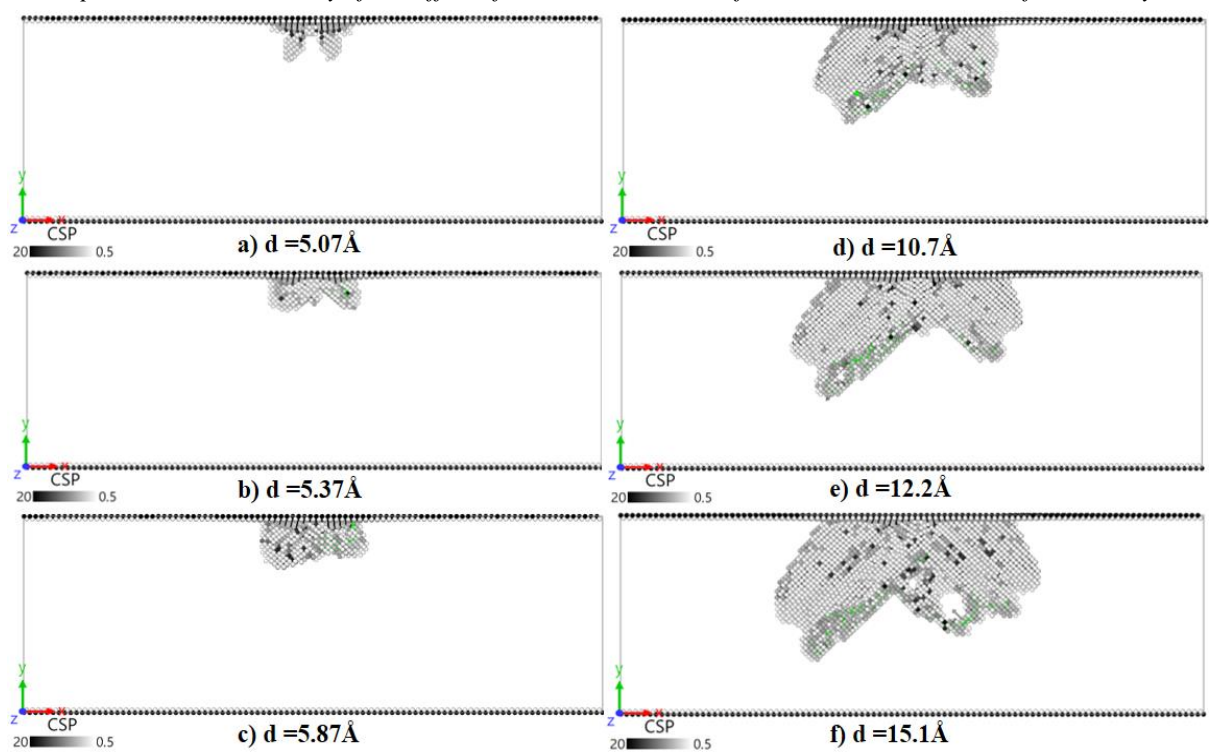


Fig III.4 CSP and DXA analysis of the atomic defects evolution across indentation of pure $V_{(010)}$.

The close-up of figure. III.4, displayed in Fig. III.5, help to comprehend better the plastic deformation mechanisms for V single crystal during indentation.

At an indentation depth of 5.37 Å, planar defects consisting of HCP stacking sequence exhibit a reflection of two twins in the (011) and ($\overline{110}$) planes, with a mirror twin plane (101), which initially formed at $\mathbf{d} = 5.07$ Å (Fig. III.4.a). this twinning occurs symmetrically four times within the same family of planes, as shown in Fig. III.5. these observations confirm that twinning is the primary deformation mechanism accompanied by slip deformation, since two segments of 1/2 < 111 > dislocations nucleate at d=5.37 Å. this observation Aligns with the findings of Grögeret al. [102]

One can understand from the schematic representation of the planes and directions of the planar defects; associated with **the flower-shaped structure observed at d = 5.87** \mathring{A} (shown in figure. III.5.c); that, four symmetry axes are clearly visible, labeled II, III, IV, and I. Moreover, four pyramids with rectangular bases form this flower structure. The faces of these pyramids correspond to the $\{101\}$, $\{110\}$, and $\{121\}$ twin planes, which are well known as the close-packed planes of BCC metals, and particularly for pure vanadium [103, 104].

Biener et al. [105] have observed similar flower-shaped structure through AFM images taken after indentation of BCC Ta.

With further indentation, $\mathbf{d} = 12.2 \, \text{Å}$, shear loops with Burgers vector a/2<111> appear (refer to Figure III.5.e). Correspondingly, a [100] dislocation type is formed by a combination of some a/2<111> dislocations. As illustrated in Fig. III.5, a horizontal extension of shear loops due to the boundary effect, that can be noticed when depth attains 15.1 Å. The deformation

Chapter III: Atomistic Study of the Effect of Semi-Coherent Interface on nano-indentation of V/Fe Bilayer of Ta and VN during nano-indentation has been revealed to exhibit similar behavior [106, 107]. Similarly, for pure V [32] and Ta [108].

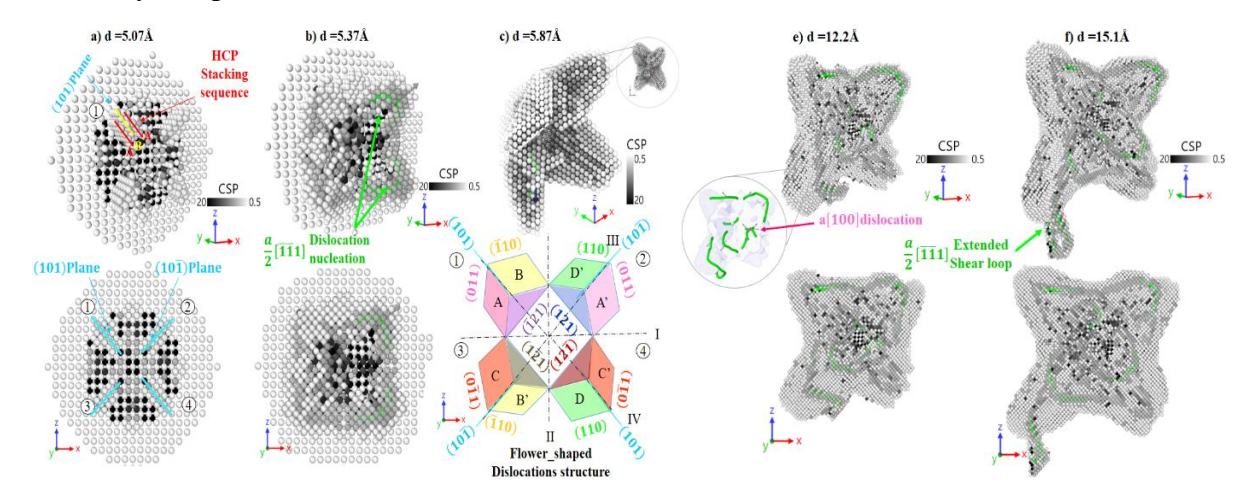


Fig III.5 Close-up of the atomic defects along plastic regime of indented $V_{(010)}$ single crystal.

III.2.2 Deformation mechanisms of $Fe_{(010)}$ single-crystal:

For Fe single crystal, the indentation curve shown in figure. III.3.a. closely resembles the Hertzian solution during the elastic stage. Then, as can be seen in Figs. III.6.a and III.7.a, the first point of yielding arises around d = 12.45 Å, indicating the initiation of plastic deformation resulting from the presence of planar defects on the activated {110} slip planes. Two perfect dislocations with Burgers vectors $\frac{a}{2} [\bar{1}1\bar{1}], \frac{a}{2} [1\bar{1}1]$, nucleate just after d=12.55Å, demonstrating slip deformation mechanism. Further dislocations with Burgers vectors a/2 < 111 > and a < 100 > appear when the indentation increases to <math>d=13.25 Å. As seen in Fig. III.6.c, these dislocations are stimulated along the {101} <111 > slip systems. Thus, slip serves as the primary plastic deformation mechanism in iron.

With more indentation at d=13.95Å, the number of dislocations increases further, leading to interactions among them. Some dislocations evolve into shear loops with Burgers vectors: a/2 <111> and a <100>, while a dislocation segment a <110> forms due to dislocation interactions. As the indenter penetrates deeper into the crystal, reaching d=14.55Å, the multiplication of both a/2 <111> and a <100> dislocations results in the formation of multiple dislocation junctions and nodes. Some of these dislocations extend into shear loops, which subsequently connect with one another. At the final stage of indentation, a horizontal shear loop extends to its maximum limit before breaking, then some defected atoms pile-up on the indented surface at d=15.15Å (see figure. III.6). these findings align well with previous studies [109, 110].

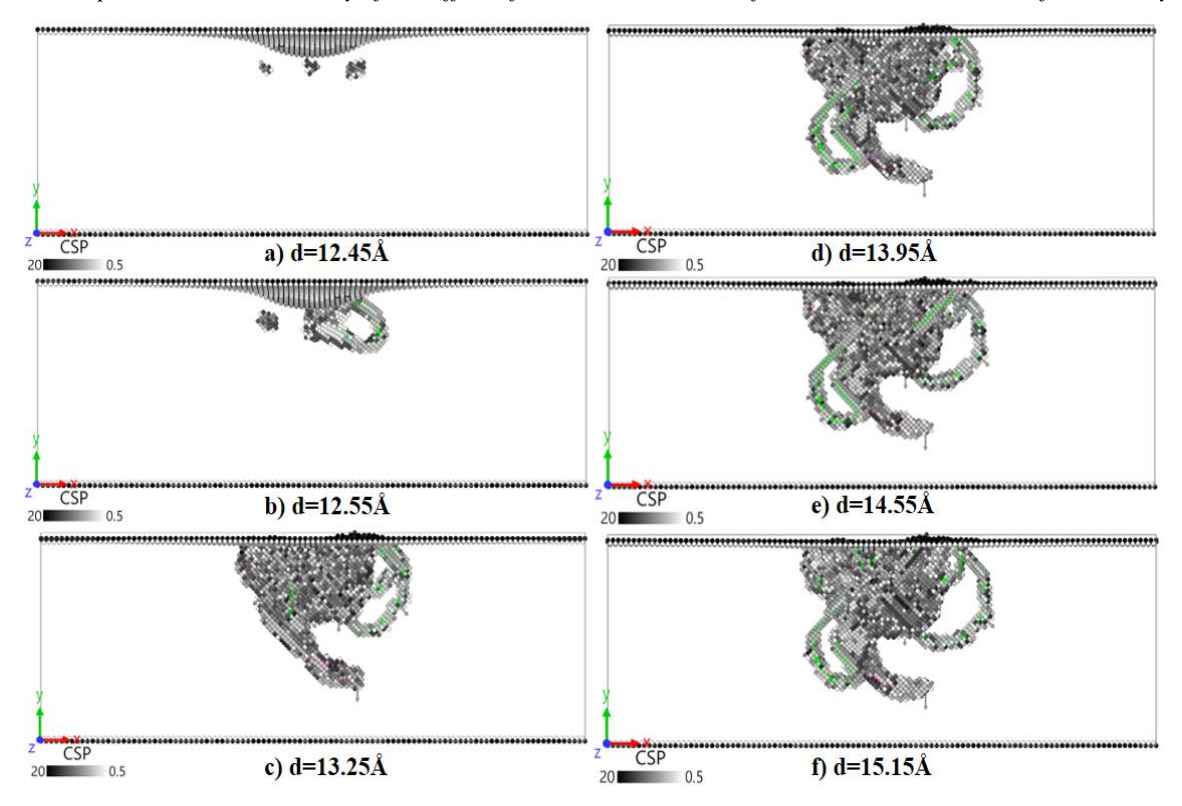


Fig III.6 CSP and DXA analysis of the atomic defects evolution across indentation of pure $Fe_{(010)}$.

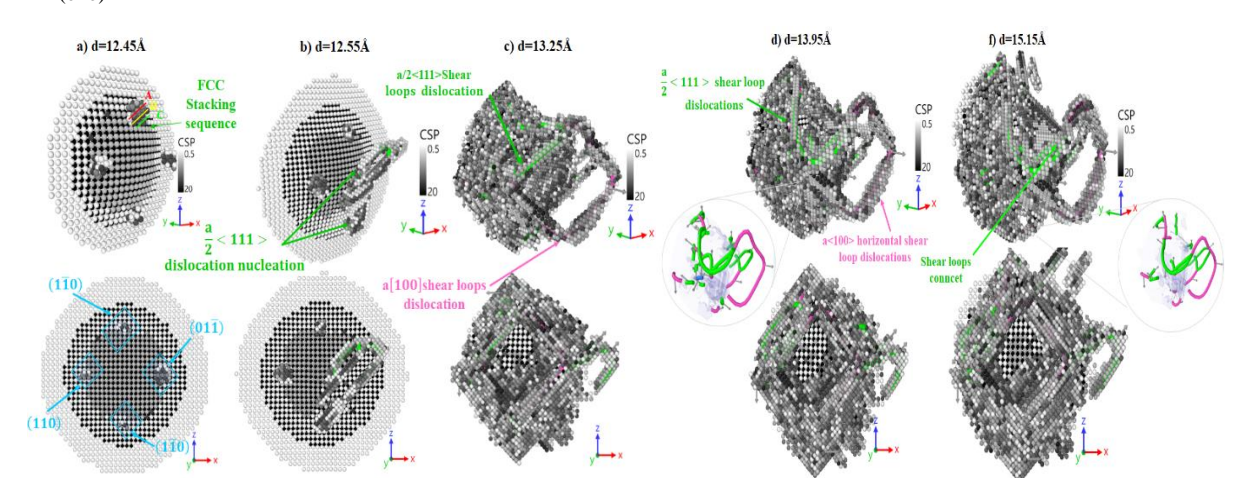


Fig III.7 Close-up of the atomic defects along plastic regime of indented Fe₍₀₁₀₎ single crystal.

The difference in deformation mechanisms for Fe and V single crystals, at the same indentation depth of d=15.1 Å, are depicted in figure. III.8. It is evident that slip is the predominant deformation mechanism in iron, where both 1/2 < 111> and <100> dislocations nucleate, glide, and interconnect, supporting results from the literature [111]. These dislocations evolve into shear loops, which then exhibit significant extension along the indentation direction. In contrast, the primary plastic deformation mode in vanadium is twinning, accompanied by reduced number of extended shear loop dislocations with Burgers vector a/2 < 111>.

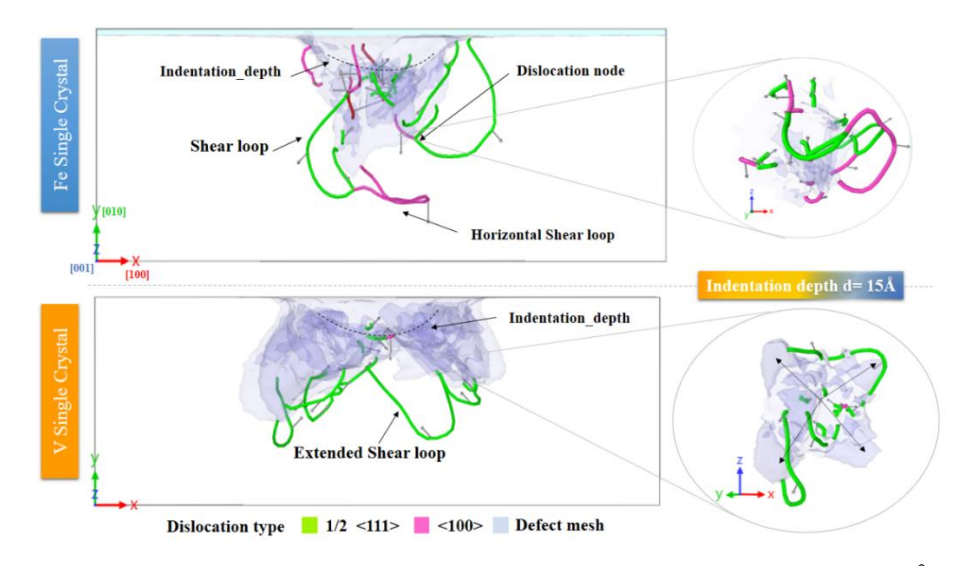


Fig III.8 Deformation mechanisms in $V_{(010)}$ and $Fe_{(010)}$ single-crystals at d = 15Å, DXA.

III.2.3 Deformation mechanisms of $V/Fe_{(010)}$ bi-layer:

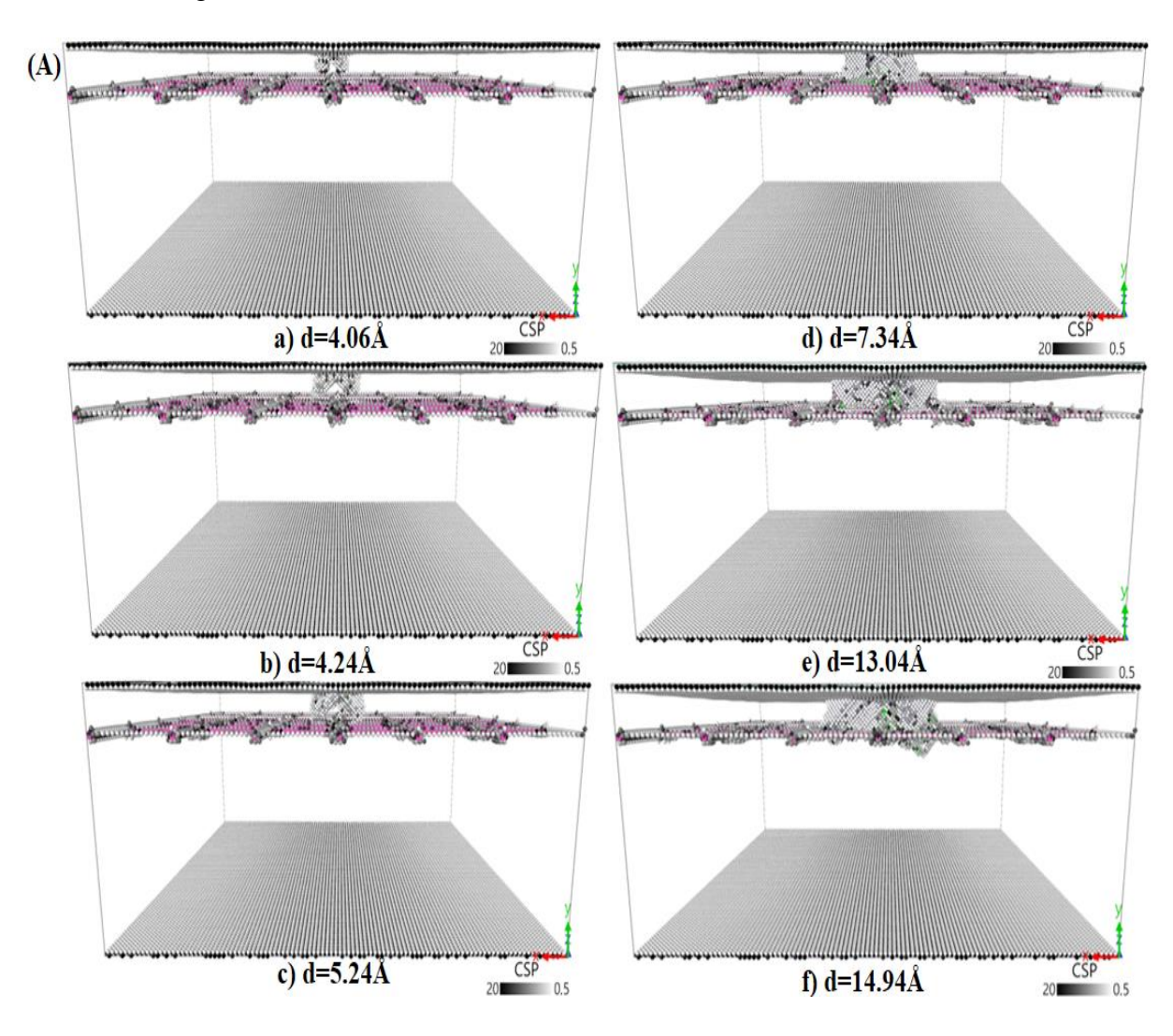
Figures III.9 (A) and III.9 (B) show the evolution of dislocations within the V/Fe system; with a vanadium layer thickness of 22Å during the indentation; providing insights into the plastic deformation mechanisms in the V/Fe multilayer. Agreeing with Hertzian law, the load increases with indentation depth increment during the initial elastic stage, as illustrated in Figure III.3(a), until it reaches 4.06Å, at which point plastic deformation initiates. **At this plastic yielding**, twinning deformation initiates through the formation of planar defects beneath the indenter. **Shortly after**, d=4.24Å, two dislocation segments with a Burgers vector of a/2<111> nucleate. Notably, the delayed onset of plastic deformation in V compared to V/Fe can be attributed to the presence of localized stress induced by the interface.

As indentation advances to d=5.24Å, some defected atoms from V layer interact with the nearest misfit dislocation (MFD) line at the interface (refer to figure III.9A), resulting in a slight strengthening of the indentation curve (Figure III.3). Nevertheless, It is also observed in Figure III.3(a) that between 4.24Å and 5.24Å, the load-depth curves of both V and V/Fe overlap. This implies that the interface has no impact on the bilayer's plastic deformation before dislocation-interface interaction, and that the mechanical response is still comparable to that of pure V.

With further indentation at d=6.24Å, dislocations with a Burgers vector of a/2<111> interact for the first time with the MFD line (see figure III.9B(c)), leading to a noticeable strengthening effect. This is also reflected in the increased hardness of V/Fe bilayer. As shown in Figure III.9B(d), at d=7.34Å, the 1/2<111> dislocations multiply and accumulate at the nearest MFD nodes. When the indenter reaches a depth of 13.04Å, dislocations continue emitting from the indented surface without penetrating through the interface.

Chapter III: Atomistic Study of the Effect of Semi-Coherent Interface on nano-indentation of V/Fe Bilayer At this point, the MFD nodes obstruct two small horizontal prismatic loops with a Burgers vector of a/2 <111>. Additionally, some dislocations accumulate at the interface inside the indented V layer.

As a result, the misfit dislocation network acts as a significant barrier to dislocation motion, stopping the prismatic loops from transferring into the Fe substrate. Furthermore, it contributes to the evolution of certain dislocations into horizontal shear loops, as shown in Figure III.9B(f). Notably, the blocking effect of the MFD network prevents also the development of formation of the flower-shaped dislocation in V/Fe bilayer system, which was typically induced by twinning in the V single crystal. Instead, the interface promotes the formation of a/2<111> horizontal shear loops and generates a repulsive force, effectively serving as a strong barrier to dislocation propagation into the Fe substrate. This hardening effect observed in the BCC/BCC semi-coherent interface is consistent across different model sizes, including a reduced model size of 150Å.



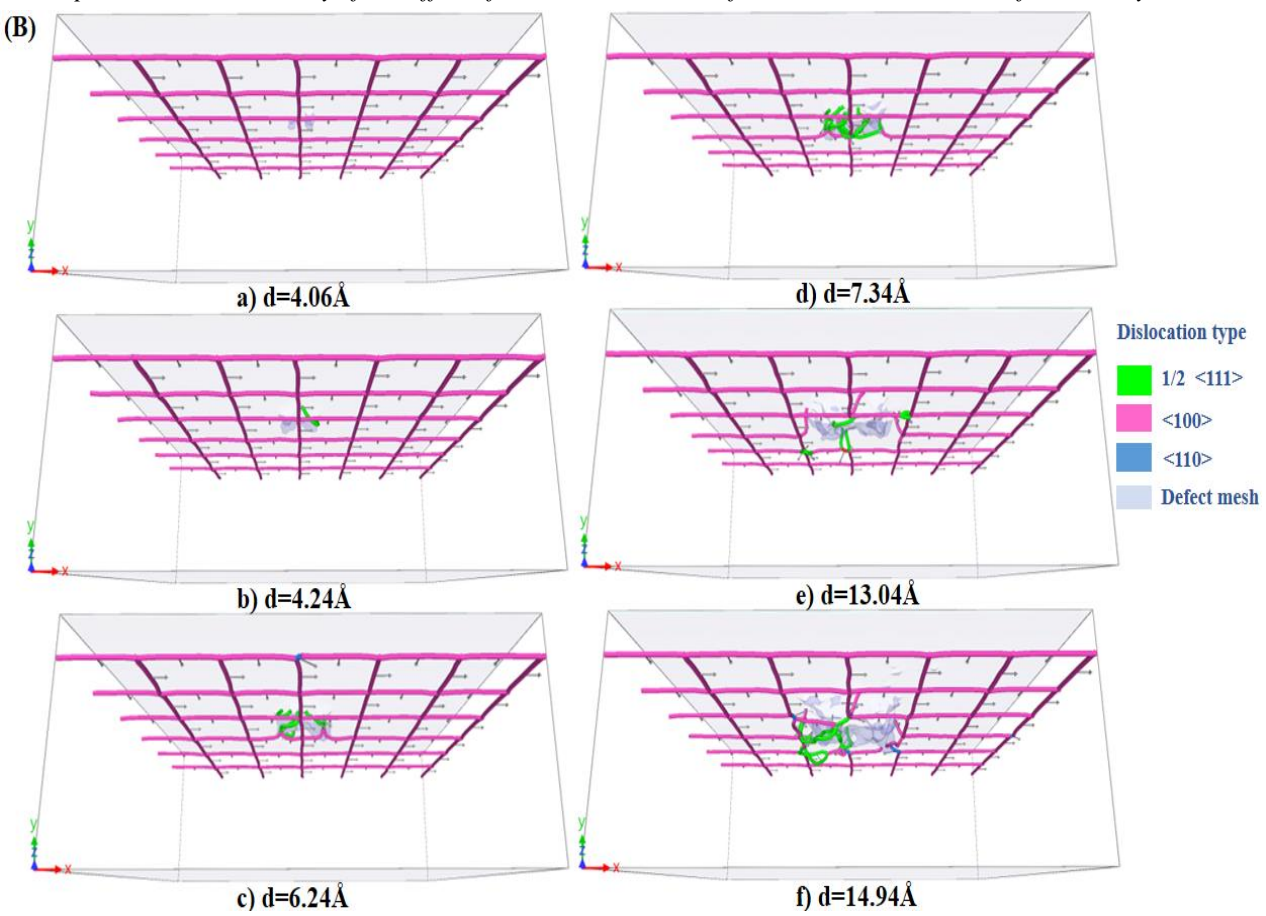


Fig III.9 A) CSP analysis of the atomic defects evolution across indentation of $V/Fe_{(010)}$. B) DXA snapshots of dislocations dynamics across plastic regime of the indented $V/Fe_{(010)}$ bilayer.

III.2.4 Evolution of dislocations under (111) indentation:

Through DXA analysis on OVITO program, we computed the total dislocation length $L_{\rm dis}$ and the number of dislocation segments $N_{\rm dis}$ in V, Fe single crystals and the V/Fe bilayer systems aiming to estimate the dislocation dynamics during indentation. Figure III.10, offers statistical details based on the previous snapshots of all three materials.

It is readily apparent that as the indentation gets deeper, the total dislocation length and the number of dislocations increases.

All three systems experience elastic deformation in the first stage, with N_{dis} and L_{dis} keep on null. The case of pure Fe shows a long elastic deformation period that extends until around 12.5 Å. In contrast, the plastic deformation of V/Fe system arises faster at d=4.24 Å.

For Stage II, both L_{dis} and N_{dis} of V and V/Fe systems progressively increase as indentation advances within the plastic regime. However, the dislocation length in V layer is greater than that of the V/Fe system at an indentation depth of 10.9 Å. which can be explained by the fact that, shear loop dislocations with Burgers vector a/2<111> are prevented by the interface in V/Fe bilayer, whereas in the pure V system, they multiply and extend easily.

From d=12.5Å (Fig. III.10), the third stage shows that, in comparison to the V and V/Fe systems, the $L_{\rm dis}$ and $N_{\rm disof}$ dislocations for Fe are significantly greater. Nevertheless, the horizontal extension of shear loops in the Fe crystal causes these dislocations to stabilize at the end of indentation. The huge amount of defective atoms in the planar defects induced by twinning deformation in the V crystal, combined with reduced dislocation activity, is the reason for the slower increase in $L_{\rm dis}$, for further indentation of pure V. Interestingly, the number of misfit dislocations (MFD) with Burgers vector a<100> in the V/Fe system stays roughly constant about 72, with $L_{\rm dis}$ =3605Å. Indicating the resilience of MFD network. Our results for the Fe system agree with those of Gao et al.[109].

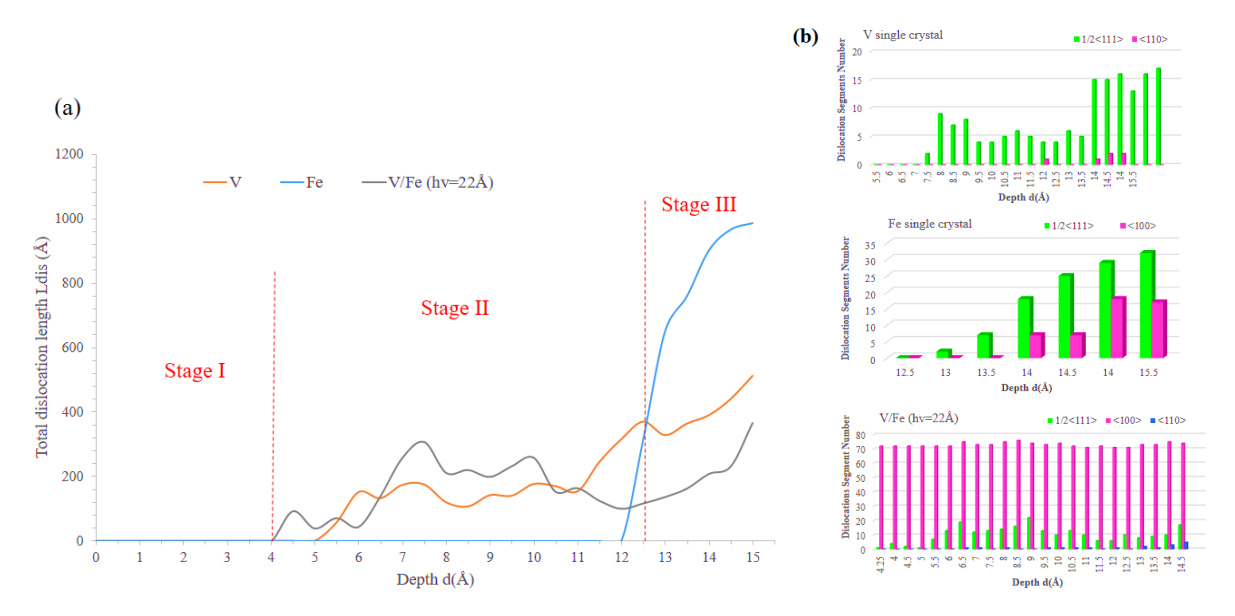


Fig III.10 (a) Development of dislocations length L_{disl} along indentation of $V_{(010)}$, $Fe_{(010)}$ single-crystals and $V/Fe_{(010)}$ bi-layer (Excluding MFD length). (b) Evolution of the dislocation segment number N_{disl} across indentation (including MFD length).

III.3 The effect of V layer thickness on the response of V/Fe:

III.3.1 Indentation curves of V/Fe bi-layer with different V layer thickness:

In this section, we examine the indentation response of V/Fe system, for the purpose to examine the effect of V layer thickness on the hardening of V/Fe bilayer induced by semicoherent interface. Compared to the load-depth curve of pure vanadium, figure III.11(a) shows the variation in the load-depth curve for V/Fe for different V layer thicknesses (h_V) ranging from 13 to 120 Å. Their corresponding hardness values are shown in figure III.11(b). The curves for h_V=80 and 100Å are excluded for the purpose of clarity. Considering that, they follow the same trend as the curve of V/Fe with h_V=120 Å. Foremost, elastic deformation is observed expanding slightly as h_V increases. It is also evident that, for V layer thicknesses of h_V \leq 30Å, the load and hardness values of the V/Fe bilayer are seen greater than those of pure vanadium. In correspondence with pure V, the V/Fe curves with h_V=50Å and

Chapter III: Atomistic Study of the Effect of Semi-Coherent Interface on nano-indentation of V/Fe Bilayer 120Å slightly converge. Furthermore, one can deduce that, when the thickness of the V layer increases, hardness decreases (see Fig III.11 (b)).

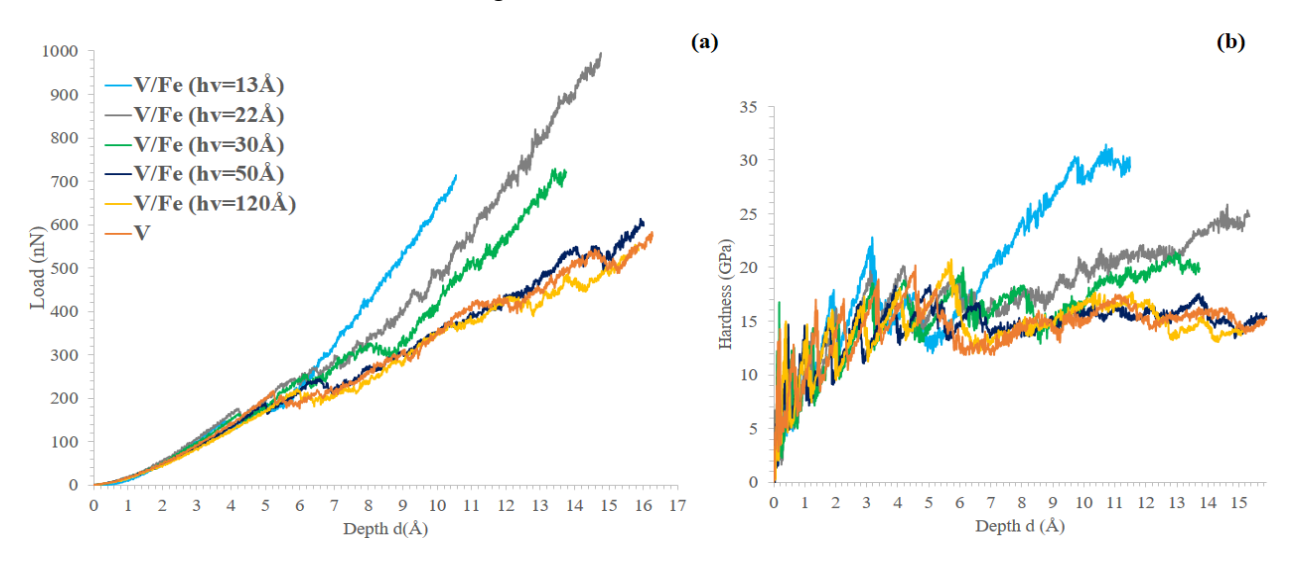


Fig III.11 Indentation load-depth & hardness-depth curves for pure $V_{(010)}$ and $V/Fe_{(010)}$ bilayer with various V layer thicknesses (hy =13, 15, 22, 30, 50, 120 Å).

III.3.2 Deformation mechanisms of V/Fe bi-layer with different V layer thickness:

Fig. III.12 shows snapshots of dislocation analysis (DXA) for different V layer thicknesses ($h_V = 13, 30, 50, 80, and 120 \text{ Å}$) at different indentation depths, to help visualize how V layer thickness correlated with interface effect along the plastic deformation of V/Fe system. For $hv=13\text{\AA}$, the initial yield point, seen at d=3.41 Å in Fig. III.11 (a) is associated with the formation of planar defects and dislocation emission beneath the indented surface. As illustrated in Fig. III.12, two dislocations with Burgers vector a/2<111> are nucleated at d=3.55Å. Owing to the closeness to the interface, these dislocations have immediate interaction with the nearest misfit dislocation (MFD) node. As single dislocation length (L_{dis}), is about 15 Å, which is greater than the thickness (h_V) of the V layer. As indentation advances to d = 7.15Å, dislocations with Burgers vectors a/2<111> interact with the MFD line and are prohibited by the interface. These dislocations slip smoothly over the {101} <111> slip systems, which are the site to the MFD nodes. Then, dislocations pile-up and extend horizontally at the interface at d = 10.15 Å, which prevents them to propagate inside the Fe substrate. Plastic deformation in the V/Fe bilayer is primarily governed by the nucleation of dislocations with a Burgers vector of a/2<111> at an indentation depth of d=4.35 Å for a V layer thickness of hv = 30 Å. The number of dislocations rises as the indentation proceeds around d=7.65Å, interacting with the nearest misfit dislocation (MFD) node without passing across the interface. As seen in Fig. III.12, these dislocations reproduce and extend horizontally over the interface at d = 13.75 Å, thereby blocking their transmission into the Fe layer. It is evident that this mechanism plays an integral role in the significant improvement in system

Chapter III: Atomistic Study of the Effect of Semi-Coherent Interface on nano-indentation of V/Fe Bilayer hardness seen in Fig. III.11 (b). For the case of hy=50Å, the plastic behavior of the V/Fe bilayer closely resembles that of pure V. The flower-like shaped structure can form freely at an indentation depth of d = 5.22 Å, after the nucleation of 1/2 < 111 > dislocations is first seen. Nevertheless, the 1/2<111> dislocations slip in the direction of the misfit dislocation (MFD) nodes at the interface and start interacting with them when **d** reaches or far exceeds 13.22 Å. With additional loading, numerous dislocations with Burgers vectors a/2<111> and a<110> become visibly obstructed at the interface, leading to the horizontal expansion of shear loops at d=15.1Å (see Fig. III.12). consequently, the interface serves as an effective barrier to dislocation transmission after their interaction with MFD nodes, which explains the slight increase in hardness observed for the $h_V = 50$ Å case. Since the plastic deformation zone stays far from the interface, the plastic deformation process for V/Fe bilayers with V layer thicknesses of hv=80 Å and 120 Å is very analogous to that of pure V. The unique structure in the shape of a flower is developed by a variety of twin planes. Furthermore, 1/2<111> shear loops can freely nucleate and extend without interacting with the interface because to the accessible free space (see Fig. III.12).

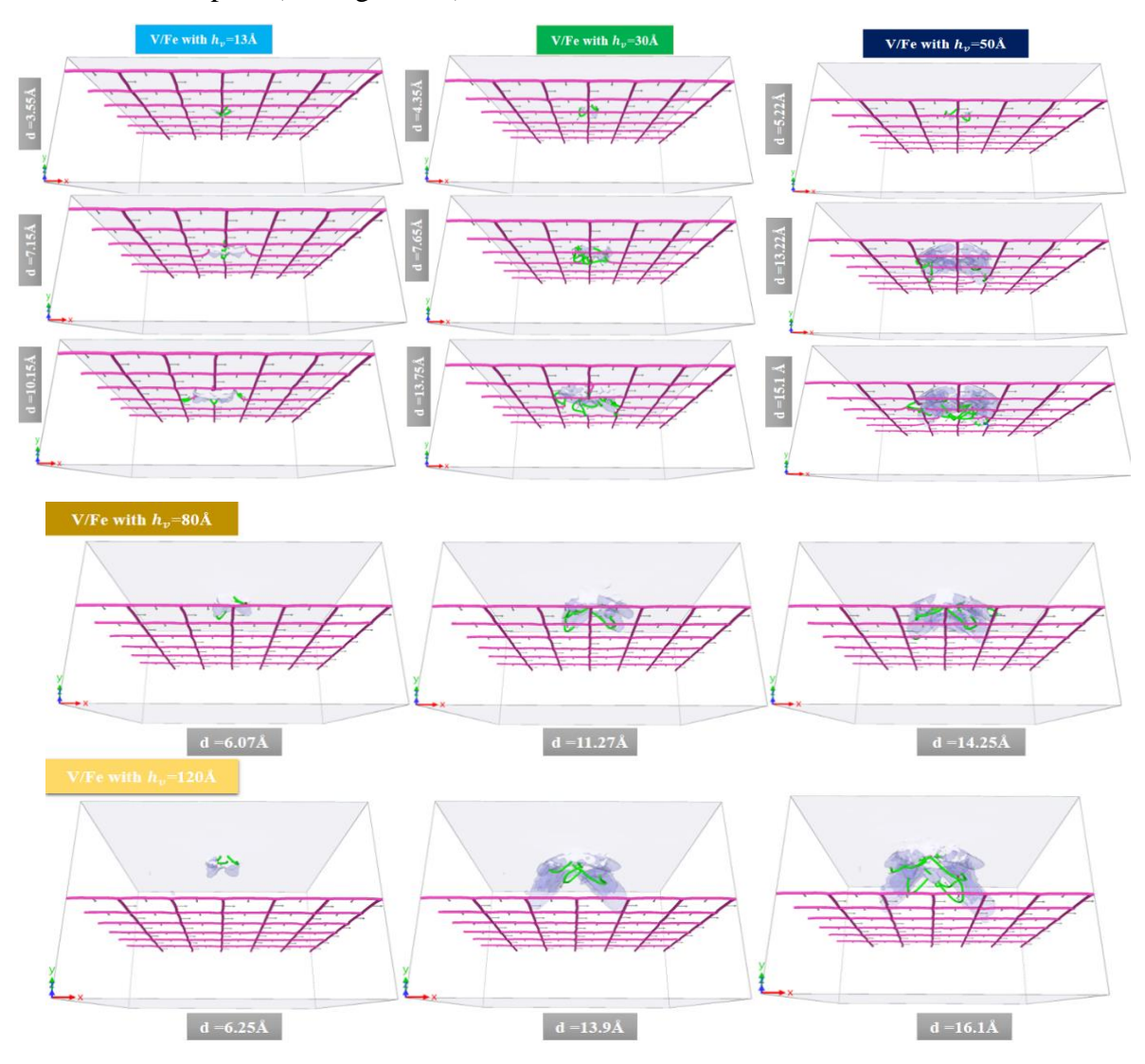


Fig III.12 DXA snapshots of dislocation evolution in V/Fe bi-layer with various V layer thicknesses (h_V =13, 30, 50, 80, 120 Å) along plastic regime.

Figure III.13 shows how the average hardness of V/Fe bilayer varies with V layer thickness comparing to the hardness of V, Fe single crystals. It is clear that the hardness of V/Fe rises with increasing h_V for V layer thicknesses below 50 Å, which is regarded as the critical thickness. It reaches significantly excessive values, especially at $h_V = 13$ and 22Å. Nevertheless, after this key thickness, the hardness progressively drops and eventually attains close to the hardness of pure V. Then, hardness values slightly diverge from those of pure V when h_V exceeds 80 and 120 Å. It is noteworthy that a film thickness of 103 Å was used to create the reference indentation curve for the single-crystalline V. As a result, the single-crystalline closely matches the bulk features of vanadium, which explains the finding that the bilayer hardness is almost identical to that of pure V for thicker V layers.

It is well-established that deformation mechanisms in metal multilayers are strongly influenced by the thickness of the deposited film. In our present case, the relationship between V layer thickness and the hardening effect induced by misfit dislocations (MFDs) is linked to the proximity of dislocation to interface. This finding aligns with the existing literature and supports a Hall-Petch-type strengthening behavior, correlating hardness with film thickness [39-42, 111, 118-120].

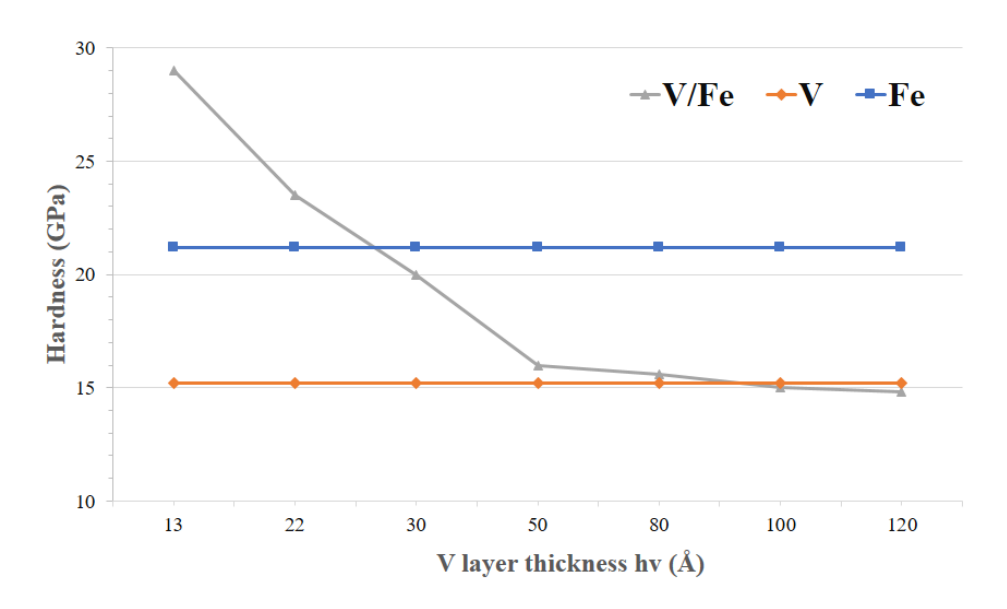


Fig III.13 Comparison of hardness between V/Fe bilayer and single crystals as a function of V layer thickness.

III.4 Indenter position effect:

A clear relationship was observed in the previous sections between the plastically deformed zone and the misfit dislocation (MFD) nodes. These nodes serve as preferential sites for dislocation glide in the V/Fe bimetal during (010) indentation and exhibit a strong ability to hinder dislocation propagation.

In this section, we propose three distinct scenarios for the indenter placement during nano-indentation along the y (010) direction. In the first scenario, denoted as "Indenter Position (A)", the indenter is placed above the V/Fe model, where the plastic zone is expected to form near the four bordering nodes of the square-grid MFD network. In "Indenter Position (B)" the indenter is aligned directly above a MFD's line, while in "Indenter Position (C)" the plastic deformation zone is anticipated to interact with a central MFD node (see Fig. III.14). shedding light on the role of MFD nodes in dislocation-interface interactions. Each of these configurations is expected to result in different outcomes, influencing the stability of the semi-coherent interface.

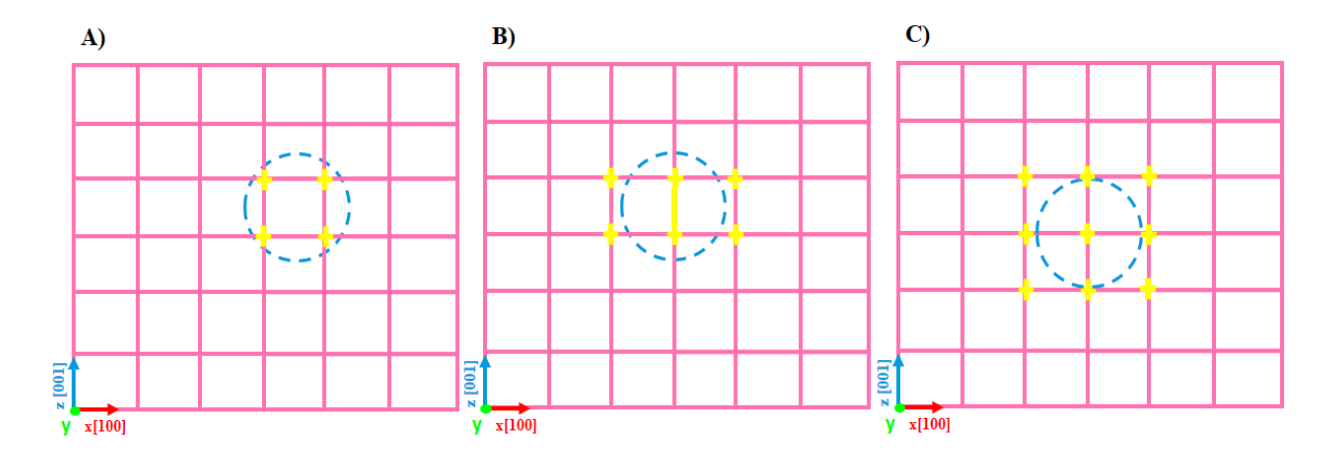


Fig III.14 Schematic illustration of the different indenter positions cases (A, B, C) above the indented surface.

III.4.1 Indentation response of V/Fe for different indenter positions:

Figure III.15 presents the load-depth and hardness-depth curves as a function of indentation depth for the V/Fe bimetal under different indenter positions (A, B, and C). It is evident that in all cases, the V/Fe follows a similar elastic deformation trend up to the first pop-in event, which occurs at different indentation depths depending on the indenter position. A noticeable distinction in the load curves appears after an indentation depth of d = 10.4 Å, persisting until the end of the loading phase (at d = 15.2 Å). Furthermore, the average hardness values at the end of indentation are 18.32 GPa, 19.5 GPa, and 23.25 GPa for indenter positions A, B, and C, respectively. Notably, the indenter position (C) exhibits the highest hardness value at the end of the indentation.

Chapter III: Atomistic Study of the Effect of Semi-Coherent Interface on nano-indentation of V/Fe Bilayer

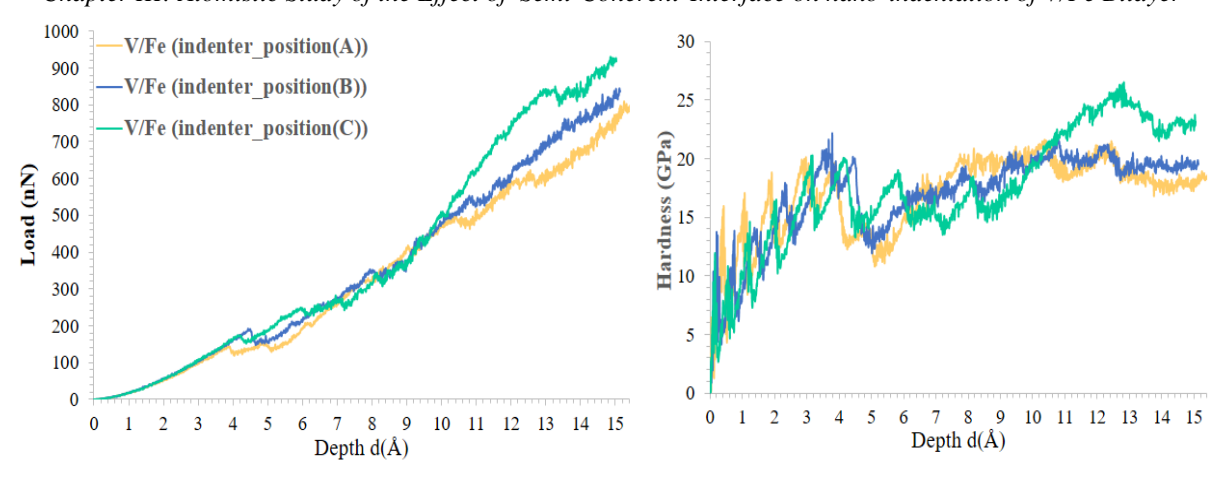


Fig III.15 Load-depth & Hardness-depth curves of V/Fe₍₀₁₀₎ for different indenter position.

III.4.2 deformation mechanisms in $V/Fe_{(010)}$ for different indenter positions:

To investigate the dislocation–interface interaction mechanisms during the plastic deformation of V/Fe for each indenter position, Figure III.16 presents Dislocation Analysis (DXA) images generated using Ovito software. Green lines represent dislocations with Burgers vector a/2 <111>, while pink and blue segments correspond to a <100> and a <110> dislocations, respectively. In the following, we describe the plastic deformation process for each indenter position separately.

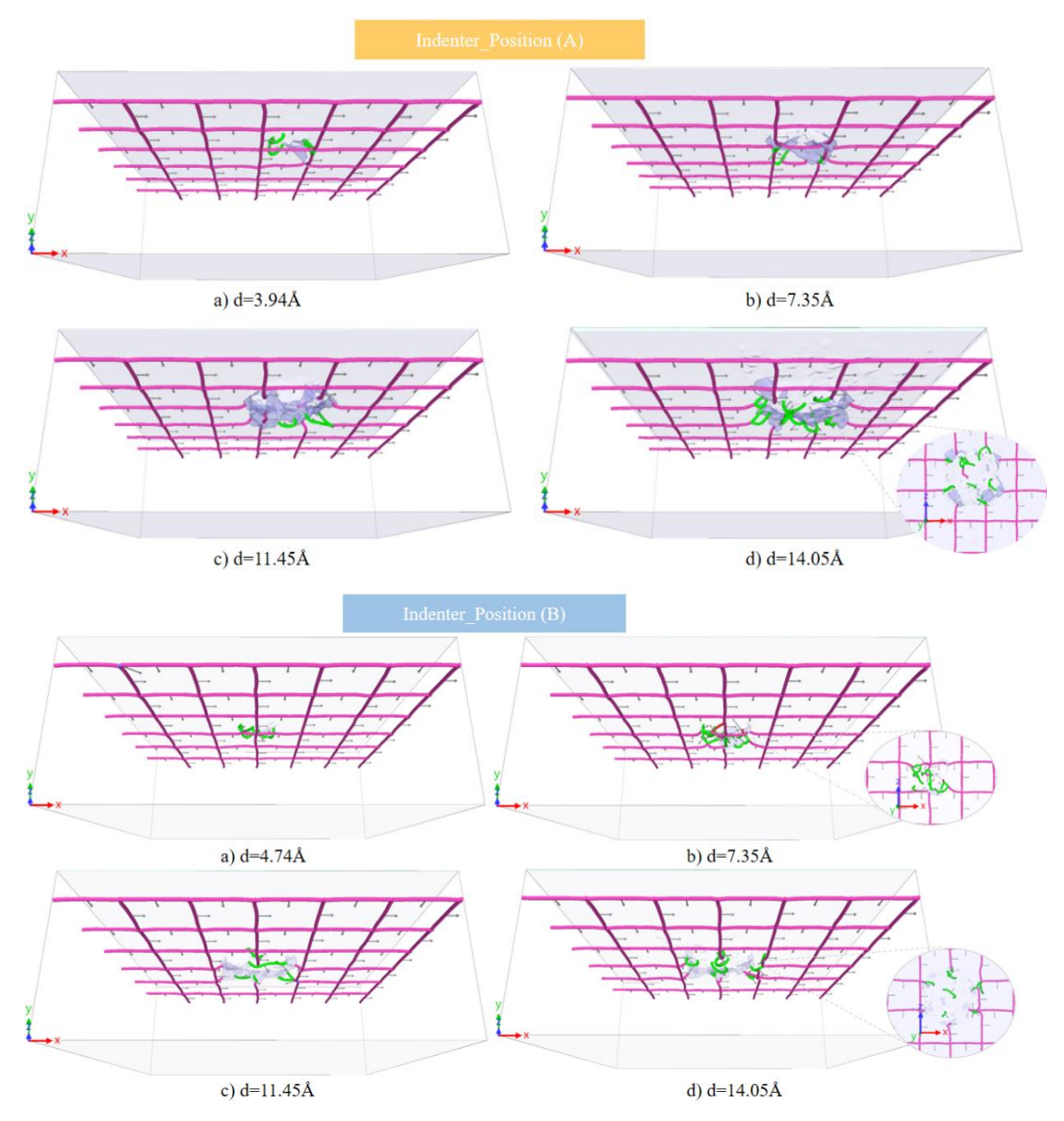
Indenter Position (A):

The V/Fe bilayer system deforms elastically until **an indentation depth of d** = 3.45Å, marking the first pop-in event in load curve. At this depth, planar defects emerge beneath the indented surface, indicating the onset of plastic deformation. Shortly after d = 3.94Å, a nucleated dislocation with Burgers vector a/2 <111>, together with some planar defects, interacts with the nearest MFD nodes. As indentation continues, at d = 7.35Å, dislocations become obstructed by the interface as they begin interacting with the four nearest MFD nodes. By d=11.45Å, this obstruction effect promotes the transformation of some a/2 <111> dislocations into horizontal shear loops (see Fig. III.16). However, when dislocations do not encounter MFD lines or nodes to interact with, they can freely glide into the Fe layer (d = 14.05Å).

Indenter Position (B):

For this case, plastic deformation in the V/Fe bilayer initiates at an indentation depth of $d=4.52\text{\AA}$, where planar defects and dislocations with Burgers vector a/2 <111> are emitted. Shortly after $d=4.74\text{\AA}$, these dislocations start interacting with the nearest MFD line. Beyond this depth, many dislocations are visibly prevented from gliding into the Fe layer by the MFD network ($d=7.35\text{\AA}$). With further indentation, the interaction of free dislocations with Burgers vector a/2 <111> extends, interacting with the six neighboring MFD nodes at $d=11.45\text{\AA}$, where the interface induces the horizontal extension of some dislocations. However, at $d=14.05\text{\AA}$, one segment of a/2 <111> dislocation is observed crossing the interface in the coherent region.

Similarly, plastic deformation begins with the formation of planar defects and the nucleation of a dislocation with Burgers vector a/2 < 111 > at d = 4.4Å. The first interaction between these dislocations and the central MFD node occurs at d = 6.09Å. By d = 7.35Å, multiple accumulated dislocations with Burgers vector a/2 < 111 > are blocked at the interface (see Fig. III.16). as indentation progresses, at d = 11.45Å, these dislocations interact with four additional adjacent MFD nodes. At d = 14.05Å, the a/2 < 111 > shear loops extend horizontally along the interface, effectively preventing further dislocation propagation into the Fe layer.



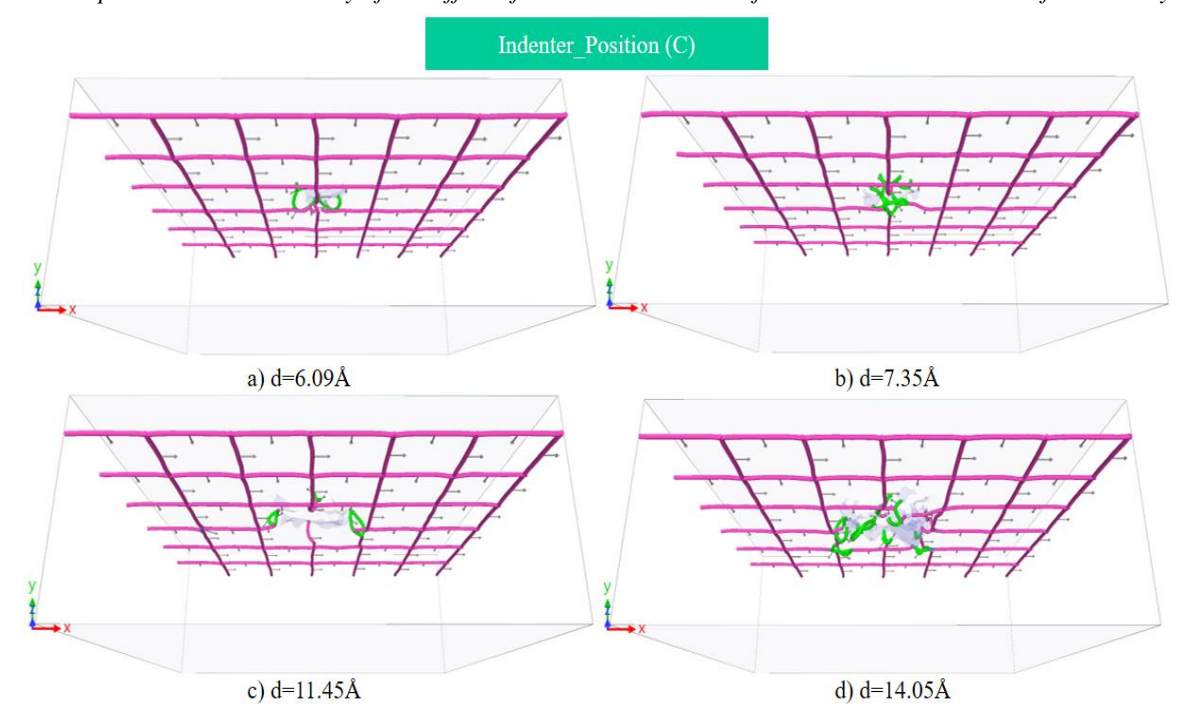


Fig III.16. DXA snapshots of dislocations dynamics across plastic regime of the indented $V/Fe_{(010)}$ bi-layer for various indenter positions.

One can deduce that, the elastic deformation mechanisms of the V/Fe bilayer system remain largely similar across different indentation positions. However, Figure III.17 highlights different dislocation-interface interactions at advanced indentation depths for each case. The primary difference lies in the number of activated MFD nodes.

In every case, early in the plastic deformation stage, free nucleated dislocations start interacting with the closest MFD node or line. As indentation progresses, the interface exerts a repulsive force that prevents dislocation from gliding into the Fe substrate. Moreover, figure III.17 illustrates that MFD nodes serve as preferential sites for dislocation propagation.

Four MFD nodes are involved during dislocation-interface contact for the case of indenter position (A), while six and nine nodes are engaged for positions (B) and (C), respectively. The indentation curves (Figure III.15) show that the highest load and hardness values are found at indentation point (C). This implies that an increased hardening effect results from the more MFD nodes participating in dislocation- interface interaction.

Chapter III: Atomistic Study of the Effect of Semi-Coherent Interface on nano-indentation of V/Fe Bilayer

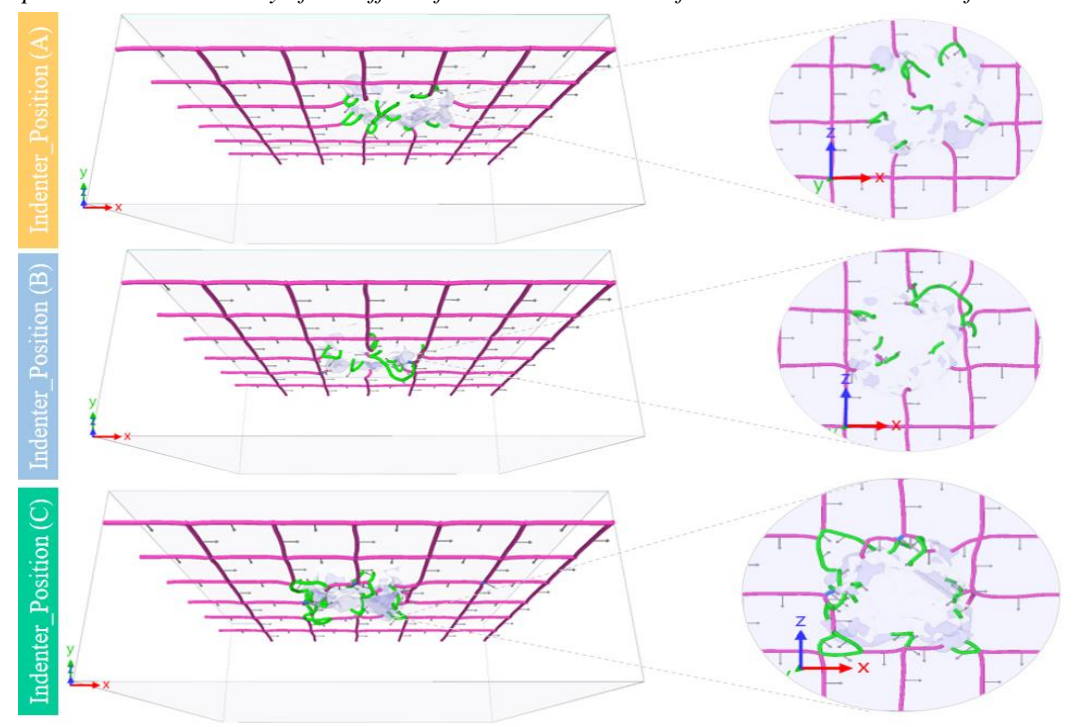


Fig III.17 Dislocation—interface interaction in V/Fe for different indenter positions, at d=15Å.

III.5 Discussion:

III.5.1 Blocking effect induced by semi-coherent interface:

In this study, we observe that the blocking effect of the BCC/BCC interface leads to a distinct evolution of dislocations into horizontal shear loops, predominantly at MFD nodes. These findings align with previous research highlighting the role of semi-coherent interfaces in the strengthening of multilayers by impeding dislocation motion. In this respect, Hoagland et al. [51] demonstrated that semi-coherent interfaces act as barriers to slip due to residual coherency stresses in regions between misfit dislocations and the formation of steps when dislocations cross the interface. In a similar vein, Cao et al [6] discovered that Ni/Al with thicknesses of nanometer-scale shows greater hardness than Ni single crystal in their nanoindentation research of Ni/Al multilayers. This phenomenon was ascribed to the semi-coherent FCC/FCC interface, which prevents dislocation propagation by exerting a repulsive force.

Additionally, Shao et al. [111] noted that hardening effect in metallic multilayers can be facilitated by semi-coherent interfaces, which act as effective obstacle to dislocation propagation. The importance of semi-coherent interfaces in strengthening FCC/FCC multilayers by blocking dislocation transmission has also been highlighted in a number of studies [112–116].

III.5.2 Barrier Mechanics:

It is evident that the MFDs' nodes in the semi-coherent interface of the V/Fe bi-layer serve as preferential sites for dislocation propagation while simultaneously acting as barriers

Chapter III: Atomistic Study of the Effect of Semi-Coherent Interface on nano-indentation of V/Fe Bilayer to their motion during the nano-indentation process. This blocking effect arises due to several key factors:

Firstly, MFDs' nodes belong to the favorable slip systems {101} <111> responsible for BCC metals. When dislocations slip towards these nodes, they experience a repulsive force generated by the strain fields surrounding the MFDs. These forces stop dislocation motion, effectively preventing their glide along the interface and their transmission into the Fe layer. During the accommodation of lattice mismatch, lattice straining leads to the creation of localized stress at these nodes, generating stress barriers [16-19]. As dislocations accumulate at these nodes, they contribute to strain hardening by generating additional stress fields, further reinforcing the blocking effect and making it increasingly difficult for subsequent dislocations to pass through.

Prior research on FCC/FCC semi-coherent interfaces has revealed this blocking mechanism [9, 16-18]. Furthermore, it was shown by Ghoniem et al.[17], that the critical resolved shear stress is related to the elastic shear modulus mismatch. Due to the image force created by this mismatch, the dislocation can pushed into the elastically softer layer. Therefore, the critical stress needed for dislocation transmission into a stiffer material is linearly proportional to the difference in elastic modulus for minor elastic mismatches, as further proved by Pacheco and Mura [18].

Another contributing factor to the blocking effect is the increased energy barrier at MFD nodes. The higher energy barrier at the nodes of MFDs, necessitates a higher energy source for free dislocations to overcome. In the present case of study, the potential energy of defective atoms surrounding the MFDs network is higher for Fe atoms (-3.40 eV) and lower for vanadium atoms (-5.19 eV), creating a variation of energy distribution at misfit dislocation nodes as shown in Figure III.18. As a result, dislocations need more energy to go through these nodes, which makes transmission into Fe layer even more difficult. This higher energy requirement is commonly referred to "**Koahler barrier**" or "**Koahler strength**," which represents the energy barrier or critical shear stress that dislocations must overcome to move through an interface between two phases [20, 21].

In the end, the combined effects of localized high stress, increased energy barriers, complex dislocation interactions, and strain accommodation makes MFDs' nodes highly effective obstacles to dislocation glide from V into Fe during nano-indentation. This, in turn, enhances the mechanical strength and hardness of the V/Fe bilayer system.

Chapter III: Atomistic Study of the Effect of Semi-Coherent Interface on nano-indentation of V/Fe Bilayer

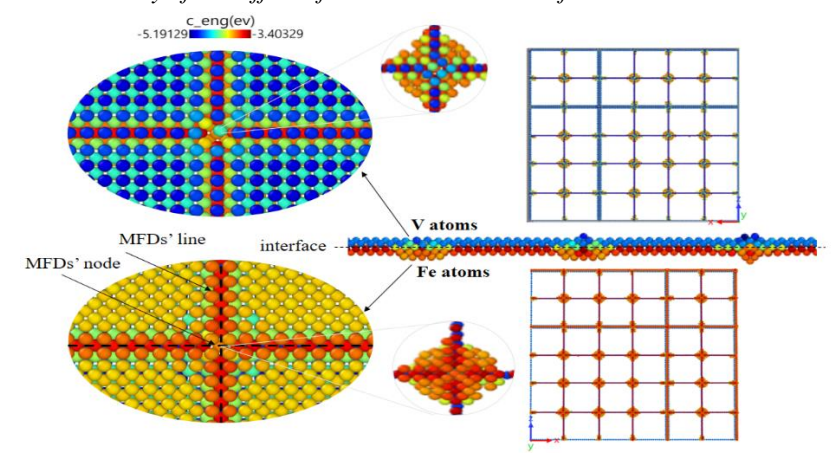


Fig III.18 Potential energy distribution of defected atoms surrounding MFD in the Relaxed V/Fe interface.

III.6 Conclusion:

In comparison with pure Fe and V single crystals; this chapter emphasizes the critical role that BCC/BCC semi-coherent interface serves in preventing dislocation propagation along plastic deformation, which significantly strengthens the indentation force and hardness of the V/Fe bilayer. This strengthening effect is particularly pronounced for thinner V layers. Further confirming the function of misfit dislocations in enhancing mechanical performance multilayers, the study of indenter position effect also shows that the blocking function of the interface works best when dislocations engage directly with MFD nodes.

Chapter IV: Atomistic investigation of the crystallographic orientation effect on V/Fe bi-layer response during nano-indentation

Summary

This chapter gives profound insights into the different misfit dislocations patterns that can be produced along the (110) and (111) crystallographic orientations, it elucidate the role of semi-coherent interfaces on the indentation response of V/Fe bi-layer.

Moreover, the anisotropic plasticity of single-crystals through systematic analysis is demonstrated.

IV.1 Indentation response of $V/Fe_{(110)}$ bi-layer vs. single-crystals:

In this section, indentation study of V/Fe₍₁₁₀₎ bi-layer compared with V₍₁₁₀₎, Fe₍₁₁₀₎ single-crystals, is presented. Aiming to examine the effect of BCC/BCC semi-coherent interface, on the indentation response of bi-layer compared to single-crystals. The lateral dimensions of the simulated samples are set respectively as (282.7*104*300) Å³ along the x, y, and z-axes. In the bilayer case, a V layer with a thickness of $h_V = 22$ Å is deposited on Fe substrate. Moreover, the same simulation conditions of the previous studied (010) indentation have applied to eliminate any divergence in the results.

The indentation load and hardness curves as a function of depth for $Fe_{(110)}$, $V_{(110)}$, and $V/Fe_{(110)}$ are presented in Figure IV.1. It can be observed that, in this crystallographic orientation, the initial stage of the indentation load curves appears relatively flat, indicating a smooth yielding behavior in both metals. This suggests a gradual transition from the elastic to the plastic regime. As the indentation depth increases, the load values also increase. Furthermore, the load curve of $V/Fe_{(110)}$ shows higher values compared to the $V_{(110)}$ single crystal but remains lower than that of $Fe_{(110)}$. Consequently, the hardness curves reveal a notable strengthening effect, with average hardness values at the end of indentation reaching 24 GPa for $Fe_{(110)}$, 15 GPa for $V_{(110)}$, and 20 GPa for $V/Fe_{(110)}$.

To gain deeper insights into the indentation response of these systems for this orientation, a systematic analysis of their plastic deformation is carried out in the following subsections. Figures IV.2, IV.4, and IV.6 illustrate the dislocation and defects evolution across the plastic regime of $Fe_{(110)}$, $V_{(110)}$, and $V/Fe_{(110)}$, respectively, using dislocation extraction algorithm (DXA) and (CSP) analysis in OVITO.

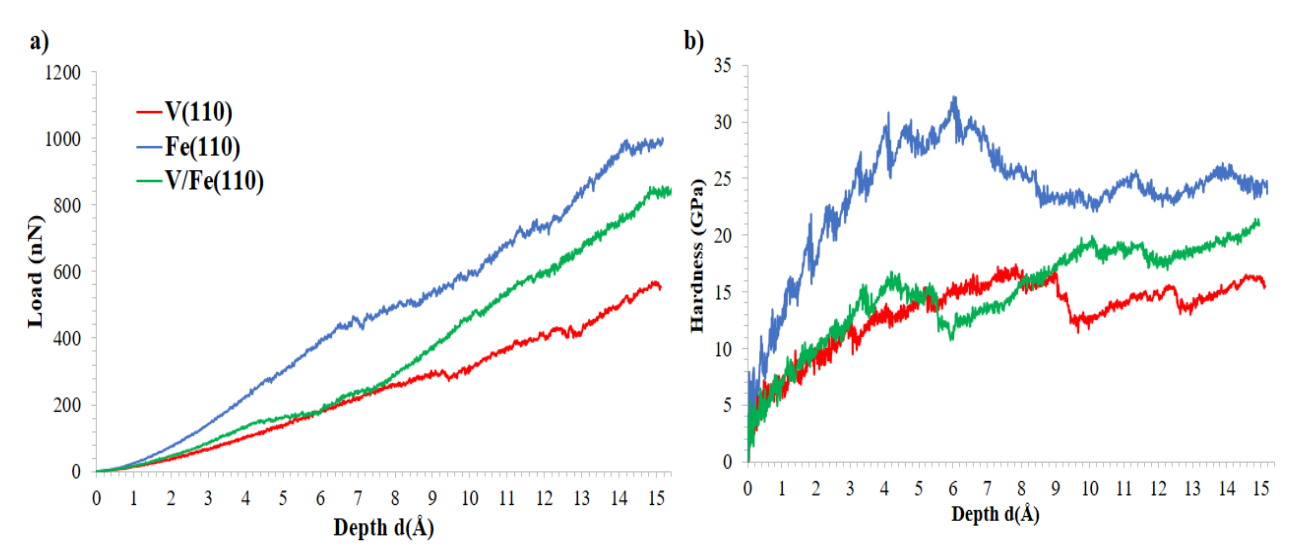


Fig IV.1 Indentation load-depth & hardness-depth curves of $V_{(110)}$, $Fe_{(110)}$ single-crystals and $V/Fe_{(110)}$ bi-layer.

IV.1.1 Deformation mechanisms of $V_{(110)}$ single-crystal:

Before reaching an indentation depth of d=9Å, the vanadium single crystal seems to deform elastically, as evidenced by the absence of a noticeable pop-in event in the load curve (Fig. IV.1). However, at an early stage of indentation ($\mathbf{d} = 3.81 \text{ Å}$), symmetrical planar defects begin to emerge beneath the indented surface (see figure. IV.2).

As indentation progresses to $d=6.01\text{\AA}$, these planar defects evolve into a diamond-shaped structure, indicating that the twinning mechanism dominates at this stage. CSP analysis of the plastically deformed region (Fig. IV.3) reveal numerous planar defects within the {110} <111> twin systems, symmetrically reflected across the (0-11), (110), and (001) planes. Interestingly, at this stage of deformation, both in-plane (along the y-direction) and out-of-plane twinning systems are activated. However, the majority of defected atoms are concentrated along the in-plane system, contributing to the formation of the diamond-shaped structure, as illustrated in figure.IV.4. With further indentation $d=8.01\text{\AA}$, the in-plane slip system turn out to be deactivated and serves as a symmetry axis, reflecting two diamond geometries. Additionally, one can notice that defected atoms propagate predominantly along the [001] direction (z-axis), indicating that deformation preferentially occurs along this axis under indentation stress. This behavior can be attributed to the activation of primary {110} <111> systems, which favor dislocation motion BCC V.

At $d=9.41\text{\AA}$, yielding in the indentation load curve marks the nucleation of dislocations with Burgers vectors a/2 <111>. As indentation continues ($d=12.71\text{\AA}$), these dislocations multiply, forming shear loops that extend along the z-axis, while twinning deformation persists through the growth of planar defects (twin boundaries).

By the end of indentation loading $d=15\text{\AA}$, some 1/2 < 111 > dislocations transform into shear loops and exhibit horizontal extension, likely due to boundary effects from the fixed layer at the bottom of the sample.

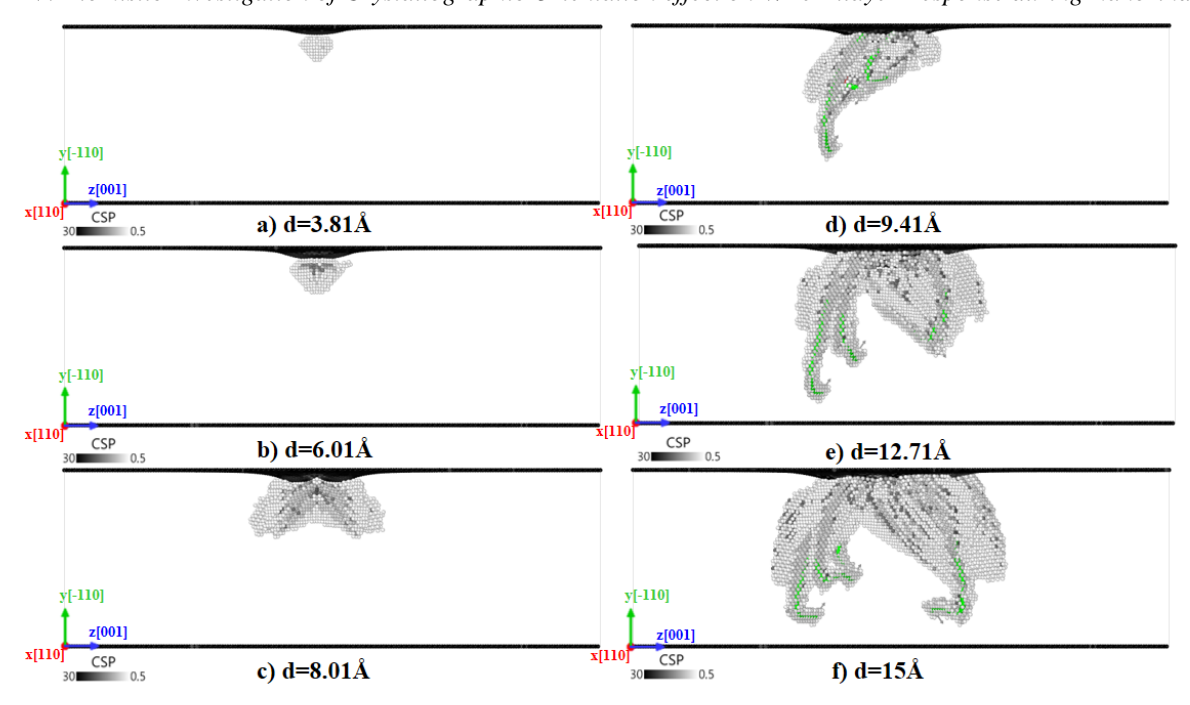


Fig IV.2 CSP and DXA analysis of the atomic defects evolution across indentation of pure $V_{(110)}$.

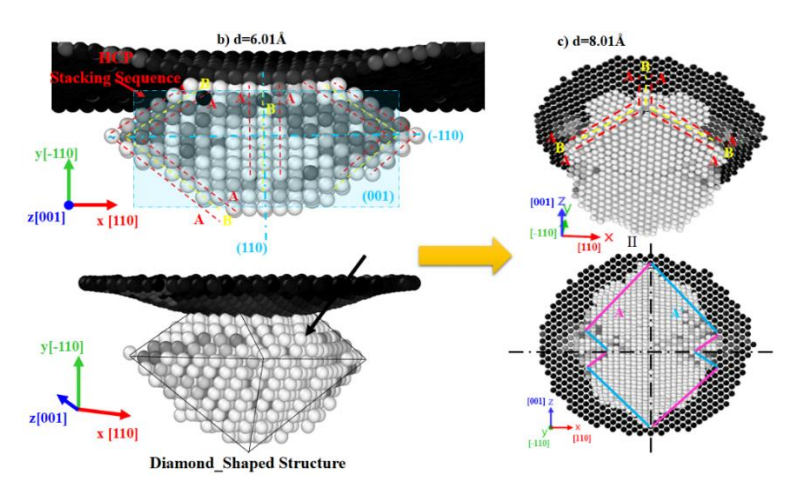


Fig IV.3 Close-up of the atomic defects along plastic regime of indented $V_{(110)}$ single-crystal, for d=6.01 and 8.01Å showing the diamond_ shaped structure.

IV.1.2 Deformation mechanisms of Fe₍₁₁₀₎ **single-crystal:**

The Fe₍₁₁₀₎ single crystal initially deforms elastically until the formation of a planar defect within the (1-10) <111> slip system beneath the indented surface **at d = 4.68** Å (see Fig. IV.4). as indentation progresses to **d=6.98**Å, three perfect dislocation segments with Burgers vectors a/2<111> nucleate along the z-direction, following the $\{011\}$ <111> slip systems, and marking a transition in the deformation mechanism. With further indentation (**d=8.08**Å), these 1/2<111> dislocations multiply and begin to intersect. This intersection results in the nucleation of additional dislocations with Burgers vectors a<100>. When **d=10.18**Å, some of the 1/2<111> dislocations start evolving horizontally into shear loops.

Notably, the ratio of dislocation segments in the $Fe_{(110)}$ single-crystal is significantly higher, as slip deformation dominates the plastic response. With continued loading (d=12.08Å),

Chapter IV: Atomistic Investigation of Crystallographic Orientation effect on V/Fe Bilayer Response during Nano-indentation dislocations with Burgers vectors a <100>, a/2 <111>, and a <110> continue to form, interacting with each other and entangle, leading to the development of nodes and junctions. These dislocations extend preferentially along the z-direction, further evolving into shear loops. At the final stage of indentation (d=15.18Å), it becomes evident that plastic deformation is primarily concentrated along the [001] direction, where the majority of slip systems are activated, driving the metal's overall deformation behavior.

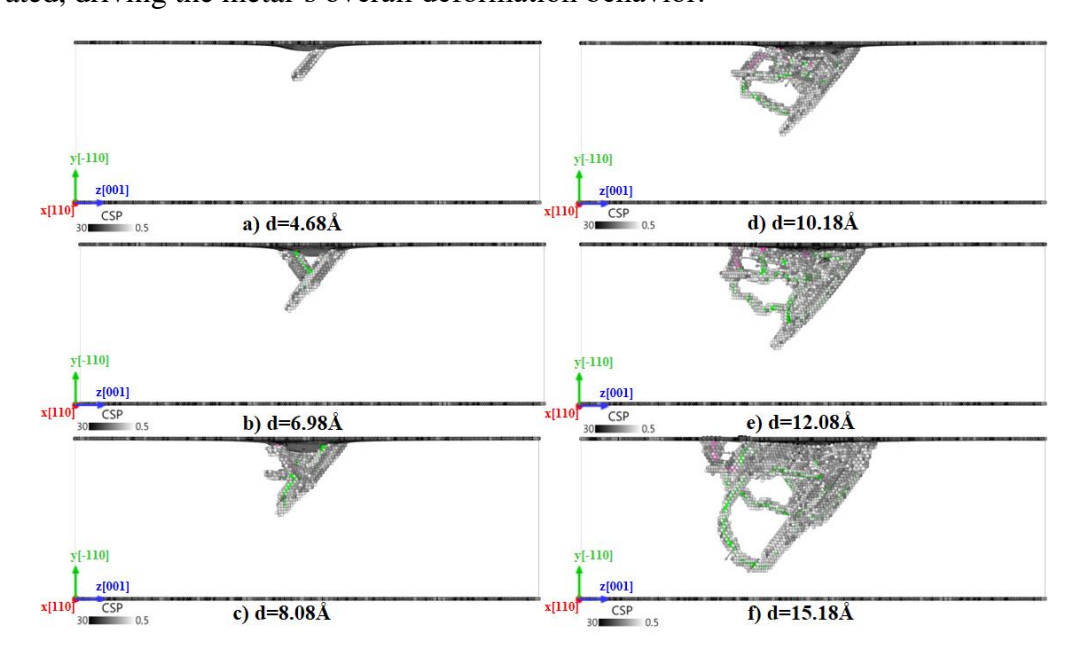


Fig IV.4 CSP and DXA analysis of the atomic defects evolution across indentation of pure Fe₍₁₁₀₎.

IV.1.3 Structural description of V/Fe(110) interface:

After stacking the Fe₍₁₁₀₎ and V₍₁₁₀₎ layers together, the lattice mismatch between these metals is accommodated through lattice straining, leading to the formation of misfit dislocations (MFDs). These dislocations are relieve to the high stress induced by lattice straining. They also increase the overall interfacial energy. For this orientation, the MFD₍₁₁₀₎ network exhibits a periodic diagonal cross-grid pattern, formed by two sets of dislocation lines with Burgers vectors, $\vec{b_1} = a/2[\vec{111}]$, and $\vec{b_2} = a/2[\vec{111}]$ besides, dislocations with Burgers vector $\vec{b_3} = a[00\bar{1}]$ are generated at the intersections of these dislocations, as illustrated in Fig. IV.5(a). similar pattern has been reported in previous studies [59, 60].

The localized stress field surrounding MFD₍₁₁₀₎ is notably greater, with compressive stress in $V_{(110)}$ atoms(~3.15 GPa) and tensile stress in $Fe_{(110)}$ atoms(about–4.85 GPa) (see Fig. IV. 5(b)). This stress is determined by averaging the three principal stress components (σ_{xx} , σ_{zz} , and σ_{yy}). In contrast, the stress in coherent regions of the interface is relatively low, exhibiting positive values in Fe and negative values in V. At the end of relaxation, the stress within each layer approaches zero, except at the interface and free surface. Moreover, it is evident that <100> MFDs induce greater stress compared to 1/2 <111> MFDs.

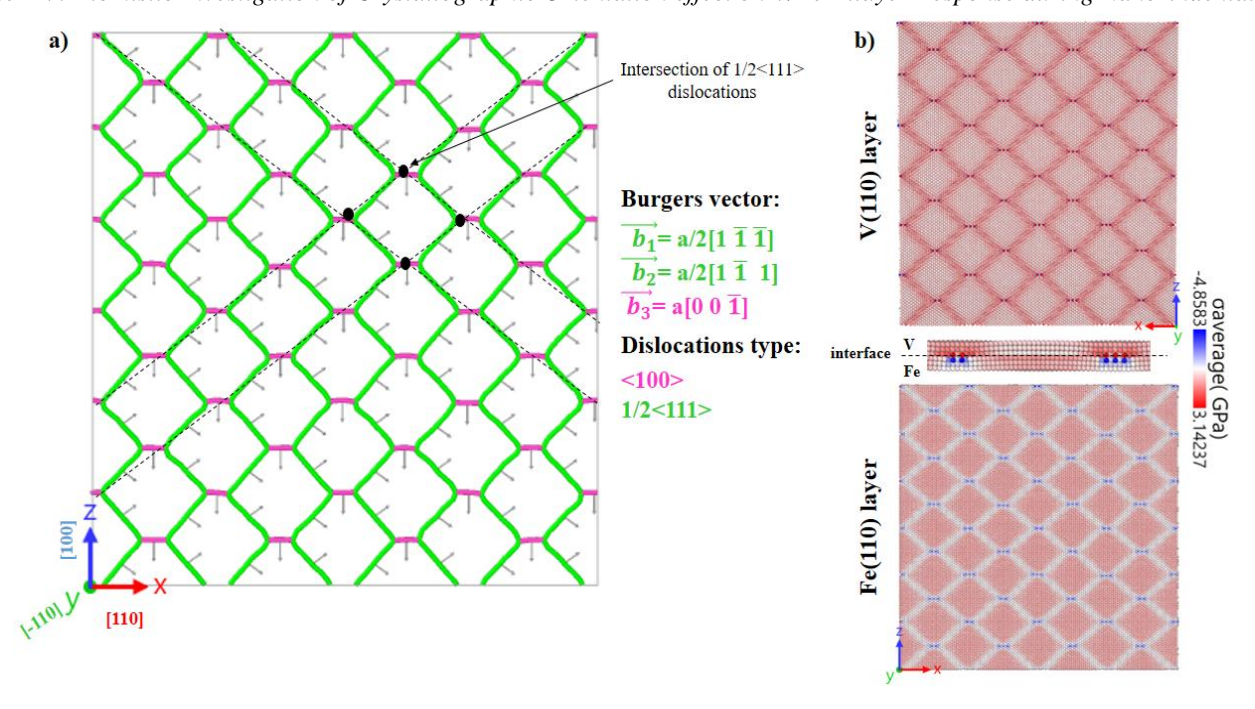


Fig IV.5 (a) Structural configuration of the MFD pattern of V/Fe₍₁₁₀₎ interface. (b) Top and bottom views of interfacial stress.

IV.1.4 Deformation mechanisms of V/Fe₍₁₁₀₎ bi-layer:

To demonstrate the crucial role of misfit dislocations (MFDs) induced by semi-coherent interfaces in determining the overall mechanical behavior of nano-scale multi-layers under indentation loading, we investigate their effect during nano-indentation of the $V/Fe_{(110)}$ bilayer in this section. Following the elastic deformation stage, plastic deformation in the $V/Fe_{(110)}$ bi-layer initiates earlier in the indentation process compared to the $V_{(110)}$ single-crystal (see Fig. IV.1). this early onset of plasticity is attributed to the pre-existing misfit dislocations (MFDs), which induce a localized stress concentration at the interface.

At an indentation depth of \mathbf{d} =3.74Å, planar defects emerge beneath the indented surface. These defects belong to the {011} <111> twin system, which is the most favorable system along the z-direction (see Fig. IV.6). As indentation progresses to \mathbf{d} = 4.14 Å, these planar defects rapidly interact with the interface, particularly with the central dislocation line of Burgers vector a<001> of the MFD₍₁₁₀₎ network. Since the V layer is relatively thin, this interaction occurs at an early indentation stage. Notably, the dislocation-interface interaction significantly strengthens the indentation load and hardness response of the V/Fe₍₁₁₀₎ bi-layer, as the MFD network applies a repulsive force, effectively blocking dislocation glide.

With further indentation, dislocations with Burgers vector a/2<111> nucleate beneath the indented surface and immediately interact with the MFDs.

When the indentation depth reaches **d=5.74**Å, the MFDs near the plastic deformation zone begin to extend along the z-direction. Simultaneously, dislocations originating from the indented surface are blocked by the interface (see Fig. IV.6).

Up until d=11.04Å, the MFD network continues to serve as an effective barrier, preventing dislocation propagation. Furthermore, dislocations from the deformed V layer exhibit horizontal gliding along the z-axis, as the limited slip systems in this crystallographic orientation restrict dislocation motion in the x and y directions.

At the final indentation depth ($\mathbf{d=15.04}\text{Å}$), it becomes evident that the V/Fe₍₁₁₀₎ interface acts as a strong dislocation barrier, significantly blocking dislocation transmission across the interface. This results in a clear hardening effect, as observed in the indentation load curve (shown in Fig.IV.1) of V/Fe₍₁₁₀₎.

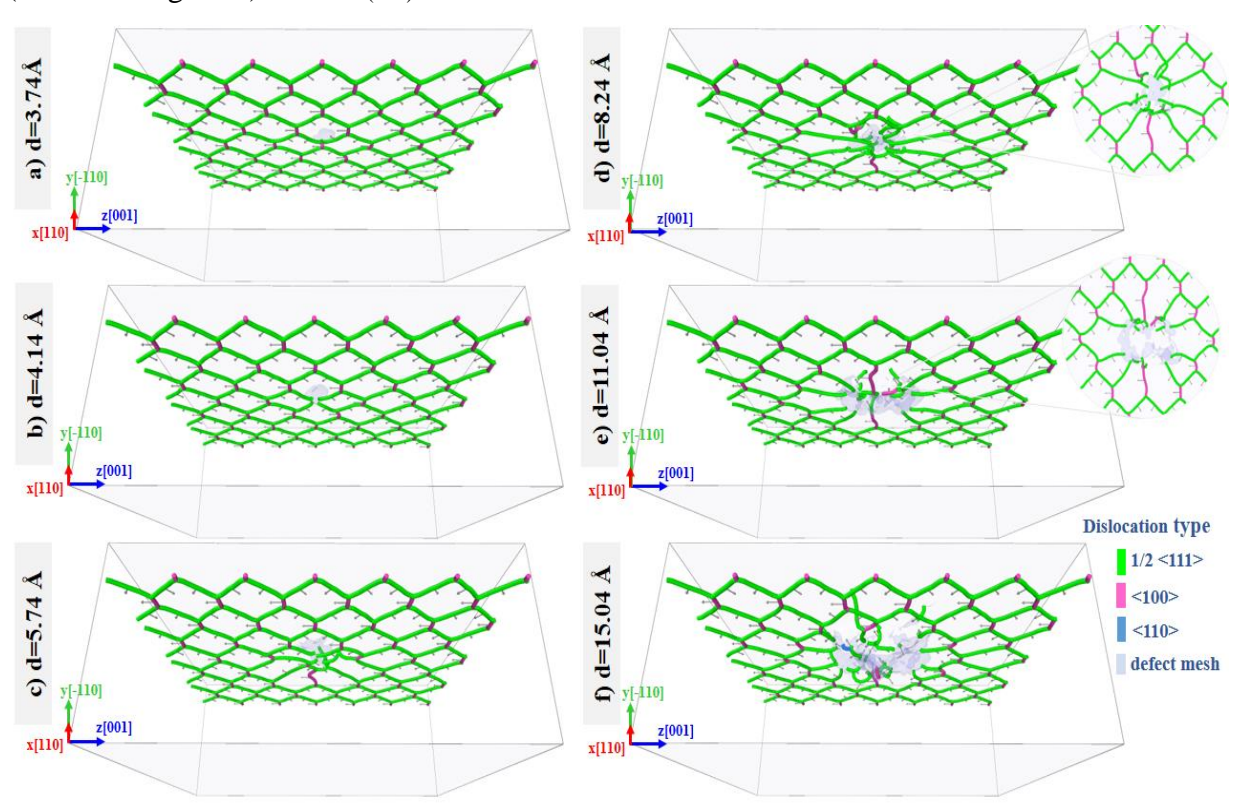


Fig IV.6 DXA snapshots of the dislocations dynamics across plastic regime of the indented $V/Fe_{(110)}$ bi-layer.

IV.1.5 Evolution of dislocations under (110) indentation:

The evolution of the total dislocation length during nano-indentation for $V_{(110)}$, $Fe_{(110)}$ single-crystals, and the $V/Fe_{(110)}$ bi-layer is shown in Fig. IV.7, providing detailed insights into the dislocation dynamics of each system. During the plastic regime (Stage II), the total dislocation length increases progressively with indentation depth in all systems. However, distinct deformation mechanisms were observed for each material.

In the case of $V_{(110)}$ single crystal, the decrease in the number of dislocations predominantly of type a/2<111> at higher indentation loads suggests that twinning mechanism dominates the plastic deformation. In contrast, the $Fe_{(110)}$ single crystal exhibits a combination of dislocations with Burgers vectors a/2<111>, a<100>, and a<110>, along with higher density and extended length, indicating that Fe primarily deforms through slip mechanism.

For the V/Fe $_{(110)}$ bilayer system, the presence of a regular and significant number of a/2<111> and <100> dislocations at the early stages of indentation strongly suggests the pre-existence of a well-relaxed and stable misfit dislocation (MFD) network. The earlier nucleation of dislocations in the bilayer system, compared to the single-crystals, is attributed to the higher localized stress induced by MFDs, which is superimposed with indentation stress. Nevertheless, the semi-coherent interface acts as a strong barrier, limiting dislocation propagation. This is evident from the reduced number of dislocations in the bilayer system compared to the V single crystal, highlighting the major blocking effect of the interface.

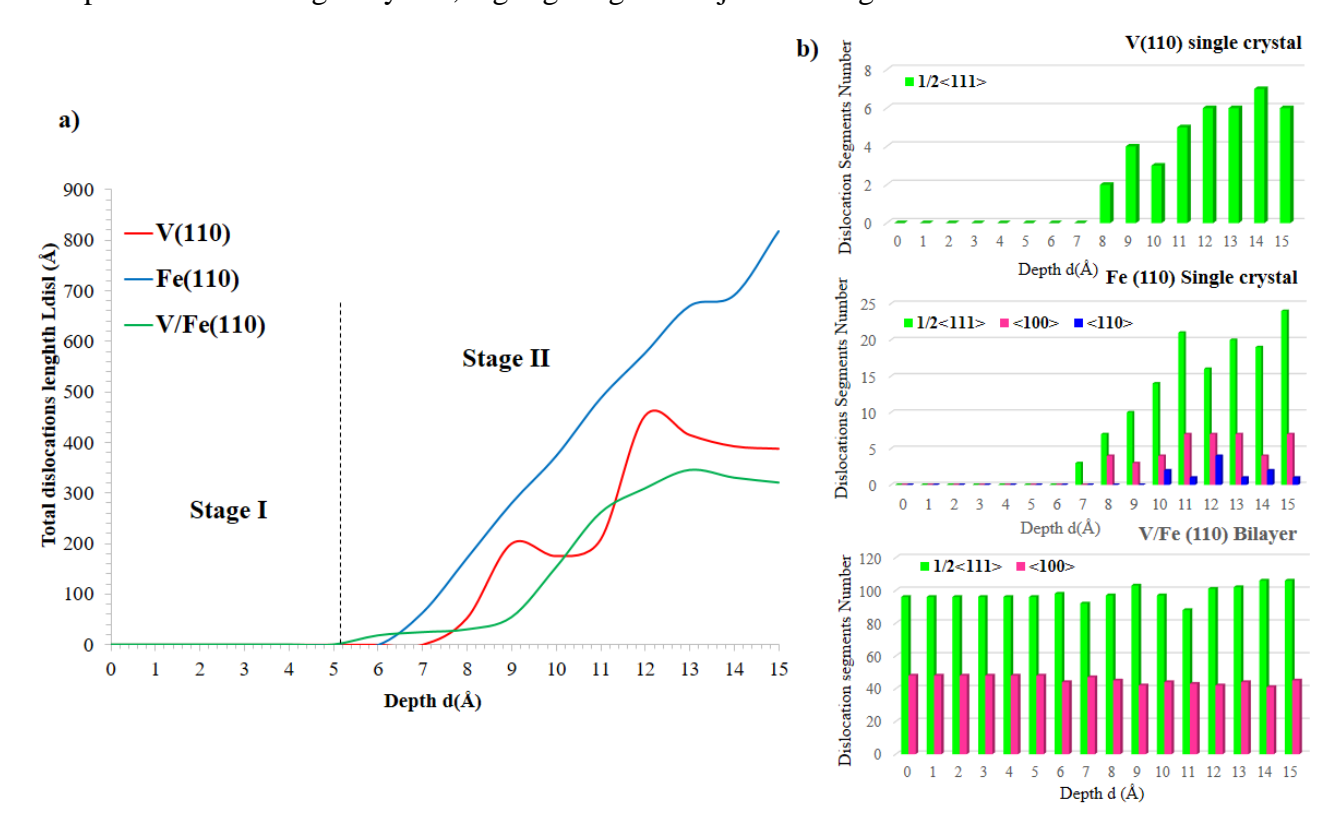


Fig IV.7 (a) Development of the dislocations length L_{disl} along indentation of $V_{(110)}$, $Fe_{(110)}$ single-crystals and $V/Fe_{(110)}$ bi-layer (Excluding MFD length). (b) Evolution of the dislocation segment number N_{disl} across indentation (including MFD length).

IV.2 Indentation response of $V/Fe_{(111)}$ bi-layer vs. single-crystals:

In this section, the nano-indentation response of $V/Fe_{(111)}$ bi-layer is compared to that of $V_{(111)}$ and $Fe_{(111)}$ single-crystals. With respect to the same simulations conditions and methodology of previous study of (010) indentation. The size of the three simulated systems is set to $(282.7\text{Å} \times 104\text{Å} \times 305.4\text{ Å})$ along the x, y, and z-axes, (single-crystal system containing about 774,940 atoms). For the bilayer system, the V layer thickness (hy) is 22 Å.

Figure IV.8 presents the indentation load-depth curves for $Fe_{(111)}$, $V_{(111)}$ single-crystals, and the $V/Fe_{(111)}$ bi-layer. As expected, the indentation load increases with depth, with the $Fe_{(111)}$ single crystal exhibiting the highest indentation force and hardness values. In comparison, the $V/Fe_{(111)}$ demonstrates a slight strengthening effect relative to the $V_{(111)}$ single crystal.

observed in the load curves of any system, apart from a very smooth yielding behavior.

Despite this, the load values continue to increase with indentation depth. At the end of the indentation loading, the average hardness values are measured as follows: 20.51GPa for Fe₍₁₁₁₎, 14.39 GP for V₍₁₁₁₎, and 17.32 GPa for V/Fe₍₁₁₁₎. These results indicate that while the bilayer system exhibits enhanced hardness compared to pure vanadium, it remains lower than that of pure iron.

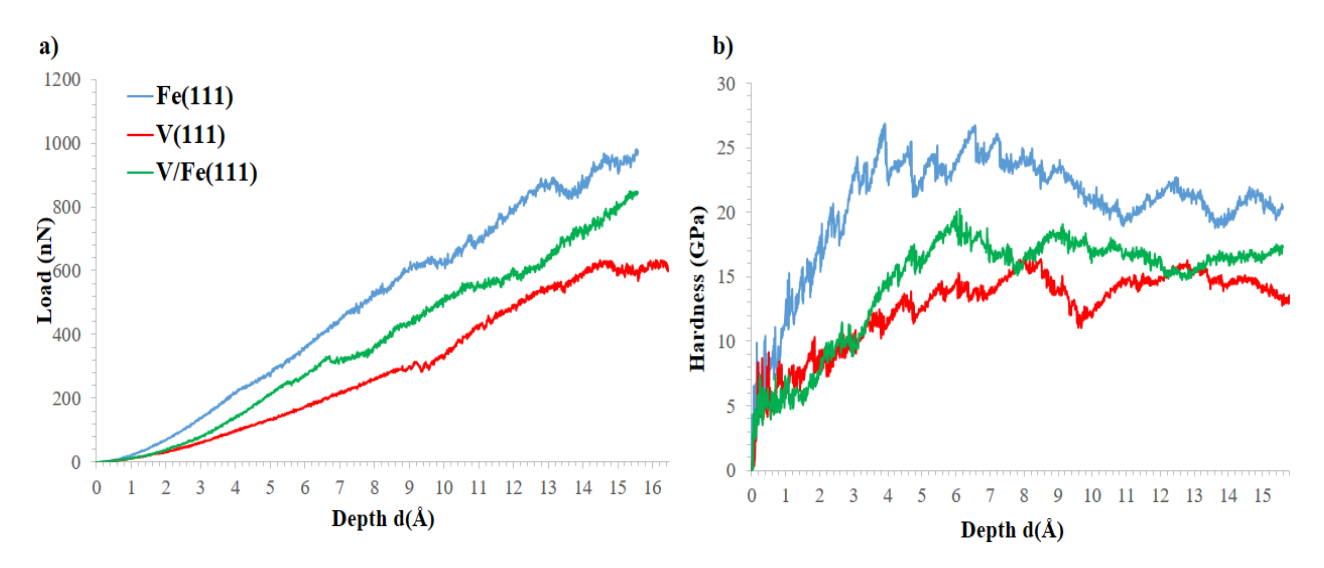


Fig IV.8 Indentation load-depth & hardness-depth curves of $V_{(111)}$, $Fe_{(111)}$ single-crystals and $V/Fe_{(111)}$ bi-layer.

IV.2.1 Deformation mechanisms of $V_{(111)}$ single-crystal:

Despite the absence of a clear elastic-plastic transition in the load curve for the $V_{(111)}$ single crystal (Fig.IV.8), CSP analysis; using Ovito software; revealed that the crystal undergoes plastic deformation during the early stages of nano-indentation. At an indentation depth of $d=4.54\text{\AA}$, defected atoms with lower CSP values were observed beneath the indented surface (refer to Fig. IV.9). As indentation progresses, at d=5.34 Å, planar defects belonging to the $\{110\}<111>$ twin systems begin to nucleate, indicating that twinning mechanism is the dominant mechanism. At $d=8.44\text{\AA}$, thick planar defects with an ABAB stacking sequence form a three-point star-shaped structure in the (100), (-10-1), and (-101) planes. Figure.IV.10 provides both 2D and 3D close-up snapshots of this structure. Despite these observations, no clear yielding is visible in the load curve at this stage.

At **d=10.44**Å, a prismatic dislocation loop with Burgers vector a/2<111> begins to form, arranging for pinching from the plastically deformed zone and simultaneously extending along the z-direction. As loading continues, more dislocations with Burgers vector a/2<111> nucleate beneath the indented surface at **d=13.44**Å.

By the end of indentation at $d=15.14\text{\AA}$, additional 1/2<111> dislocations nucleate and propagate along the z-direction. It can be concluded that the y[111] and z[11-2] directions in

Chapter IV: Atomistic Investigation of Crystallographic Orientation effect on V/Fe Bilayer Response during Nano-indentation V(111) correspond to the primary slip systems of BCC vanadium for this orientation, which facilitates dislocation glide. Therefore, promotes plastic deformation in these directions.

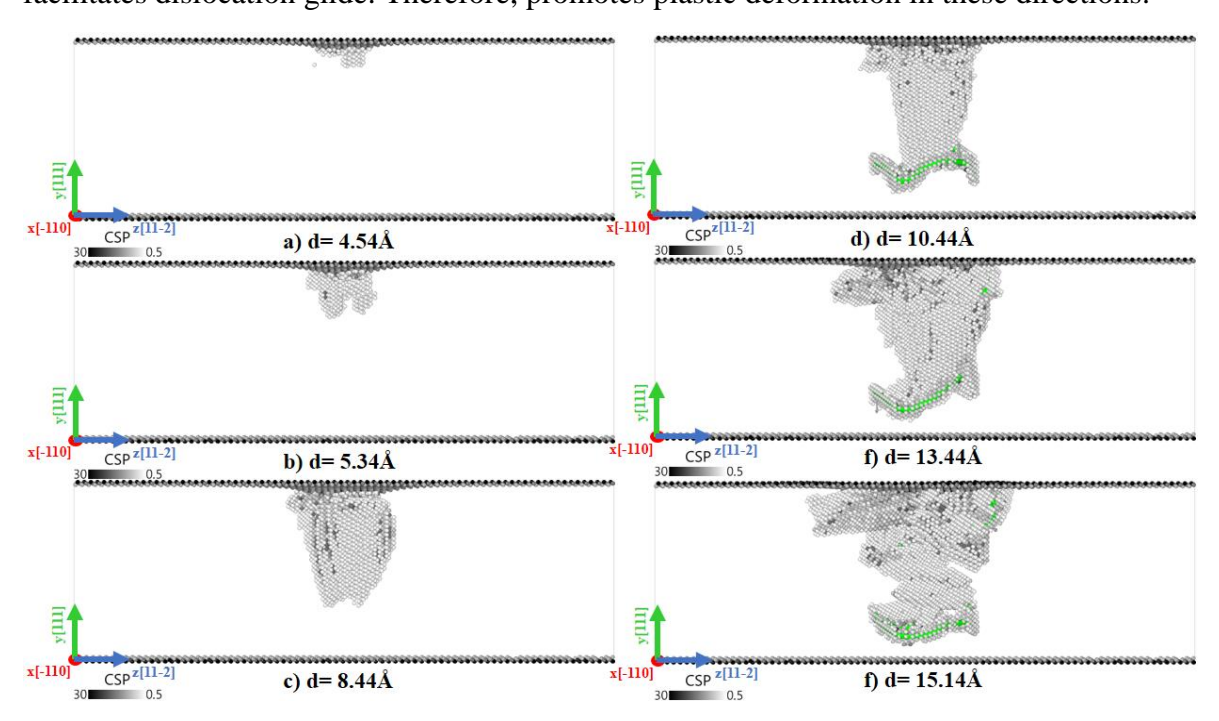


Fig IV.9 CSP and DXA analysis of the atomic defects evolution across indentation of pure

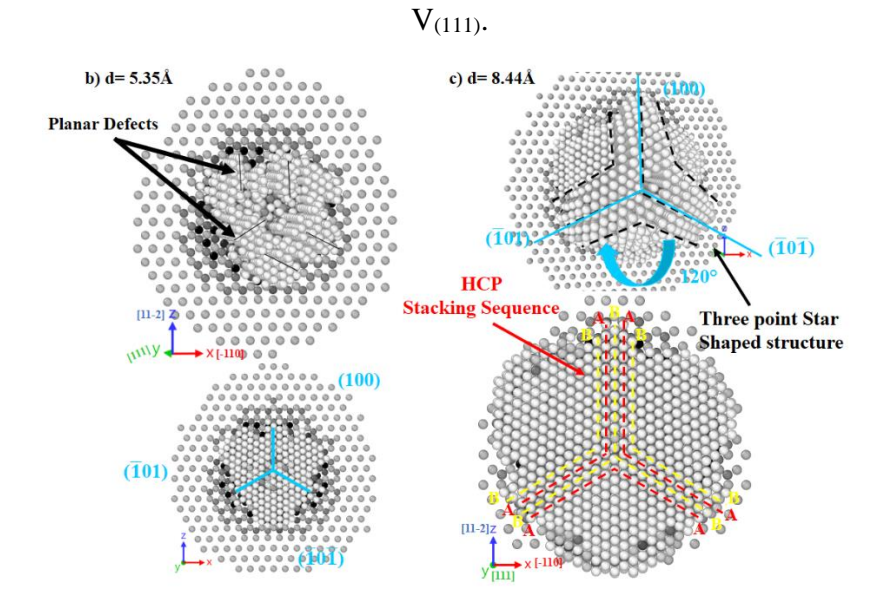


Fig IV.10 Close-up of the atomic defects along plastic regime of indented $V_{(111)}$ single crystal. At d=5.35 and 8.44Å showing three-point star structure.

IV.2.2 Deformation mechanisms of Fe₍₁₁₁₎ **single-crystal:**

After the elastic deformation regime, the presence of defected atoms with lower CSP values beneath the indented surface confirms that the $Fe_{(111)}$ single crystal undergoes plastic deformation at an indentation depth ($\mathbf{d=4.19\mathring{A}}$), despite the absence of any yielding in the load curve. At $\mathbf{d=4.99\mathring{A}}$, a planar defect forms along the (112)<111> slip system. As loading continues, at $\mathbf{d=7.59\mathring{A}}$, the nucleation of two dislocations with Burgers vectors a/2<111> and a<100> is observed (see Fig. IV.11). when $\mathbf{d=9.59\mathring{A}}$, the dislocations begin to propagate

Chapter IV: Atomistic Investigation of Crystallographic Orientation effect on V/Fe Bilayer Response during Nano-indentation clearly. Further loading at **d=11.59Å** leads to the multiplication of 1/2<111> and <100> dislocations, which interact and form junctions and nodes.

By the end of indentation at d=15.09Å, some of the 1/2<111> dislocations have extended into shear loops. The increased number of nucleated dislocations results in the accumulation and interconnection of dislocations. From these observations, it can be deduced that the slip deformation in Fe₍₁₁₁₎ occurs most easily along the z and y directions, which correspond to the primary slip systems of BCC metals.

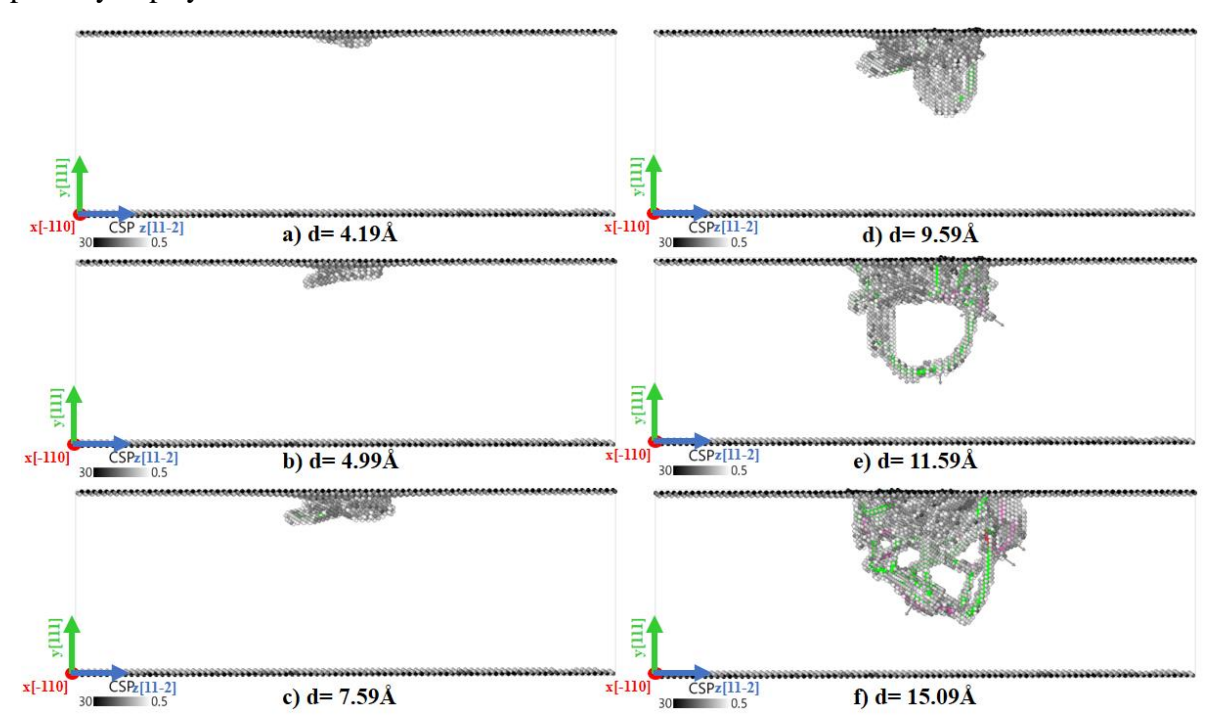


Fig IV.11 CSP, DXA analysis of the atomic defects evolution across indentation of pure $Fe_{(111)}$.

IV.2.3 Structural description of $V/Fe_{(111)}$ interface:

After relaxation, the final configuration of the V/Fe₍₁₁₁₎ interface reveals a periodic hexagonal misfit dislocation (MFD) pattern, which arises from the lattice mismatch between the two metals (Fig. IV.12). Similar to previous studies [59], the MFDs network primarily consists of three dislocations with Burgers vectors: $\vec{b_1} = a[110]$, $\vec{b_2} = a[10\bar{1}]$, and $\vec{b_3} = a[0\bar{1}]$ Furthermore, the misfit dislocation network generates localized stress fields in the surrounding lattices. The average of the principal stresses (σ_{xx} σ_{zz} , and σ_{yy}) in the atoms surrounding MFDs, as shown in Fig. IV.12(b). These localized stresses can reach significant magnitudes near the MFDs, with a tensile stress observed for Fe atoms (-4.81 GPa) and a compressive stress for V atoms (about 3.64 GPa). In contrast, the coherent regions at the interface maintain stable structures under low stress. This stress is tensile on the V side and compressive on the Fe side. Additionally, the central regions of each layer tend to exhibit nearly zero average stress.

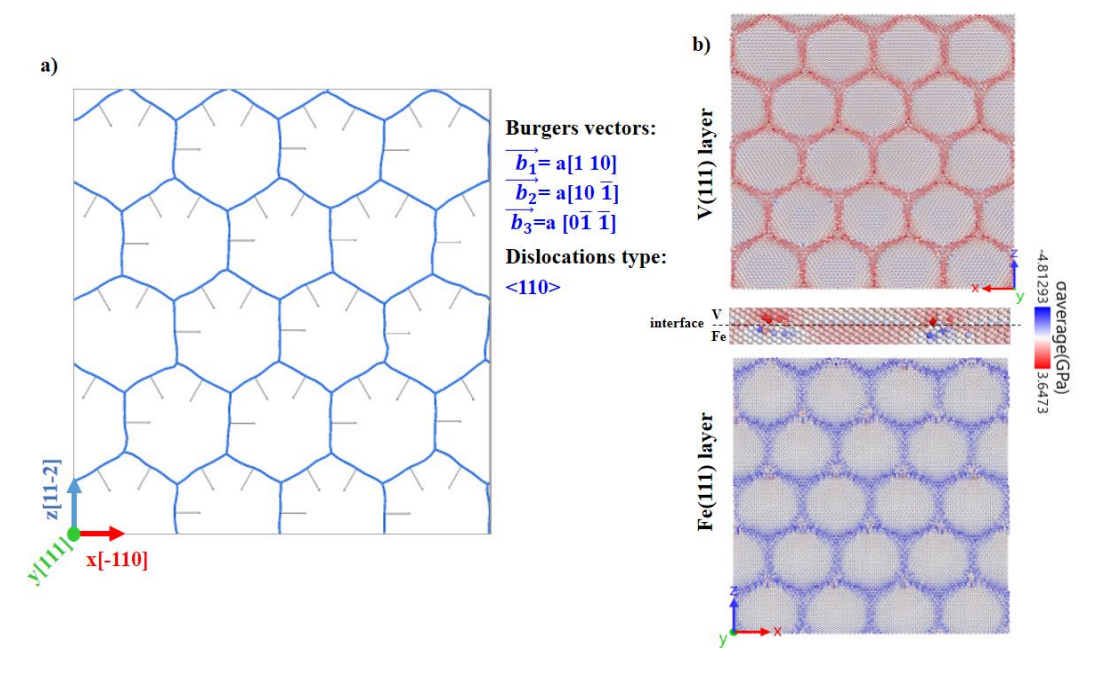


Fig IV.12 (a) Structural configuration of the MFD pattern of V/Fe₍₁₁₁₎ interface. (b) Top and bottom views of interfacial stress.

IV.2.4 Deformation mechanisms of V/Fe(111) bi-layer:

During the indentation of the V/Fe $_{(111)}$ bilayer, the system initially deforms elastically, with no defects under the indented surface. As indicated by the DXA analysis using Ovito software, Plastic deformation in the indented V layer begins with the nucleation of planar defects beneath the indented surface **at a depth of d=3.9Å** (Fig. IV.13). although, the yielding in the indentation curve is smooth. There is a distinctive pseudo-elastic behavior, which also observed in $V_{(111)}$ and $Fe_{(111)}$ single-crystals. Additionally, the misfit dislocation (MFD) network in the (111) orientation appears unstable. At the earlier stage of plastic deformation, dislocation loops with Burgers vectors a/2<111> form at the nodes of the MFDs, indicating the weakness of this interface. At an indentation depth of **d=4.9Å**, the nucleated planar defects interact with the nearest MFD nodes, and a 1/2<111> dislocation loop forms within these nodes. This loop then extends horizontally due to the blocking effect of the interface.

As indentation continues to d=6.09Å, additional dislocations with Burgers vector a/2<111> propagate from the indented surface and interact with the misfit dislocations.

However, by **d=7.6Å**, these dislocations are blocked by the MFDs, causing them to evolve into shear loops which extend horizontally in the preferred {101}<111> and {112} <111> slip systems at interface, without penetrating the Fe layer (Fig. IV.13). at this stage, the interface acts as a strong barrier to dislocation propagation.

After **d=10.99**Å, some planar defects are able to pass through the interfacial coherent regions into the Fe substrate, as they no longer encounter by MFDs to interact with.

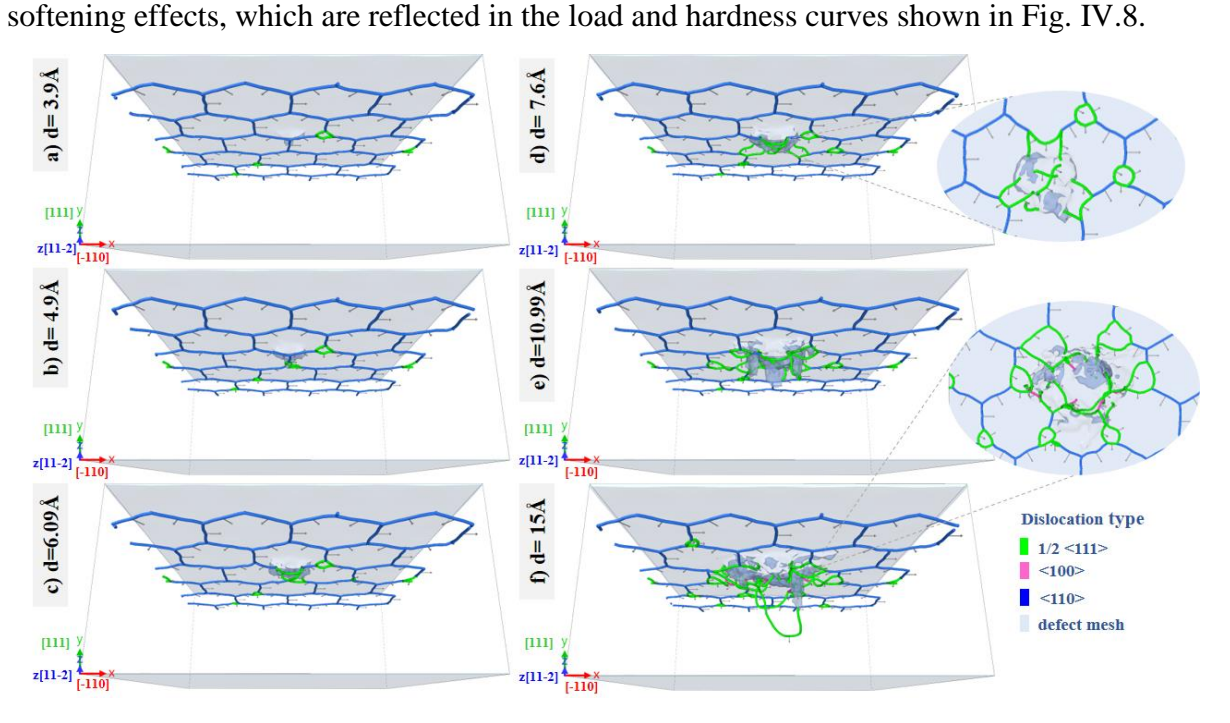


Fig IV.13 DXA snapshots of the dislocations dynamics across plastic regime of the indented $V/Fe_{(110)}$ bi-layer.

IV.2.5 Evolution of dislocations under (111) indentation:

From Figure IV.14, one can observe that the total dislocation length for $V_{(111)}$ is significantly reduced compared to other crystallographic orientations, indicating that twinning is the dominant plastic deformation mechanism in this crystal, even though few dislocations are nucleated during advanced plastic deformation. Which can be attributed to the limited slip systems available in this crystallographic orientation. In contrast, for $Fe_{(111)}$, the number of dislocation segments, including both 1/2 < 111 > and < 100 > dislocations, is considerably higher. Additionally, it is apparent that the total dislocation length increases with increasing indentation depth for all materials.

For the $V/Fe_{(111)}$ bi-layer, the dislocation evolution during nano-indentation differs somewhat from that observed in (010) and (110) interfaces. In the early stages of indentation, dislocation loops form at the nodes of the misfit dislocations (MFDs) in stages I and II (see Figure IV.14). Interestingly, the increased number of 1/2<111> dislocation loops at these MFDs nodes highlights the instability and weakness of the interface. These dislocations evolve horizontally, a characteristic behavior of the interface itself, which explains the continuous increase in the total dislocation length during stage II.

As loading continues, the number of dislocations increases, leading to a reduced number of <110> dislocations (see Figure IV.14). which primarily formed the (111) semi-coherent interface. that allows more space for the coherent region, thus enabling dislocation propagation

Chapter IV: Atomistic Investigation of Crystallographic Orientation effect on V/Fe Bilayer Response during Nano-indentation into the Fe layer. Once the interface loses its ability to block dislocation propagation (stage III), both the dislocation length and number increase further with indentation depth. After d=10Å.

This behavior suggests that MFDs drops its blocking effect.

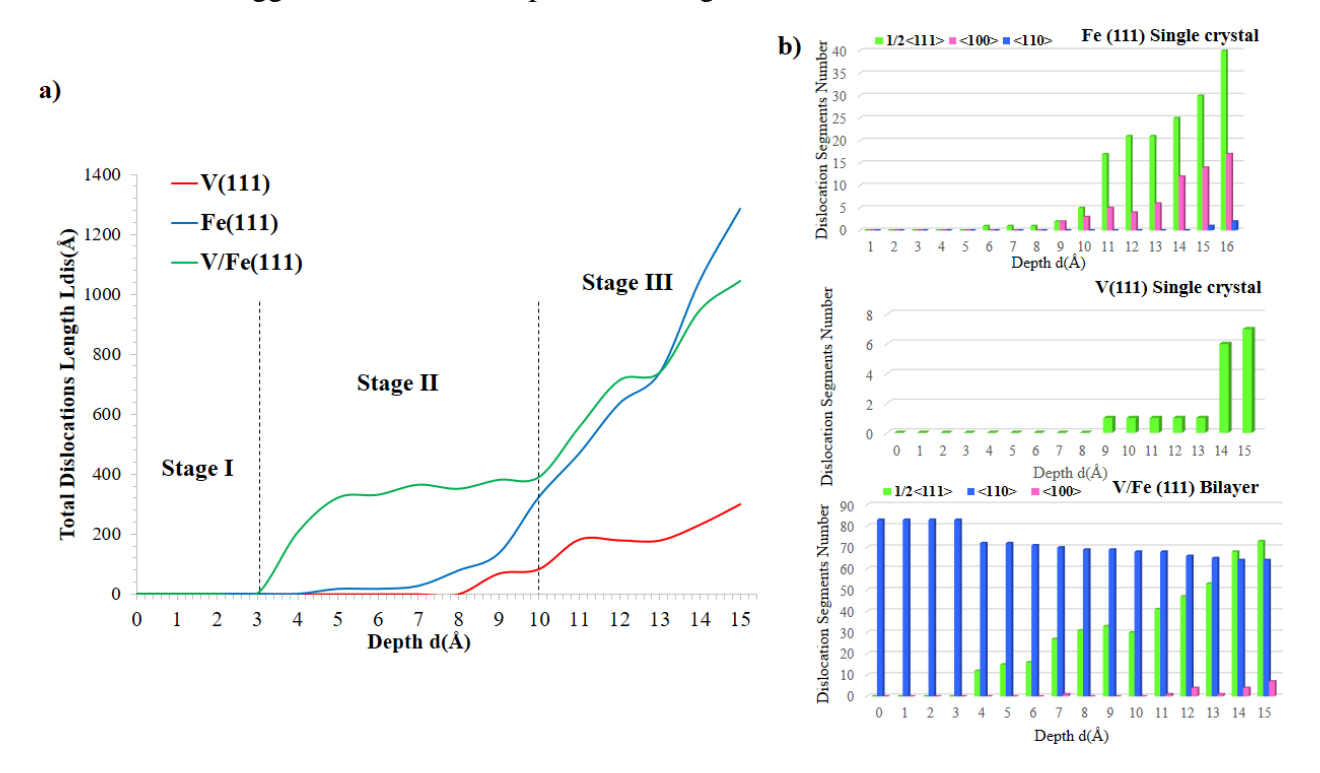


Fig IV.14 (a) Development of dislocations length L_{disl} along indentation of $V_{(111)}$, $Fe_{(111)}$ single-crystals and $V/Fe_{(111)}$ bi-layer (Excluding MFD length). (b) Evolution of the dislocation segment number N_{disl} across indentation (including MFD length).

IV.3 Discussion:

IV.3.1 Anisotropic plasticity of BCC V and Fe:

From the indentation load curves of single-crystals with (110), (111) orientations and the previously studied (010) indentation in Chapter III, it is evident that the mechanical behavior of the V and Fe during indentation is orientation-dependent. This crystallographic dependence of surface behavior is commonly observed in BCC metals [105-126].

It is recognized that slow twinning typically has a minimal effect on the observed stress, whereas immediate twinning is characterized by the rapid formation of twinned regions, resulting in significant load drops [70, 71]. This observation aligns with behavior observed in for both Fe and V, in the (110) and (111) orientations, where the load curves are relatively flat, making the transition from the elastic to plastic regimes indistinct. In contrast, the initial yielding associated with dislocation nucleation was clearly pronounced in the (010) indentation for both V and Fe. Demonstrating that, in BCC metals, twinning can induce pseudo-elastic behavior prior to macroscopic yielding. Moreover, the forces required for yielding at (110), (111), and (010) orientations are: 114.4nN, 135.25nN, and 138.46nN for V single crystal, and 271.48nN, 281.94nN, and 501.35nN for Fe single crystal, respectively. These results indicate that the indentation force required for plastic deformation is lowest at the (110) orientation and

Chapter IV: Atomistic Investigation of Crystallographic Orientation effect on V/Fe Bilayer Response during Nano-indentation highest at the (010) and (111) orientations. One can also deduce that, for all crystallographic orientations, twinning deformation was the dominant plastic deformation mode in V single-crystal, alongside the nucleation of some dislocations with Burgers vectors a/2<111>, which evolve into shear loops at an advanced stages of indentation. In contrast, slip deformation was the primary mode of plastic deformation in Fe single crystal, characterized by

the multiplication and extension of <100> and 1/2<111> dislocations. Table IV.1 sums up the

total dislocation length of single-crystals for the different orientations.

Vanadium	V(010)	V(110)	V(111)
Total dislocation length (Å)	402.4Å	387.79Å	300.58Å
Iron	Fe(010)	Fe(110)	Fe(111)
Total dislocation length (Å)	883.9Å	818.27Å	1285.59Å

Table IV.1 Total dislocations length L_{dsil} for V and Fe $\,$ single-crystals at $\,$ d=15Å for different crystallographic orientations

A close examination using DXA and CSP analysis, performed with Ovito software, revealed that the plastically deformed zone of V single-crystal, at nearly the same indentation depth $(\mathbf{d} \approx 8 \text{\AA})$, exhibited distinct structural shapes of twinning deformation. Specifically, flower, diamond, and three-point-star shaped structures were observed in the (100), (110), and (111) orientations, respectively (see Fig. IV.15). These differences can be attributed to the limited number of activated slip systems in each crystallographic orientation, highlighting the intrinsic orientation dependence of V single crystal. This unique twinning deformation anisotropy, was previously observed, by Biener et al. [105], using the high-resolution atomic force microscopy. They conducted indentation experiments on $Ta_{(100)}$, $Ta_{(110)}$, and $Ta_{(111)}$ single crystals. And identical flower-shaped structure, similar to that observed in $V_{(010)}$, with activated $\{110\}$ </br>
111> and $\{112\}$ 111> slip systems, has seen in $Ta_{(100)}$. Additionally, a two-fold surface symmetry has observed for $Ta_{(110)}$ and a three-fold symmetry for $Ta_{(111)}$, which equivalents the findings for BCC V single crystal in our research.

Goel et al. [119], also observed this twinning anisotropy in tantalum during nano-indentation across different orientations through simulations. They found that the mechanism of plastic deformation in Ta during nano-indentation was primarily driven by the formation and motion of prismatic dislocation loops with 1/2<111> and <100> types across all three orientations (100), (110), and (111), besides to the formation and migration of twin boundaries. These findings suggest that twinning plays a dominant role over dislocation nucleation in driving plasticity in tantalum during nano-indentation. In contrast, the plastic deformation of Fe single crystal was dominated by slip deformation in all orientations, where dislocations with Burgers vectors a/2<111>, a<100>, and a<110> were nucleated and extended, eventually evolving into

Chapter IV: Atomistic Investigation of Crystallographic Orientation effect on V/Fe Bilayer Response during Nano-indentation shear loops at advanced stages of indentation. However, consistent with previous studies [124,125,127], orientation dependence in terms of dislocation density, indentation force, and hardness is also evident in BCC iron. Another factor contributing to the orientation-dependent mechanical behavior of V and Fe may be the surface energy asymmetry in BCC crystals, since the lattice spacing and density can vary for each orientation. Previous studies have confirmed that the (110) surface exhibits the lowest surface energy compared to the (100) and (111) surfaces [128, 129]. Therefore, the crystallographic orientation significantly affects both the

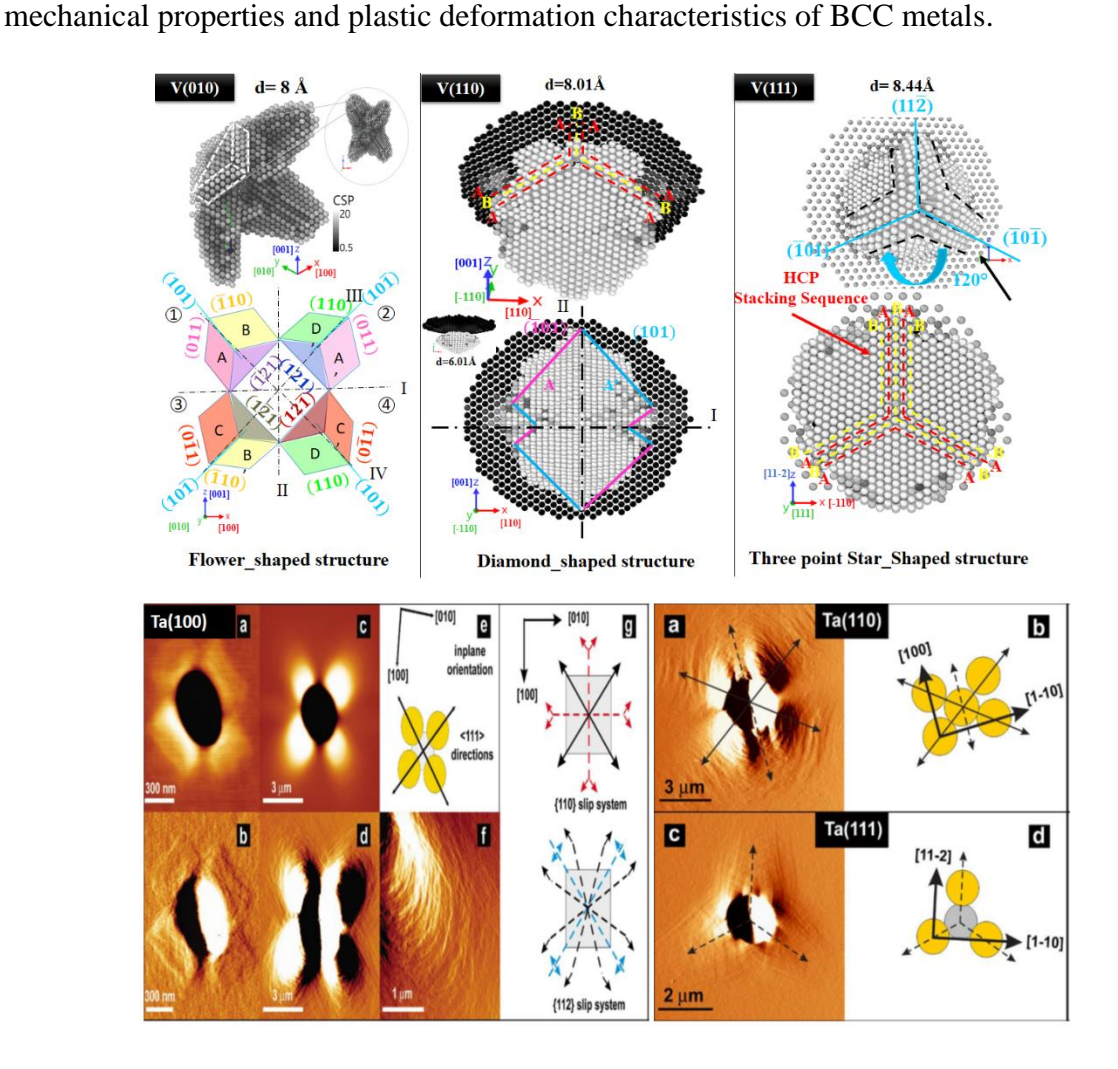


Fig IV.15 A) MD images of indented $V_{(010)}$, $V_{(110)}$, and $V_{(111)}$ showing the twinning anisotropy of Vanadium. B) AFM images indented $Ta_{(100)}$, $Ta_{(110)}$, and $Ta_{(111)}$ single-crystals [105]

IV.3.2 Influence of semi-coherent interfaces for different crystallographic Orientations:

The mechanical behavior of the V/Fe bi-layer also exhibits orientation-dependence during indentation, as shown in Fig.IV.16. It is evident that the indentation loads at the end of the indentation process are lower for the (010) orientation and higher for both the (110) and (111) orientations. Conversely, hardness is greater for the (010) indentation and lower for the (111) indentation, indicating variations in the contact area for each crystallographic orientation.

Furthermore, despite the different misfit dislocation (MFD) network patterns generated in each crystallographic orientation of the V/Fe bi-layer, a similar blocking effect mechanism of MFDs is observed, with many dislocations being blocked by the (010), (110), and (111) interfaces (see Fig. IV.18). However, the V/Fe (111) semi-coherent interface can be categorized as the weakest interface compared to the (010) and (110) interfaces. Since, it can lose this effect at advanced indentation loading. Additionally, in terms of stability, dislocation loops with Burgers vectors a/2<111> readily form at the MFD₍₁₁₁₎ nodes at an early stage of indentation, adding stress to the interface and contributing to its weakness.

Fig. IV.17 demonstrates that local shear strain and von_Mises stress distribution are higher for the (111) indentation resulting from the elevated dislocation density, and the different dislocation-interface interactions as shown in Fig.IV.18c. In contrast, von_Mises stress is more localized at the (110) interface.

One can deduce that, at a certain level of (111) indentation loading, the nodes of the MFD act as barriers to dislocation propagation, evolving them into horizontal shear loops. Nevertheless, this blocking effect can disappear when there are no MFD to interact with, allowing dislocations to easily propagate into the Fe layer at higher loading stages.

This can be explained by the wider MDF spacing in the (111) interface (see Table IV.2 and Fig. IV.18). consequently, the MFDs' nodes are the most effective sites for blocking dislocation propagation, as demonstrated in Chapter III.

As a result, the blocking effect is also governed by the misfit dislocation spacing (lattice misfit). Furthermore, the orientation dependence of the bi-layer along indentation has been observed in previous studies [132-134], supporting Koehler's theory [20] and aligning with other research on FCC/FCC bilayer systems [22].

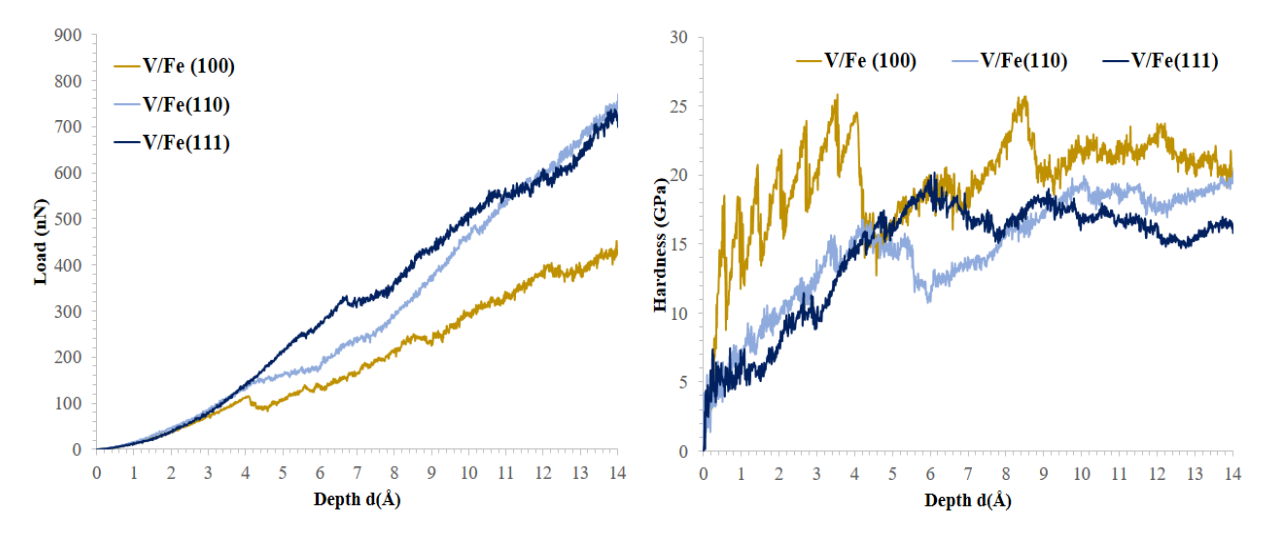


Fig IV.16 Indentation load-depth & hardness-depth curves of V/Fe bi-layer for different crystallographic orientations.

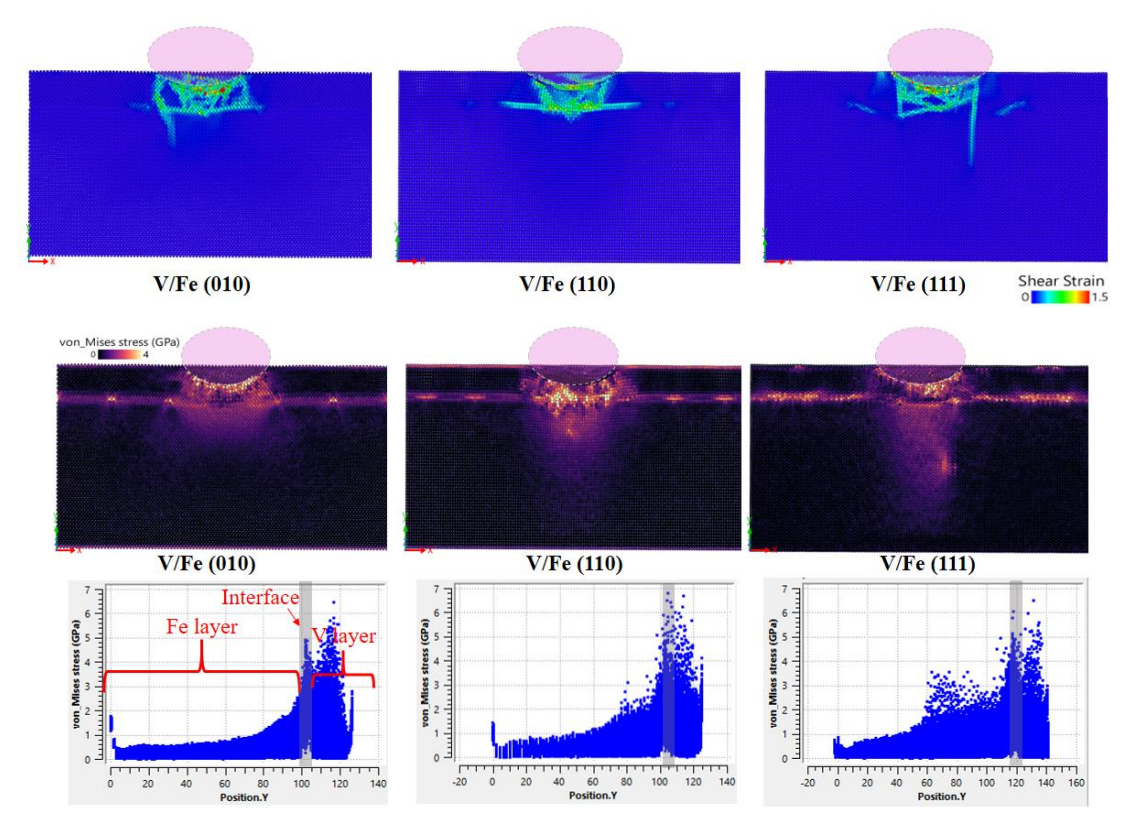


Fig IV.17. Atomic Shear strain and Von_Mises stress dispersions in V/Fe bilayer for different orientations, at d=13Å.

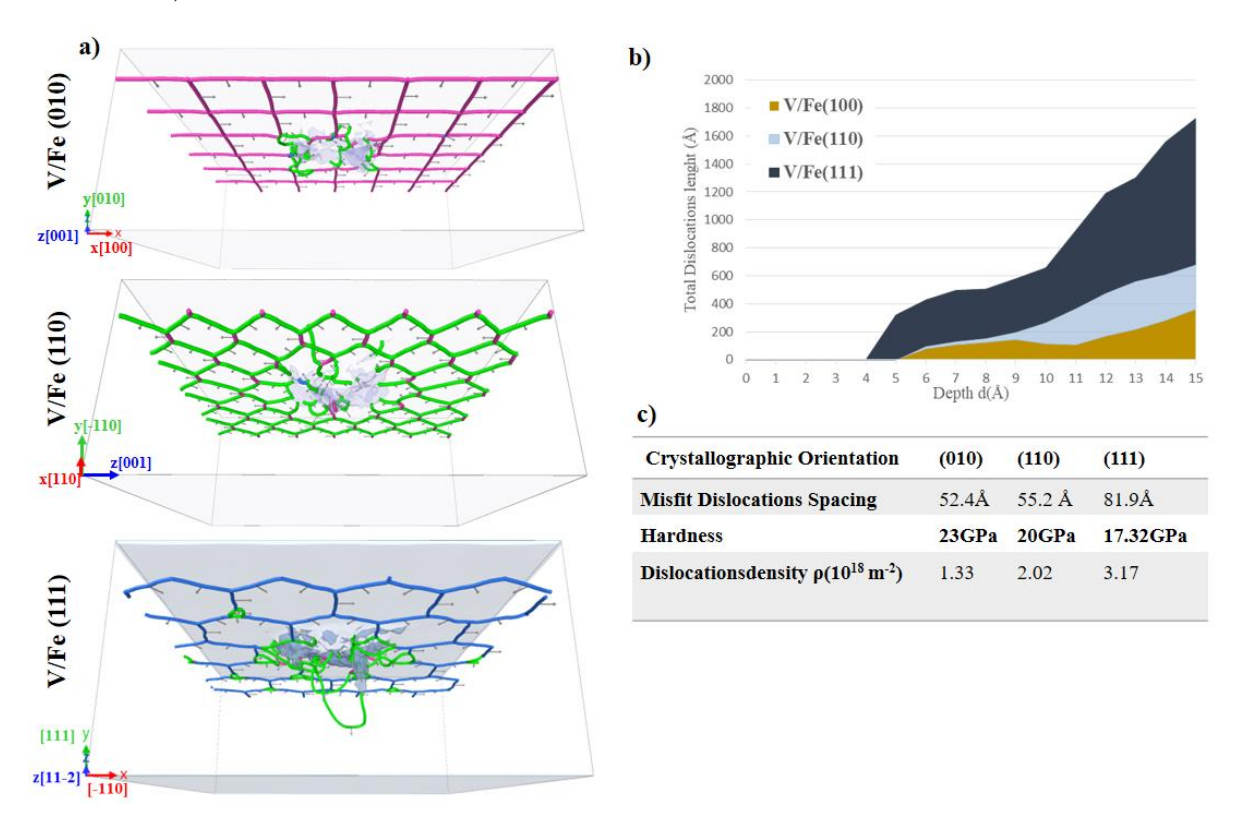


Fig IV.18 a) DXA snapshots of the dislocation dynamics of V/Fe. b) Total dislocations length-depth along plastic stage of $V/Fe_{(010)}$, $V/Fe_{(110)}$, and $V/Fe_{(111)}$ bi-layers. c) MFD spacing, hardness, and dislocation density of V/Fe with crystallographic orientations at the end of indentation.

IV.6 Conclusion:

To summarize, our study has shown that, despite the distinct structural characteristics of the (110) and (111) interfaces, the V/Fe semi-coherent interface exhibits a strengthening effect during nano-indentation by effectively hindering dislocation transmission. However, the wider misfit dislocation spacing in the (111) interface reduces this barrier effect, allowing some dislocations to propagate into the Fe layer at advanced indentation loading. Additionally, we have demonstrated the pronounced anisotropic plasticity of V and Fe single crystals, highlighting the critical role of crystallographic orientation in their mechanical response.

Chapter V: Atomistic Insights into the Inverse Effect of Semi-Coherent Interfaces during Nano-indentation of Fe/V Bilayer, Fe-V-Fe, and V-Fe-V multilayers

Summary

In this chapter, we investigate the impact of BCC/BCC semi-coherent interfaces on the indentation response of Fe/V bi-layer.

Accordingly, the indentation response of Fe/V, V/Fe bi-layers are compared to Fe-V-Fe, and V-Fe-V multilayers elucidating the inverse effect of Fe/V semi-coherent interfaces. Moreover, the effect of Fe layer thickness on the behavior of Fe/V bi-layer is examined.

V.1 Indentation response of Fe/ $V_{(010)}$ and Fe-V-Fe, V-Fe-V multi-layers:

In this section, we present a comparative study of the deformation mechanisms during (010) nano-indentation of the Fe/V bi-layer system and the Fe-V-Fe and V-Fe-V multi-layers. Aiming to examine the impact of Fe/V semi- coherent interfaces. It is important to note that we maintained the same simulation conditions as those used in the previously studied V/Fe bilayer system to ensure consistency.

Figure V.1 displays the indentation load and hardness curves for all studied systems. In the initial elastic deformation stage, all systems exhibit similar behavior. However, differences become apparent with the onset of the first yield point. Notably, each system shows distinct load values under advanced indentation, with the V/Fe bilayer demonstrating clear strengthening. In contrast, the Fe/V system exhibits an apparent softening, resulting in the lowest load and hardness values at the end of indentation loading.

One can observe that, figure V.1 reveals two yield points for the Fe/V bilayer system and three for the Fe-V-Fe and V-Fe-V multilayers. To further elucidate the deformation mechanisms in each system, we used the dislocation analysis (DXA), to examine the plastic deformation mechanisms separately in the following subsections.

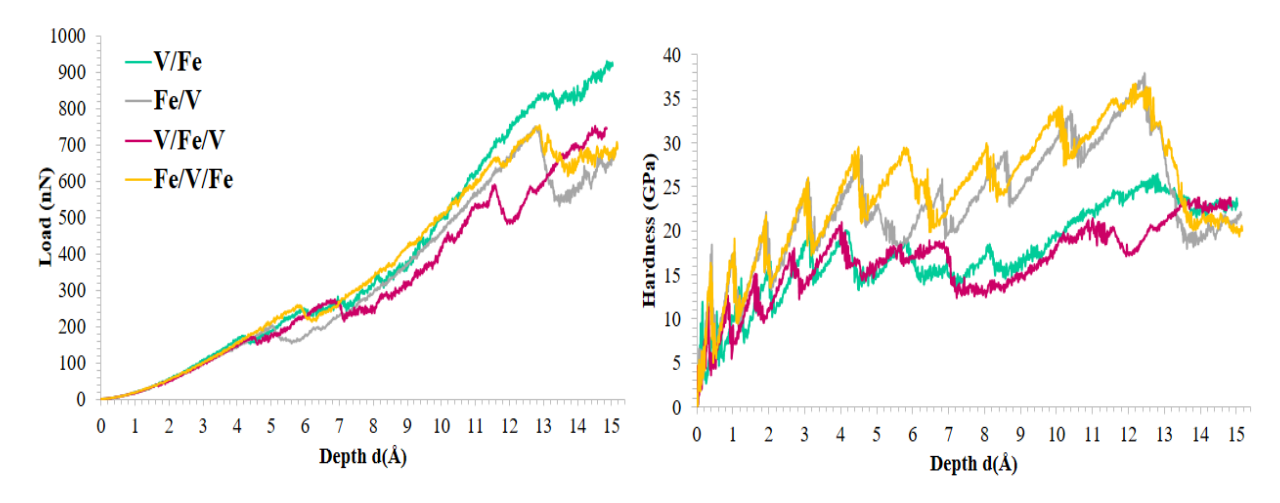


Fig V.1 Indentation load-depth & hardness-depth of V/Fe, Fe/V bi-layers and, Fe-V-Fe, and V-Fe-V multi-layers.

V.1.1 Deformation mechanisms of Fe/ $V_{(010)}$ bi-layer:

The Fe/V bi-layer initially deforms elastically under indentation until the first yield point occurs at d=5.1Å (see Fig.V.2). At this point, the Fe layer remains in the elastic regime with no detectable defects under the indented surface. However, a prismatic loop dislocation with Burgers vector a/2<111> is observed at the central node of the misfit dislocation network (MFD) along the loading direction (refer to Fig. V.2(a)). One can understand that, the formation of this dislocation loop is originated after the decomposition of the <100> misfit dislocations.

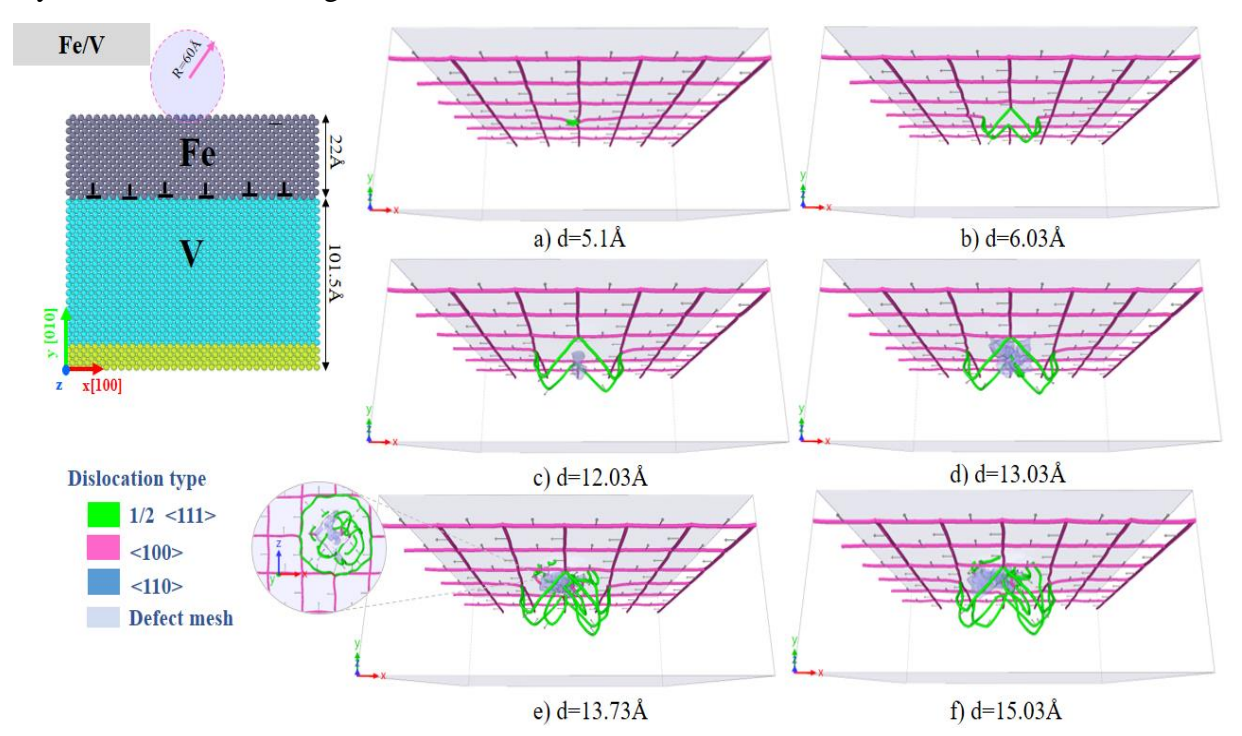
Chapter V: Atomistic insights into the inverse effect of semi-coherent interfaces during nano-indentation of Fe/V With more indentation ($\mathbf{d=6\mathring{A}}$), this prismatic loop extends along the {101}<111> slip systems inside V layer and subsequently evolves into four shear loops. Notably, no dislocations are detected beneath the indented surface of the Fe layer.

At d=12.03Å, planar defects begin to nucleate from the Fe layer within the V layer, alongside the extension of the previous 1/2<111> dislocation shear loops.

This phenomenon can be attributed to the rise of localized stress at the Fe interfacial atoms. Concurrently, the load values continue to increase until reaching a second yield point.

At the second yield point (**d=13.03Å**), the nano-indentation force induces plastic deformation of Fe layer. Leading to the formation of planar defects and the nucleation of two dislocations with Burgers vectors a/2<111>), beneath the indented surface, as shown in Fig.V.2. While the 1/2<111> shear loops in the V layer remain active and continue to glide inside V layer.

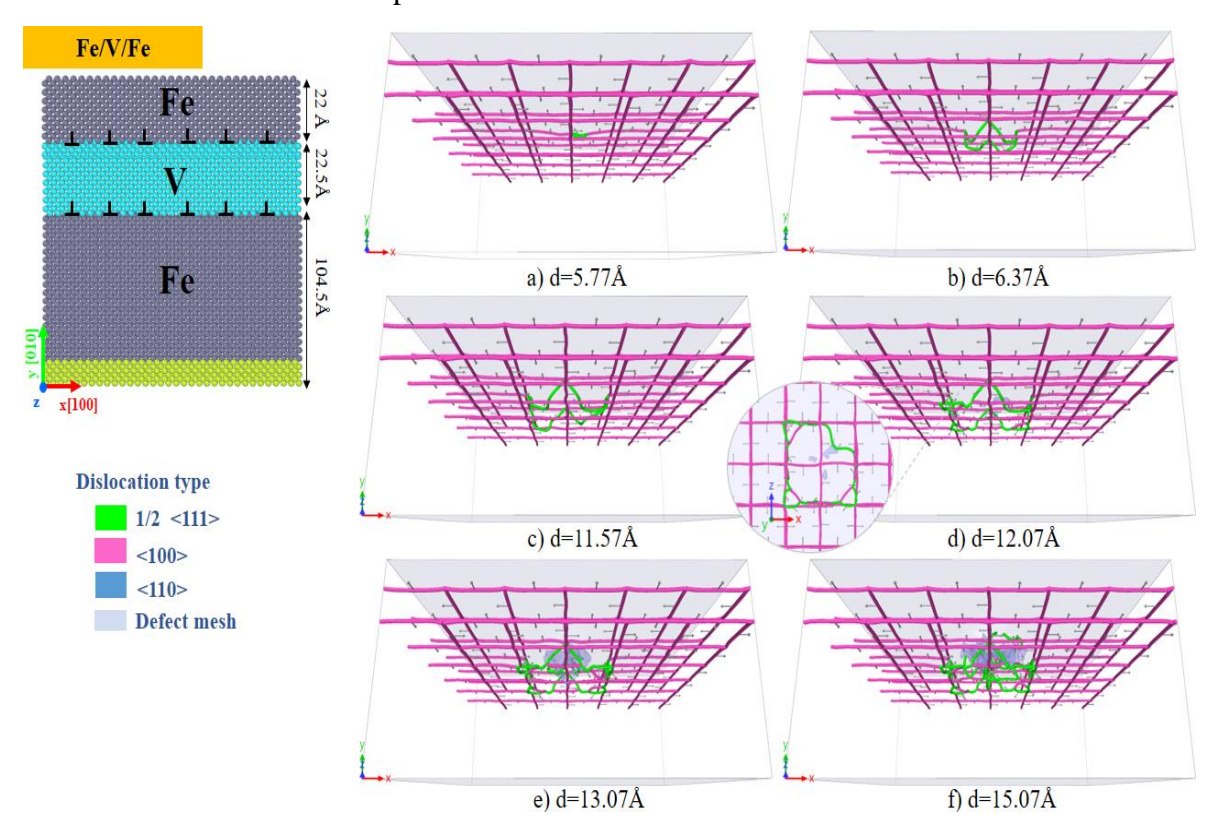
Thus, the plastic deformation of the Fe/V bi-layer is governed by two primary mechanisms: an initial deformation occurring in the V layer and the subsequent principal plastic deformation of the indented Fe layer. With further indentation (**d=13.73Å**), numerous dislocations with Burgers vectors a<100> and a/2<111> are generated in the indented Fe layer and propagate easily toward the V layer due to the absence of obstructive MFDs. Finally, **at d=15.03Å**, some of the 1/2<111> dislocations evolve into extended shear loops which glide from Fe into V layers without interacting with the interface.



FigV.2 DXA snapshots of dislocation dynamics along plastic deformation of Fe/V bi-layer for specific depths.

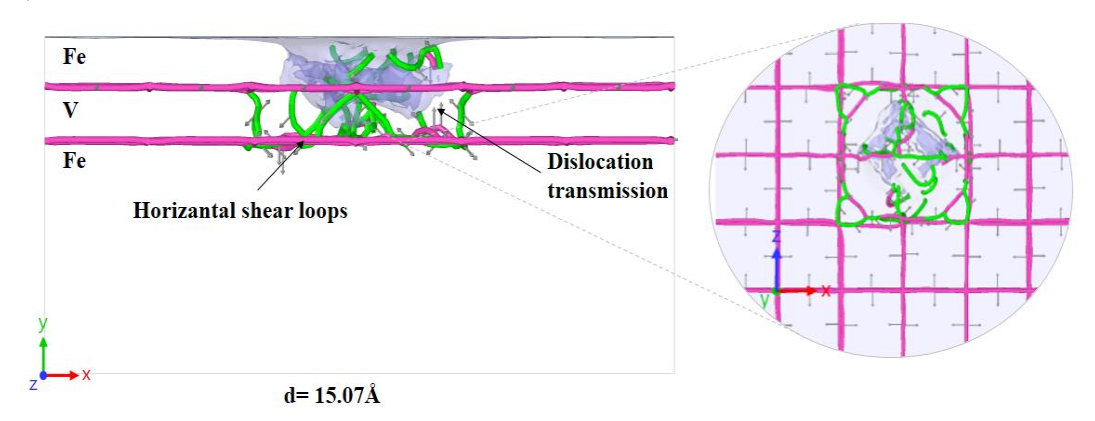
V.1.2 Deformation mechanisms of Fe-V-Fe multilayer:

For the Fe-V-Fe multilayer system, two identical semi-coherent interfaces are generated, forming a MFD with a squared grid pattern (see Fig. V.3). We denote these interfaces as (Fe/V)_{MDF} and (V/Fe)_{MDF}. From snapshots (a) to (c) in Figure V.3, it is evident that the initial plastic deformation of the Fe-V-Fe multilayer closely resembles that of the Fe/V bi-layer system, nevertheless a prolonged elastic deformation can be noticed for Fe-V-Fe multi-layer. The first yield point at d=5.77Å, observed in the load curve (see Fig.V.1), marks the nucleation of a prismatic loop dislocation with Burgers vector a/2<111> due to the decomposition of the central node of the (Fe/V)_{MDF} interface. This prismatic loop rapidly extends inside the V layer at d=6.37Å (see Fig.V.3(b)), and subsequently propagates along the four {110}<111> slip systems in the V layer, while no dislocations are detected under the top indented Fe surface. With further indentation, the extended 1/2<111> shear loops inside V layers and interact with the subsequent (V/Fe)_{MDF}. Generating a second yield point of indentation curve at **d=11.57**Å (see Fig.V.1), along with a noticeable increase in load values can be seen. At this stage, the (V/Fe)_{MDF} of the second interface act as a barrier to dislocation propagation, transforming the incoming 1/2<111> dislocations from the V layer into horizontal shear loops (see Fig.V.3 at d=12.07Å) and preventing their glide into the lower Fe layer. Subsequently, at the third yield point (d=13.07Å), dislocations begin to nucleate from the indented surface of Fe layer. These dislocations subsequently emit and propagate easily into the subsequent V layer, as there are no MFD nodes or lines to impede them.



FigV.3 DXA snapshots of dislocation dynamics along plastic deformation of Fe-V-Fe multilayer for specific depths.

Chapter V: Atomistic insights into the inverse effect of semi-coherent interfaces during nano-indentation of Fe/V Conversely, by the end of indentation at d=15.07Å, the $(V/Fe)_{MDF}$ demonstrate a strong aptitude to block dislocation transmission into the substrate Fe layer. Figure V.4 provides a close-up of this blocking effect, showing numerous dislocations aligned horizontally along the $(V/Fe)_{MFD}$ interface.



FigV.4 Close-up picture showing the blocking effect of V/Fe_(MFDs) interface at the end of indentation.

V.1.3 Deformation mechanisms of V-Fe-V multilayer:

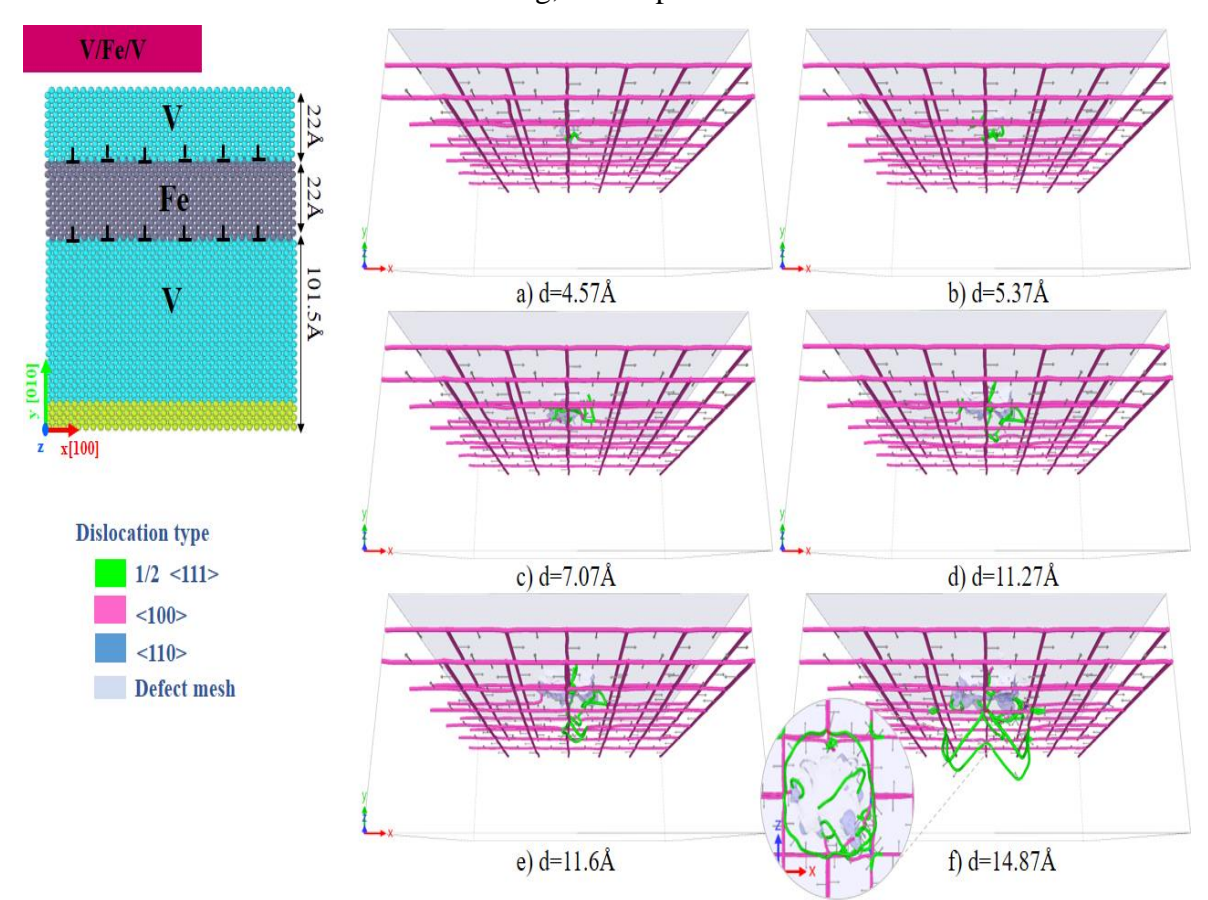
The deformation of V-Fe-V multilayer system, initiates with an elastic response until the first yield point at **d=4.57Å** (Fig.V.1), indicating the onset of the plastic regime through the nucleation of planar defects beneath the indented V layer. These defects rapidly propagate inside V layer and then interact with the central node of the (V/Fe)_{MDF}, forming a prismatic loop dislocation with a Burgers vector of a/2<111>. However, this prismatic loop is seen blocked from moving toward the Fe layer. It extends and piles-up inside the top V layer. At **d=5.37Å**, two dislocation segments with a Burgers vector of a/2<111> nucleate from the indented surface.

With further indentation at $d=7.07\text{\AA}$, these dislocations interact with $(V/Fe)_{MDF}$ interface, which prevent them from gliding into the subsequent Fe layer. By $d=11.27\text{\AA}$, numerous 1/2<111> dislocations within the deformed V layer evolve into horizontal shear loops that are blocked by the interface (see Fig.V.5). However, when it does not encounter any MFD nodes, one segment of 1/2<111> dislocation successfully transfers into the next Fe layer.

The stress held by this dislocation, combined with the high localized stress at the MFD nodes of the second interface, induces the formation of a new prismatic loop at the central node of the $(Fe/V)_{MDF}$ along the indentation direction. This event corresponds to the second yield point on the load curve at $d=11.6\text{\AA}$ (Fig. V.1).

Similarly, to what was seen in the Fe/V bilayer system, a prismatic loop is observed to extend easily into the lower V layer due to the relative weakness of that interface. At the end of indentation (**d=14.87Å**), the plastic response of the V-Fe-V system is characterized by two primary deformation mechanisms. The principal deformation occurs in the top V layer under the applied indentation force, while the secondary deformation occurs in the bottom V layer.

Chapter V: Atomistic insights into the inverse effect of semi-coherent interfaces during nano-indentation of Fe/V The latter is associated with the decomposition of the (Fe/V)_{MDF} resulting from the higher stress transmitted from dislocations activated in the Fe layer, demonstrating that the V/Fe interface is more resistant under indentation loading, in comparison to Fe/V interface.



FigV.5 DXA snapshots of dislocation dynamics along plastic deformation of V-Fe-V multilayer for specific depths.

V.2 The effect of Fe layer thickness on the response of Fe/V:

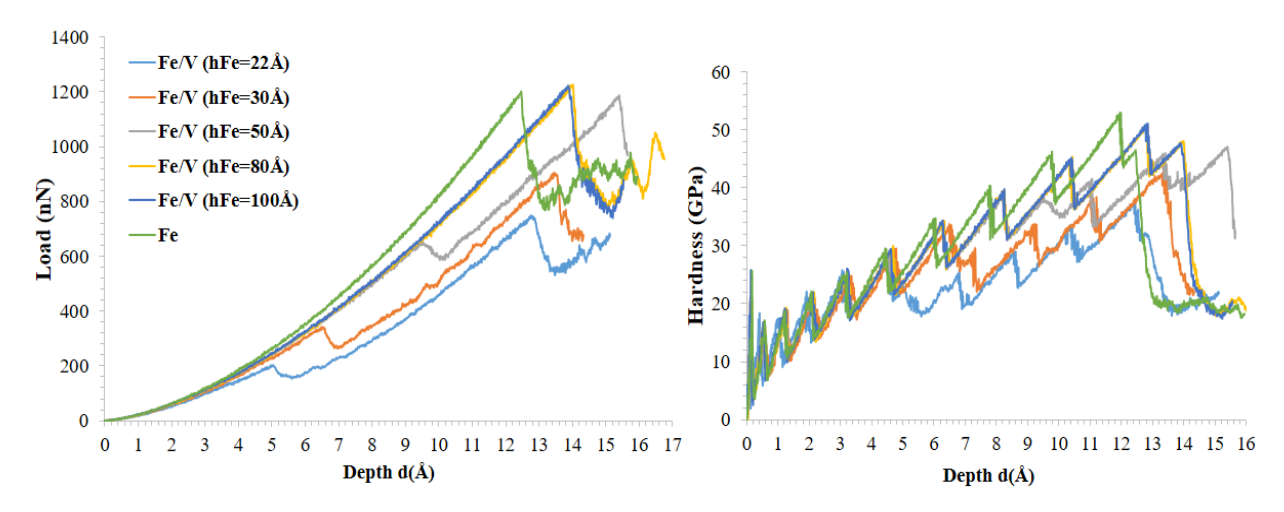
V.2.1 Indentation curves of Fe/ V bi-layer with different Fe layer thicknesses:

To investigate the effect of Fe layer thickness on the indentation response of the Fe/V bilayer system, we performed nano-indentation on Fe/V samples with varying Fe layer thicknesses (h_{Fe} =30, 50, 80, and 100Å). Figure V.6 presents the indentation load and hardness curves for these samples.

It can be observed that for Fe/V bilayers with Fe layer thicknesses of 50Å or less, the indentation curves exhibit two distinct yield points. Additionally, their load curves are lower compared to those of Fe single crystal. However, for Fe/V bi-layers with thicker Fe layers (h_{Fe} = 80 and 100 Å), only single yield point appears at higher indentation load. Moreover, their load curves resemble that of Fe single crystal more closely.

It is evident that the depth of the first yield point corresponds to increases of Fe layer thicknesses for h_{Fe} =50Å or less. Meanwhile, the depth of the second yield point increases linearly with increasing Fe layer thickness, eventually stabilizing for thicker Fe layers. Moreover, it can be concluded that the depth of yield point for pure Fe is lower than that of

Chapter V: Atomistic insights into the inverse effect of semi-coherent interfaces during nano-indentation of Fe/V Fe/V bilayers with h_{Fe} =80 and 100Å, possibly because the Fe layer has not yet reached its bulk properties yet.



FigV.6 Indentation load-depth & hardness-depth curves for pure $Fe_{(010)}$ and $Fe/V_{(010)}$ bi-layer with various Fe layer thicknesses ($h_{Fe} = 22, 30, 50, 80, 100 \text{ Å}$).

V.2.2 Deformation mechanisms of Fe/V bi-layer with different Fe layer thicknesses:

The DXA analysis of dislocation development using Ovito, presented in Fig.V.8, demonstrates that the plastic deformation mechanisms for Fe/V bilayers with h_{Fe} =30 Å and h_{Fe} =50Å are similar to those observed for Fe/V with h_{Fe} =22Å, as previously discussed in Section V.1.1. In these cases, plastic deformation in the bilayer system initiates, from the first yield point, through the decomposition of MFD inside the softer V layer, while the indented Fe layer deforms elastically. A second yield point marks the onset of plastic deformation beneath the indented surface, leading to significant softening. In contrast, Fe/V bilayers with h_{Fe} =80Å and h_{Fe} =100Å exhibit deformation behavior similar to that of a pure Fe single crystal.

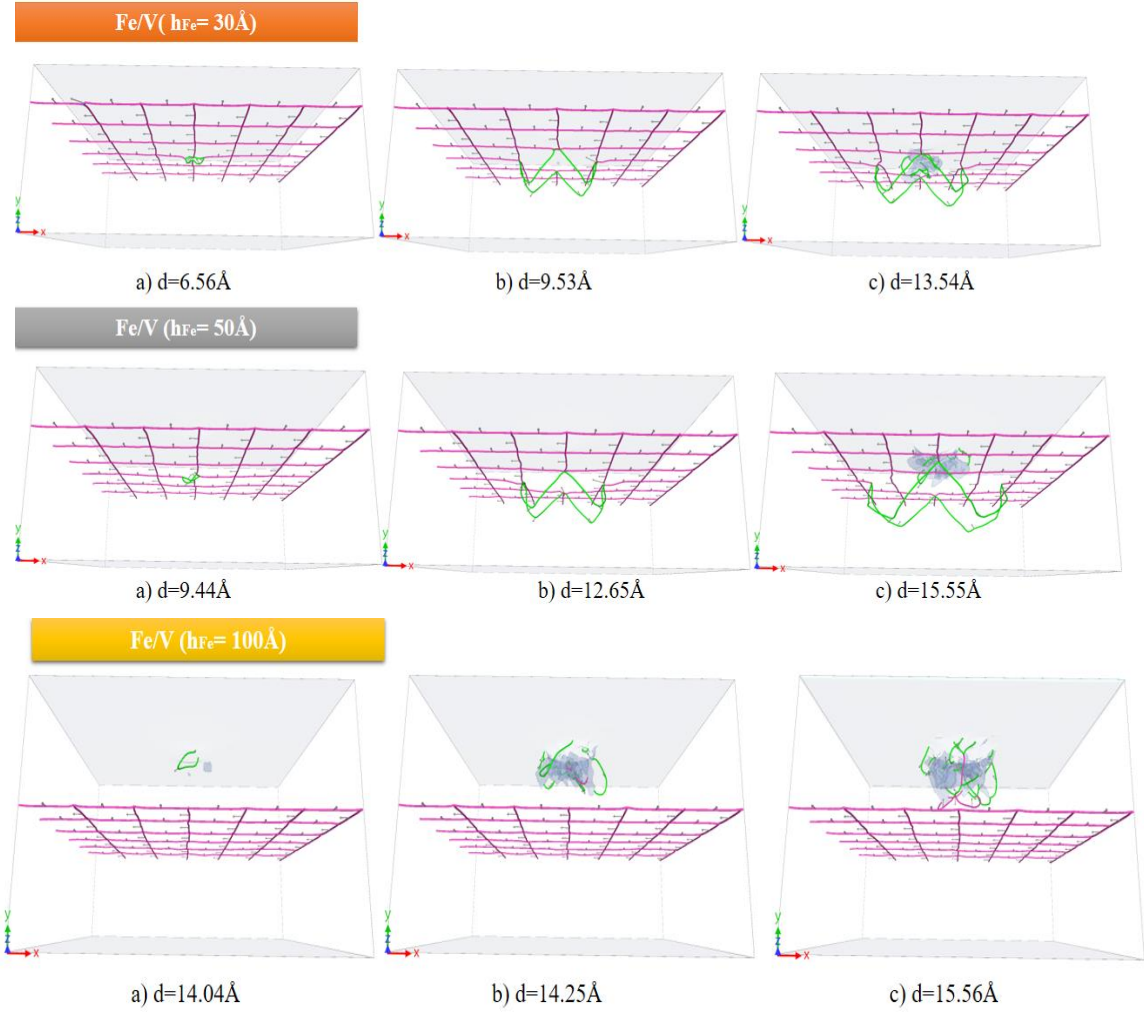
For h_{Fe} =30Å, the Fe/V bi-layer deforms elastically until the first yield point, located at d=6.18Å, which is attributed to the decomposition of MFD dislocations within the V layer. At this stage, a 1/2<111> prismatic dislocation loop nucleates at an MFD node and subsequently propagates and extends easily inside the V layer with increasing indentation depth (d =9.53 Å), while the indented Fe layer continues to deform elastically. When dislocations are emitted from the indented surface, signaling the onset of the plastic regime, the second yield point is observed in the indentation load curve. At this stage, dislocations with Burgers vectors a/2<111> and a<100> propagate within the Fe layer and easily transmit into the V layer (d=13.54Å). (See Fig. V.8).

For $h_{Fe}=50\text{Å}$, the first yield point occurs at a greater indentation depth (d=9.44Å) compared to thinner Fe layers, indicating the nucleation of a 1/2<111> prismatic loop in the MFDs and its subsequent propagation inside the V layer (d=12.65Å). As indentation loading progresses

Chapter V: Atomistic insights into the inverse effect of semi-coherent interfaces during nano-indentation of Fe/V (d=15.55Å), the indented Fe layer begins to deform plastically through dislocation nucleation and propagation, marking the second yield point.

For h_{Fe} =100Å, the deformation behavior of the Fe/V bilayer closely resembles that of pure Fe, though the first yield point is delayed. In this case, the interface does not significantly influence on the overall mechanical response since it is far from the primary loading region. As a result, the deformation mechanism is dislocation motion, and the plastic deformation occurs primarily inside the Fe layer, leading to a single yield point in the indentation load curve. (See Fig. V.6).

From figure.V.9, it is evident that the softening effect observed in Fe/V bilayers is induced by the decomposition of MFDs within the softer V layer and exhibits a linear relationship with Fe layer thickness. Which is more pronounced for thinner Fe layers (h_{Fe} =22, 30, and 50Å), resulting in lower hardness. After the critical thickness h_{Fe} =50Å, as the Fe layer thickness increases, the interface effect diminishes, leading to an increase in both indentation force and hardness. This effect correlates with the invers-Hall-Petch effect. In contrast, in the case of V/Fe bi-layer (studied in Chapter III), hardness and indentation force were observed to increase with increasing V layer thickness. Following Hall-Petch strengthening effect.



FigV.8 DXA snapshots of dislocation dynamics along plastic deformation of Fe/V bi-layer designed for various Fe film thickness for different indentation depths.

Chapter V: Atomistic insights into the inverse effect of semi-coherent interfaces during nano-indentation of Fe/V

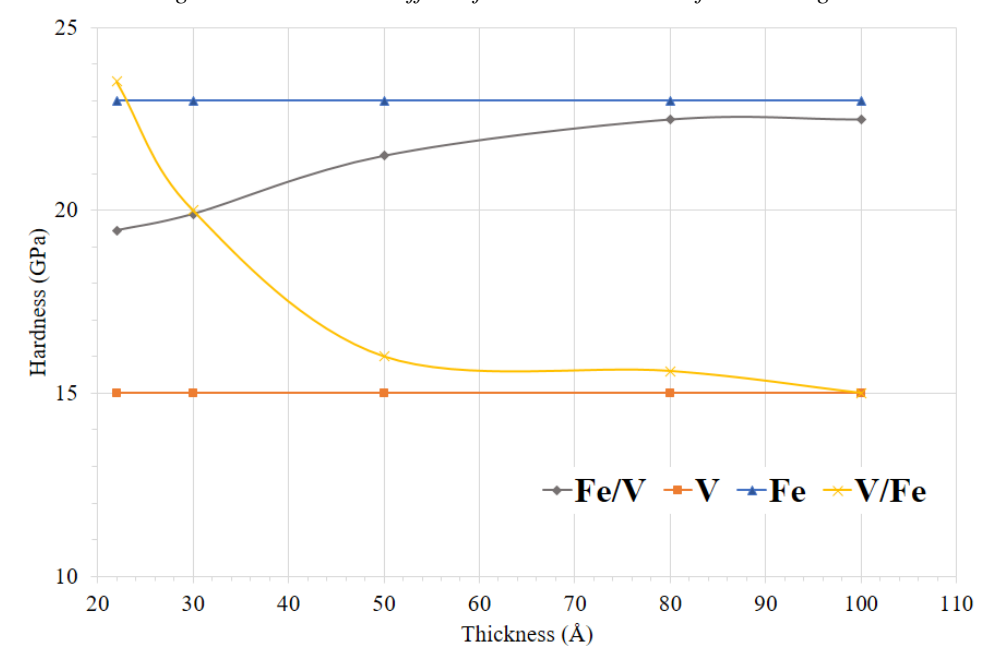


Fig V.9 Illustration of the asymmetry of Hardness variation in Fe/V and V/Fe bi- layers based on film thickness, compared to pure Fe and V.

V.3 Discussion:

V.3.1 MFD From barrier to transmitter:

One can deduce that, the misfit dislocation (MFD) network in BCC/BCC bilayer systems has opposite effects during nano-indentation. A strengthening effect is observed in the V/Fe bi-layer, whereas a softening effect is evident in the Fe/V bi-layer.

The MFD in V/Fe act as barrierto dislocation propagation, confining plastic deformation within the indented V layer. In contrast, the misfit dislocations in Fe/V facilitate rather than hinder dislocation motion and can even serve as nucleation sites for dislocations, as evidenced by the decomposition of MFD into dislocation loop from the MFD's node of the Fe/V interface before the onset of plastic deformation in the Fe layer. These contrasting effects are strongly linked to the stress and energy barrier mechanisms discussed in Chapter III. Moreover, it becomes more apparent proximate the interfaces.

Figure V.10 illustrates how differences in stress direction and energy distribution lead to opposite dislocation-interface interactions in the V/Fe and Fe/V bi-layers. In both interfaces, misfit dislocations accommodate the lattice mismatch between the two crystals. So that, the MFD nodes are regions of intense localized lattice straining, which generates stress fields in their vicinity:

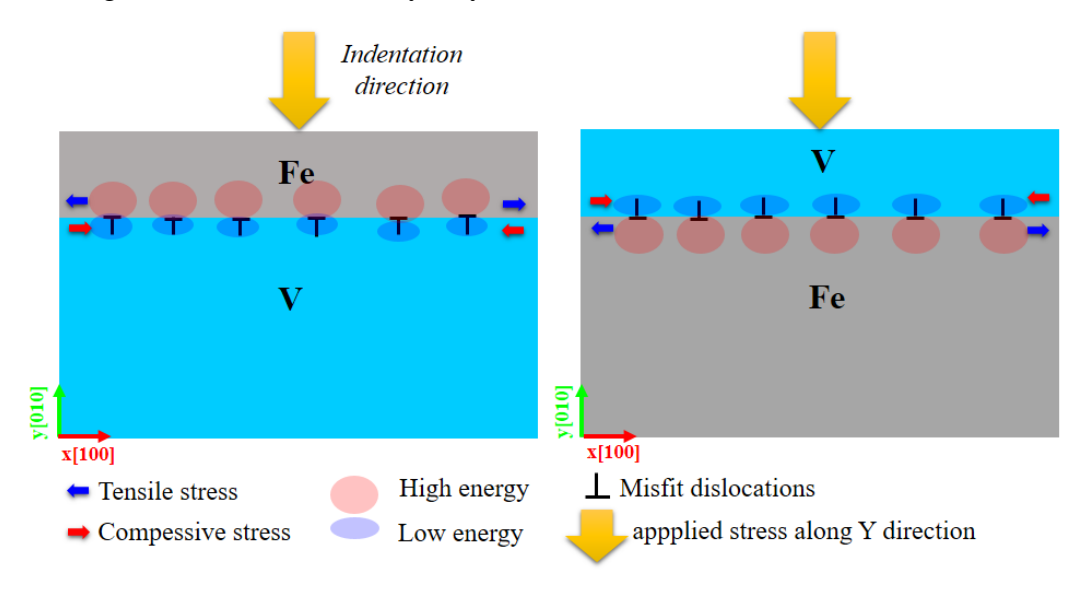
- Compressive stress (positive) in the V lattice.
- Tensile stress (negative) in the Fe lattice.

During nano-indentation of the Fe/V system, the applied stress aligns with the stress generated by the lattice straining at MDF. This alignment results in a localized accumulation of stress at

Chapter V: Atomistic insights into the inverse effect of semi-coherent interfaces during nano-indentation of Fe/V the V interfacial atoms, leading to interface deformation through the nucleation of a 1/2<111> prismatic dislocation loop beneath the indentation direction (at the central node). Consequently, the accumulated stress at the Fe/V interface makes the MFDs act as dislocation sources, promoting dislocation nucleation into the softer V layer and thereby facilitating plastic deformation.

Conversely, in the V/Fe system, the stress due to lattice straining and the applied indentation stress act in opposite directions, generating a repulsive force at the interface. This repulsion strengthens the MFD network; preventing dislocations from penetrating the Fe layer (see Fig. V.10). As a result, dislocations originating in the indented V layer are constrained to extend laterally rather than crossing into Fe.

Furthermore, the energy levels of atoms at the MFD nodes play a critical role in determining dislocation mobility. In the Fe/V bilayer, the lower energy of vanadium atoms facilitates the decomposition of MFD inside V layer during indentation. In contrast, in the V/Fe interface, the higher energy of Fe atoms at the MFD nodes increases the energy required for dislocations to transfer across the interface. This effectively enhances the blocking mechanism and reinforcing the hardening effect in the V/Fe bilayer system.



FigV.10 Schematic illustration of the difference in stress and energy of MFDs for V/Fe and V/Fe bi-layers.

V.3.2 Koehler Theory:

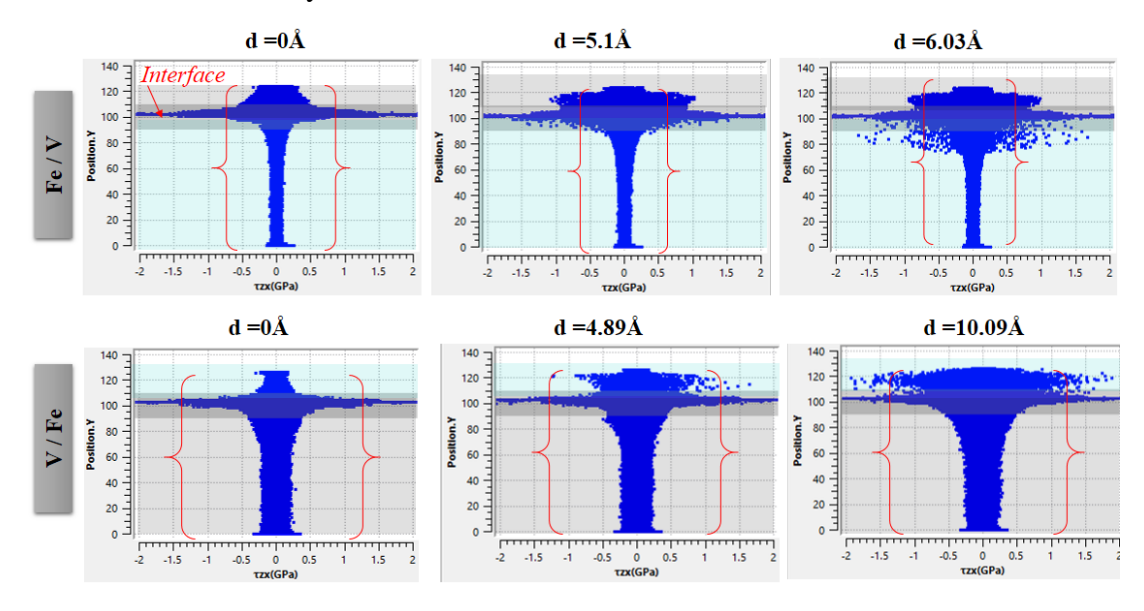
Koehler was the first who demonstrate the concept of barrier mechanics (modulus mismatch) in 1970 [20]. He focused on the modulus mismatch, specifically the difference in shear modulus, to calculate the stress required a dislocation to move from a soft layer into a hard layer against its elastic image at the interface. He concluded that alternating layers of materials with high and low elastic constants would increase the resolved shear stress needed to drive dislocations through the layered structure.

Chapter V: Atomistic insights into the inverse effect of semi-coherent interfaces during nano-indentation of Fe/V To maximize this strengthening effect, he proposed that the elastic constants of the two materials should differ as much as possible. In addition, dislocations' line energy (energy per unit length) should exhibit a significant contrast between the materials. Koehler stated that in large single crystals composed of materials A and B. if the material B has a higher line energy, dislocations would preferentially remain in material A. Consequently, greater external stress would be required to force dislocations from A into B [20].

Zeng et al. [135] employed a phase-field dislocation dynamics (PFDD) model to simulate the slip transmission process in FCC bi-metal systems with semi-coherent interfaces (e.g., Cu-Ni, Ag-Au, Al-Pt). Their study revealed that the critical stress required for slip transmission is asymmetric and depends on the transmission direction that is, whether the dislocation originates from one material and transmits into the other. They found that dislocation transmission is generally easier when moving from the material with a larger lattice parameter and lower shear modulus than the material with a smaller lattice parameter and higher shear modulus, while the reverse requires higher stress.

This asymmetry arises from the energy needed to form the residual dislocation at the interface, which is influenced by the relative differences in lattice parameters and elastic moduli of the two materials, leading to a path-dependent transmission behavior. Our results aligns well with these observations.

In our case of study, the stress required for dislocation transmission exceeds the critical shear stress for slip transmission in the Fe/V interface, as shown in Fig.V.11. Leading to the decomposition of the MFD node inside the V layer (at d=5.1Å) before plastic deformation occurs in the indented Fe layer. Conversely, even under higher indentation loading (d=10.09Å), the shear stress in the V layer remains below the critical shear stress for transmission.



FigV.11 Shear stress τ_{xz} (GPa) distribution in V and Fe atoms for both Fe/V and V/Fe bilayer systems at different indentation depths.

Chapter V: Atomistic insights into the inverse effect of semi-coherent interfaces during nano-indentation of Fe/V Similar asymmetrical effects of the semi-coherent interfaces observed in the study of V/Fe and Fe/V bilayers have also been reported in previous studies on FCC/FCC bilayers. Notably, these effects have been documented in Cu/Ni and Ni/Cu [5, 15, 19]. Al/Ni and Ni/Al [21, 23, 24]. Al/Cu and Cu/Al [26]. Au/Cu and Cu/Au [11, 27]. Ag/Cu and Cu/Ag [14]. and Ag/Ni and Ni/Ag [22]. For instance Tian et al. [26] found that the stress barrier at the Cu-Al interface was lower than that at the Al-Cu interface. Similarly, Wu et al. [11] investigated the mechanical behavior of Au/Cu/Au multilayers under nano-indentation using molecular dynamics (MD) simulations and concluded that the Au/Cu semi-coherent interface was stronger than the Cu/Au interface, in terms of dislocation transmission. Furthermore, Li and Zhang [27] have found that Au/Cu interfaces acted as strong barriers to dislocation motion, whereas dislocations nucleated at the Cu/Au interface and propagated toward the Au layer.

Interestingly, our findings reveal similar inverse effects in BCC/BCC semi-coherent interfaces; specifically in the W/Ta and Ta/W, bi-layers (refer to Appendix B).

V.3.3 Effect of Fe layer thickness:

The effect of Fe layer thickness during nano-indentation of Fe/V bilayer has a great reliance with the vicinity of interface, indicating the important role of the semi-coherent interfaces. When the Fe layer thickness falls below 50Å, the Fe/V system experiences softening due to interface-induced plasticity. This behavior aligns with the inverse Hall-Petch effect, where a reduction in Fe layer thickness leads to a decrease in hardness. However, as the Fe layer becomes thicker, its hardness gradually approaches that of bulk Fe. Beyond this point, dislocation motion emerges as the dominant deformation mechanism within the Fe layer, as the interface is sufficiently distant from the indented surface to have a reduced influence.

This outcome is largely consistent with previous findings. For instance, during nano-indentation of a Ni/Cu bilayer system, both hardness and indentation force were observed to increase with increasing Ni film thickness [136].

Similarly, Zhao et al. [22] conducted molecular dynamics (MD) simulations of nano-indentation on Ag–Ni multilayers with varying modulation periods. Their results showed that both hardness and maximum indentation force increased with the increase of thickness of the Ni layer and the modulation period. Additionally, Yang et al. [137] studied the nano-indentation response of Ti/TiN multilayers with different thickness ratios. They found that the deformation mechanisms were strongly influenced by interface misfit dislocations, which played a crucial role in the strengthening of Ti/TiN multilayers. Their study also revealed that as the Ti layer thickness decreased, dislocations were more frequently observed crossing the second Ti/TiN interface.

Notably, our results align well with the study by Wang et al. [138], who reported that hardness increased with increasing Ta layer thickness while decreasing Cu layer thickness gave increased hardness. The similar trend is observed in our findings (see Fig. V.9), where the

Chapter V: Atomistic insights into the inverse effect of semi-coherent interfaces during nano-indentation of Fe/V variations in the thickness of V and Fe in both V/Fe and Fe/V bilayers directly influences the hardness of the indented layer.

V.4 Conclusion:

This chapter demonstrated the inverse effect of semi-coherent interfaces, revealing that the mechanical response of the Fe/V bi-layer differs significantly from that of V/Fe. Specifically, misfit dislocations decompose first within the V layer while the indented Fe layer remains in the elastic deformation stage, resulting in two distinct yield points in the indentation curve. This phenomenon was further validated in Fe-V-Fe and V-Fe-V multilayer systems. Additionally, an analysis of Fe layer thickness in the Fe/V system confirmed that the inverse effect of the semi-coherent interface becomes negligible for thicker Fe layers, as bulk-like deformation mechanisms dominate.

Chapter VI: Atomistic Investigation of the Mechanical Response of V/Fe bi-layer during Uniaxial Tension and Compression

Summary

In this chapter, the effect of loading direction on the mechanical response of V/Fe bi-layer under in-plane uniaxial tension and compression is investigated and compared to Fe and V single-crystals.

Through analyzing stress-strain curves and studying the different deformation mechanisms, we provide further insights into the effect of BCC/BCC semi-coherent interfaces on the mechanical response of multi-layers.

VI.1 Stress-strain (σ - ϵ) response of V/Fe bi-layer vs. single-crystals:

In this section, we analyze the stress-strain response of V/Fe bi-layer (including a semi-coherent interface) in comparison to the response of Fe and V single-crystals under in-plane uniaxial tensile and compressive loadings. All simulations were conducted under identical conditions.

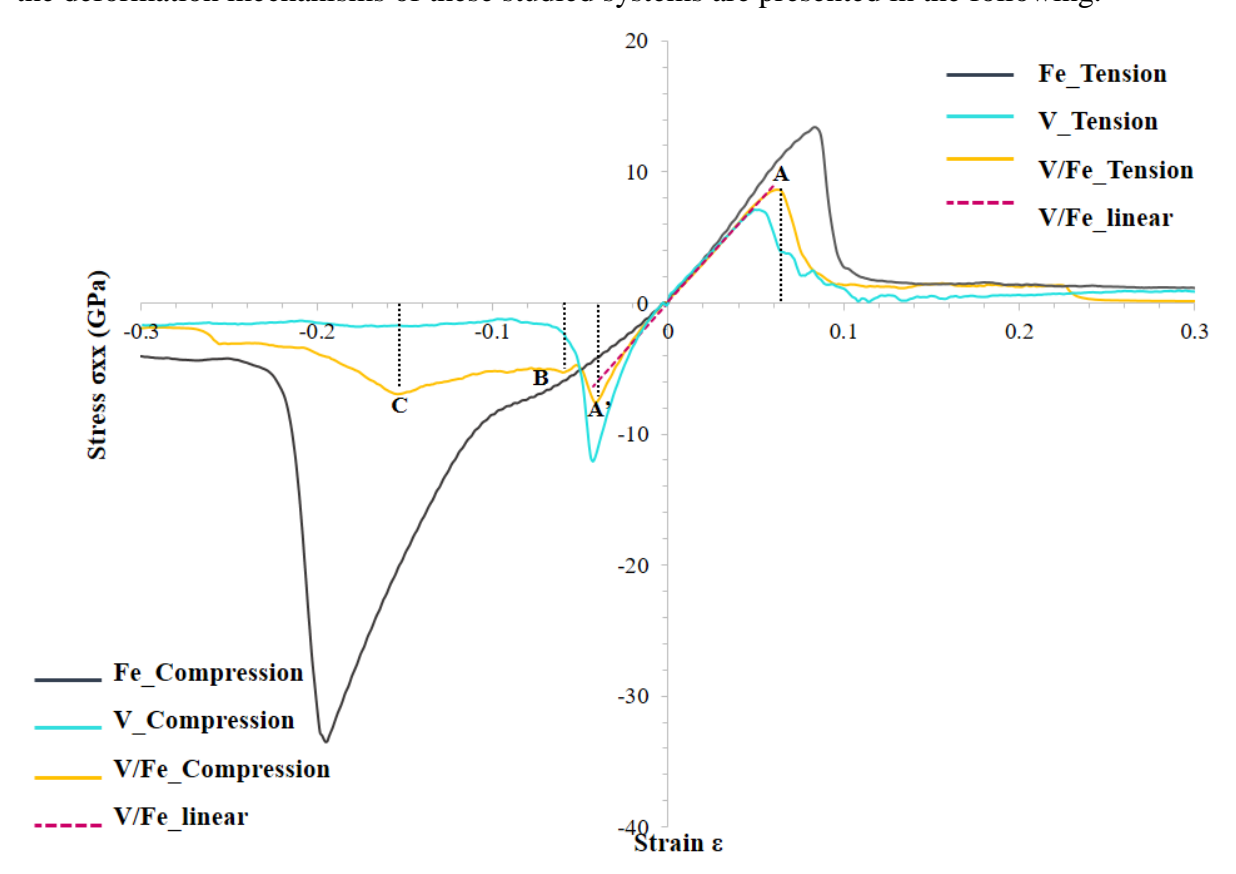
Tensile Loading Response

The stress-strain curves for the single crystals and bilayer system, presented in Fig.VI.1, indicate that all systems exhibit elastic behavior under tensile loading. Notably, the Young's modulus of Fe is higher than that of both the V single crystal and the V/Fe bilayer, following the order ($E_{Fe} > E_{V/Fe} > E_{V}$). As strain increases, stress increases in all systems until reaching their respective yield strengths: $\sigma_{yFe}=13.399$ GPa, $\sigma_{yV}=7.089$ GPa for Fe and V single-crystals, and $\sigma_{yV/Fe}=8.628$ GPa for V/Fe bilayer. A sharp drop in stress follows, indicating the onset of plastic deformation after yield point. Moreover, one can notice that, the strain to yielding is higher for Fe single crystal (about $\varepsilon_{yFe}=8.3\%$) and lower for V single crystal ($\varepsilon_{yV}=5.2\%$), while the V/Fe bilayer exhibits an intermediate value ($\varepsilon_{yV/Fe}=6.2\%$). Additionally, the flow stress, which represents the material's resistance to plastic deformation, is: $\sigma_f=1.12$ GPa for Fe single crystal and $\sigma_f=1.2$ GPa for the case of V/Fe bilayer, which are higher than the flow stress for V single crystal, (about 0.84GPa). This suggests that the V/Fe bilayer system enhances strength compared to V single crystal. A summary of the critical stress values for Fe, V, and the V/Fe bilayer under both tension and compression is provided in TableVI.3.

Compressive Loading Response

Under compressive loading, Fe exhibits the highest flow stress (σ_{fFe} =4.15GPa), followed by the V/Fe bilayer (σ_{f} v/Fe =3.35GPa) and V single crystal (σ_{f} v/Fe =3.35GPa). However, an asymmetry between the tensile and compressive stress-strain curves is evident across all systems. Fig. VI.1 shows that while both pure metals demonstrate higher resilience under compression, the V/Fe bilayer exhibits noticeable softening. This is reflected in the difference between its tensile and compressive Young's moduli ($E_{(V/Fe)T} > E_{(V/Fe)C}$). Interestingly, the compressive stress-strain curves exhibit nonlinearity, indicating a pseudo-elastic regime for Fe, V, and the V/Fe bilayer. However, one can notice that, stress increases with strain until a sudden drop marks yield points. In Fe and V, a single yielding point is observed, whereas the V/Fe bilayer exhibits two yield points in its compressive stress curve. Furthermore, it is apparent that the V/Fe bilayer undergoes the shortest elastic deformation regime, with strain-to-yield values of ε_{yFe} =19.5%, ε_{yV} =4.3%, and $\varepsilon_{yV/Fe}$ =4%. Moreover, the yield strength under compression follows the trend: (σ_{yFe} =33.49GPa > σ_{yV} =12.059GPa, > $\sigma_{yV/Fe}$ =7.57 GPa). After yield points, all systems exhibit a stress drop before stabilizing with increasing strain. The flow stress, which represents the stress at which a material continues to deform plastically under a constant strain

the deformation mechanisms of these studied systems are presented in the following.



FigVI.1 Stress-Strain (σ - ϵ) curves of V and Fe single-crystals compared with V/Fe bi-layer during uniaxial tension and compression.

	Young's	Yield	Strain to	Flow stress
	Modulus E	strength σ_y	yielding ϵ_y	σf
Fe_Tension	169.38 GPa	13.399 GPa	8.3%	1.12 GPa
V_Tension	136.305 GPa	7.089 GPa	5.2%	0.84 GPa
V/Fe_Tension	146.96 GPa	8.63 GPa	6.2%	1.2 GPa
Fe_Compression	100.82 GPa	33.49 GPa	19.5%	4.15 GPa
V_Compression	128.86 GPa	12.059 GPa	4.3%	1.62 GPa
V/Fe_Compression	129 GPa	7.57 GPa	4%	3.3 GPa

Table VI.1 Values of the Young's modulus E, yield strength σ_y , strain to yielding ε_y and Flow stress σ_f , during uniaxial tension and compression of V and Fe single crystals and V/Fe bilayer.

VI.2 Deformation mechanisms of single-crystals under uniaxial tension and compression:

In this section, we employ common neighbor analysis (CNA) and the dislocation extraction algorithm (DXA), as implemented in the OVITO software, to investigate the deformation mechanisms of single crystals under uniaxial tensile and compressive loadings. These analyses provide detailed insights into atomic-scale structural changes and dislocation evolution during deformation.

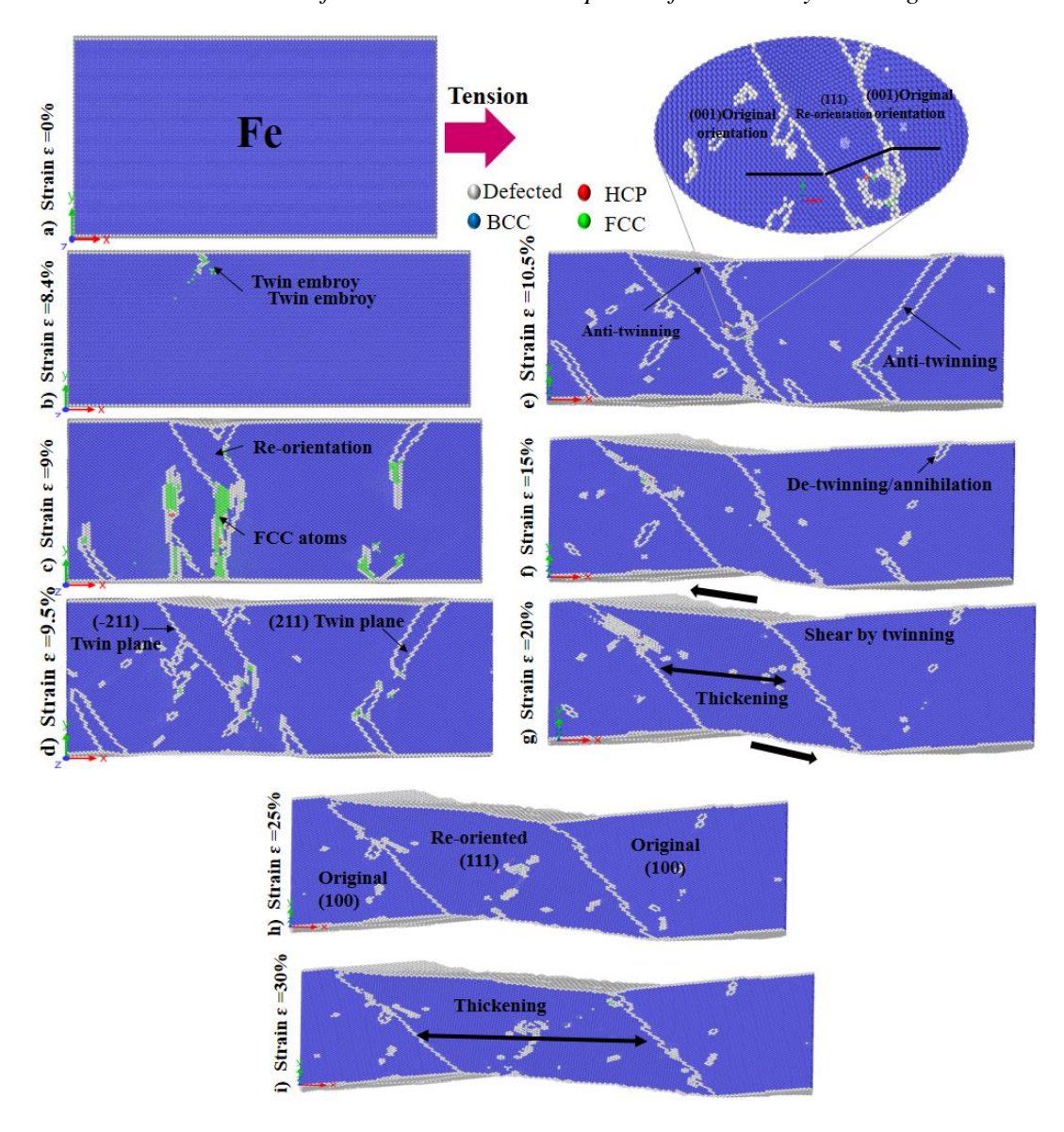
VI.2.1 Deformation mechanisms of Fe single-crystal during tension:

Fig. VI.2 illustrates the plastic deformation mechanisms of Fe single-crystal under uniaxial tension. Plasticity initiates with the formation of twin embryo or twin nuclei at the free surface after the yield point at **strain rate** ε =**8.4%**. This is followed by a phase transition, where some BCC atoms transform into an FCC structure. This transition appears to precede the reorientation of the original (100) BCC structure, which is driven by anti-twinning deformation. At strain ε =**9%**, multiple {112} twin planes nucleate, indicating that the dominant deformation mechanisms are twinning and anti-twinning during uniaxial tension of Fe.

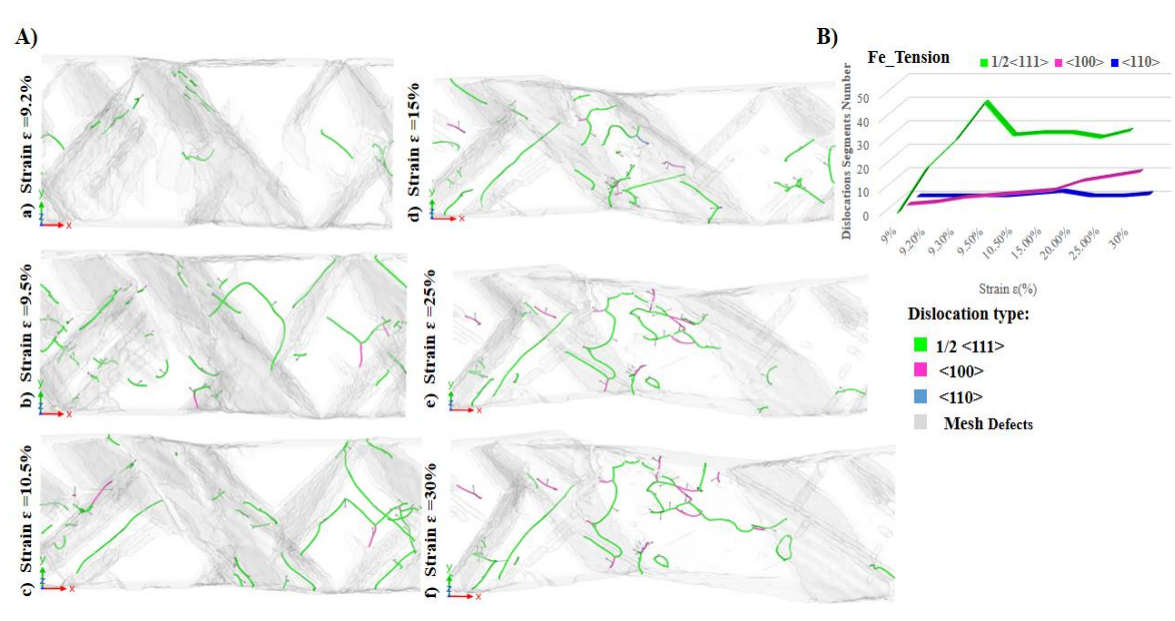
With further straining ε =9.5%, one can note that anti-twinning deformation is accompanied by slip deformation, as evidenced by the nucleation of a/2<111> dislocations at a strain of 9.2% which then propagate easily with further stretching (see Fig. VI.3). The anti-twinning mechanism along (112) and (11-2)<111> twin systems leads to the pronounced reorientation of the original BCC Fe₍₁₀₀₎ structure into Fe₍₁₁₁₎ re-oriented structure inside the twin planes (see Fig. VI.2).

At a strain rate ε =10.5%, the number of dislocation segments multiplies and extends, reaching a peak of 40 dislocation segments (see Fig.VI.3). Additionally, a<100> dislocations emerge at the intersection of a/2<111> dislocations. As the strain increases to ε =15%, twinning annihilation (or de-twinning) occurs, alongside noticeable thickening of the reoriented antitwinned region.

When $\varepsilon=20\%$, a shear by twinning can be noticed. Finally, at $\varepsilon=30\%$, the (111) re-oriented region continues to expand, and prismatic loops begin to form within the stretched Fe structure (see Fig. VI.3).



FigVI.2 Common neighbor analysis of Fe single-crystal during uniaxial tension at different strain rates (ε =8.4, 9, 9.5, 10.5, 15, 20, 25, and 30%).



FigVI.3 A) DXA snapshots of dislocation in Fe single-crystal under tension. B) Evolution of dislocation segments number along plastic regime.

VI.2.2 Deformation mechanisms of V single-crystal during tension:

The plastic deformation of V single crystal under tensile loading exhibits notable differences compared to Fe single crystal deformation. Initially, plastic deformation begins with a phase transition, where 12.5% of BCC atoms transform into FCC structure at ε =6.2% of straining (see Fig.VI.4). As strain increases to ε =8%, this phase transition becomes more pronounced, with 50% of the atoms transforming into FCC or amorphous structures. However, Fig. VI.4 confirms that this phase transition is temporary, as the number of FCC atoms decreases with further stretching.

When the strain rate is about 9%, twinning and anti-twinning nucleate and propagate, accompanied by a progressive reorientation of the crystal along successive (2-11) planes. DXA analysis at ε =9.2%, reveals the nucleation of three dislocations with Burgers vectors a/2<111>, indicating slip deformation (see Fig.VI.5). When the strain reaches 10.5%, anti-twinning deformation leads to the reorientation of the original $V_{(100)}$ BCC structure into $V_{(111)}$, as demonstrated in Fig. VI.4. Nevertheless, due to the limited number of active twin systems, the stretched V single crystal forms three distinct structural regions: Reoriented (111) region/Original (100) BCC region/Reoriented (111) region. This contrasts with the response of Fe single crystal, where deformation led to an original/reoriented/original structural pattern. Additionally, the number of dislocation segments decreases and stabilizes, indicating a different deformation behavior compared to Fe. Notably, no de-twinning was observed in the V single crystal. Up to 15% of straining, anti-twinning remains the dominant plastic deformation mechanism, alongside the extension of a few a/2<111> and <100> dislocations. At $\varepsilon=20\%$, further straining leads to the thickening of the reoriented $V_{(111)}$ BCC region, along with the nucleation of additional (211) twin planes, forming a V-shaped anti-twinning structure. By the end of deformation at $\varepsilon=30\%$, the sample exhibits twisting, indicating the relative weakness of the V single crystal. The absence of fracture may be attributed to the nonperiodic boundary conditions applied along the y and z directions.

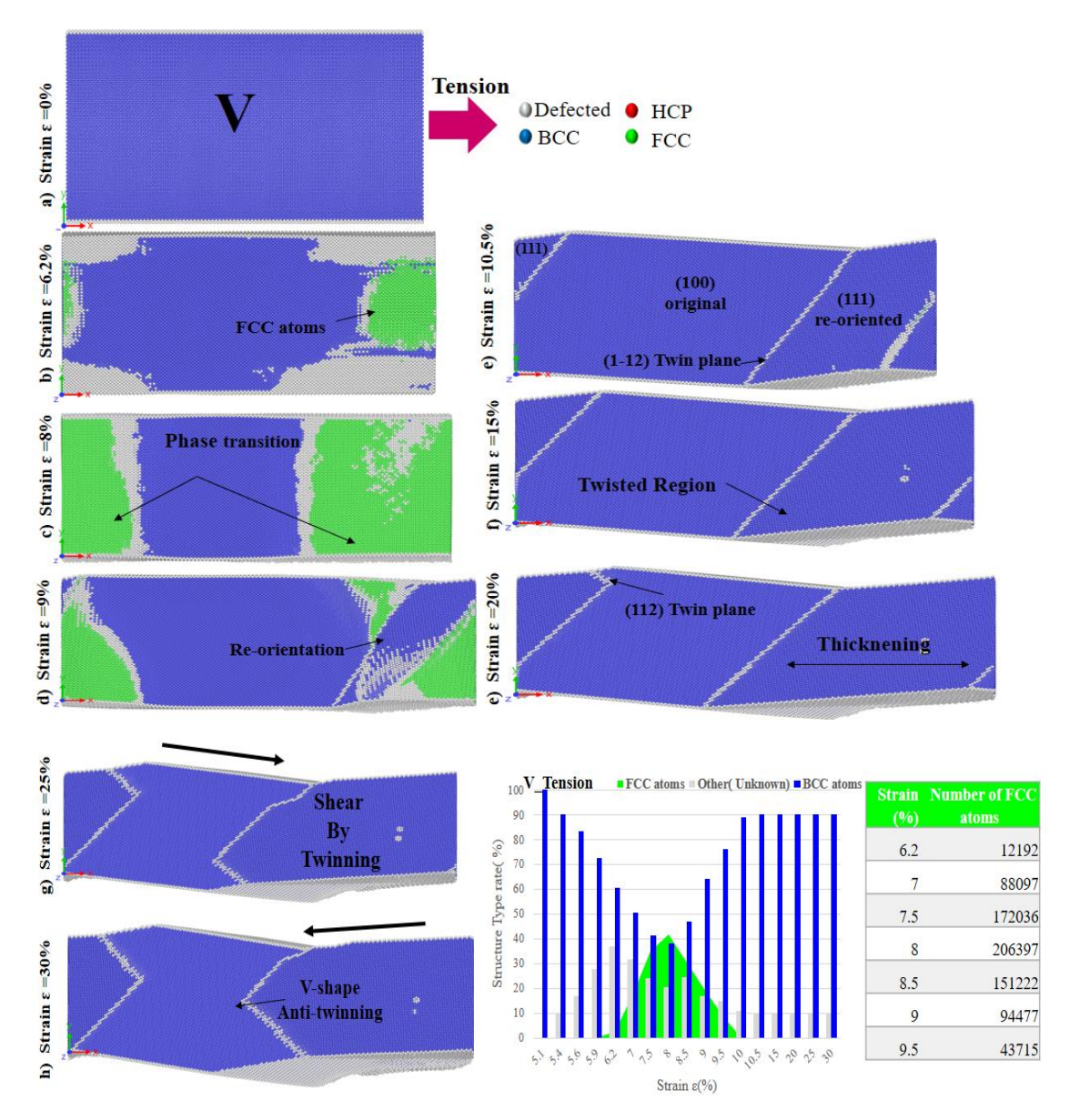


Fig VI.4 Common neighbor analysis of V single-crystal during uniaxial tension at different strain rates (ε =6.2, 8, 9, 10.5, 15, 20, 25, and 30%). Histogram of structure type rate gray color represents amorphous structure.

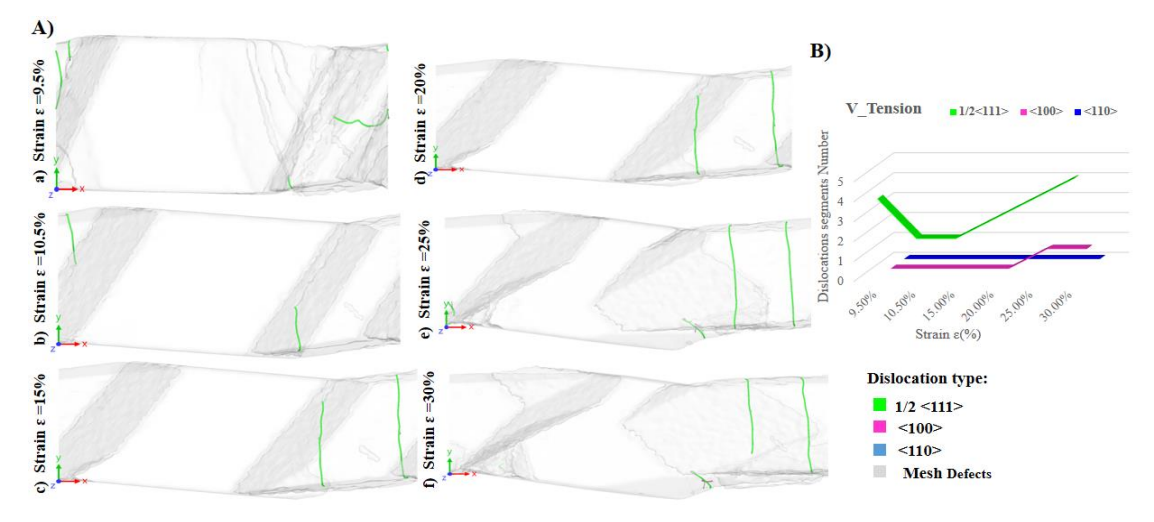
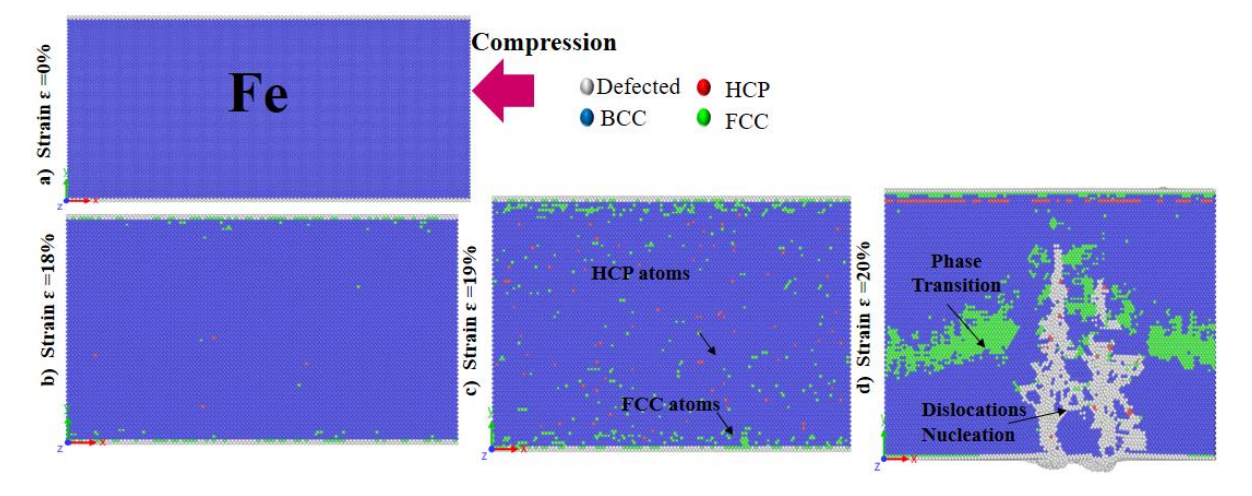


Fig VI.5 A) DXA snapshots of dislocation in V single-crystal under tension. B) Evolution of dislocation segments number along plastic regime.

VI.2.3 Deformation mechanisms of Fe single-crystal during compression:

As demonstrated by the stress-strain curve, the elastic deformation of the Fe single crystal is relatively prolonged, with a strain to yielding of **19.5%**. However, the CNA analysis reveals the presence of a small fraction of HCP (0.2%) and FCC (1.2%) atoms, corresponding to approximately 965 and 6,986 atoms, respectively, at a strain rate ε =18%. (See Fig. VI.6 and Fig.VI.7). This observation explains the pseudo-elastic regime of the Fe single crystal under compressive loading, as indicated by the non-linearity of the stress-strain curve beyond 10% of straining. This suggests that a phase transition occurs prior the onset of plastic deformation. With further compression at $\varepsilon=19\%$, the number of FCC and HCP atoms increases, though no significant defects are observed. At $\varepsilon=20\%$, when the yielding of the stress curve occurs, permanent plastic deformation initiates, primarily through slip deformation. At this stage, the nucleation of dislocations with Burgers vectors a/2<111> and a<110> from the free surface can be observed, along with an increase in phase transition activity. Specifically, 5.7% of BCC atoms transform into FCC (approximately 33304 atoms), while 1848 atoms adopt an HCP structure. However, with continued straining, the ratio of FCC-transformed atoms decreases and the phase transition effect diminishes. The histogram of structural types in Fig.VI.6 illustrates the variation in phase transition activity during plastic deformation of the Fe single crystal. At $\varepsilon=23\%$, the number of dislocation segments increases significantly, with approximately 400 dislocation segments with Burgers vectors a/2<111> and over 100 segments with Burgers vectors a<100>, indicating that dislocation slip is the dominant plastic deformation mechanism in the compression of Fe single crystals (see Fig.VI.7.B). When the strain reaches 25%, reoriented regions emerge, suggesting that slip deformation is accompanied by twinning and anti-twinning mechanisms. At the final deformation stage $\varepsilon=30\%$, the number of dislocations increases intensely. Additionally, highly localized shear stress at the center of the sample leads to pronounced buckling. This suggests that during uniaxial compression, slip deformation is the dominant plastic deformation mechanism, followed by anti-twinning.



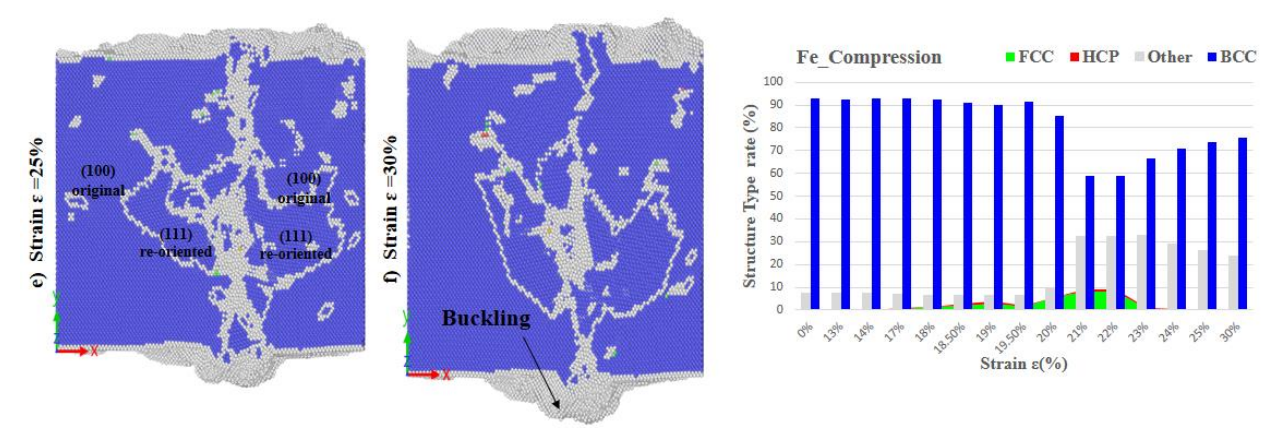


Fig VI.6 Common neighbor analysis of Fe single-crystal during uniaxial compression at different strain rates (ε =18, 19, 20, 25, and 30%). Histogram of structure type rate gray color represents amorphous structure.

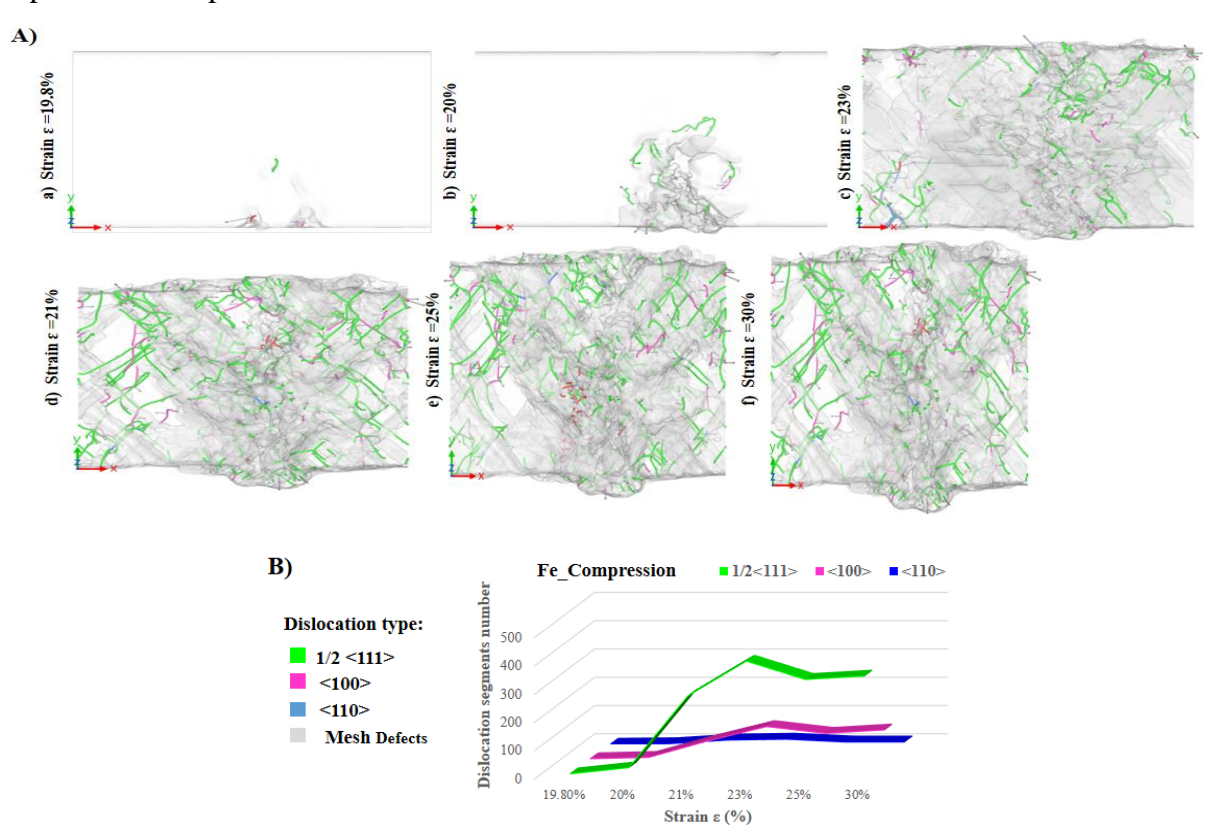


Fig VI.7 A) DXA snapshots of dislocation in Fe single-crystal under compression. B) Evolution of dislocation segments number along plastic regime.

VI.2.4 Deformation mechanisms of V single-crystal during compression:

The plastic deformation of V single crystal initiates through the nucleation of twin boundaries along the (101) and (10-1) planes from the free surface, accompanied by phase transition, where some BCC atoms transform into FCC atoms. This transformation contributes to the pseudo-elastic behavior observed prior the yield point at ε =4.3%(see Fig.VI.1). At ε =5.5%, the nucleation of dislocations with Burgers vectors a/2<111> and a<100> becomes evident, marking plastic deformation by slip. With further compression ε =10%, plastic

deformation evolves as a combination of anti-twinning (characterized by the re-orientation of the $V_{(100)}$ into $V_{(111)}$, phase transition, and slip deformation (refer to Fig.VI.8).

With more compression $\varepsilon=15\%$, the number of dislocations increases significantly (see Fig. VI.9); however, their total count remains lower than that observed in the compressed Fe single crystal. Additionally, the increasing presence of HCP and FCC atoms confirms that phase transition is an integral part of the plastic deformation mechanism, rather than merely a precursor to anti-twinning deformation, as observed during tensile loading. Beyond **20%** of straining, anti-twinning deformation becomes more pronounced, as evidenced by the progressive re-orientation of the crystal structure (see Fig.VI.8).

Finally, at the end of straining $\varepsilon=30\%$, a shear band and buckling appear, resulting from highly localized stress due to dislocation accumulation and their interactions.

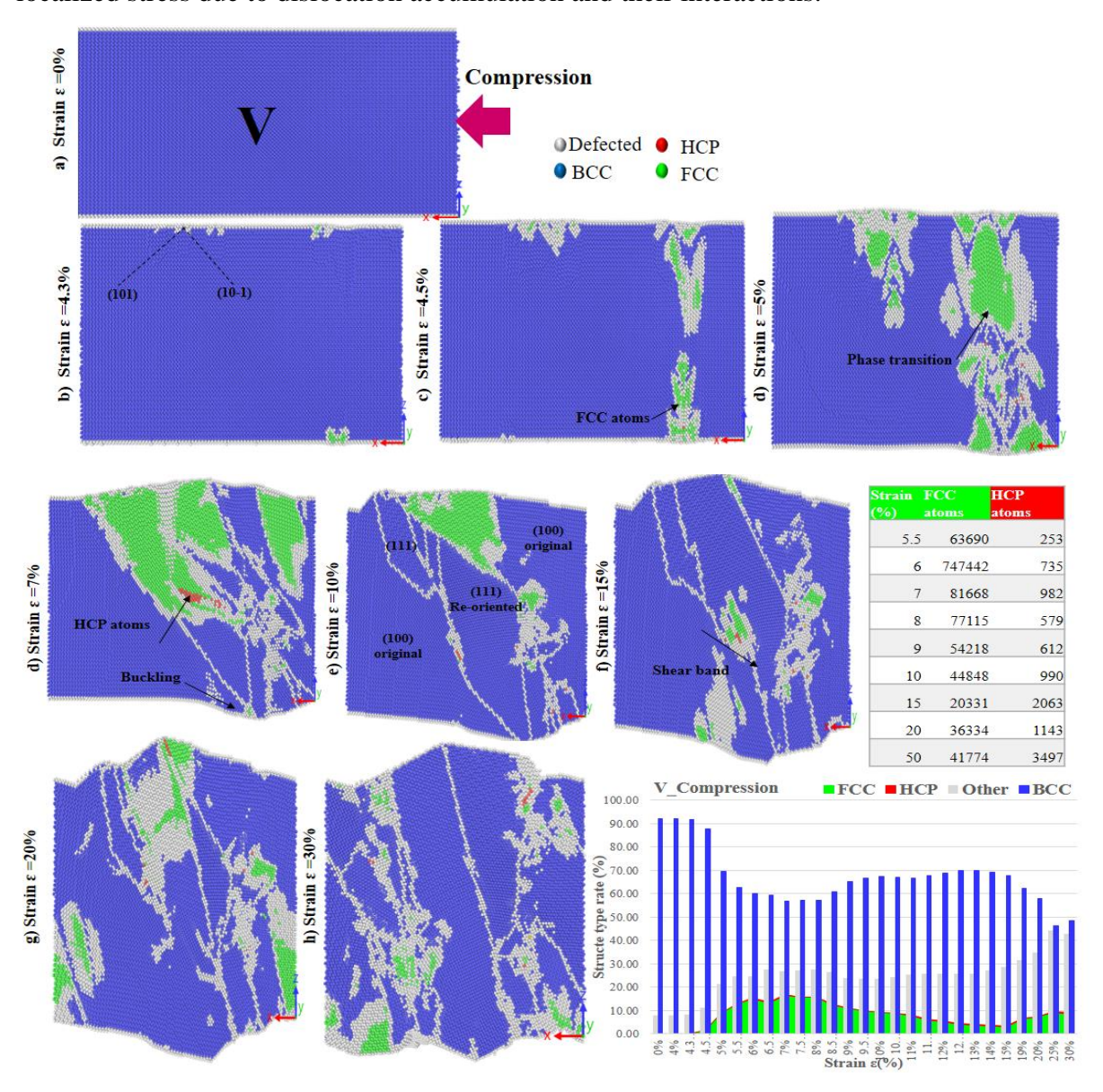


Fig VI.8 Common neighbor analysis of V single-crystal during uniaxial Compression at different strain rates (ε =18, 19, 20, 25, 30%). Histogram of structure type rate gray color represents amorphous structure.

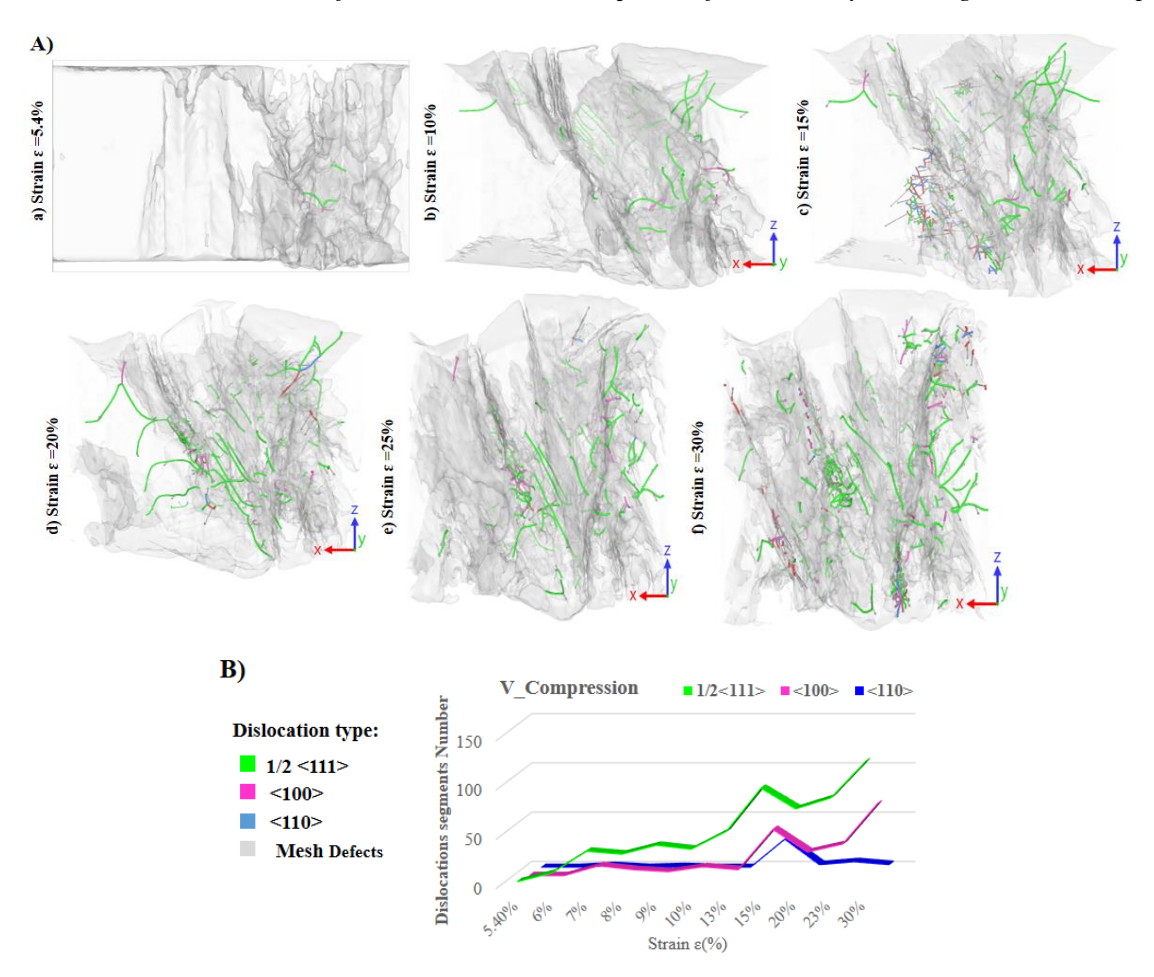


Fig VI.9 A) DXA snapshots of dislocation in V single-crystal under compression. B) Evolution of dislocation segments number along plastic regime.

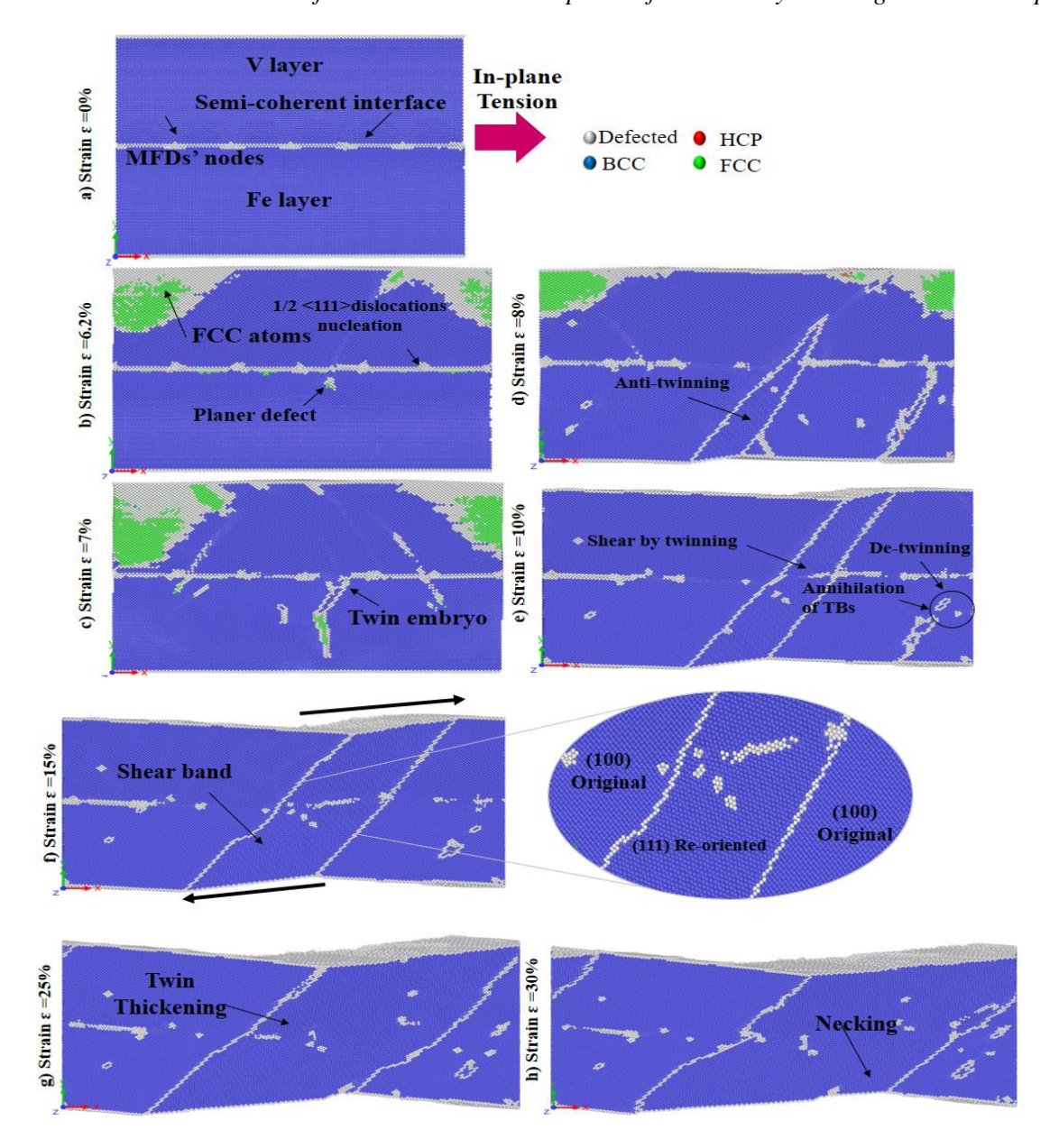
VI.3 The mechanical response of V/Fe during tension and compression: VI.3.1 Deformation mechanisms of V/Fe bi-layer during uniaxial tension:

To analyze the plastic deformation of the V/Fe bi-layer (with a semi-coherent interface) under in-plane uniaxial tension, we utilized common neighbor analysis (**CNA**) and dislocation analysis (**DXA**) as implemented in Ovito software. The results are presented in Fig. VI.10 and Fig. VI.11, providing a detailed examination of the plastic deformation mechanisms. From 0% to ε =6.2%, the V/Fe bi-layer deforms elastically, producing a linear stress-strain response. During this stage, no detectable defects appear in both V and Fe layers or even at the interface, indicating the stability of the misfit dislocation (MFD) network, despite the pre-existing of higher localized stresses at the interface. When the yield point occurs at ε =6.2% (Fig.VI.1, point A), plastic deformation initiates simultaneously in both V and Fe layers as well as along the interface. At this point: Tensile stress induces a phase transition in the V layer, with 2.8% of BCC atoms (20,589 atoms) transforming into FCC. The MFD network begins to decompose, initiating the nucleation and propagation of dislocations with Burgers vectors a/2<111>, originating from the interface and extending inside the V layer (see Fig.VI.11). In the meanwhile, planar defects start to form within the Fe layer. At strain rate ε =7%, lattice distortion becomes more pronounced, originating from the MFD at the interface and extending

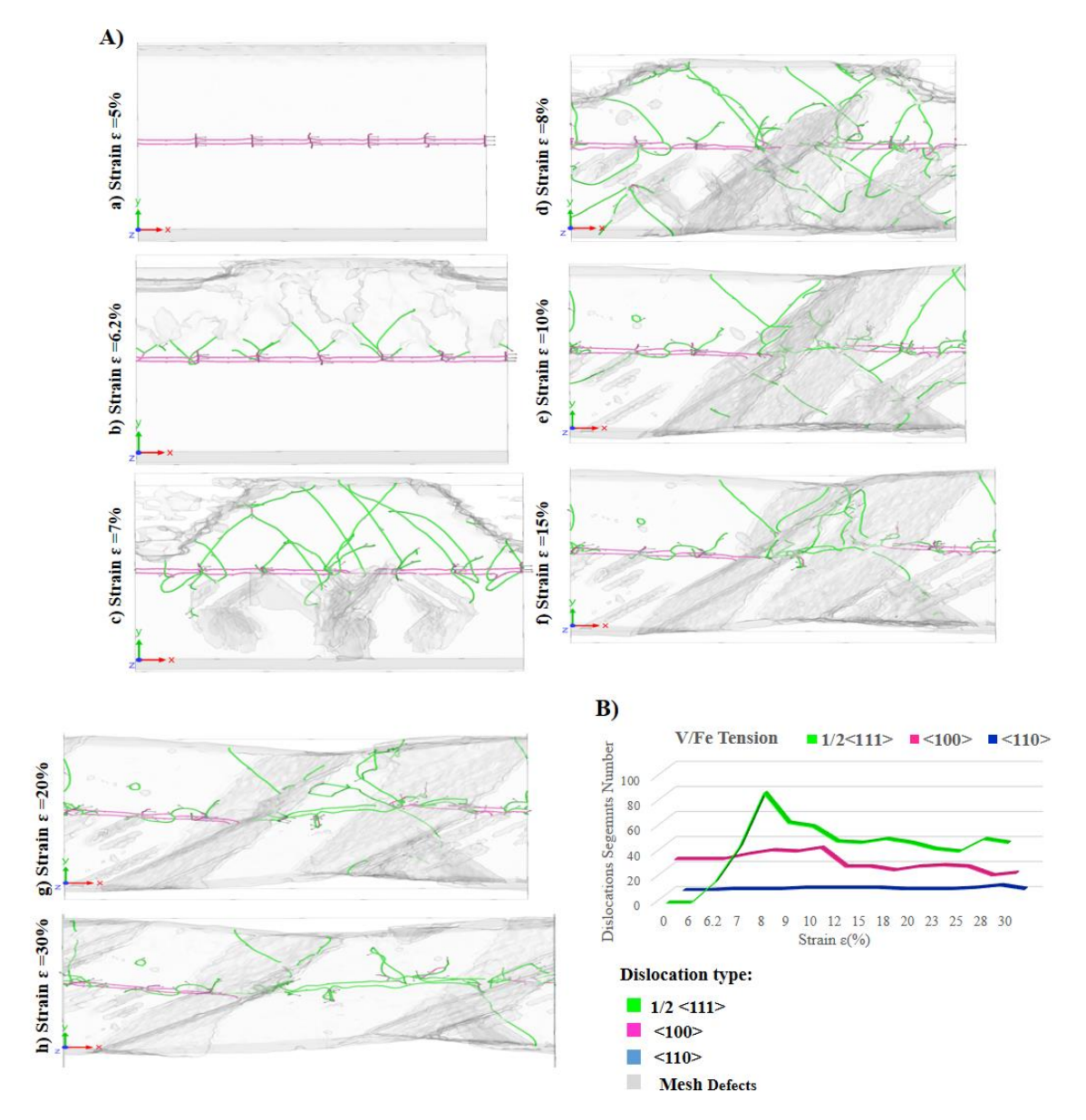
into the Fe layer, which suggests the formation of twin embryo s at the interface, alongside the propagation of dislocations into the Fe layer (refer to Fig. VI.10). At $\varepsilon=8$ %((Fig.VI.10d), the twin boundary (TB) in the Fe layer expands along the preferred {112}<111> twin systems, leading to a significant reorientation of the original (100) BCC structure into (111) BCC between twin boundaries. This indicates that anti-twinning is the dominant deformation mechanism in the Fe layer, similar to what was observed during the tensile deformation of Fe single crystals. Conversely, in the V layer, plastic deformation is primarily governed by dislocation slip, characterized by the emission and propagation of additional dislocations from the interface.

With further straining $\varepsilon=10\%$, the phase transition in the V layer ends (see Fig. VI.13). Instead, anti-twinning deformation emerges in the successive {112} planes in both the V and Fe layers, further facilitating the reorientation of (100) BCC structure into (111) BCC between twin boundaries. Additionally, some twin boundaries undergo annihilation, or de-twinning that is observed in the Fe layer. When the strain is $\varepsilon=15\%$, shear deformation by twinning becomes evident throughout the V/Fe bilayer, indicating that plastic deformation is primarily accommodated by a combination of slip and anti-twinning mechanisms. At this stage: The number of a/2 <111> dislocations significantly increases, particularly inside the V layer. While Anti-twinning is seen as the dominant deformation mode in the Fe layer. This analysis highlights that plastic deformation in the V/Fe bilayer is primarily facilitated by dislocation slip in the V layer and anti-twinning in Fe layer, with contributions from phase transitions and twin boundary evolution. With more stretching $\varepsilon=25\%$, the number of dislocation segments develops regularly throughout the entire system (see Fig.VI.11.B). Additionally, a significant thickening of the twinned (re-oriented) shear band is observed, driven by continued antitwinning activity. As the applied stress continues to rise, the material undergoes plastic flow, characterized by a stable increase in stress values (flow stress).

At the end of tensile loading ε =30%, necking begins to form in the region where multiple dislocations and anti-twins are concentrated. Furthermore, the total dislocation length within the specimen at this strain reaches 2105.38Å, compared to 411.255 Å for V single crystal indicating substantial dislocation multiplication and strain accumulation, at a strain rate of 8%. These observations suggest that the plastic deformation of V/Fe bilayer is accompanied by strain hardening, leading to higher mechanical strength compared to the V single crystal.



FigVI.10 Common neighbor analysis of V/Fe bi-layer system during in-plane uniaxial tension at different strain rates (ε =6.2, 7, 8, 10, 15, 25, and 30%).



FigVI.11 A) DXA snapshots of dislocation in V/Fe bi-layer under tension. B) Evolution of dislocation segments number along plastic regime.

VI.3.2 Deformation mechanisms of V/Fe bi-layer during uniaxial compression:

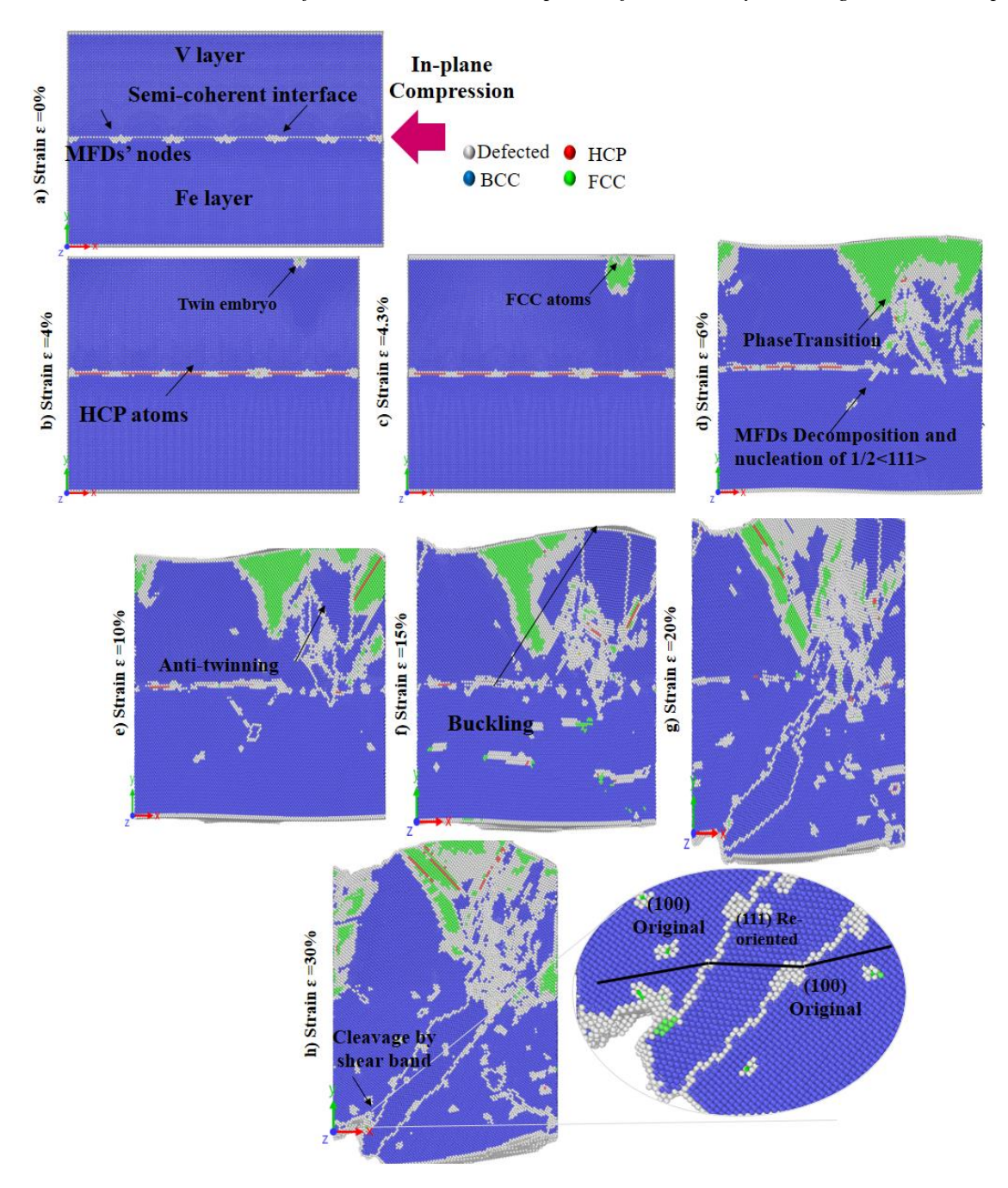
During in-plane uniaxial compression, the V/Fe bi-layer exhibits a shorter elastic deformation regime compared to tensile loading. At **a strain rate** ε = **4%**, the plastic deformation initiates in the V layer with the nucleation of twin planes from the free surface, corresponding to the first yield point (A') in the stress-strain curve. Nevertheless, the presence of HCP atoms surrounding the misfit dislocation (MFD) lines suggests that a pseudo-elastic regime is present before the first apparent yielding as seen in the stress curve (Fig.VI.1). With further compression, the plastic deformation of V layer is initially governed by phase transition, where 5% of BCC atoms transform into FCC structure at ε = **4.3%**. (See Fig.VI.12), while the Fe layer continues to deform elastically.

At the second yield point (B) $\varepsilon \approx 6\%$, dislocations with Burgers vectors a/2<111> nucleate from the interface inside the Fe layer. These dislocations originate from the decomposition of misfit dislocations at interface, which serves as a source of dislocation generation. Simultaneously, the phase transition in the V layer intensifies, with 7.5% of BCC atoms transforming into FCC (see Fig.VI.13).

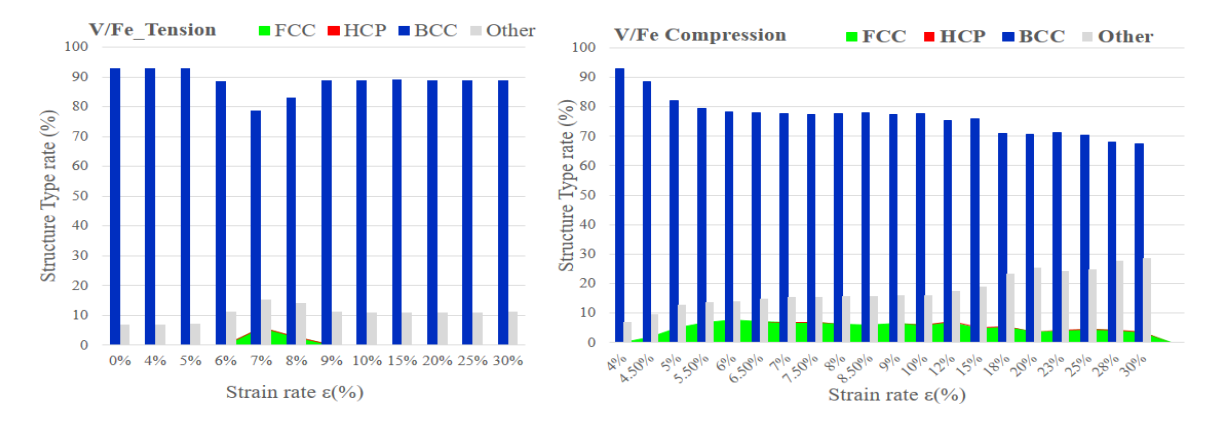
Subsequently, at a strain ε = 10% the plastic deformation of the Fe layer is predominantly governed by slip deformation, as indicated by the propagation and interaction of approximately 100 dislocation segments with Burgers vectors a/2<111>. Meanwhile, in the V layer, the phase transition continues (5.9% of FCC and 0.3% of HCP atoms are detected), along with limited dislocation activity and anti-twinning deformation. Fig.VI.13 confirms that, as in compression of the V single crystal, the phase transition remains present throughout plastic deformation but at a lower fraction. Besides the extension of few dislocation, and anti-twin. At higher strain levels (ε = 20% until 25%), the plastic deformation of the V layer evolves into anti-twinning along preferred {110} and {112}<111> twin systems, while few dislocations pile up from the interface into the V layer. In contrast, the plastic deformation of the Fe layer is mainly dominated by slip, with the emission and propagation of over 200 dislocation segments, resulting in a total dislocation length of 7735.8 Å.

Notably, the original BCC $Fe_{(100)}$ layer undergoes re-orientation into $Fe_{(111)}$, indicating the formation of anti-twinning. This combination of anti-twinning in V and Fe layers leads to the formation of a shear band. Eventually, massive dislocation emission and propagation across the entire system ends in cleavage formation at a strain $\varepsilon = 25\%$.

At the final stage of compression $\varepsilon = 30\%$, the total dislocation length (L_{disl}) reaches 9,375.24Å, which is significantly higher than that observed during tensile loading (2,105.38 Å for the V/Fe bilayer system).



FigVI.12 Common neighbor analysis (CN) of V/Fe bi-layer during in-plane uniaxial compression at different strain rates (ε =4, 4.3, 5.9,7, 10, 15, 20, 30%).



FigVI.13 Histogram of structure type rate during the tensile and compressive loadings showing the ratio of phase transition during deformation of V/Fe bi-layer.

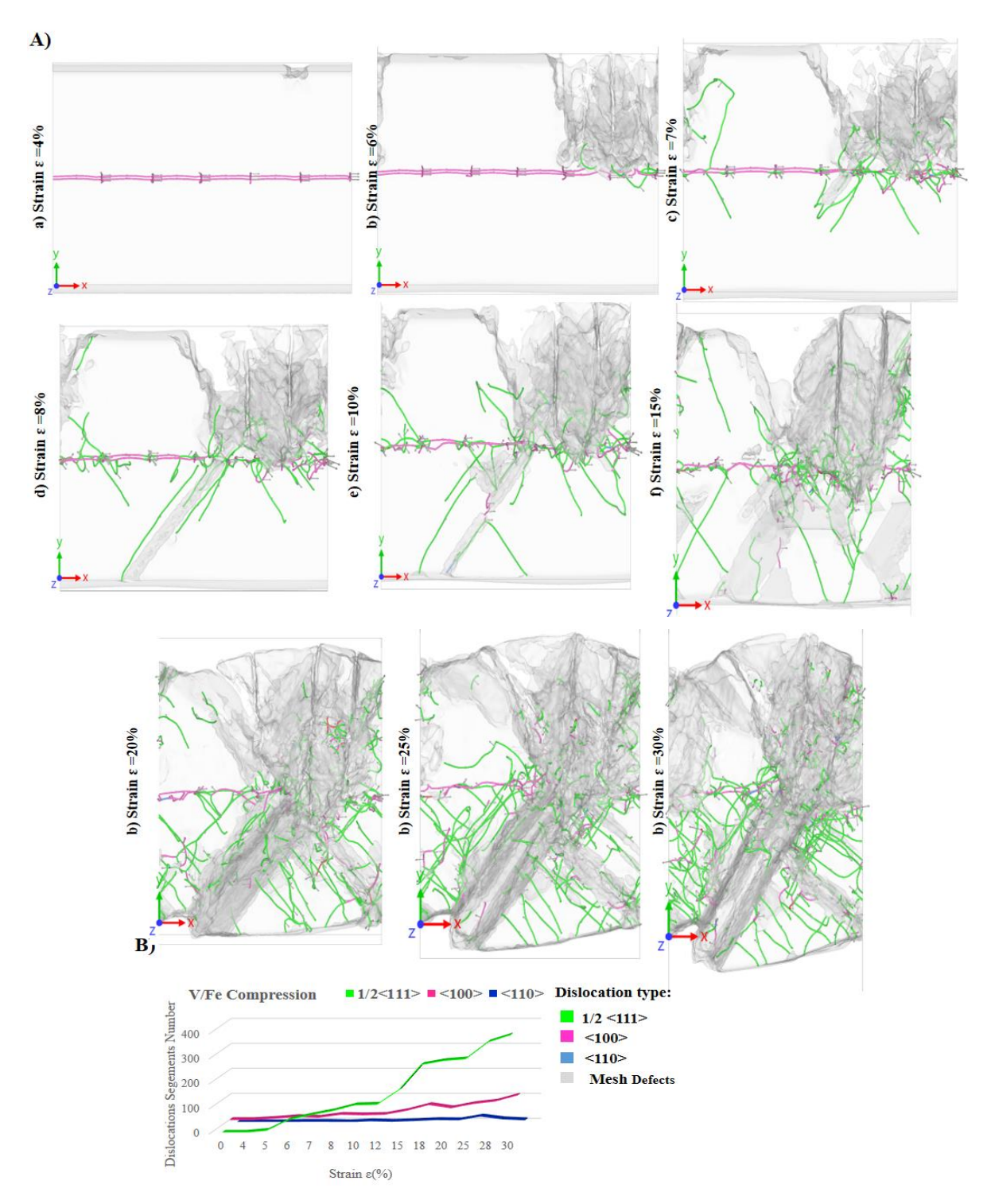


Fig VI.14 A) DXA snapshots of dislocation in V/Fe bi-layer under compression. B) Evolution of dislocation segments number along plastic regime.

VI.3.3 Deformation mechanisms of interface during in-plane tension and compression:

The permanent deformation of the V/Fe semi-coherent interface initiates through the decomposition of <100> misfit dislocations (MFDs) into 1/2<111> shear loops. However, a unique asymmetry of this response is observed:

- During tensile loading, MFD tend to decompose preferentially inside the V layer.
- During compressive loading, they decompose more easily inside the Fe layer.

This asymmetry arises due to the initial stress distribution at the interface before loading.

As a result of lattice mismatch accommodation, the V interfacial atoms experience compressive stress, while the Fe interfacial atoms are subjected to tensile stress (see Chapter III). This mismatch leads to a localized stress concentration within the MFD network.

When uniaxial in-plane tension is applied to the V/Fe bilayer, localized shear strain accumulates in the V interfacial atoms, particularly along the MFD lines. In contrast, under compressive loading, shear strain is generated in the Fe interfacial atoms. This behavior is schematically illustrated in Fig.VI.15, which depicts the plastic deformation mechanisms of the V/Fe interface under both tension and compression.

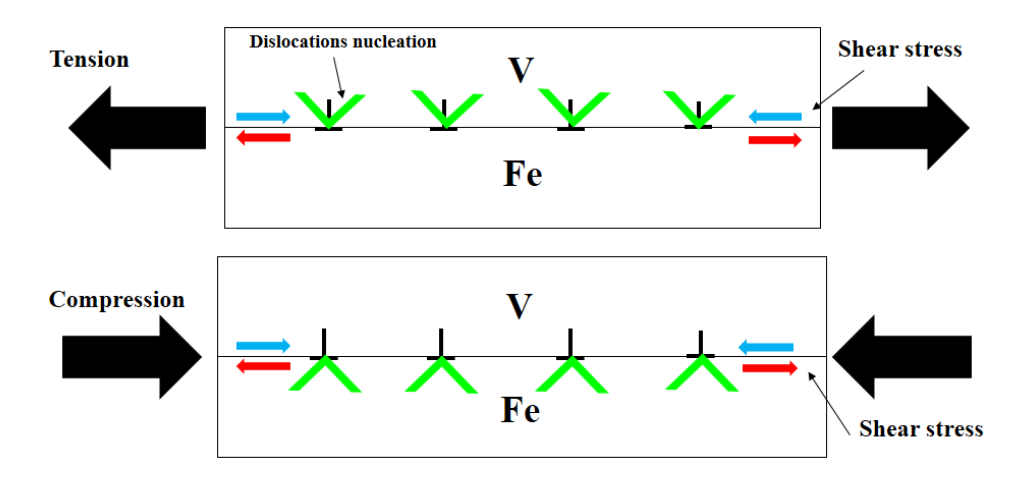
From Fig.VI.16, it is evident that the magnitude of localized shear strain at the interface differs depending on the loading mode:

- During tensile loading, higher shear strain is observed within the V layer.
- During compressive loading, higher shear strain is concentrated within the Fe layer.

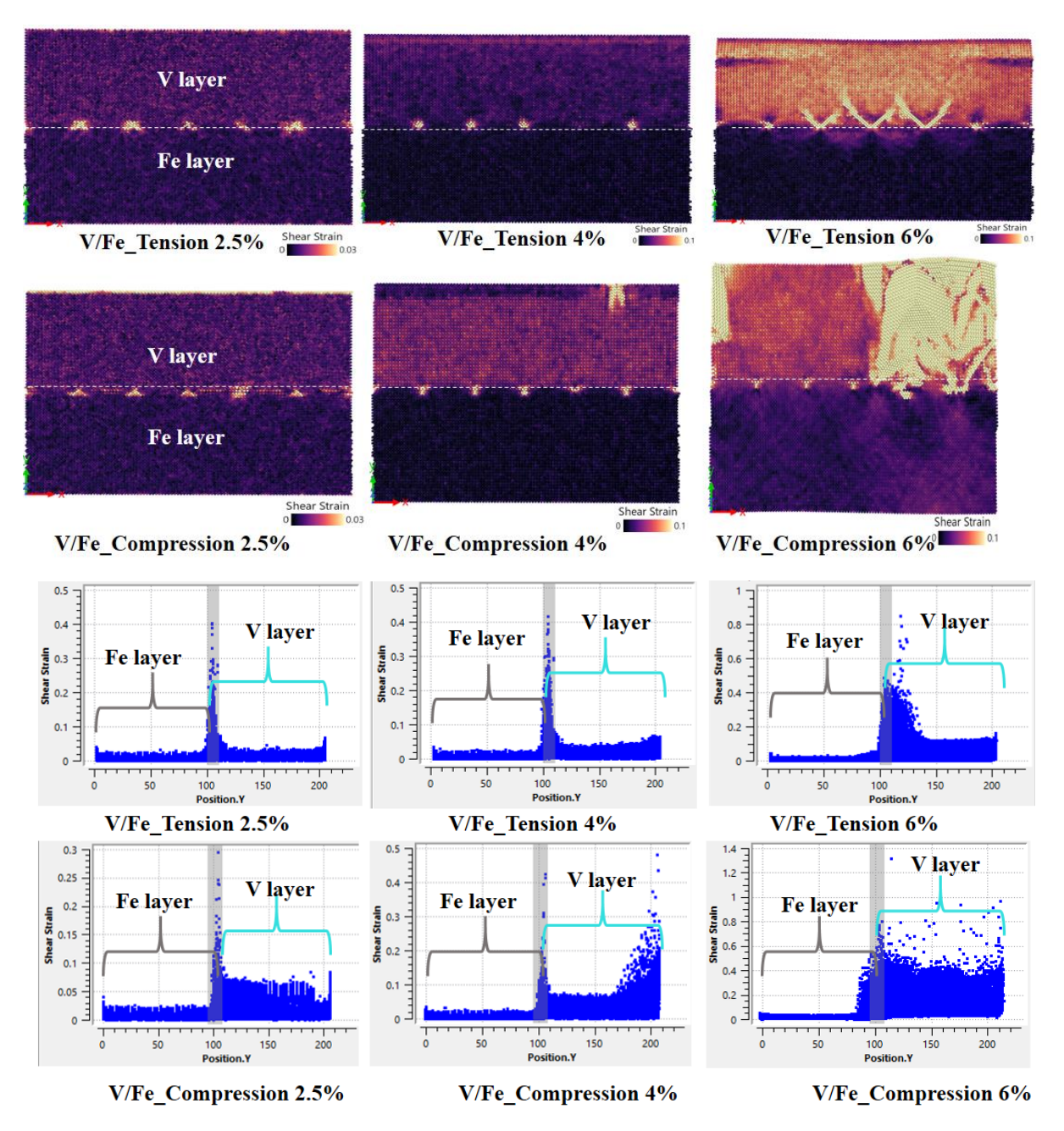
This trend is regular across different strain rates, including the A, A', and B yield points identified in Fig.VI.1. Additionally, the localized shear strain increases progressively with increasing applied stress.

This observation helps to explain the dissimilar behavior of misfit dislocation propagation. I.e. in tension, MFD preferentially decompose and propagate inside the V layer. Whereas, in compression, MFD dissociate and propagate more easily into the Fe layer.

At the end, it is clear that the plastic deformation of the semi-coherent interface is highly dependent on the loading direction. So that, the presence of semi-coherent interface contributes to the strain hardening in the V/Fe bilayer, with a more pronounced effect in tension. Furthermore, the interface serves as a primary source for dislocation nucleation, significantly influences the overall mechanical response of the system.



FigVI.15 Schematic illustration of the creation of shear strain induced by MFD's decomposition during the plastic response of V/Fe bi-layer.



FigVI.16 Atomistic shear strain in V/Fe during uniaxial in-plane Tension and compression before and along the initiation of plastic deformation (Strain rates ε =2.5, 4, and 6%).

VI.4 Discussion:

VI.4.1 Anisotropic plasticity of V and Fe single-crystals:

Twinning deformation in body-centered cubic (BCC) crystals involves distinct mechanisms under uniaxial tension and compression. Previous studies [139-150] have significantly contributed to the understanding of twinning-induced plasticity in BCC metals, providing insights into the fundamental mechanisms governing their deformation behavior.

In the present study, iron (Fe) and vanadium (V) exhibit distinct mechanical responses under tensile and compressive loading due to their anisotropic plasticity and slip system characteristics:

In tension, BCC Fe demonstrates higher yield strength and significant strain hardening, compared to V with plastic deformation primarily governed by anti-twinning, de-twinning, and slip deformation at advanced loading, leading to shear band formation and twin thickening. BCC V, in contrast, exhibits lower yield strength and minor strain hardening. Its deformation is mainly dominated by anti-twinning, accompanied by phase transitions and limited slip deformation, ultimately resulting in a twisted sample. However, under compression, both Fe and V deform predominantly by slip, contributing to their higher strength. This behavior aligns with prior studies, which have shown that BCC Fe and V exhibit anisotropic plasticity due to their loading-direction dependence (tension vs. compression).

Sainath et al. [139] demonstrated the opposite tension-compression asymmetry in BCC Fe, concluding that Fe nanowires with an initial (100) orientation deform predominantly by twinning on the {112}<111> twin system under tensile loading, whereas dislocation slip is the primary deformation mechanism under compression. Similarly, Healy et al. [145] observed that BCC Fe micro-pillars deform primarily by slip under compressive loading. The sequence of twinning, anti-twinning/de-anti-twinning, and slip deformation during uniaxial tension has also been reported in BCC tungsten (W) and tantalum (Ta) through both experiments and simulations.

Moreover, Wang et al. [140] used in situ transmission electron microscopy (TEM) to study W nanowires under <110> tension and observed the nucleation and growth of anti-twins. This anti-twinning process involved a 1/3<111> shear displacement on the successive {112} planes, in contrast to ordinary twinning, which exhibited an opposite 1/6<111> shear displacement. Their molecular dynamics (MD) simulations further confirmed that anti-twinning during tensile stress is followed by de–anti-twinning, leading to anti-twin shrinkage due to stress relaxation and dislocation formation. Zhong et al. [148] reported that deformation twinning in BCC Ta nano-crystals proceeds via reluctant twin growth. Using in situ TEM observations, they revealed a dynamic growth-controlled twinning mechanism, characterized by Moiré fringes resulting from inclined twin boundaries. After deformation, the nano-crystal experienced twinning-induced reorientation, while a competition between twin growth and dislocation plasticity was observed in smaller-diameter Ta single crystals.

Li et al. [147] investigated twinning dynamics in nano-scale BCC tungsten and observed the formation of six-layer twin embryos and three-layer discrete twin thickening. They proposed that "zonal dislocation" mechanisms primarily control twinning dynamics in BCC metals. In another study [141], Li et al. used MD simulations to demonstrate that certain BCC nanowires (Mo, W, and Fe) exhibit super-elasticity via a reversible twinning mechanism under uniaxial tension. They found that twinning/de-twinning in the {112}<111> system enables reversible

strain, whereas the slip mechanism involving full dislocations leads to permanent plastic deformation, particularly in BCC vanadium.

On the other hand, experimental studies on commercially pure BCC V by Lindley et al. [149] found that V deforms plastically by dislocation slip during tensile loading. However, at T=20K, twinning deformation was observed, which aligns with our results. Additionally, tensioncompression asymmetry has been attributed to the competition between twinning and antitwinning, as demonstrated by uniaxial tension and compression experiments on [001] and [011] oriented molybdenum nano-pillars [150]. According to their findings: The (100) orientation exhibits a negative Schmid factor (v) for the $(\overline{112})[1\overline{11}]$ twinning system, leading to higher compressive strength compared to tensile strength. Conversely, this orientation has a positive (v) for the $(2\overline{11})[\overline{11}1]$ anti-twinning system, resulting in higher tensile strength compared to compressive strength in the (110) orientation. As a result, compressive flow stresses are higher than tensile flow stresses in the [001] orientation, while the reverse is observed in the [011] orientation. The phase transition observed during tension loading of V single crystals in this study occurred just before crystal reorientation due to anti-twinning deformation. Pan et al. [146] also reported that deformation twinning and stress-induced phase transitions are the dominant mechanisms in nano-crystalline Ta, based on their MD simulations. Similar to our findings, stress-induced BCC-to-FCC and BCC-to-HCP phase transitions were also observed during the plastic deformation of V single crystals under compression.

The findings of the present study, combined with previous experimental and computational work, highlight the complex deformation mechanisms in BCC metals, particularly the combination between twinning, anti-twinning, slip, and phase transitions. The tension-compression asymmetry observed in Fe and V further reinforces the significance of loading-direction-dependent plasticity in BCC systems, which is critical for understanding their mechanical performance under extreme conditions.

VI.4.2 Tension/compression asymmetry of V/Fe Bi-layer:

Our results reveal that the Young's modulus, yield stress, strain to yielding, and flow stress of the V/Fe system are significantly influenced by the loading direction. This indicates a pronounced asymmetry in the mechanical response of the V/Fe bilayer under in-plane uniaxial tension and compression.

During tensile loading, a single yield point is observed, suggesting that plastic deformation initiates simultaneously in both V and Fe layers, as well as at interface. In contrast, the stress-strain curve of V/Fe during compression exhibits two distinct yield points. The first yield point corresponds to the plastic deformation of the softer V layer, while the second yield point is associated with the decomposition of misfit dislocations (MFDs) and their propagation inside

Fe layer. Notably, V layer remains the softer phase under both tensile and compressive loadings.

To further interpret the yielding points in both tension and compression, it is recommended to correlate each point on the stress-strain curves with the corresponding atomic snapshots at the same depths in the above-shown figures.

A strong anisotropic plasticity is evident in both Fe and V layers within the V/Fe bilayer system. Under tensile loading, the Fe layer primarily undergoes anti-twinning deformation, whereas in compression, its deformation is predominantly governed by slip mechanisms. Conversely, in the V layer, plastic deformation during tension is mainly characterized by slip and phase transition, whereas under compression, phase transition and anti-twinning become dominant deformation modes. Consequently, a significant competition between twinning and full-slip mechanisms is observed in both V and Fe layers during tension and compression. This anisotropic plastic response, influenced by the loading direction, has previously been reported in V and Fe single-crystals.

Tensile loading

Mi et al. [54] have investigated the atomic structure, tensile properties, and dislocation behavior of $Fe_{(110)}/W_{(110)}$ interface using molecular dynamics (MD) simulations. They observed the nucleation of dislocation loops from the interface into the softer Fe layer. Furthermore, the semi-coherent $BCC_{(110)}/BCC_{(110)}$ interface exhibited a noticeable strengthening effect during tensile loading.

Similarly, in the Ni/Cu bilayer system with a semi-coherent interface, dislocations preferentially nucleated in the Cu layer during tensile loading. Dislocations with Burgers vector parallel to the tensile direction moved more easily, leading to strengthening effect in the bilayer compared to single-crystal Cu [151]. Wei et al. [158] demonstrated that the presence of an interface in the W/W₃₀Cu₃₀ BCC bilayer system contributed to strengthening during in-plane tensile loading. Dislocation propagation occurred most readily in the softer W₃₀Cu₃₀ solution phase. In Cu/Ag multilayers with a cube-on-cube orientation, most dislocations were first observed nucleating in the Ag layer during uniaxial tension. This is attributed to Ag's lower stacking fault energy relative to Cu [154]. Correspondingly, in the Cu/Ta bilayer system, dislocations initially nucleated in the softer Cu layer. However, at higher strain rates, dislocation emission into the Ta layer became more pronounced [159].

Compressive loading

In despite that dislocation tend to nucleate in the softer layer under both tensile and compressive loading; it is more common to observe two distinct yielding points in the compressive stress-strain response of metallic multilayers. In our research, the mechanical behavior of the V/Fe bilayer during in-plane compression follows a similar trend which have

observed in Fe/Al bilayers under compressive loading [155]. Initially, dislocation nucleation occurs in the bulk of the weaker metal, Al, leading to the first yielding event. The second vielding event in the stress-strain curve corresponds to dislocations nucleating within the Fe region, originating from the incoherent interface. A similar two-yield points behavior has been reported in other metallic multilayers. For instance: Pang et al. [152] have observed that the first yielding point in Cu/Ni bilayers corresponds to plastic deformation in the softer Cu layer, while the second turning point marks the onset of plasticity in the harder layer Ni. The stressstrain curves of Cu/Al during compression [153], also displayed two distinct yield points across all strain rate loadings. After the elastic deformation phase, the perfect misfit dislocation at the interface dissociated into Shockley partial dislocations and stair-rod dislocations. While the stair-rod dislocations remain stationary at their initial positions, the Shockley partial dislocations rapidly migrate into the Al layer and accumulate at the opposite interface. This compressive response trend of bi-layers has also been reported in other study [156]. Interestingly, Schwarz et al. [56] observed that, during the compression of an Al/Ni bimetal, the majority of dislocations formed inside the Ni layer rather than in Al. They attributed this phenomenon to the orientation of the grain boundaries in Ni, which were not perpendicular to the compression direction. This misalignment led to shear deformation of the grain boundaries (i.e., the interface). Moreover, the grain boundaries themselves exhibited plastic deformation, characterized by an increase in structural ordering within the boundary region.

Phase transition

In addition, phase transitions commonly occur as part of the plastic deformation mechanisms of metallic multilayers. For instance, in Cu/Zr multilayers, the Zr layer; initially in the HCP structure; completely transforms into the BCC structure under out-of-plane compression, while the Cu layer undergoes plastic deformation primarily by slip. However, this phase transition in Zr from HCP to BCC is significantly suppressed at higher simulation temperatures (600K) [157]. Similarly, in Ti/N-Ti bilayers, HCP atoms in the Ti layer transform into the BCC structure under in-plane compression [137].

Decomposition of Misfit dislocation under tension/compression

Understanding the evolution of plastic deformation along the semi-coherent interface during tension and compression is crucial. Interestingly, a tension-compression asymmetry is also observed at the semi-coherent interface of the studied V/Fe bilayer. This is attributed to the creation of shear strain at the interface, which is more pronounced in V interfacial atoms during tension, whereas under compression, the shear strain becomes more dominant in the Fe interfacial atoms.

This load-direction-dependent behavior aligns well with previous findings. It is well established that in metallic multilayers with semi-coherent or incoherent interfaces, plastic deformation under tensile loading initiates first in the softer layer. In such cases, dislocations or defects originate from the interface, which serves as a nucleation site for dislocations. Several studies support this phenomenon:

Chen et al. [53], have revealed that the dynamic evolution of misfit dislocation patterns at semi-coherent interfaces plays a crucial role in determining preferred dislocation nucleation sites and the shear sliding mechanism. They found that under biaxial in-plane tension, the misfit dislocation network remained largely unchanged. However, during uniaxial in-plane compression, the initial misfit dislocation patterns around the nodes became distorted and spread dissimilarly within the interface, as observed in Cu/Ni and Cu/Ag bimetals.

Additionally, our findings are in agreement with the work of Shao et al. [50], who reported that under biaxial tension, three Shockley partial dislocations with Burgers vectors pointing outward from each node were simultaneously emitted into the Cu layer. In contrast, under biaxial compression, three Shockley partials were emitted into the Ni layer. More broadly, previous studies have established that the activation of slip systems in BCC metals differs between tension and compression. This asymmetry arises for the reason that the shear stress required to move a dislocation in one direction is different from the shear stress needed to move the same dislocation in the opposite direction [68]. This fundamental principle helps to explain the asymmetric mechanical response of the V/Fe bilayer and its semi-coherent interface.

VI.5 Conclusion:

Our findings reveal that the anisotropic plasticity of Fe and V single crystals contributes to the loading direction dependence (tension/compression) of their mechanical response. Plasticity in both Fe and V was predominantly governed by anti-twinning, whereas under compression, slip became the dominant deformation mechanism. Consequently, the V/Fe bilayer also exhibits pronounced tension-compression asymmetry. The V/Fe bilayer system exhibited a strengthening effect under in-plane tensile loading, characterized by a single yielding point. In contrast, under compressive loading, a softening effect was observed, accompanied by two distinct yielding points. A key factor influencing this asymmetry is the generation of shear strain at the interfacial atoms; localized in V during tension and in Fe during compression. This shear strain drives the decomposition of misfit dislocations in V and Fe, during tension and compression, respectively, thereby governing the plastic deformation behavior of each layer.

Conclusion

Limitations of MD simulations:

Molecular Dynamics (MD) simulations is a powerful tool for investigating the mechanical behavior of metallic bilayers under nano-indentation, tensile, and compressive loading. However, it comes with several essential limitations. One major challenge is the short simulation timescales, often reserved by computational resources, which prevent the capture of long-term deformation mechanisms. To overcome this, researchers frequently resort to increase the loading rate or reducing the simulation cell size or both, that introduces additional drawbacks. In MD simulations, the finite system's size can significantly influence the results, making it difficult to accurately replicate the bulk properties and the large-scale deformation phenomena. This limitation is particularly pronounced in nano-indentation studies due to the well-known indentation size effect, which complicates the precise determination of hardness and elastic properties. Goel et al. [121] demonstrated that indentation depth in MD simulations is too superficial, resulting in overestimated harnesses' values. As shown in Fig.1, hardness values stabilize and align more closely with experimental data when the indentation depth exceeds 40 nm.

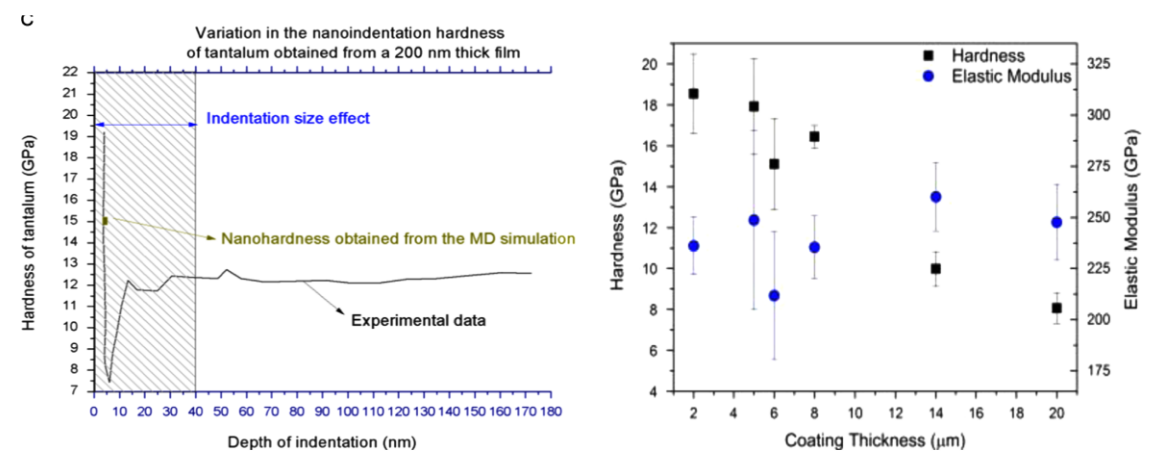


Fig.1 Size effect driven Nano-indentation hardness of tantalum obtained from the experiments For a 200 nm-thick tantalum thin film, the MD simulation values showed notable deviations compared to experimental results [121].

Moreover, the reliability of MD simulation outcomes heavily depends on the accuracy of the interatomic potentials used, which may not fully capture all atomic interactions during plastic deformation especially in complex systems like metallic multi-layers. Additionally, initial conditions, such as strain rate in tensile test, periodic boundary conditions, and thermodynamic parameters (e.g., NVT and NPT ensembles), can significantly influence the results and potentially introduce artifacts. These limitations collectively challenge the ability of MD simulations to precisely determine the mechanical behavior of materials, often necessitating experimental validation. Despite these challenges, MD simulations and experimental methods serve as complementary approaches.

General Conclusion:

This thesis provides novel insights into the role of semi-coherent interfaces in the mechanical response of bilayer systems by investigating the interaction between the V-Fe interface and the evolving plastic zone during nano-indentation, tension, and compression loadings, using atomistic simulation. Moreover, we systematically analyzed the effects of indented layer thickness, indenter position, and crystallographic orientation. The key findings are summarized as follows:

(1) Hardening effect of semi-coherent interface during nano-indentation of the V/Fe bilayer

First, the plastic deformation mechanisms of V and Fe single crystals exhibit distinct characteristics. V deforms primarily through a combination of twinning and dislocation slip, whereas Fe undergoes slip-dominated deformation. While, the interface significantly strengthens the V/Fe bilayer by obstructing dislocation motion through the misfit dislocation (MFD) network. This hardening effect arises due to dislocation-interface interactions, where MFDs' nodes serve as key barriers to dislocation motion during nano-indentation, promoting the horizontal evolution of shear loops. This hardening effect is more pronounced for thinner V layers. Below a critical thickness of approximately 50Å, hardness increases as the V layer thickness decreases, in agreement with the Hall-Petch model. However, when the V layer thickness exceeds 80 Å, the bilayer's deformation behavior approaches that of bulk V.

(2) Crystallographic orientation influence

The unique twinning anisotropy of BCC V during nano-indentation accelerates dislocation nucleation, displaying distinct structural patterns: flower-like in (100), diamond-shaped in (110), and three-point-star in (111) orientation. In contrast, Fe single crystals primarily deform via slip orientation-dependent due to the variations in dislocation density. Despite differences in interface structural patterns and dislocation-interface interactions, all crystallographic orientations (100), (110), and (111) exhibit a blocking effect induced by MDF that contributes to system hardening. However, the (111) semi-coherent interface demonstrates the weakest blocking effect due to its higher misfit dislocation spacing, leading to reduced stability and weaker dislocation-interface interactions at advanced indentation.

(3) Inverse effect of semi-coherent during nano-indentation of Fe/V bilayer

In Fe/V bilayers, the interface promotes softening, as MFD nodes serve as dislocation sources, enabling the decomposition of misfit dislocations inside V layer, while the indented Fe layer deforms elastically. This behavior aligns with Koehler's strength theory for metallic multilayers. The inverse effects of semi-coherent interfaces were also observed in V-Fe-V and Fe-V-Fe multilayers, reflecting trends seen in FCC/FCC systems. Moreover, consistent with

the inverse Hall-Petch effect, hardness decreases with decreasing Fe layer thickness below (~50Å), and softening occurs due to interface-induced plasticity.

(4) Tension/compression asymmetry in the V/Fe bilayer

In agreement with previous studies, Fe and V single crystals exhibit anisotropic plasticity. Anti-twinning dominates in tension, whereas dislocation slip governs plasticity in compression. Additionally, phase transitions were observed in both tension and compression for V single crystals. Moreover, the mechanical response of the V/Fe bilayer exhibits significant asymmetry between tensile and compressive loading. During Tension: Strengthening occurs due to the simultaneous cooperation between dislocation slip in the V layer (originating from the decomposition of MFD) and anti-twinning in the Fe layer, leading to a single yield point of stress-strain curves. Whereas, Softening is observed during compression as deformation initiates in the softer V layer via phase transition, causing the main yield point in the stressstrain curve, while Fe initially deforms elastically. With further compression, misfit dislocations decompose inside Fe, activating slip deformation and leading to the second yield point. This tension/compression asymmetry of the V/Fe bilayer is driven by shear strain evolution at the interface. During tension, shear strain in V interfacial atoms facilitates the decomposition of misfit dislocations inside the V layer. While, higher shear strain in Fe interfacial atoms promotes misfit dislocation's decomposition inside the Fe layer, during compression.

The findings of this thesis significantly contribute to the understanding of how semi-coherent interfaces influence the mechanical behavior of nanoscale metallic multilayers.

Future work:

This conclusion pave the way for addressing several research gaps. Future work could focus on optimizing the modulation period of BCC multilayers to enhance the strengthening effects of semi-coherent interfaces. This may involve systematically varying layer thicknesses. Further work could concentrate on exploring the influence of HCP/HCP semi-coherent interfaces on the mechanical response of multi-layers to gain deeper insights into the deformation mechanisms of interfaces.

- [1] Greene, J. E. (2017). Review Article: Tracing the recorded history of thin-film sputter deposition: From the 1800s to 2017. *Journal of Vacuum Science & Technology A: Vacuum, Surfaces, and Films*, 35(5). https://doi.org/10.1116/1.4998940
- [2] Smallman, R, E.; Ngan, A.H.W. (2014). Chapter 10 Surfaces, Grain Boundaries and Interfaces. Modern physical metallurgy (Eighth edition). Pages 415-442. https://doi.org/10.1016/B978-0-08-098204-5.00010-9
- [3] Priester, Louisette. (2006). Les joints de grains : de la théorie à l'ingénierie matériaux métallourgie. (EDP SCIENCES). ISBN : 1-4237-8956-3
- [4] Romanov, A. E., Wagner, T., & Rühle, M. (1998). Coherent To Incoherent Transition in Mismatched Interfaces, *Scripta Materialia*, Volume 38, Issue 6, 1998, Pages 869-875, ISSN 1359-6462, https://doi.org/10.1016/S1359-6462(97)00570-8.
- [5] Saraev, D., & Miller, R. E. (2006). Atomic-scale simulations of nanoindentation-induced plasticity in copper crystals with nanometer-sized nickel coatings. *Acta Materialia*, *54*(1), 33–45. https://doi.org/10.1016/j.actamat.2005.08.030
- [6] Cao, Y., Zhang, J., Liang, Y., Yu, F., & Sun, T. (2010). Mechanical and tribological properties of Ni/Al multilayers A molecular dynamics study. *Applied Surface Science*, 257(3), 847–851. https://doi.org/10.1016/j.apsusc.2010.07.079
- [7] Tian, Y. Y., Li, J., Hu, Z. Y., Wang, Z. P., & Fang, Q. H. (2017). Molecular dynamics study of plastic deformation mechanism in Cu/Ag multilayers. *Chinese Physics B*, 26(12). https://doi.org/10.1088/1674-1056/26/12/126802
- [8] Yin, F., Zhao, Y., Yu, S., & Pang, W. (2019). Molecular dynamics studies on the interface evolution characteristics and deformation mechanisms of Cu/Al multilayers during compression process. *Journal of Applied Physics*, 125(2). https://doi.org/10.1063/1.5055901
- [9] Fang, Q., Tian, Y., Li, J., Wang, Q., & Wu, H. (2019). Interface-governed nanometric machining behaviour of Cu/Ag bilayers using molecular dynamics simulation. *RSC Advances*, 9(3), 1341–1353. https://doi.org/10.1039/C8RA08676A
- [10] Medyanik, S. N., & Shao, S. (2009). Strengthening effects of coherent interfaces in nanoscale metallic bilayers. *Computational Materials Science*, 45(4), 1129–1133. https://doi.org/10.1016/j.commatsci.2009.01.013
- [11] Wu, C. da, & Jiang, W. X. (2018). Molecular dynamics study on deformation and mechanics of nanoscale Au/Cu multilayers under indentation. *Journal of Molecular Modeling*, 24(9). https://doi.org/10.1007/s00894-018-3792-7

- [12] Chauniyal, A. Dehm, G. Janisch, R. (2021). On the role of pre-existing defects in influencing hardness in nanoscale indentations Insights from atomistic simulations. *Journal of the Mechanics and Physics of Solids*. Volume 154, 104511, ISSN 0022-5096, https://doi.org/10.1016/j.jmps.2021.104511.
- [13] Shao, S. Akasheh, F. Wang, J. Liu. Y. (2017) Alternative misfit dislocations pattern in semi-coherent FCC {100} interfaces. *Acta Materialia*. doi: 10.1016/j.actamat.2017.10.052.
- [14] Li, J., Lu, H., Ni, Y., & Mei, J. (2011). Quasicontinuum study the influence of misfit dislocation interactions on nanoindentation. *Computational Materials Science*, *50*(11), 3162–3170. https://doi.org/10.1016/j.commatsci.2011.05.045
- [15] Guiqiang, I. Rui, SH. Lin, Y. Jiajie, H. Jingjing, CH. (2021). Mechanism Analysis of Mechanical Properties for Cu-Ni Bilayers with Semi-Coherent Interface: A Molecular Simulation . *TRIBOLOGY*, 41(5): 647-656. DOI: 10.16078/j.tribology.2020126.
- [16] Anderson, P. M., Rao, S., Cheng, Y., & Hazzledine, P. M. (2000). *The critical stress for transmission of a dislocation across an interface: results from peierls and embedded atom models*. DOI: 10.1557/PROC-586-267.
- [17] Ghoniem, N. M., & Han, X. (2005). Dislocation motion in anisotropic multilayer materials. *Philosophical Magazine*, 85(24), 2809–2830. https://doi.org/10.1080/14786430500155338
- [18] Pacheco, E.S. and Mura, T. (1969) Interaction Between and Screw Dislocation and Bimetallic Interface. *J. Mech. Phys.* Sol. 17, 163-170.
- [19] Rao, S.I., Hazzledine, P.M. & Dimiduk, D.M. (1994). Interfacial Strengthening in Semi-Coherent Metallic Multilayers. *MRS Online Proceedings Library*. 362, 67–77 https://doi.org/10.1557/PROC-362-67
- [20] Koehler, J.S. Phys. Attempt to Design a Strong Solid*. Rev. B2, 547, (1970), DOI: https://doi.org/10.1103/PhysRevB.2.547
- [21] Anderson, P.M., Xin, X. (2000). The Critical Shear Stress to Transmit A Peierls Screw Dislocation Across A Non-slipping Interface. In: Chuang, T.J., Rudnicki, J.W. (eds) Multiscale Deformation and Fracture in Materials and Structures. *Solid Mechanics and Its Applications*, vol 84. Springer, Dordrecht. https://doi.org/10.1007/0-306-46952-9 6
- [22] Zhao, Y., Peng, X., Fu, T., Sun, R., Feng, C., & Wang, Z. (2015). MD simulation of nanoindentation on (001) and (111) surfaces of Ag-Ni multilayers. *Physica E: Low-Dimensional Systems and Nanostructures*, 74, 481–488. https://doi.org/10.1016/j.physe.2015.08.020
- [23] Cao, Y., Zhang, J., Liang, Y., Yu, F., & Sun, T. (2010). Mechanical and tribological properties of Ni/Al multilayers A molecular dynamics study. *Applied Surface Science*, 257(3), 847–851. https://doi.org/10.1016/j.apsusc.2010.07.079

- [24] Sung, P. H., Wu, C. da, & Fang, T. H. (2012). Investigation of nanomechanical properties of Al/Ni and Ni/Al nanomultilayers under nanobending using molecular dynamics simulation. *Computational Materials Science*, 56, 43–48. https://doi.org/10.1016/j.commatsci.2012.01.004
- [25] Wu, C. da, & Jiang, W. X. (2018). Molecular dynamics study on deformation and mechanics of nanoscale Au/Cu multilayers under indentation. *Journal of Molecular Modeling*, 24(9). https://doi.org/10.1007/s00894-018-3792-7
- [26] Tian, X., Cui, J., Yang, M., Ma, K., & Xiang, M. (2020). Molecular dynamics simulations on shock response and spalling behaviors of semi-coherent {111} Cu-Al multilayers. International Journal of Mechanical Sciences, 172. https://doi.org/10.1016/j.ijmecsci.2019.105414
- [27] Li, Y. P., Zhu, X. F., Tan, J., Wu, B., Wang, W., & Zhang, G. P. (2009). Comparative investigation of strength and plastic instability in Cu/Au and Cu/Cr multilayers by indentation. *Journal of Materials Research*, 24(3), 728–735. https://doi.org/10.1557/jmr.2009.0092
- [28] Hoagland, R. G., Kurtz, R. J., & Henager, C. H. (2004). Slip resistance of interfaces and the strength of metallic multilayer composites. *Scripta Materialia*, 50(6), 775–779. https://doi.org/10.1016/j.scriptamat.2003.11.059
- [29] Cihan, E., Jungjohann, K., Argibay, N. *et al.* Effect of Environment on Microstructure Evolution and Friction of Au–Ni Multilayers. *Tribol Lett* **68**, 30 (2020). https://doi.org/10.1007/s11249-019-1245-9
- [30] Rao, S. I., & Hazzledine, P. M. (2000). Atomistic simulations of dislocation-interface interactions in the Cu-Ni multilayer system. *Philosophical Magazine A: Physics of Condensed Matter, Structure, Defects and Mechanical Properties*, 80(9), 2011–2040. https://doi.org/10.1080/01418610008212148
- [31] Amaya-Roncancio, S., Restrepo-Parra, E., Marcela Devia-Narvaez, D., Fernando Arias-Mateus, D., & María Gómez-Hermida, M. (2014). Molecular dynamics simulation of nanoindentation in Cr, Al layers and Al/Cr bilayers, using a hard spherical nanoindenter. *DYNA*, 81(186), 102–107. https://doi.org/10.15446/dyna.v81n186.39190
- [32] Feng, C., Peng, X., Fu, T., Zhao, Y., Huang, C., & Wang, Z. (2017). Molecular dynamics simulation of nano-indentation on Ti-V multilayered thin films. *Physica E: Low-Dimensional Systems and Nanostructures*, 87, 213–219. https://doi.org/10.1016/j.physe.2016.10.019
- [33] Ou, X., Sietsma, J., & Santofimia, M. J. (2016). Molecular dynamics simulations of the mechanisms controlling the propagation of bcc/fcc semi-coherent interfaces in iron. *Modelling and Simulation in Materials Science and Engineering*, 24(5). https://doi.org/10.1088/0965-0393/24/5/055019

- [34] Demkowicz, M. J., & Thilly, L. (2011). Structure, shear resistance and interaction with point defects of interfaces in Cu-Nb nanocomposites synthesized by severe plastic deformation. *Acta Materialia*, *59*(20), 7744–7756. https://doi.org/10.1016/j.actamat.2011.09.004
- [35] Wang, J., Zhang, R. F., Zhou, C. Z., Beyerlein, I. J., & Misra, A. (2014). Interface dislocation patterns and dislocation nucleation in face-centered-cubic and body-centered-cubic bicrystal interfaces. *International Journal of Plasticity*, 53, 40–55. https://doi.org/10.1016/j.ijplas.2013.07.002
- [36]Wang, J., Hoagland, R. G., Hirth, J. P., & Misra, A. (2008). Atomistic simulations of the shear strength and sliding mechanisms of copper-niobium interfaces. *Acta Materialia*, *56*(13), 3109–3119. https://doi.org/10.1016/j.actamat.2008.03.003.
- [37] Shao, S., & Medyanik, S. N. (2010). Interaction of dislocations with incoherent interfaces in nanoscale FCC-BCC metallic bi-layers. *Modelling and Simulation in Materials Science and Engineering*, *18*(5). https://doi.org/10.1088/0965-0393/18/5/055010
- [38] Xu, K., Zhai, H., He, L., Ni, Y., Lu, P., Wang, G., & Liu, X. (2022). Atomistic simulations of mechanical response of a heterogeneous fcc/bcc nanolayered composite. *Journal of Physics: Condensed Matter*, *34*(38), 385703. https://doi.org/10.1088/1361-648X/ac8194
- [39] Meyers, M. A., Mishra, A., & Benson, D. J. (2006). Mechanical properties of nanocrystalline materials. In *Progress in Materials Science* (Vol. 51, Issue 4, pp. 427–556). https://doi.org/10.1016/j.pmatsci.2005.08.003
- [40] Hodes, G. (2007). When small is different: Some recent advances in concepts and applications of nanoscale phenomena. *Advanced Materials*, 19(5), 639–655. https://doi.org/10.1002/adma.200601173
- [41] Zhou, Q., Xie, J. Y., Wang, F., Huang, P., Xu, K. W., & Lu, T. J. (2015). The mechanical behavior of nanoscale metallic multilayers: A survey. *Acta Mechanica Sinica/Lixue Xuebao*, 31(3), 319–337. https://doi.org/10.1007/s10409-015-0401-1
- [42] Misra, A. Demkowicz, M.J. Wang, J. & Hoagland, R.G. (2008). The multiscale modeling of plastic deformation in metallic nanolayered composites. *JOM*, 60, 39–42. https://doi.org/10.1007/s11837-008-0047-6
- [43] Fu, T., Zhang, Z., Peng, X., Weng, S., Miao, Y., Zhao, Y., Fu, S., & Hu, N. (2019). Effects of modulation periods on mechanical properties of V/VN nano-multilayers. *Ceramics International*, 45(8), 10295–10303. https://doi.org/10.1016/j.ceramint.2019.02.084
- [44] Gao, F., Peng, X., Huang, C., Yue, X., Yang, B., Sun, S., & Fu, T. (2018). Modulation period dependent mechanical properties of Cu/Fe metallic multilayered films. *AIP Advances*, 8(4). https://doi.org/10.1063/1.5023462

- [45] Chauniyal, A., & Janisch, R. (2023). How Coherent and Semi-Coherent Interfaces Govern Dislocation Nucleation in Lamellar TiAl Alloys. *Advanced Engineering Materials*, 25(15). https://doi.org/10.1002/adem.202300121
- [46] Chauniyal, A., & Janisch, R. (2020). Influence of lattice misfit on the deformation behaviour of α2/γ lamellae in TiAl alloys. *Materials Science and Engineering: A*, 796. https://doi.org/10.1016/j.msea.2020.140053
- [47] Lu, L., Huang, C., Pi, W., Xiang, H., Gao, F., Fu, T., & Peng, X. (2018). Molecular dynamics simulation of effects of interface imperfections and modulation periods on Cu/Ta multilayers. *Computational Materials Science*, 143, 63–70. https://doi.org/10.1016/j.commatsci.2017.10.034
- [48] Li, J. C., Song, H. Q., Wang, J. W., & Shen, J. (2014). Atomic Study of Semi-Coherent Interfacial Structure at Fe[110]/TMC[001] (TM=V, Nb and Ta) Interfaces. *Advanced Materials Research*, 1081, 232–236. https://doi.org/10.4028/www.scientific.net/amr.1081.232
- [49] Jiménez-Sáez, J. C., Pérez-Martín, A. M. C., & Jiménez-Rodríguez, J. J. (2012). Mechanical characterization of Co/Cu multilayered nanowires. *Journal of Nanoscience and Nanotechnology*, 12(6), 4710–4716. https://doi.org/10.1166/jnn.2012.4896
- [50] Shao, S., Wang, J., Beyerlein, I. J., & Misra, A. (2015). Glide dislocation nucleation from dislocation nodes at semi-coherent {111} Cu-Ni interfaces. *Acta Materialia*, 98, 206–220. https://doi.org/10.1016/j.actamat.2015.07.044
- [51] Hoagland, R. G., Mitchell, T. E., Hirth, J. P., & Kung, H. (2002). On the strengthening effects of interfaces in multilayer fee metallic composites. *Philosophical Magazine A: Physics of Condensed Matter, Structure, Defects and Mechanical Properties*, 82(4), 643–664. https://doi.org/10.1080/01418610208243194
- [52] Wang, Y., Li, J., Lu, W., Yuan, F., & Wu, X. (2019). Enhanced co-deformation of a heterogeneous nanolayered Cu/Ni composite. *Journal of Applied Physics*, 126(21). https://doi.org/10.1063/1.5121625
- [53] Chen, X. Y., Kong, X. F., Misra, A., Legut, D., Yao, B. N., Germann, T. C., & Zhang, R. F. (2018). Effect of dynamic evolution of misfit dislocation pattern on dislocation nucleation and shear sliding at semi-coherent bimetal interfaces. *Acta Materialia*, *143*, 107–120. https://doi.org/10.1016/j.actamat.2017.10.012
- [54] Mi, S. T., Wu, C. Y., Liu, L. C., Fan, J. L., & Gong, H. R. (2021). Atomic structure, tensile property, and dislocation behavior of Fe-W interfaces from molecular dynamics simulation. *Journal of Physics Condensed Matter*, *33*(14). https://doi.org/10.1088/1361-648X/abdb66
- [55] Ding, J., Li, Z., Wang, W., Ma, Y., Liu, W., & Liang, C. (2022). Evaluation of structural and mechanical strength of symmetric tilt interface in W/Fe composite laminate using

- molecular dynamics. *Journal of Physics and Chemistry of Solids*, 168. https://doi.org/10.1016/j.jpcs.2022.110800.
- [56] Schwarz, F., & Spolenak, R. (2024). Investigating strengthening and softening mechanisms in Al/Ni multilayers via molecular dynamics simulations of uniaxial compression. *Journal of Applied Physics*, *135*(9). https://doi.org/10.1063/5.0190198
- [57] Gang, C., ChuanJie, W., & Peng, Z. (2017). The role of interface in uniaxial tensile process of nano-scale bilayer Cu/Ni. *Computational Materials Science*, *131*, 21–27. https://doi.org/10.1016/j.commatsci.2017.01.036
- [58] Yang, H., Zhu, L., Zhang, R., Zhou, J., & Sun, Z. (2020). Influence of high stacking-fault energy on the dissociation mechanisms of misfit dislocations at semi-coherent interfaces. *International Journal of Plasticity*, *126*. https://doi.org/10.1016/j.ijplas.2019.09.016
- [59] Chen, E. Y., Dingreville, R., & Deo, C. (2018). Misfit dislocation networks in semi-coherent miscible phase boundaries: An example for U–Zr interfaces. *Computational Materials Science*, *154*, 194–203. https://doi.org/10.1016/j.commatsci.2018.07.065
- [60] Chen, K., Xie, H., Qie, Y., & Deng, H. (2022). Molecular dynamics simulation study of helium bubble growth on W/Ta semi-coherent interface. *Journal of Nuclear Materials*, *558*, 153340. https://doi.org/https://doi.org/10.1016/j.jnucmat.2021.153340
- [61] Meyers, M. A., & Chawla, K. K. (2008). Mechanical Behavior of Materials (2nd ed.) "Imperfections: Point and Line" Defects. *Cambridge: Cambridge University Press*.
- [62] G. I. Taylor. (1934). "The Mechanism of Plastic Deformation of Crystals. Part I. Theoretical," *Proceedings of the Royal Society of London A: Mathematical, Physical and Engineering Sciences*, vol. 145, pp. 362-387, 1934.
- [63] Hirth, J.P. (1985). A brief history of dislocation theory. *Metall Trans A*. 16, 2085–2090 https://doi.org/10.1007/BF02670413
- [64] Hiroshi, N. (2014). Defects in Metals. *In Physical Metallurgy: Fifth Edition* (Vol. 1, pp. 561–637). Elsevier Inc. https://doi.org/10.1016/B978-0-444-53770-6.00006-X
- [65] Chang, J. Cai, W. Bulatov, V. V. and Yip, S. (2001). "Dislocation motion in BCC metals by molecular dynamics," *Materials Science and Engineering: A*, Vols. 309 310, pp. 160-163.
- [66] Hull, D. Bacon, D.J. (2011). Chapter 1-Defects in Crystals, Introduction to Dislocations (Fifth Edition), *Butterworth-Heinemann*, Pages 1-20, ISBN 9780080966724. https://doi.org/10.1016/B978-0-08-096672-4.00001-3
- [67] Dezerald, L., Rodney, D., Clouet, E. et al. (2016). Plastic anisotropy and dislocation trajectory in BCC metals. *Nat Commun* 7, 11695 https://doi.org/10.1038/ncomms11695
- [68] Lagerlöf, K.P.D. (1993). On deformation twinning in b.c.c. metals. *Acta Metallurgica et Materialia*. Volume 41, Issue 7. Pages 2143-2151, ISSN 0956-7151. https://doi.org/10.1016/0956-7151(93)90384-5.

- [69] Christian, J.W. Mahajan, S. (1995). Deformation twinning. *Progress in Materials Science*, Volume 39, Issues 1–2, Pages 1-157, ISSN 0079-6425, https://doi.org/10.1016/0079-6425(94)00007-7.
- [70] Beyerlein, I. J., Zhang, X., & Misra, A. (2014). Growth twins and deformation twins in metals. *Annual Review of Materials Research*, 44, 329–363. https://doi.org/10.1146/annurev-matsci-070813-113304
- [71] S. Mahajan. (2002). Deformation Twinning. *Encyclopedia of Materials: Science and Technology, Elsevier*, Pages 1-14, ISBN 9780080431529, https://doi.org/10.1016/B0-08-043152-6/01809-X.
- [72] Zhu, Y.T. Liao, X.Z. Wu, X.L. (2012). Deformation twinning in nanocrystalline materials. *Progress in Materials Science*, Volume 57, Issue 1, Pages 1-62, ISSN 0079-6425, https://doi.org/10.1016/j.pmatsci.2011.05.001.
- [73] Official website of LAMMPS code https://www.lammps.org.
- [74] Official webesite of Ovito software https://www.ovito.org/.
- [75] Frenkel, D. Smit, B. (2002). Chapter 4 Molecular Dynamics simulations, Understanding Molecular Simulation (Third Edition). *Academic Press*, Pages 97-124, ISBN 9780323902922, https://doi.org/10.1016/B978-0-32-390292-2.00012-X.
- [76] Alder, B. J. Wainwright, T. E. (1957). Phase Transition for a Hard Sphere System. *J. Chem. Phys.*; 27 (5): 1208–1209. https://doi.org/10.1063/1.1743957
- [77] Ciccotti, G., Dellago, C., Ferrario, M. et al. (2022). Molecular simulations: past, present, and future. (*a Topical Issue in EPJB*). *Eur. Phys. J.* B 95, 3 https://doi.org/10.1140/epjb/s10051-021-00249-x
- [78] Official website of Sandia laboratories https://www.sandia.gov
- [79] Plimpton, S.J. Thompson, A.P. (2012). Computational aspects of many-body potentials. *MRS Bull.* 37 513–521, https://doi.org/10.1557/mrs.2012.96.
- [80] Müser, M. H., Sukhomlinov, S. v., & Pastewka, L. (2023). Interatomic potentials: achievements and challenges. In Advances in Physics: X (Vol. 8, Issue 1). Taylor and Francis Ltd. https://doi.org/10.1080/23746149.2022.2093129.
- [81] Rassoulinejad-Mousavi, S. M., & Zhang, Y. (2018). Interatomic Potentials Transferability for Molecular Simulations: A Comparative Study for Platinum, Gold and Silver. *Scientific Reports*, 8(1). https://doi.org/10.1038/s41598-018-20375-4
- [82] Becker, C.A. Tavazza, F. Trautt, Z.T. and Buarque de Macedoc, R.A. (2013). "Considerations for choosing and using force fields and interatomic potentials in materials science and engineering". *Current Opinion in Solid State and Materials Science*, 17, 277-283. DOI: 10.1016/j.cossms.2013.10.001.

- [83] Hale, L. M., Trautt, Z. T., & Becker, C. A. (2018). Evaluating variability with atomistic simulations: The effect of potential and calculation methodology on the modeling of lattice and elastic constants. *Modelling and Simulation in Materials Science and Engineering*, 26(5). https://doi.org/10.1088/1361-651X/aabc05
- [84] Hafez Haghighat, S. M., Fikar, J., & Schäublin, R. (2008). Effect of interatomic potential on the behavior of dislocation-defect interaction simulation in α-Fe. *Journal of Nuclear Materials*, 382(2–3), 147–153. https://doi.org/10.1016/j.jnucmat.2008.08.017
- [85] Olsson, P. A. T. (2009). Semi-empirical atomistic study of point defect properties in BCC transition metals. *Computational Materials Science*, 47(1), 135–145. https://doi.org/10.1016/j.commatsci.2009.06.025
- [86] Mendelev, M. I., Han, S., Son, W. J., Ackland, G. J., & Srolovitz, D. J. (2007). Simulation of the interaction between Fe impurities and point defects in V. *Physical Review B Condensed Matter and Materials Physics*, 76(21). https://doi.org/10.1103/PhysRevB.76.214105
- [87] Choi, W. M., Kim, J. S., Ko, W. S., Kim, D. G., Jo, Y. H., Sohn, S. S., Lee, S., & Lee, B. J. (2021). Computational design of V-CoCrFeMnNi high-entropy alloys: An atomistic simulation study. *Calphad: Computer Coupling of Phase Diagrams and Thermochemistry*, 74. https://doi.org/10.1016/j.calphad.2021.102317
- [88] Misra, P. K. Prasanta K. (2012). Chapter 1 Basic Properties of Crystals. *Physics of condensed matter*. Academic Press. 2012,Pages 1-35, ISBN 9780123849540, https://doi.org/10.1016/B978-0-12-384954-0.00001-3.
- [89] Howe, J.M. and Howe, J.M. (1997). Interfaces in Materials: Atomic Structure, Thermodynamics and Kinetics of Solid-Vapor, Solid-Liquid and Solid-Solid Interfaces. Wiley-Interscience publication. (*Epitaxial layers*).p185. ISBN 0471138304, 9780471138303.
- [90] Goel, S., Cross, G., Stukowski, A., Gamsjäger, E., Beake, B., & Agrawal, A. (2018). Designing nanoindentation simulation studies by appropriate indenter choices: Case study on single crystal tungsten. *Computational Materials Science*, *152*, 196–210. https://doi.org/10.1016/j.commatsci.2018.04.044
- [91] Chen, C., Li, H., Xiang, H., & Peng, X. (2018). Molecular dynamics simulation on B3-GaN thin films under nanoindentation. *Nanomaterials*, 8(10). https://doi.org/10.3390/nano8100856
- [92] Ghaffarian, H., Karimi Taheri, A., Ryu, S., & Kang, K. (2016). Nanoindentation study of cementite size and temperature effects in nanocomposite pearlite: A molecular dynamics simulation. *Current Applied Physics*, *16*(9), 1015–1025. https://doi.org/10.1016/j.cap.2016.05.024

- [93] Imran, M., Hussain, F., Rashid, M., & Ahmad, S. A. (2012). Dynamic characteristics of nanoindentation in Ni: A molecular dynamics simulation study. *Chinese Physics B*, 21(11). https://doi.org/10.1088/1674-1056/21/11/116201
- [94] Ziegenhain, G., Urbassek, H. M., & Hartmaier, A. (2010). Influence of crystal anisotropy on elastic deformation and onset of plasticity in nanoindentation: A simulational study. *Journal of Applied Physics*, 107(6). https://doi.org/10.1063/1.3340523
- [95] Zimmerman, J. A., Webb, E. B., Hoyt, J. J., Jones, R. E., Klein, P. A., & Bammann, D. J. (2004). Calculation of stress in atomistic simulation. *Modelling and Simulation in Materials Science and Engineering*, 12(4). https://doi.org/10.1088/0965-0393/12/4/S03
- [96] Stukowski, A. (2010). Visualization and analysis of atomistic simulation data with OVITO-the Open Visualization Tool. *Modelling and Simulation in Materials Science and Engineering*, 18(1). https://doi.org/10.1088/0965-0393/18/1/015012
- [97] Faken, D. & Jónsson, H. (1994). Systematic analysis of local atomic structure combined with 3D computer graphics. *Computational Materials Science*. (Vol. 2). https://doi.org/10.1016/0927-0256(94)90109-0
- [98] Li, D., Wang, F. C., Yang, Z. Y., & Zhao, Y. P. (2014). How to identify dislocations in molecular dynamics simulations? *Science China: Physics, Mechanics and Astronomy* (Vol. 57, Issue 12, pp. 2177–2187). Science in China Press. https://doi.org/10.1007/s11433-014-5617-8 [99] Möller, J. J., & Bitzek, E. (2016). BDA: A novel method for identifying defects in bodycentered cubic crystals. *MethodsX*, 3, 279–288. https://doi.org/10.1016/j.mex.2016.03.013
- [100] Fischer-Cripps, A. C. (2007). Nanoindentation. *Mechanical Engineering Series* 1, *Springer Science & Business Media*. DOI 10.1007/978-1-4419-9872-9_1.
- [101] Johnson, K.L. (1985). Contact mechanics. Cambridge University Press, London.
- [102] Gröger, R., Chlup, Z., & Kuběnová, T. (2018). Deformation twinning in vanadium single crystals tested in compression at 77 K. *Materials Science and Engineering A*, 737, 413–421. https://doi.org/10.1016/j.msea.2018.09.030
- [103] Meyers, M.A., Chawla, K.K. (2008). Mechanical Behavior of Materials (2nd ed.). *Cambridge: Cambridge University Press.* ISBN: 9780511810947. DOI: 10.1017/CBO9780511810947.
- [104] Weinberger, C. R., Boyce, B. L., & Battaile, C. C. (2013). Slip planes in bcc transition metals. *International Materials Reviews* (Vol. 58, Issue 5, pp. 296–314). *Maney Publishing*. https://doi.org/10.1179/1743280412Y.0000000015
- [105] Biener, M. M. Biener, J., Hodge, A. M., & Hamza, A. v. (2007). Dislocation nucleation in bcc Ta single crystals studied by nanoindentation. *Physical Review B Condensed Matter and Materials Physics*, 76(16). https://doi.org/10.1103/PhysRevB.76.165422

- [106] Fu, T., Peng, X., Wan, C., Lin, Z., Chen, X., Hu, N., & Wang, Z. (2017). Molecular dynamics simulation of plasticity in VN(001) crystals under nanoindentation with a spherical indenter. *Applied Surface Science*, *392*, 942–949. https://doi.org/10.1016/j.apsusc.2016.09.130 [107] Ruestes, C. J. Stukowski, A. Tang, Y. Tramontina, D. R. Erhart, P. Remington, B. A., Urbassek, H. M. Meyers, M. A. & Bringa, E. M. (2014). Atomistic simulation of tantalum nanoindentation: Effects of indenter diameter, penetration velocity, and interatomic potentials on defect mechanisms and evolution. *Materials Science and Engineering A*, *613*, 390–403. https://doi.org/10.1016/j.msea.2014.07.001
- [108] Remington, T. P., Ruestes, C. J., Bringa, E. M., Remington, B. A., Lu, C. H., Kad, B., & Meyers, M. A. (2014). Plastic deformation in nanoindentation of tantalum: A new mechanism for prismatic loop formation. *Acta Materialia*, 78, 378–393. https://doi.org/10.1016/j.actamat.2014.06.058
- [109] Gao, Y., Ruestes, C. J., & Urbassek, H. M. (2014). Nanoindentation and nanoscratching of iron: Atomistic simulation of dislocation generation and reactions. *Computational Materials Science*, 90, 232–240. https://doi.org/10.1016/j.commatsci.2014.04.027
- [110] Luu, H. T., Dang, S. L., Hoang, T. V., & Gunkelmann, N. (2021). Molecular dynamics simulation of nanoindentation in Al and Fe: On the influence of system characteristics. *Applied Surface Science*, 551. https://doi.org/10.1016/j.apsusc.2021.149221
- [111] Shao, S., Zbib, H. M., Mastorakos, I., & Bahr, D. F. (2013). Effect of interfaces in the work hardening of nanoscale multilayer metallic composites during nanoindentation: A molecular dynamics investigation. *Journal of Engineering Materials and Technology*, *135*(2). https://doi.org/10.1115/1.4023672
- [112] Beyerlein, I. J., Li, Z., & Mara, N. A. (2022). Mechanical Properties of Metal Nanolaminates. *Chemical Engineering and Materials Science*. (52) 281-304 https://doi.org/10.1146/annurev-matsci-081320
- [113] Akasheh, F., Zbib, H. M., Hirth, J. P., Hoagland, R. G., & Misra, A. (2007). Interactions between glide dislocations and parallel interfacial dislocations in nanoscale strained layers. *Journal of Applied Physics*, *102*(3). https://doi.org/10.1063/1.2757082
- [114] Trandinh, L., Kang, W. J., & Cheon, S. S. (2013). Nanoindentation simulation of dislocation evolution in substrate/film systems. *Journal of Nanoscience and Nanotechnology*, *13*(12), 8207–8216. https://doi.org/10.1166/jnn.2013.8218
- [115] Zheng, S. J., Wang, J., Carpenter, J. S., Mook, W. M., Dickerson, P. O., Mara, N. A., & Beyerlein, I. J. (2014). Plastic instability mechanisms in bimetallic nanolayered composites. *Acta Materialia*, 79, 282–291. https://doi.org/10.1016/j.actamat.2014.07.017

- [116] Wang, J., Zhou, Q., Shao, S., & Misra, A. (2017). Strength and plasticity of nanolaminated materials. *Materials Research Letters*, 5(1), 1–19. https://doi.org/10.1080/21663831.2016.1225321
- [117] Wu, C. da, & Jiang, W. X. (2018). Molecular dynamics study on deformation and mechanics of nanoscale Au/Cu multilayers under indentation. *Journal of Molecular Modeling*, 24(9). https://doi.org/10.1007/s00894-018-3792-7
- [118] Choi, Y., van Vliet, K. J., Li, J., & Suresh, S. (2003). Size effects on the onset of plastic deformation during nanoindentation of thin films and patterned lines. *Journal of Applied Physics*, 94(9), 6050–6058. https://doi.org/10.1063/1.1615702
- [119] Jian, Wang., Amit, Misra. (2014). Strain hardening in nanolayered thin films. *Current Opinion in Solid State & Materials Science*, 18(1), 19-28. doi: 10.1016/J.COSSMS.2013.10.003
- [120] Satish, I., Rao., P., M., Hazzledine., Dennis, M., Dimiduk. (1994). Interfacial Strengthening in Semi-Coherent Metallic Multilayers. *MRS Proceedings*, 362(1):67-77. doi: 10.1557/PROC-362-67
- [121] Goel, S., Beake, B., Chan, C. W., Haque Faisal, N., & Dunne, N. (2015). Twinning anisotropy of tantalum during nanoindentation. *Materials Science and Engineering: A*, 627, 249–261. https://doi.org/10.1016/j.msea.2014.12.075
- [122] Sainath, G., & Choudhary, B. K. (2016). Orientation dependent deformation behaviour of BCC iron nanowires. *Computational Materials Science*, 111, 406–415. https://doi.org/10.1016/j.commatsci.2015.09.055
- [123] Yalcinkaya, T., Brekelmans, W. A. M., & Geers, M. G. D. (2008). BCC single crystal plasticity modeling and its experimental identification. *Modelling and Simulation in Materials Science and Engineering*, 16(8). https://doi.org/10.1088/0965-0393/16/8/085007
- [124] Lu, C., Gao, Y., Michal, G., Zhu, H., Huynh, N.N., Tieu, A.K. (2009). Molecular Dynamic Simulation of Effect of Crystallographic Orientation on Nano-Indentation/Scratching Behaviors of BCC Iron. (eds) Advanced Tribology. Springer, Berlin, Heidelberg. https://doi.org/10.1007/978-3-642-03653-8_181
- [125] Gao, Y., Brodyanski, A., Kopnarski, M., & Urbassek, H. M. (2015). Nanoscratching of iron: A molecular dynamics study of the influence of surface orientation and scratching direction. *Computational Materials Science*, 103, 77–89. https://doi.org/10.1016/j.commatsci.2015.03.011
- [126] Duesbery, M. S., & Vitek, V. (n.d.). (1998). Plastic anisotropy in b.c.c. transition metals. *Acta Materialia*, Volume 46, Issue 5, , Pages 1481-1492, ISSN 1359-6454, DOI https://doi.org/10.1016/S1359-6454(97)00367-4

- [127] Kositski, R., & Mordehai, D. (2015). Depinning-controlled plastic deformation during nanoindentation of BCC iron thin films and nanoparticles. *Acta Materialia*, *90*, 370–379. https://doi.org/10.1016/j.actamat.2015.03.010
- [128] Zhang, J. M., Ma, F., & Xu, K. W. (2003). Calculation of the surface energy of bcc metals by using the modified embedded-atom method. *Surface and Interface Analysis*, 35(8), 662–666. https://doi.org/10.1002/sia.1587
- [129] Jin, HS. Ri, KS., Choe, YM. & Yang, H. (2022). Evaluation of surface energy and its anisotropy for bcc transition metals by modified embedded atom method. *Indian J Phys 96*, 3099–3104 https://doi.org/10.1007/s12648-021-02237-4
- [130] Zhou, Q., Xie, J. Y., Wang, F., Huang, P., Xu, K. W., & Lu, T. J. (2015). The mechanical behavior of nanoscale metallic multilayers: A survey. *Acta Mechanica Sinica/Lixue Xuebao*, 31(3), 319–337. https://doi.org/10.1007/s10409-015-0401-1
- [131] Imran, M., Hussain, F., Rashid, M., & Ahmad, S. A. (2012). Molecular dynamics study of the mechanical characteristics of Ni/Cu bilayer using nanoindentation. *Chinese Physics B*, 21(12). https://doi.org/10.1088/1674-1056/21/12/126802
- [132] Fazeli, S., & Khatiboleslam Sadrnezhaad, S. (2019). Molecular dynamics simulation of plastic deformation and interfacial delamination of NiTi/Ag bilayer by cyclic-nanoindentation: Effects of crystallographic orientation of substrate. *Computational Materials Science*, 168, 229–245. https://doi.org/10.1016/j.commatsci.2019.05.032
- [134] Doan, D. Q., Fang, T. H., & Chen, T. H. (2021). Interfacial and mechanical characteristics of TiN/Al composites under nanoindentation. *International Journal of Solids and Structures*, 226–227. https://doi.org/10.1016/j.ijsolstr.2021.111083
- [135] Zeng, Y. Hunter, A. Beyerlein, I.J. Koslowski, M. (2015). A phase field dislocation dynamics model for a bicrystal interface system: An investigation into dislocation slip transmission across cube-on-cube interfaces. *International Journal of Plasticity*, Volume 79, 2016, Pages 293-313, ISSN 0749-6419. https://doi.org/10.1016/j.ijplas.2015.09.001.
- [136] Shinde, A.B. Patil, Sh. Patil, P. Salunkhe, R. Sande, R. Pawar, S. Patil, V. (2022). Dislocation and deformation analysis of Cu-Ni thin films during Nano-indentation using molecular dynamics simulation approach. *Materials Today: Proceedings*, Volume 49,Pages 1453-1461, https://doi.org/10.1016/j.matpr.2021.07.226.
- [137] Yang, W. Ayoub, G. Salehinia, I. Mansoor, B. Zbib, H. (2018). The effect of layer thickness ratio on the plastic deformation mechanisms of nanoindented Ti/TiN nanolayered composite. *Computational Materials Science*, Pages 488-498, 0256, https://doi.org/10.1016/j.commatsci.2018.08.021.
- [138] Wang, J. Shi, J. Lu, Y. Jin, G. Wang, J. Jiang, Y. Zhou, Q.(2022). Deformation evolution of Cu/Ta nanoscale multilayer during nanoindentation by a molecular dynamics study. *Surface*

- *and Coatings Technology.* Volume 441, 2022, 128562, ISSN 0257-8972, https://doi.org/10.1016/j.surfcoat.2022.128562.
- [139] Sainath, G., & Choudhary, B. K. (2016). Orientation dependent deformation behaviour of BCC iron nanowires. *Computational Materials Science*. 111, 406–415. https://doi.org/10.1016/j.commatsci.2015.09.055
- [140] Wang, J., Zeng, Z., Wen, M., Wang, Q., Chen, D., Zhang, Y., Wang, P., Wang, H., Zhang, Z., Mao, S. X., & Zhu, T. (2020). Anti-twinning in nanoscale tungsten. *Sci Adv*. 3;6(23):eaay2792. doi: 10.1126/sciadv.aay27920
- [141] Li, S., Ding, X., Deng, J., Lookman, T., Li, J., Ren, X., Sun, J., & Saxena, A. (2010). Superelasticity in bcc nanowires by a reversible twinning mechanism. *Physical Review B Condensed Matter and Materials Physics*, 82(20). https://doi.org/10.1103/PhysRevB.82.205435
- [142] Kim, J. Y., Jang, D., & Greer, J. R. (2012). Crystallographic orientation and size dependence of tension-compression asymmetry in molybdenum nano-pillars. *International Journal of Plasticity*, 28(1), 46–52. https://doi.org/10.1016/j.ijplas.2011.05.015
- [143] Sainath, G., Goyal, S., & Nagesha, A. (2020). Plasticity through De-twinning in twinned BCC nanowires. *Crystals*, 10(5). https://doi.org/10.3390/cryst10050366
- [144] Tian, X., Li, D., Yu, Y., You, Z. J., Li, T., & Ge, L. (2017). Atomistic simulation study of deformation twinning of nanocrystalline body-centered cubic Mo. *Materials Science and Engineering:* A, 690, 277–282. https://doi.org/10.1016/j.msea.2017.02.105
- [145] Healy, C. J., & Ackland, G. J. (2011). MD Simulations of Compression of Nanoscale Iron Pillars. *Mater. Res. Soc. Symp.* Proc, 1369. https://doi.org/10.1557/opl.2011
- [156] Pan, Z. L., Li, Y. L., & Wei, Q. M. (2008). Molecular dynamics simulation of nanocrystalline tantalum under uniaxial tension. *Solid State Phenomena*, 139, 83–88. https://doi.org/10.4028/www.scientific.net/SSP.139.83
- [147] Li, X., Zeng, Q., & Wang, J. (2022). Twinning dynamics in nanoscale body-centered cubic tungsten. *Scripta Materialia*, 220. https://doi.org/10.1016/j.scriptamat.2022.114930
- [148] Zhong, L., Zhang, Y., Wang, X., Zhu, T., & Mao, S. X. (2024). Atomic-scale observation of nucleation- and growth-controlled deformation twinning in body-centered cubic nanocrystals. *Nature Communications*, 15(1). https://doi.org/10.1038/s41467-024-44837-8
- [149] Lindley, T.G. Smallman, R.E.The plastic deformation of polycrystalline vanadium at low temperatures, *Acta Metallurgica*, Volume 11, Issue 5,1963,Pages 361-371,ISSN 0001-6160, https://doi.org/10.1016/0001-6160(63)90161-5.
- [150] Tian, X., Li, D., Yu, Y., You, Z. J., Li, T., & Ge, L. (2017). Atomistic simulation study of deformation twinning of nanocrystalline body-centered cubic Mo. *Materials Science and Engineering:* A, 690, 277–282. https://doi.org/10.1016/j.msea.2017.02.105

- [151] Gang, Ch. Jie, W.Ch. Peng, Zh. (2017). The role of interface in uniaxial tensile process of nano-scale bilayer Cu/Ni, *Computational Materials Science*, Volume 131, 2017, Pages 21-27, ISSN 0927-0256, https://doi.org/10.1016/j.commatsci.2017.01.036.
- [152] Pang, W., Liu, A., Yang, K. et al. (2024). The effect of interface structures on deformation behavior of Cu/Ni multilayer by molecular dynamics. *Journal of Materials Research* 39, 1057–1072 https://doi.org/10.1557/s43578-024-01291-y
- [153] Yin, F. Zhao, Y. Yu, S, Pang,W. (2019). Molecular dynamics studies on the interface evolution characteristics and deformation mechanisms of Cu/Al multilayers during compression process. *J. Appl. Phys.* 125 (2): 025112. https://doi.org/10.1063/1.5055901
- [154] Zheng, Y., Shen, L., Li, Q., Ye, H., Zhang, H., & Zhang, J. (2017). Hetero interface and twin boundary mediated strengthening in nano-twinned Cu//Ag multilayered materials. *Nanotechnology*, 28(41), 415705. https://doi.org/10.1088/1361-6528/aa847c
- [155] el Chlouk, Z. G., Shehadeh, M. A., & Hamade, R. F. (2020). The Effect of Strain Rate and Temperature on the Mechanical Behavior of Al/Fe Interface Under Compressive Loading. *Metallurgical and Materials Transactions A: Physical Metallurgy and Materials Science*, 51(5), 2573 2589. https://doi.org/10.1007/s11661-020-05709-0
- [156] Lin, Z. Pang, W. Xin, K. Feng, X. Yin. F. (2020). The effect of loading strain rates on deformation behavior of Cu/Fe composite. *Physics Letters A*, Volume 388, 2021,127070, ISSN 0375-9601, https://doi.org/10.1016/j.physleta.2020.127070.
- [157] Hsu, K-Ch. Chen, J-Y. Fang, T-H. Lin, M-H. (2018).Size-dependent strength and interface-dominated deformation mechanisms of Cu/Zr multilayer nanofilms. *Results in Physics*, Volume 11, 2018, Pages 684-689, ISSN 2211-3797, https://doi.org/10.1016/j.rinp.2018.10.010.
- [158] Wei, W. Chen, L. Gong, HR. Fan, JL. (2019). Strain-stress relationship and dislocation evolution of W-Cu bilayers from a constructed n-body W-Cu potential. *J Phys Condens Matter*. 31(30):305002. doi: 10.1088/1361-648X/ab1a8a.
- [159] Lu,L. Huang, Ch. Pi, W. Xiang, H. Gao, F. Fu, T. Peng, X. (2017). Molecular dynamics simulation of effects of interface imperfections and modulation periods on Cu/Ta multilayers. *Computational Materials Science*, Volume 143,2018, Pages 63-70, https://doi.org/10.1016/j.commatsci.2017.10.034.
- [160] Chen, Y. Fang, J. Liu, L. Hu, W. Gao, N. Gao, F. and Deng, H. (2019), "Development of the interatomic potentials for W-Ta system", *Computational Materials Science*, 163, 91-99. DOI: 10.1016/j.commatsci.2019.03.021.
- [161] Daw, M.S. Foiles, S.M. Baskes, M.I. (1993). The embedded-atom method: a review of theory and applications. *Mater. Sci.* Rep. 9 251–310, https://doi.org/10.1016/0920-2307(93)90001-u.

- [162] Baskes, M. I. (1992). Modified embedded-atom potentials for cubic materials and impurities. *PHYSICAL REVIEW B* (Vol. 46). DOI: 10.1103/physrevb.46.2727.
- [163] Baskes, M. I., Lee, B. J., Kim, H., & Koo Cho, Y. (2001). Second nearest-neighbor modified embedded atom method potentials for bcc transition metals. *Physical Review B Condensed Matter and Materials Physics*, 64(18). https://doi.org/10.1103/PhysRevB.64.184102.

Appendix A: Evaluation and Selection of Interatomic Potential

Through conducting preliminary simulations of nano-indentation, we aim to establish a strong foundation of simulation modal. That goes beyond carefully selecting the most suitable interatomic potential for our research. To achieve this, we performed nano-indentations on vanadium (V) and iron (Fe) single crystals, evaluating three widely used interatomic potentials developed for these metals to determine the most appropriate one for our simulations.

Two single-crystal specimens of vanadium and iron, each with lateral dimensions of $151.3\text{Å} \times 54.2\text{Å} \times 151.3\text{Å}$ along the x, y, and z directions, respectively, were subjected to nanoindentation. A spherical indenter with a radius of R = 35 Å, moving at a velocity of 0.1 Å/ps, was employed using a repulsive force approach. The time step was set to 0.001 ps. Periodic boundary conditions were applied in the x and z directions, while a non-periodic boundary condition (PSP) was imposed along the y direction, where the indentation was performed. To prevent the displacement of atoms, a 10 Å thick fixed layer was maintained at the bottom of each sample. The equilibrium configurations of both systems were obtained through energy minimization using the conjugate gradient algorithm. Subsequently, an NVT (Nose-Hoover) thermostat ensemble was applied at T = 0.1 K to suppress thermal fluctuations that could affect the indentation results.

Under these nano-indentation conditions, simulations were performed for both metals using three different interatomic potentials to examine their influence on mechanical behavior throughout the indentation process:

- EAM1 (Mendelev et al.): An embedded-atom method (EAM) interatomic potential developed to describe metallic bonding between Fe and V atoms [86].
- EAM2 (Olsson et al.): A well-established EAM potential specifically designed for V and Fe metals [85].
- 2NN_MEAM (Choi et al.): A second-nearest-neighbor modified embedded-atom method (2NN MEAM) potential tailored for the V-Fe binary system [87].

These interatomic potentials were sourced from the Interatomic Potentials Repository hosted by the National Institute of Standards and Technology (NIST), U.S. Department of Commerce, which provides validated force fields for various materials, each optimized for specific applications. The 2NN MEAM potential for the V-Fe system was obtained directly from its developers via the official 2NN MEAM Interatomic Potentials website.

Interatomic potentials description:

In this study, two approaches are implemented in the selected interatomic potentials to describe the interactions between vanadium (V) and iron (Fe) atoms.

The first approach is the classical Embedded Atom Method (EAM), which is widely used for modeling metallic systems. EAM accounts for both pairwise interactions and many-body effects, making it particularly effective for accurately capturing metallic bonding and the cohesive behavior of transition metals.

The EAM interatomic potential was first introduced in the 1970s [161] and has since been extensively developed and refined for various metal systems. In EAM, the total energy of the system is expressed as:

$$E = \frac{1}{2} \sum_{ij} V_{ij} (r_{ij}) + \sum_{i} F_{i} (\rho_{i})$$
 (A.1) [161]

Here, E represents the total energy of the system, V_{ij} denotes the pairwise interaction potential between atoms i and j, which are separated by a distance r_{ij} , and F_i corresponds to the embedding energy of atom i within the local electron density ρ_i .

The Modified Embedded Atom Method (MEAM) was first introduced; in 1992 by Baskes and colleagues [162]. In its initial form, known as the first nearest-neighbor MEAM (1NN MEAM), only interactions between first-nearest neighbors were considered. However, to address the limitations of 1NN MEAM in modeling BCC transition metals, Baskes et al. developed the second nearest-neighbor MEAM (2NN MEAM) in 2001 [163]. This refined potential significantly improved the description of BCC metals and was subsequently extended to a wide range of transition metals, including Fe, Cr, Mo, W, V, Nb, and Ta.

More recently, in 2021, Choi et al. [87] further expanded the 2NN MEAM framework to incorporate various binary systems, including the V-Fe system, enhancing its applicability to metallic multilayers and alloys.

The MEAM pair potential is designed to compute non-bonded interactions across a wide range of materials. It serves as an extension of the original EAM by incorporating angular-dependent forces, making it well-suited for modeling metals and alloys with FCC, BCC, HCP, and diamond cubic structures, as well as materials with covalent bonding, such as silicon and carbon. In the MEAM formulation, the total energy E of a system of atoms is expressed as:

$$E = \sum_{i} \left\{ F_{i}(\bar{\rho}_{i}) + \frac{1}{2} \sum_{i \neq j} \phi_{ij}(r_{ij}) \right\}$$
 (A.2) [163]

In the MEAM formulation, F represents the embedding energy, which depends on the local atomic electron density. The term \emptyset corresponds to the pair potential interaction, which is summed over all neighboring atoms J surrounding atom I within a defined cutoff distance.

Similar to EAM, the multi-body nature of MEAM arises from the embedding energy term, which captures the influence of the surrounding atomic environment on each individual atom.

	EAM1	EAM2 (Olsson)	2NN_MEAM
	(Mendelev)		(Lee)
Bulk Modulus B(GPa)	B _V = 156	B _V = 161	$B_V = 157$
	$B_{Fe}=178$	B _{Fe} =168	B _{Fe} =173
Cohesive energy E _c (eV)	$E_{c(V)} = -5.019$	$E_{c(V)} = -5.31$	$E_{c(V)} = -5.30$
	$E_{c(Fe)} = -3.995$	$E_{c(Fe)} = -4.28$	$E_{c(Fe)} = -4.29$
Lattice constant(Å)	$a_{V}=3.03$	$a_{V}=3.03$	$a_V = 3.031$
	$a_{Fe} = 2.8553$	$a_{Fe} = 2.87$	$a_{Fe} = 2.863$

Table A.1 Bulk modulus B (GPa), cohesive energy $E_c(eV)$, and lattice constant(Å) for V and Fe according to each used potential in this study.

Indentation response of Fe, and V single-crystals for different potentials:

Figure A.1 presents the indentation load vs. depth curves for Fe and V single crystals using the three different interatomic potentials. In all cases, the load gradually increases with indentation depth until the first yielding event, which is marked by a sudden drop in load values. Interestingly, this yielding transition is absent in the case of the MEAM potential for both V and Fe, resulting in a linear indentation curve with no distinct transition between the elastic and plastic deformation regimes.

Additionally, Figure A.1 demonstrates that the EAM1 (Mendelev) potential closely follows the Hertzian solution for the elastic regime in both Fe and V single crystals, a behavior also observed with EAM2 (Olsson). However, a notable difference is that the EAM2 potential overestimates the yield stress compared to EAM1, leading to an earlier onset of plastic deformation. Moreover, the EAM1 potential exhibits the most extended elastic regime, whereas EAM2 results in a quicker transition to plasticity for both Fe and V.

The fluctuations observed in the indentation curves for both EAM potentials suggest variations in the plastic deformation mechanisms, likely caused by the generation and interaction of dislocations. In contrast, the 2NN_MEAM (Lee) potential produces flat indentation curves for both Fe and V single crystals, indicating a different mechanical response.

To gain deeper insight into the plastic deformation mechanisms in Fe and V single crystals across all tested interatomic potentials, dislocation extraction analysis (DXA) using OVITO is employed in the following section to illustrate the evolution of dislocations during indentation.

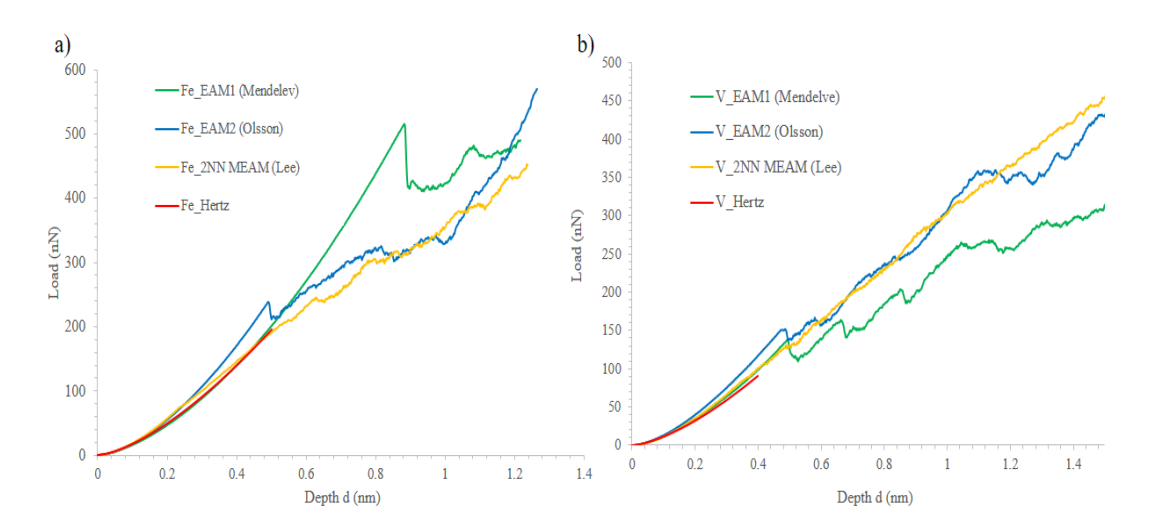


Fig A.1 Indentation load-depth curves for Fe and V single-crystals, using different interatomic potentials.

Deformation mechanisms of Fe and V single crystals:

Fig A.2 and A.3 present the DXA analysis for Fe and V single crystals at the same advanced indentation depth (d=1.2nm for Fe and d=1.4nm for V), to describe the plastically deformed region beneath the indented surface in the three different cases of interatomic potential. Dislocations development analysis demonstrate that there are not any perfect dislocation segments detected in the plastic deformation region at an advanced indentation loading d=1.2nm of Fe single crystal in the case of 2NN_MEAM (Lee) potential. While there is just one dislocation segment with Burgers vector a/2 <111>, detected in V single crystal at an indentation depth d=1.4nm. However, 0.5% and 0.1% of HCP atoms can be found under the indented surface of Fe and V specimens respectively, besides some FCC atoms, which indicates the phase transition during the plastic deformation.

In the case of the EAM potentials, more dislocation segments can perceived in the plastic deformation zone for both metals. For the case of EAM1 (Mendeleve) potential, 19 dislocations segments with Burgers vectors a/2<111> and a<100> are seen propagated under the indented surface of Fe sample besides the appearance of some FCC atoms. Indicating that slip deformation is the main deformation mechanism during indentation of BCC iron. While, four dislocation segments with Burgers vectors a/2<111> are detected in V specimen at d=1.4nm. In the meanwhile, many planer defects may reflect each other indicating that twining deformation may dominates the plastic deformation of BCC vanadium. Conversely, increased number of dislocation segments is observed in the case of EAM2 (Olsson) potential for both Fe and V. Only perfect dislocations emission are seen in the indented Fe and V specimens with Burgers vectors a/2<111> and a<100>, and no planer defects can be seen. Considerably, greater number (14 dislocations segments) is noticed for V single crystal. One can deduce that the EAM2 (Olsson) potential over generates the dislocations without allowing for the phase transition or twining deformation. While, 2NN_MEAM (Lee) potential underestimate the

dislocations propagation even though the advanced stage of indentation for both iron and vanadium. It seems like this potential is more suitable for phase transition. That explain the flat indentation curves obtained through this potential. In contrast, the EAM1 (Mendeleve) potential provides reasonable approximation of dislocation emission, phase transition and twin planes.

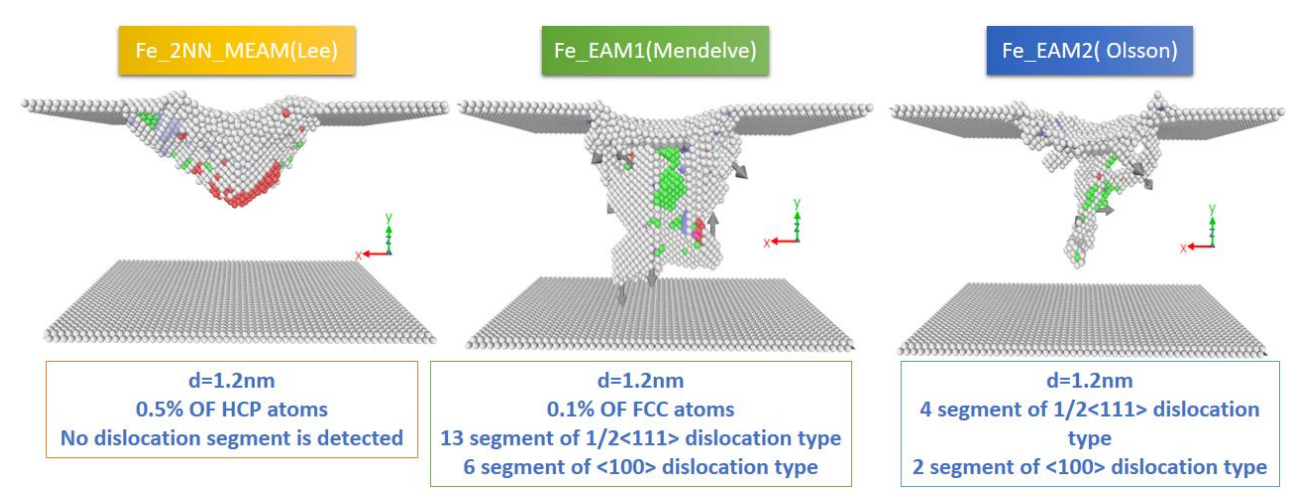


Fig A.2 DXA analysis for Fe single crystal at d=1.2nm for different interatomic potentials (Red atoms represent HCP atoms, FCC atoms on green and defected atoms are on gray color)

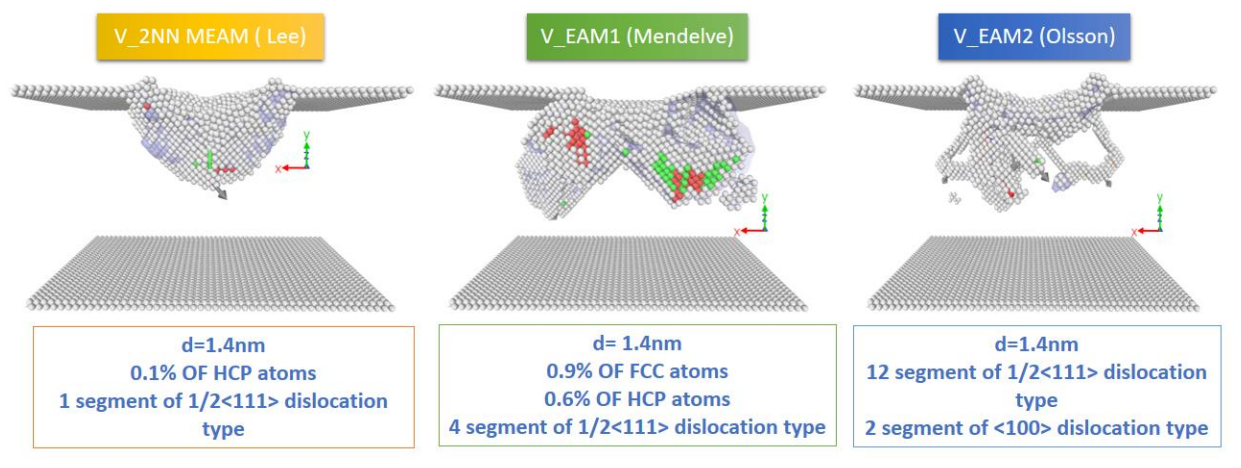


Fig A.3 DXA analysis for V single crystal at d=1.4 nm for different interatomic potentials.

The EAM potential developed by Mendelev was originally designed for point defect calculations, offering a balance between accuracy at the defect level and the ability to handle large supercells. This allows it to capture both short-range electronic effects and long-range strain fields effectively [86]. Olsson [85] expanded on this by developing EAM potentials for Fe and V, using them to investigate point defect properties. The parameters of this potential ensure continuity of the third-order elastic constants and are fitted to cohesive energies. However, the higher cohesive energy in this potential may contribute to an overestimation of dislocation emission. In contrast, the 2NN MEAM potential, developed by Baskes and colleagues, has been shown to be crucial for accurately modeling complex atomic rearrangements during phase transitions. This potential also provides better predictions for phase stability, which is key for understanding the behavior of metals under varying thermodynamic conditions. These findings support the conclusion that the choice of interatomic

potential significantly impacts the resulting deformation mechanisms, especially with regard to the description of elastic-plastic deformations and the generation of dislocations and planar defects. This aligns with the predictions from numerous previous studies.

Conclusion:

This study led us to the conclusion that the choice of the interatomic potential has a strong implication on the outcomes of Nano indentation process. It can affect the incidences of elastic deformation and/or the description of dislocation generation at advanced indentation stage.

Appendix B: Atomistic Insights into the Invers Effects of Semi-Coherent Interfaces during Nano-indentation of Ta/W and W/Ta Bilayers

For the study of BCC/BCC semi-coherent interfaces during nano-indentation of Ta/W and W/Ta bilayers, we followed the same simulation methodology as used for the nano-indentation of the V-Fe bilayer described in Chapter II. The only difference lies in the model size, which was adjusted to $319.12 \times 104.2 \times 319.12$ Å, to account for the minor lattice mismatch between Ta and W metals. Ta and W single crystals have lattice constants of $a_{Ta} = 3.291$ Å and $a_{W} = 3.1586$ Å, respectively, resulting in a 1.91% lattice mismatch. This mismatch leads to longer misfit dislocation spacing and larger coherent regions. Despite this, the Ta-W bilayer with semi-coherent interfaces exhibits the same misfit dislocation (MFD) network for the (100) crystallographic orientation. The interatomic potential used for this study is the one developed by Y. Chen et al. (2019) [160], which is well-suited for our work, as it provides the best description of both elastic and plastic deformation mechanisms for the Ta-W bimetal system.

Nano-indentation curves of Ta/W and W/Ta bilayer systems compared with single crystals:

The nano-indentation curves shown in Fig. B.1 reveal that the W single crystal exhibits the highest load values, while the Ta single crystal shows the lowest. The Ta/W bilayer system demonstrates a strengthening effect, whereas the W/Ta bilayer system shows a softening effect. In terms of hardness, at the end of the indentation, W proves to be the hardest material, followed by the Ta/W bilayer, which also contributes to the hardening of the system. Conversely, the W/Ta bilayer displays the lowest hardness values. To understand the underlying mechanisms behind these strengthening and softening effects observed in the W-Ta bilayer systems, a detailed analysis of the plastic deformation behavior in each system is provided below, beginning with the individual W and Ta single crystals.

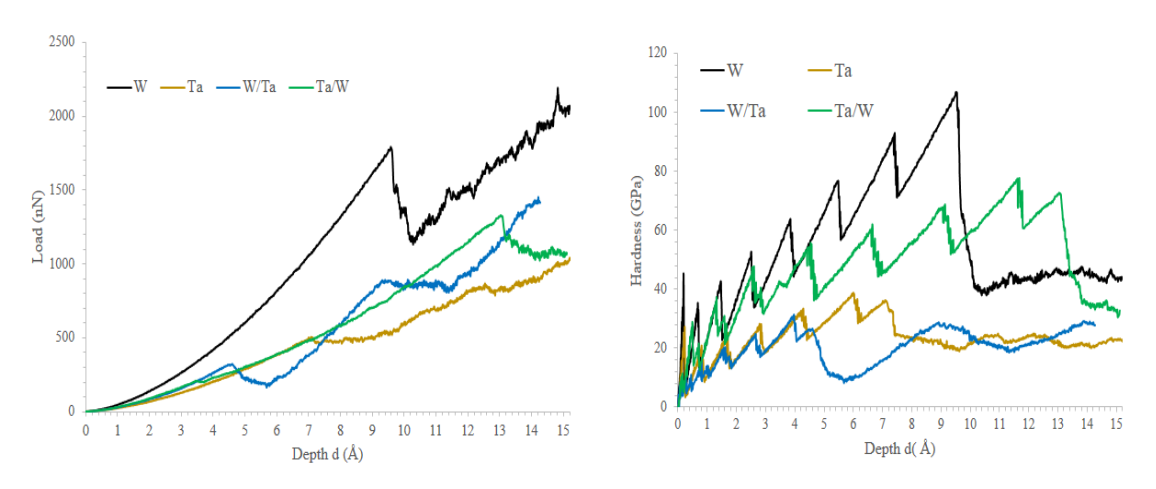


Fig B.1 Indentation load-depth & hardness-depth curves of $Ta_{(010)}$, W(010) single-crystals, and $Ta/W_{(010)}$, $W/Ta_{(010)}$ bi-layers.

Plastic deformation of Ta single crystal:

The plastic deformation of the Ta single crystal initiates at an indentation depth of d=7.14Å (see Fig. B.2) through the nucleation of planar defects in the {101} <111> twin system, indicating that twinning is the predominant deformation mechanism. At d=7.94Å, the plastic deformation transitions into slip deformation, with four dislocation segments with Burgers vectors a/2 <111> nucleating beneath the indented surface. As indentation progresses to d=8.54Å, more dislocations are generated and propagate along the preferred slip systems. By d=11.44Å, a shear loop with Burgers vector a/2 <111> extends vertically through the specimen. At d=13.44 Å, additional dislocations evolve into 1/2 <111> shear loops, and continue to extend until d=15Å. It can be inferred that the plastic deformation of the Ta single crystal is governed by a competition between twinning and slip mechanisms. During the early stages of plastic deformation, twinning dominates, but as indentation proceeds, slip deformation becomes the primary mechanism, driven by the emission and transmission of 1/2 <111> and <100> dislocations.

Plastic deformation of W single crystal:

For the W single crystal, plastic deformation is delayed compared to the Ta single crystal, as evidenced by the sharp drop in load values shown in Fig. B.1. this suggests the nucleation of dislocations with Burgers vectors a/2 <111> at d=9.72Å (see Fig. B.3). At d=10.22Å, the number of dislocations increases, and they interact with each other, generating additional dislocations with Burgers vectors a <100>. As the indentation progresses to d=11.52Å, further emission of 1/2 <111> and <100> dislocations is observed. These dislocations evolve into shear loops at d=12.72Å. The extension and interaction of these dislocations lead to the formation of nodes and junctions at d=13.52Å. By the end of the indentation, at d=15Å, it can be concluded that slip deformation is the primary deformation mechanism in the W single crystal. The plastic deformation of Ta is a combination of slip and twinning, starting with twinning, as observed in the V single crystal. However, the plastic deformation of the W single crystal more closely resembles the slip deformation mechanism observed in the Fe single crystal.

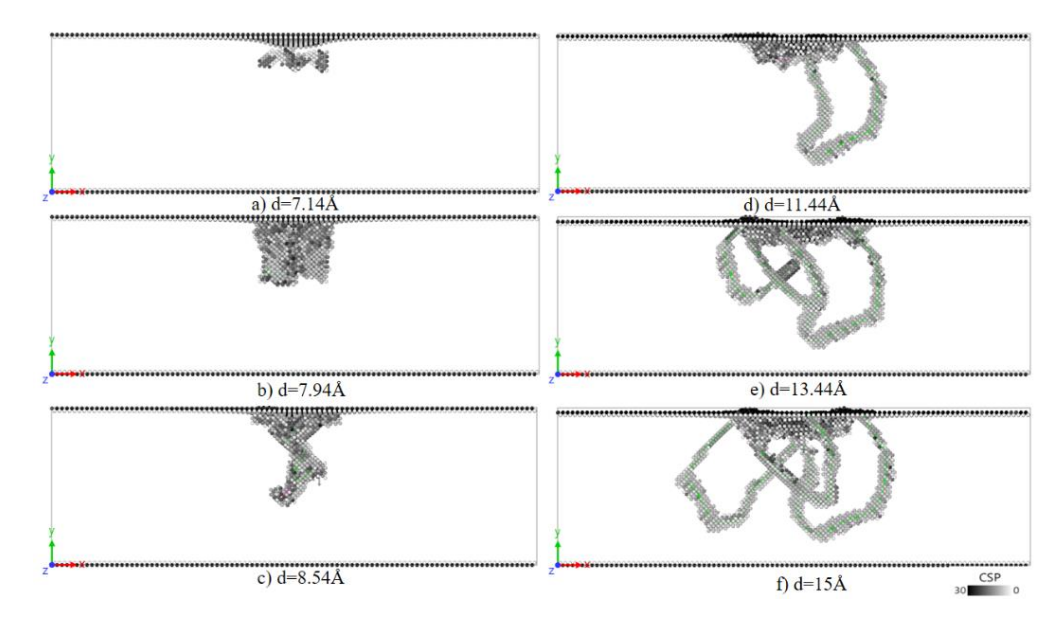


Fig B.2 CSP (cento-symmetry parameter) analysis for defected atoms during plastic deformation of Ta single crystal at different indentation depths.

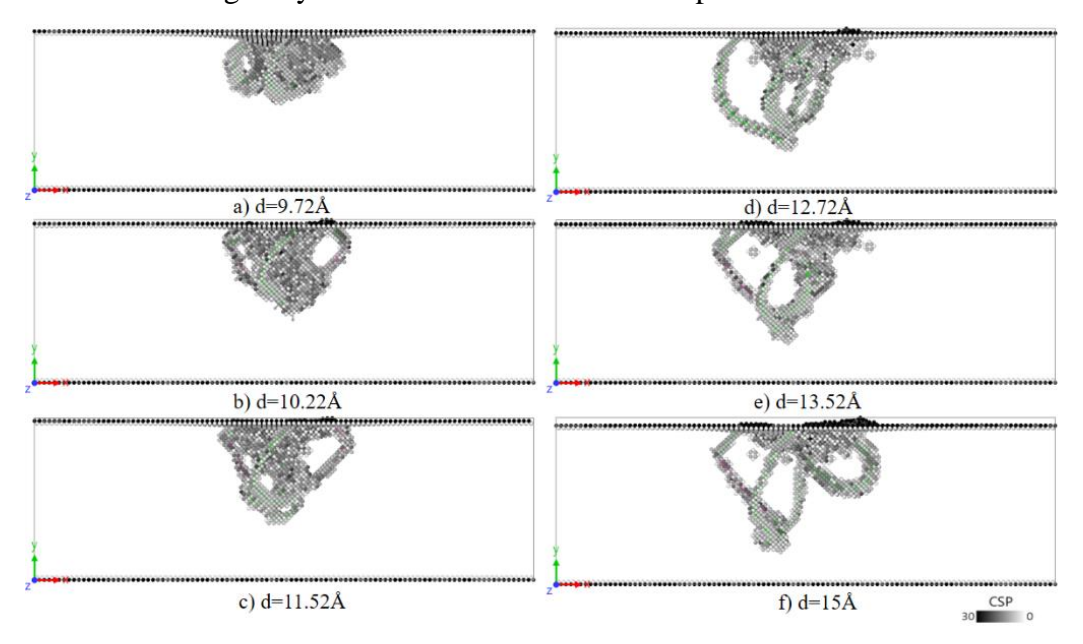


Fig B.3 Cento-Symmetry analysis (CSP) for defected atoms during plastic deformation of W single crystal with different indentation depths.

Plastic deformation of Ta/W bilayer:

The Ta/W bilayer system initially deforms elastically until a slight yield point appears in the load curve. This yield point is attributed to the nucleation of a dislocation loop with a Burgers vector a/2 <111> at an MFD node at d=3.6Å (see Fig. B.4). This nucleation is likely induced by the stress from indentation loading, as the other MFD nodes remain unaffected, and the Ta layer continues to deform elastically.

The nucleated dislocation loop extends horizontally and accumulates in the Ta layer without disrupting the system's elastic regime at d=5.53Å. Subsequently, planar defects nucleated from the indented surface interact with this dislocation loop, revealing the blocking effect of the interface. Notably, the dislocation-interface interaction does not cause a drop in the indentation curve, indicating that the MFD network effectively acts as a barrier to dislocation transmission.

At d=9.13Å, dislocations become trapped at the interface, unable to penetrate the W layer. As indentation proceeds to d=12.93Å, shear loops with Burgers vectors a/2 <111> extend horizontally along the interface but do not transmit into the W layer. With further indentation (d = 13.4 Å), new prismatic loops with a/2 <111> Burgers vectors nucleate at several MFD nodes, causing the sharp yielding observed in the load curve (Fig. B.1).

By the end of indentation (d=15Å), defected atoms from the indented surface begin to penetrate the W layer, as they no longer encounter MFDs to interact with. However, the sustained horizontal extension of dislocations at the interface confirms the significant blocking effect of MFDs, which ultimately contributes to the observable hardening at the final stages of indentation.

Plastic deformation of W/Ta bilayer:

The W/Ta bilayer system initially deforms elastically until a sudden drop in load values, which occurs due to the rapid expansion of 1/2 <111> shear loops in four directions within the Ta layer at d=4.6Å. This expansion results from the decomposition of misfit dislocations inside the Ta layer (see Fig. B.5), while the top W layer continues to deform elastically. At d=9.4Å, a significant extension of these dislocations is observed within the Ta layer, indicating the onset of extensive plastic deformation. As indentation progresses to d=12.3Å, planar defects nucleate from the indented surface, accompanied by defected W atoms penetrating the Ta layer, leading to the second yielding event in the load curve (Fig. B.1). By d=13.3Å, numerous dislocations with Burgers vectors a/2 <111> and a <100>, initially emitted from the W indented surface, propagate freely into the Ta layer without encountering any significant barriers. Finally, at the end of indentation (d =15Å), multiple dislocations interact and continue to propagate unhindered, as no effective obstacles are present to restrict their motion.

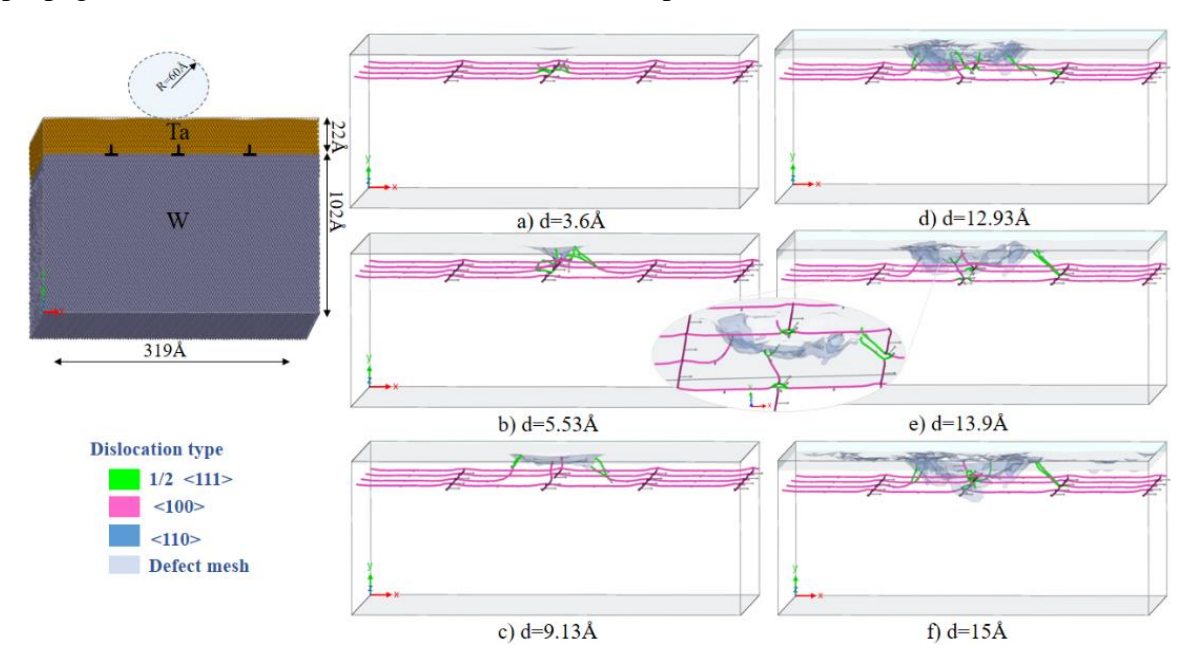


Fig B.4 dislocations evolution analysis (DXA) during plastic deformation of Ta/W bilayer system at different indentation depths.

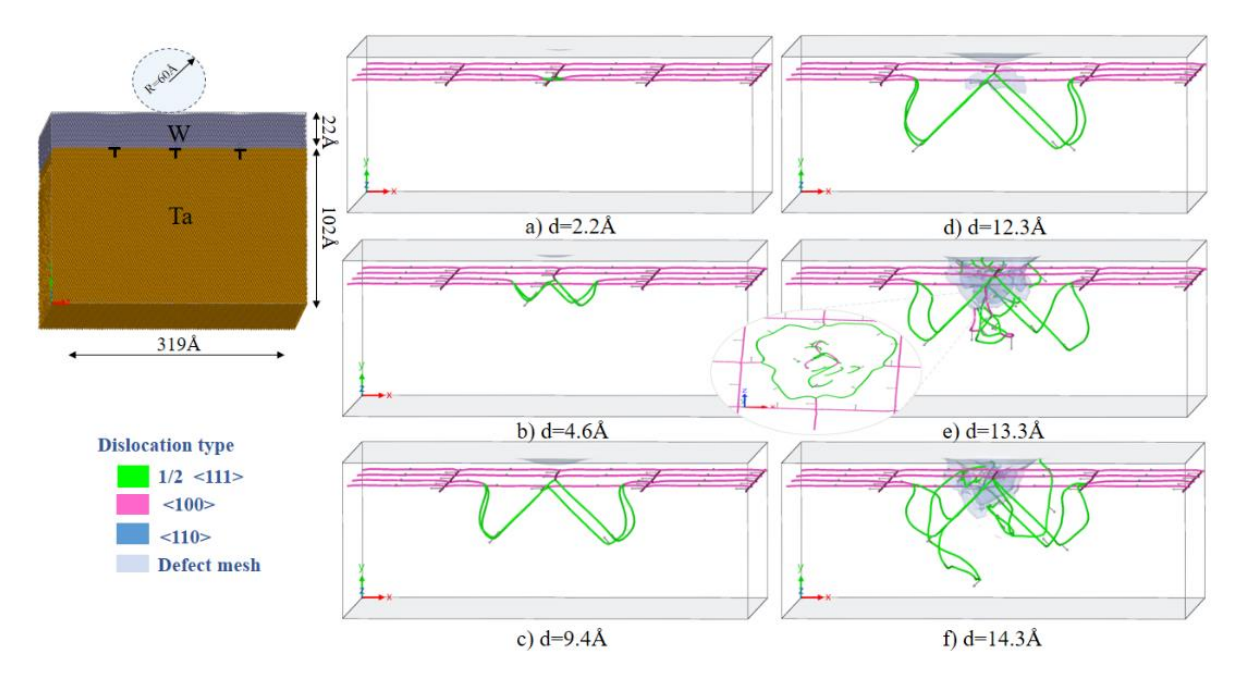


Fig C.5 dislocations evolution analysis (DXA) during plastic deformation of W/Ta bilayer system at different indentation depths.

Conclusion:

The BCC/BCC semi-coherent interface exhibits opposing effects in Ta/W and W/Ta bilayer systems, leading to strengthening in the first and softening in the later. In the Ta/W bilayer system, the interface acts as a barrier to dislocation propagation, effectively enhancing the material's resistance to plastic deformation. Conversely, in the W/Ta bilayer system, the interface facilitates dislocation slip due to the decomposition misfit dislocation (MFD) nodes, allowing them to move easily into the Ta layer, even while the W indented surface remains in the elastic regime.

These dissimilar effects were previously observed in V-Fe bilayers, further reinforcing their significance. Notably, for the first time, our study provides direct validation of Koehler's (1970) theoretical predictions, where he proposed W and Ta as an ideal BCC bimetal system to illustrate his theory of energy and stress barriers in multilayers. This breakthrough marks the first experimental confirmation of a 54-year-old assumption, bridging decades of theoretical insight with computational evidence.

Abstract

This thesis investigates the role of BCC/BCC semi-coherent interfaces on the mechanical response of V/Fe bilayers under nano-indentation, tension, and compression. Using atomistic simulations, we analyze the effects of layer thickness, indenter position, and crystallographic orientation. Our findings reveal that the V/Fe interface acts as a dislocation barrier during nano-indentation, enhancing hardness through blocking dislocation propagation. This effect is more pronounced for thinner V layers, aligning with the Hall-Petch model. On the other hand, in Fe/V bilayers, the interface promotes dislocation propagation, allowing the decomposition of lattice dislocations in the substrate and leading to a softening effect consistent with the inverse Hall-Petch effect. These results are also observable in the V-Fe-V and Fe-V-Fe multilayers. Under uniaxial loading, analytical investigations of plastic deformation mechanisms during tension and compression reveal a complex interplay between anti-twinning/ twinning and slip deformations in both V and Fe layers. Tension strengthens the V/Fe bilayer due to the decomposition of misfit dislocation inside V layer and anti-twinning in Fe. Whereas, Softening is observed during compression as deformation initiates in the softer V layer via phase transition. While misfit dislocations decompose inside Fe, activating slip deformation. This tension/compression asymmetry of the V/Fe bilayer is driven by shear strain evolution at the interface. This study provides fundamental insights into dislocation-interface interactions, strengthening mechanisms, and deformation anisotropy in nano-scale metallic multilayers.

Résumé

Cette thèse explore les interactions dislocation-interface, les mécanismes de renforcement et l'anisotropie de déformation dans les multicouches métalliques nanométriques. À travers des simulations de la dynamique moléculaire, nous analysons la réponse mécanique des bicouches V/Fe sous nano-indentation, traction et compression, en tenant compte de l'épaisseur des couches, de la position de l'indenteur et de l'orientation cristallographique. Nos résultats montrent que l'interface V/Fe agit comme une barrière aux dislocations sous nano-indentation, renforçant la dureté, en particulier pour des couches de vanadium inférieures à 50Å, conformément au modèle de Hall-Petch. En revanche, dans les bicouches Fe/V, l'interface favorise la propagation des dislocations, permettant la décomposition des dislocations de réseau dans le substrat et entraînant un adoucissement en accord avec l'effet inverse de Hall-Petch. Sous chargement uniaxial, la bicouche V/Fe se renforce en traction grâce à la décomposition des dislocations dans V et l'anti-maclage dans Fe, tandis qu'en compression, une transformation de phase dans V et la décomposition des dislocations dans Fe induisent un adoucissement. Cette asymétrie est dictée par l'évolution des contraintes de cisaillement à l'interface.

ملخص

تستكشف هذه الأطروحة تفاعلات الانخلاعات مع الواجهة، وآليات التقوية، وعدم تجانس التشوه في الطبقات المعدنية النانوية. من خلال محاكاة الديناميكيات الجزيئية، نقوم بتحليل الاستجابة الميكانيكية للطبقات الثنائية V/Fe تحت تأثير الاختراق النانوي، والشد، والضغط، مع الأخذ بعين الاعتبار سمك الطبقات، وموضع المُخترِق، والاتجاه البلوري. تُظهر نتائجنا أن واجهة V/Fe تعمل كحاجز أمام الانخلاعات أثناء الاختراق النانوي، مما يؤدي إلى زيادة الصلابة، لا سيما في الطبقات الرقيقة من الفاناديوم التي تقل سماكتها عن 50Å، وذلك وفقًا لنموذج Hall-Petch. وعلى العكس، في الطبقات الثنائية Fe/V، تسهّل الواجهة انتشار الانخلاعات، مما يؤدي إلى التلبين، بما يتماشى مع التأثير العكسي لـ Hall-Petch. تحت تأثير التحميل الأحادي المحور، تزداد صلابة الطبقة الثنائية V/Fe عند تعرضها للشد بسبب تحلل الانخلاعات في الفاناديوم وظاهرة "مضاد التوأمة" في الحديد إلى حدوث التليين.